



Universität für Bodenkultur Wien

Department für Nanobiotechnologie

Vorstand: Univ. Prof. Dr. José Luis Toca-Herrera

Betreuer: Prof. Dr. Wolfgang Knoll

DEVELOPMENT OF AN OLFACTORY BIO-NANO-SENSOR SYSTEM
BASED ON
REDUCED GRAPHENE OXIDE FIELD EFFECT TRANSISTOR

Dissertation

zur Erlangung des Doktorgrades

an der Universität für Bodenkultur Wien

Eingereicht von

Dipl. Ing. Caroline Kotlowski

Wien, Mai 2016

Abstract

The evolutionary conservation of the sense of smell tells how important and well-functioning it is. Olfactory proteins (odorant binding proteins, OBPs) are capturing selectively a set of small molecules and therefore deciding which ones are sensed to be odorous and which ones not. Inspired by these proteins, the latest generation of biosensors relies on the binding capabilities of odorant binding proteins, communicatively linked to an electronic transducer. Along these lines a reduced graphene oxide field effect transistor is presented in this thesis, functionalized by an odorant binding protein, for the real-time detection of unlabeled small molecules - like odorants - in a concentration dependent manner. The results demonstrate the suitability of AmelOBP14 - the odorant binding protein from the honey bee *Apis mellifera* - for biosensors, when immobilized, it is able to bind and discriminate selectively ligands. Furthermore the recombinant odorant binding proteins can be engineered adapting the affinity range of the sensor. The biosensor is demonstrated for the screening of potential interaction partners of odorant binding proteins from the beetle *Tribolium castaneum*. The OBPs TcasOBP9A and B were identified as capture molecules for agriculture pest markers 6-Methyl-5-hepten-2-one (Sulcatone) and 3-Octanol. Deciphering the odorant's capability i) to interact with proteins and ii) to activate the insect's olfactory response of the antenna was investigated with two biosensors, in-vitro and in-vivo. The in-vitro method is an OBP-functionalized reduced graphene oxide - field effect transistor (rGO-FET) based sensor which monitors the odorant interaction with the odorant binding protein. A second, orthogonal method was capable to identify the odorant's capability to activate the insect's olfactory response of the antenna in-vivo.

Beside the detection of weak binding small ligands for odorant binding proteins, applications for medical diagnostics like the detection of the interaction of antibodies, food derived toxins and aptamer based hormone detection is shown with the biosensor.

This thesis introduces the bioelectro-interfacial nano-sensor for real-time and high-throughput, quantitative analysis of protein-ligand interactions based on reduced graphene oxide - field effect transistor sensing.

Keywords

Reduced graphene oxide field effect transistor, liquid gate, biosensor, olfaction, odorant binding protein, molecular recognition, Langmuir model, antibody-antigen interaction, food toxins, aptamer, immobilization

Abbreviations

ΔI_{DS}	Change in source-drain current
AmelOBP14	Odorant binding protein 14 of the honey bee <i>Apis mellifera</i>
BmorPBP1	Pheromone binding protein 1 from the silk moth <i>Bombyx mori</i>
CD	Circular dichroism
DNA	Deoxyribonucleic acid
FT-IR	Fourier transform infrared spectroscopy
k_{on}	Reaction rate constant of the association; [$s^{-1} * M^{-1}$]
k_{off}	Reaction rate constant of the dissociation; [s^{-1}]
K_A	Affinity constant defined as k_{on}/k_{off} ; [M^{-1}]
OBP	Odorant binding protein
PNA	Peptide nucleic acid
rGO-FET	Reduced graphene oxide field effect transistor
TcasOBP9A & Tcas OBP9B	Odorant binding protein 9 A and B of the red flour beetle <i>Tribolium castaneum</i>
Θ	Surface coverage
$C_{Odorant}$	Concentration of the odorant

Content

1 INTRODUCTION	6
1.1 Biosensor definition	6
1.2 Graphene for bio-sensing	7
1.2.1 Structure.....	7
1.2.2 Properties of graphene.....	7
1.3 Bio-electronic sensing applications	8
2 PRODUCTION OF GRAPHENE	9
2.1 Overview	9
2.2 Synthesis of reduced Graphene Oxide (rGO)	10
3 THEORETICAL ASPECTS	11
3.1 Zero band gap calculations of ideal graphene	11
3.2 Band gap in graphene	12
3.2.1 Single layer graphene on SiO ₂	12
3.2.2 Bilayer graphene.....	13
3.3 Semiconducting field effect transistor	14
4 INSECT OLFACTION	15
4.1 Odorant binding proteins	16
4.2 AmelOBP14	16
4.3 TcasOBP9A & TcasOBP9B	17
4.4 BmorPBP1	18
5 ELECTRICAL MEASUREMENTS	20
6 LANGMUIR MODEL BASED AFFINITY EVALUATION	21
7 AIMS OF THE THESIS	25
8 SUMMARY OF RESULTS AND THEIR SIGNIFICANCE	26
9 PAPERS	28

9.1 Electronic Olfactory Sensor Based on <i>A.mellifera</i> Odorant Binding Protein 14 on a Reduced Graphene Oxide Field-Effect Transistor (supplementary information attached).....	28
9.2 Electronic Biosensing with Functionalized rGO FETs.....	47
9.3 Electronic Olfactory Biosensor Based on Honeybee Odorant Binding Protein 14 on a rGO FET	59
9.4 Honey bee odorant-binding protein 14: effects on thermal stability upon odorant binding revealed by FT-IR spectroscopy and CD measurements (supplementary information attached)	88
9.5 Insights into structural features determining odorant affinities to honey bee odorant binding protein 14 (supplementary information attached)	102
9.6 Monitoring Crop Disease Markers by Odorant Binding Proteins of <i>Tribolium castaneum</i> – Electroantennograms versus Reduced Graphene-Oxide Based Electronic Biosensor	114
10 FURTHER PRELIMINARY DATA.....	131
10.1 Aptamer based 17 β -estradiol sensing with rGO-FET	131
10.2 Kinetic analysis of the aptamer –17 β -estradiol	131
11 REFERENCES	133

1 Introduction

1.1 Biosensor definition

A sensor is defined as a component which responds qualitatively or quantitatively to its environment, sensing either physical (heat, temperature, humidity, pressure, acoustic, light, acceleration, or chemical stimuli (pH, ion-strength, electrochemical potential). The physical or chemical effects are recorded and electrically transduced. A biosensor additionally has an analyte sensitive biological recognition element, which is a biologically derived material or a biomimetic receptor. The recognition is transduced electrochemically, optically, piezo-electrically, gravimetrically or pyro-electrically.

Historically, the demand to monitor glucose in diabetes patients drove the development of one of the very first biosensors. The need for analytical and diagnostic tools for diseases, environmental and agricultural issues, etc. is continuously growing, new discoveries including but not limited to disease markers, foodborne pathogens and toxins, crop pest markers, of antibiotics or genetic engineering in food, vitamins are potential recognition elements for biosensor applications.

Recently biosensor developments are intended to go beyond analyte sensing of known molecular interactions, but to screen for unknown binding ligands and therefore enable field effect transistor based analytical bio-chemistry.

1.2 Graphene for bio-sensing

1.2.1 Structure

The discovery of the graphene's intriguing electrical properties (Nobel prize in Physics in 2010), paved the way for surface sensitive sensor applications. Graphene is defined as one, or a few layer of two dimensional carbon lattice [1]. Figure 1 shows schematically the graphene sheet honeycomb like structure consisting of sp^2 hybridized carbon atoms (Figure 1, left side). Such nano-sheets serve as exciting new material whose properties are steadily rediscovered to be more than one would suggest. The graphene's optical, magnetic, thermal, and mechanical properties idle potential for new bio-sensing applications [2,3,4].

1.2.2 Properties of graphene

However, the ongoing discovery of substrate dependent electron transfer properties are attributing graphene to be a building block material with tunable electronic features: it's electronic structure is enabling electrochemical sensing, electro-chemiluminescence, electro-catalysis, electrochemical energy conversion and various field effect transistor designs (FETs) [5,6].

This thesis focuses on bio-sensing with graphene based field effect transistors (FETs) aiming the design of a biosensor for the real-time detection of weak binding small molecules (~200 MW). In the last few years it was shown that graphene based FETs have a significant potential for classical sensing molecular interactions, e.g. antigen-antibody. In particular the potential for fluorescent or electrochemical label free bio-sensing is given by the surface sensitive electronic properties of graphene based FETs. The following figure 1 shows schematically the graphene based FET principle (Figure 1 right side).

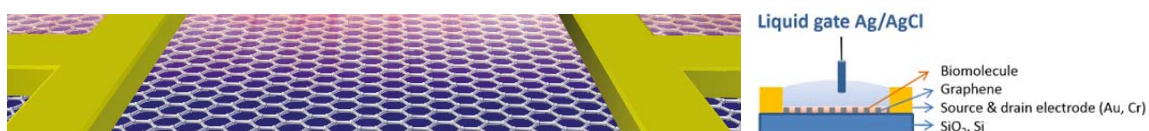


Figure 1. Graphene based field effect transistor. Left side: Graphene with its hexagonal crystal structure between gold electrodes. Right side: Scheme of the biosensor setup showing the source and drain electrodes, the gate electrode for tuning of the transistor, the semiconducting graphene based layer and the bio-recognition layer in liquid.

1.3 Bio-electronic sensing applications

Graphene FET based biosensors have shown enhanced performance in terms of sensitivity and field effect mobility. One-dimensional nanomaterials such as carbon nanotubes and silicon nanowires are competing in sensitivity and selectivity, however, graphene as a two-dimensional material shows similar potential [7,8] and offer additionally robustness and flexibility [9].

This chapter will emphasize recent progresses graphene based FETs in the detection of biological molecules like DNA or proteins. This started with the study by Mohanty et al in 2008 which shows the detection of DNA [10], followed by the more complex DNA mismatch identification [11], and recently the ultrasensitive detection of DNA was also realized (Figure 2) [12].

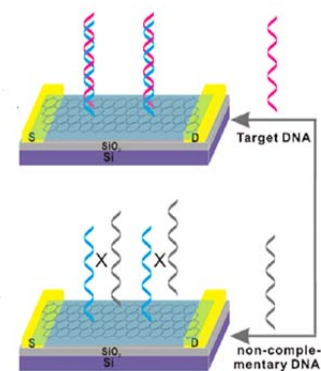


Figure 2. (Source: Cai et al. [12]) Scheme of the graphene based FET biosensor for the detection of DNA by PNA-DNA hybridization, and target binding or non-target induced stopped binding.

Next to DNA sensing, a successful concept is the use of proteins. The immobilization on the graphene is causing transistor responses if the analyte is bound. This was shown for the analytes: Immunoglobulin E protein [13], glucose [14], catecholamine [15], malaria infected cell recognition [16], and the ultrasensitive detection of the prostate specific cancer marker [17] (Figure 3).

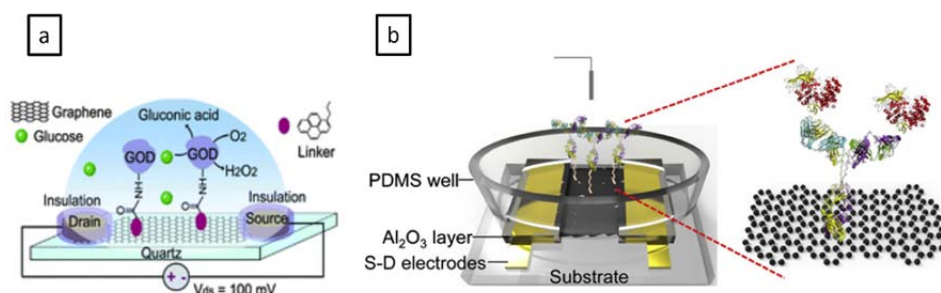


Figure 3. (a) (Source: Huang et al. [14]) Schematic illustration of the biosensor for the detection of glucose with glucose oxidase as recognition element; (b) (Source: Kim et al. [17]) Biosensor scheme for sensing of alpha1-antichymotrypsin / prostate specific antigen complex formation.

2 Production of graphene

2.1 Overview

Historically the first graphene production was realized by mechanical exfoliation using adhesive tape by Novoselov and colleagues in 2004 [18]. Notably, these graphene sheets were used to realize the first protein-aptamer sensing with FETs. Figure 4 shows Atomic force images of a graphene sheet obtained by this method before and after the functionalization with aptamers [13]. Common methods for the production of graphene and their advantages and drawbacks were reviewed by Bai and Shen in 2011, and listed in table 1 [19], some of these methods were used for the fabrication of FETs and used for bio-sensing applications (Table 2).

In this thesis the chemical reduction of graphene oxide was applied for the production of graphene based FETs, which is offering a low cost, simple and efficient method, compared to mechanical exfoliation and chemical vapor deposition grown graphene.

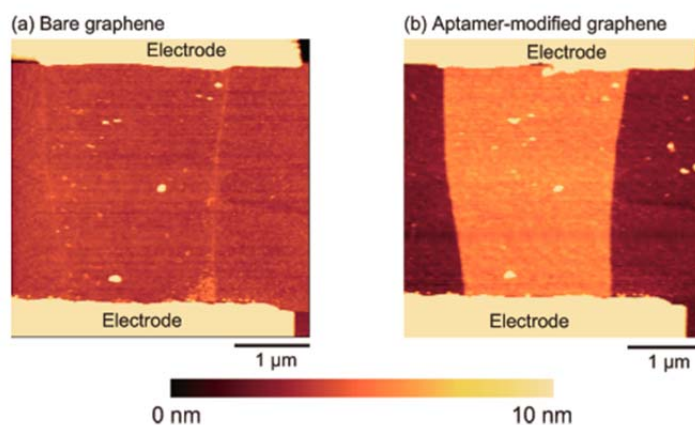


Figure 4. (Source: Ohno et al. [13]) (a) Atomic force microscopic image of a graphene based FET with a bare graphene layer between the electrodes. (b) Atomic force microscopic image of the graphene based FET with an aptamer-modified graphene layer between the electrodes.

Table 1. (Source: Bai et al. [19]) Advantages and disadvantages of various graphene synthesis techniques. (Abbreviations: GN=graphene; CVD=chemical vapor deposition; CNTs=carbon nanotubes; CMG=chemically modified graphene; GO=graphene oxide; RGO=reduced graphene oxide)

Synthesis technique	Description	Product	Advantages	Disadvantages
micromechanical exfoliation	exfoliation from bulk graphite using Scotch tape	GN particles	simple process, few defects	small area, low yield,
CVD	surface segregation of carbon or decomposition of hydrocarbons.	GN films	large area	low yield, poor scalability
epitaxial growth	high temperature evaporation of Si on SiC wafer surfaces	GN films	few defects	costly method, small area, low yield
longitudinal "unzipping" of CNTs	Ar plasma etching or edge oxidation	GN nanoribbons	high yield, controllable widths, smooth edges	poor scalability
organic synthesis	stepwise organic reactions to extend polycyclic aromatic hydrocarbons	GN quantum dots (QDs)	few defects, easy scalability	small area, costly method
colloidal suspension	exfoliation suspension of graphite or graphite derivatives	CMG/GO/RGO nanosheets	high yield, large area, easy scalability	significant numbers of defects

Table 2. Graphene synthesis technique combined with biosensing applications.

Technique	Biosensing application	Reference
Mechanical exfoliation	Immunoglobulin E protein-aptamer complex detection	[13]
Chemical vapor deposition epitaxial growth	Bacteria and metabolic activities; catecholamines from cells	[14, 15]
Chemical exfoliation	alpha1-antichymotrypsin	[17]

2.2 Synthesis of reduced Graphene Oxide (rGO)

The production of rGO-sheets is performed in three steps: oxidizing graphite, which expands the crystal structure, thus breaking the inter-layer pi-electron compound which leads to exfoliation, and finally resulting the graphene-oxide sheets are reduced with hydrazine to obtain graphene (Figure 5). Since the obtained result is usually not completely reduced graphene it has become common to refer to it as reduced graphene oxide. Methods for the reduction of graphite commonly base on Hummer's method [22]. The obtained GO is exfoliated by stirring in water, also ultra-sonication has been reported [23]. Chemical, thermal and electrochemical reduction methods are used, whereas the thermo-chemical reduction with hydrazine is commonly used [20, 21, 24].

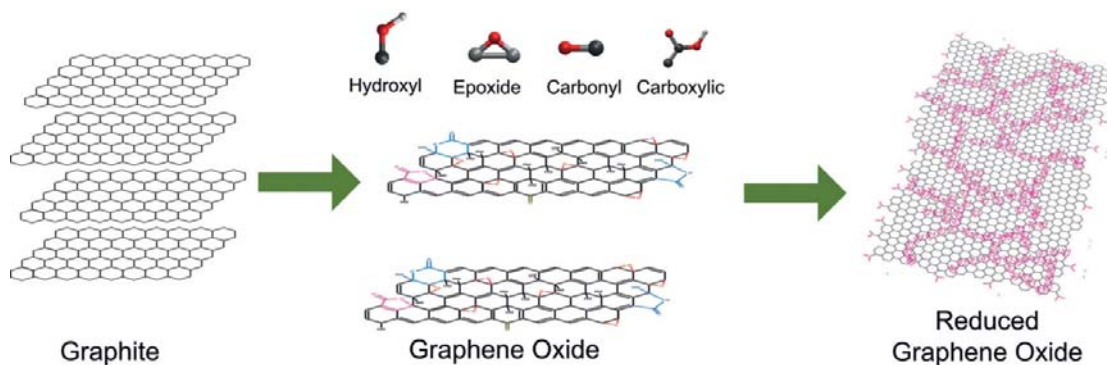


Figure 5. (Source: Bonaccorso et al. [25]) Graphene oxide synthesis and reduction. Graphite is oxidized to graphene oxide as suggested by Hummer [22]. Graphene oxide consists of variously bound oxygen and other atoms. The subsequent reduction cannot remove all impurities and is therefore called reduced graphene oxide.

3 Theoretical aspects

3.1 Zero band gap calculations of ideal graphene

The electronic band structure of an ideal two dimensional single atom graphene layer is unique, and it is given by the sp^2 -hybridized carbon atoms, which are arranging in a hexagonal lattice (Figure 6 (a)). The calculated ideal band structure, visualized in Figure 6 (b) in grey, is sandglass-shaped with the two cones joined at the Fermi level – called the point of neutrality or Dirac point. The two-dimensional diagram is shown in Figure 6 (c). The cone-shaped bands near the Fermi level are relevant for electronics, and are understood as conduction and valence bands. As metals have no gap between the conduction and valence band, graphene is described by Novoselov et al. 2004 and 2005 as “metallic” [18, 26]. (Figure 6 (b,c)). Doping of the graphene lattice or the influence by an electric field will induce either an electron or an electron-hole transport (Figure 6 (d)). In the case of an electron dominated transport – a so called n-type doped material – the fermi level has a positive value. If the carrier transport is dominated by electron holes – a p-type doped material – the fermi level is lowered and has a negative value.

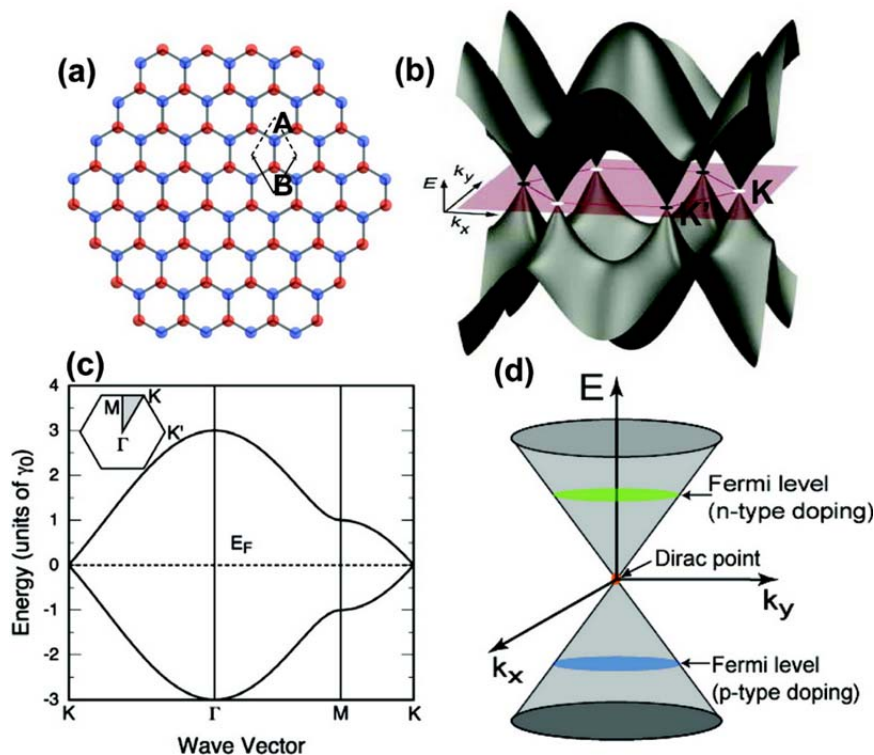


Figure 6. (Source: Avouris et al. [4]) (a) Hexagonal crystal structure of graphene with two carbon-atoms containing unit cell. (b) The three dimensional electronic band structure of graphene. (c) Dispersion of the electronic states of graphene. (d) Schema of the band structure with the Dirac point connecting the π - and π^* -states. The Fermi level indicates the doping state and the electrons or holes as transport carrier.

3.2 Band gap in graphene

3.2.1 Single layer graphene on SiO₂

Meyer et al. discovered experimentally that the graphene surface is not ideally flat. Graphene's hilly topography impacts the band structure, resulting in a band gap. This finding fundamentally revised our understanding of graphene introducing a theoretical basis for its semiconducting properties. The discrepancy between the ideal-flat graphene (previous section) and a waved graphene can be explained by the influence of the subjacent bulk material, which is commonly SiO₂. This was discussed theoretically and investigated experimentally by Meyer and colleagues [27, 28] stating that: i) a graphene layer interacts with its carrying substrate favoring different distances between lattice carbon atoms and the surface, thus yielding a waved structure, ii) monoatomic layers are not thermodynamically stable, as atoms are reorganizing to isles, and iii) impurities (doping) of graphene are virtually inevitable and favor waved surfaces [29]. Graphene was investigated experimentally by electron diffraction [28] and with scanning tunneling microscopic measurements [30]. Figure 7 shows schematically the ideal flat (a) and the wave form (b) of graphene. The diffraction patterns for crystal structures of solids are showing dots. Different results were obtained with graphene that showed blurred dots. This was attributed to the out of plane positioning carbon atoms (Figure 7 (c-e)).

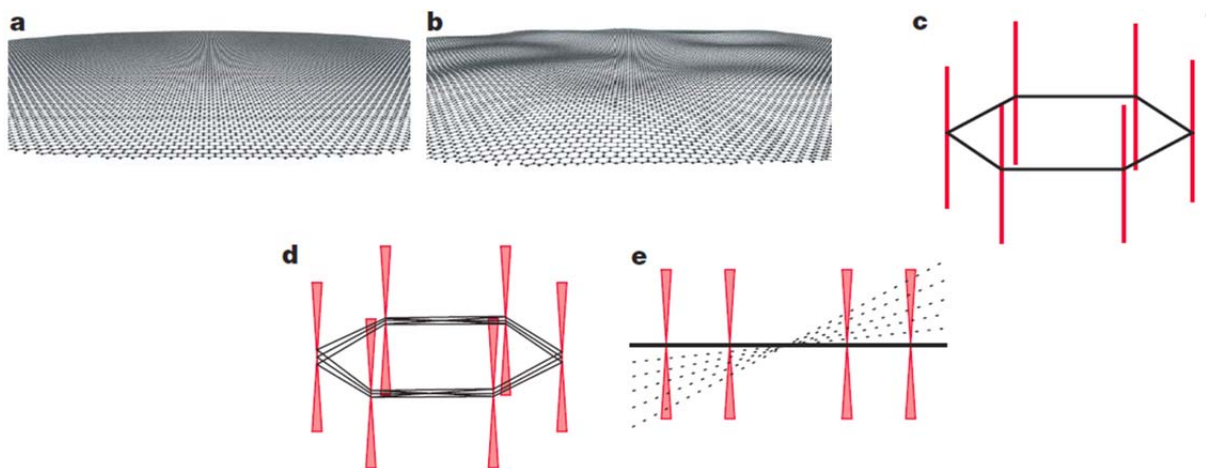


Figure 7. (Source: Meyer et al.[27]) (a) Flat ideal graphene crystal. (b) Corrugated graphene crystal. The quantitative visualization of the experimentally found roughness of the graphene layer. (c) The diffraction intensities of a flat graphene sheet are a set of rods (red) are perpendicular to the layer (black). (d) The diffraction intensities for a corrugated graphene layer the diffracting beams turn into cone-shaped volumes, so the diffraction spots become changed in large angles (dotted lines) in (e).

Figure 8 shows the scanning tunneling microscopic measurements of graphene on a SiO₂ substrate, which is presenting in a waved shape (a), and a detail view of the “honeycomb” shaped lattice (b).

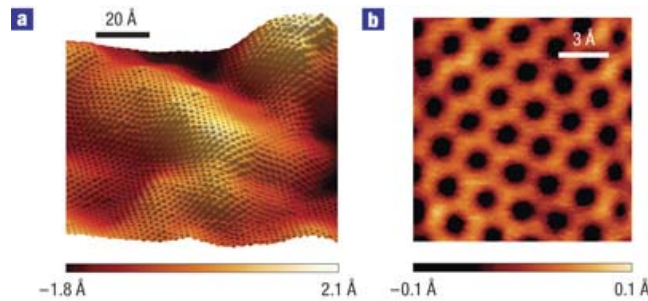


Figure 8. (Source: Zhou et al. [30]) The graphene surface topography is shown. (a) Graphene flake on a SiO₂ substrate measured with a constant-current scanning tunneling microscopy (1 V, 50 pA). (b) The scanning tunneling microscopic topography (constant-current, 0.15 V, 40 pA) close-up of the graphene shows the “honeycomb structure” of two dimensional graphene.

3.2.2 Bilayer graphene

Rutter and colleagues measured the surface potential distribution of bilayer graphene showing for the first time asymmetries in electron rich and electron hole rich regions at the nanometer scale, as well as the change of these by an applied gate potential (Figure 9) [31].

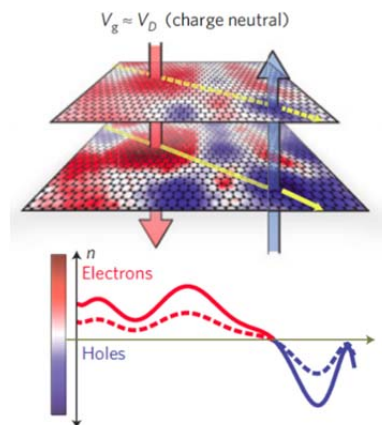


Figure 9. (Source: Rutter et al. [31]) Bilayer graphene potential energy asymmetries at varying gate voltage for electron and hole puddles. Top: Schematics of the spatial inhomogeneity of the layer densities in bilayer graphene at different gate potentials.

3.3 Semiconducting field effect transistor

The electric field effect of the graphene based FETs was shown experimentally by Novoselov and colleagues with showing the characteristic conductance dependence on the gate voltage (Figure 10) [19, 30]. This characteristic conductivity depends linearly on the gate potential unless it is relatively close to the Dirac point, therefore Novoselov and colleagues are referring to graphene as material with “metallic” properties.

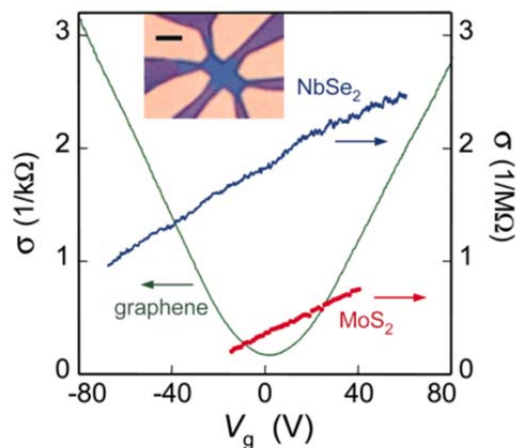


Figure 10. (Source: Novoselov et al. [26]) Electric field effect of one layer graphene. Electrical conductivity change of two dimensional NbSe₂, two dimensional MoS₂, and graphene as a function of gate voltage. In the inset the device for these measurements is shown (an optical microscopic image in white light) layer (bluer region in the center) placed on oxidized silicon wafer (gate electrode) and gold contacts as electrodes (scale bar is 5 μm).

It is discussed that graphene as a single layer of carbon atoms has a two dimensional sheet-like structure and is having unconventional “metallic” behavior as its electron gas is presented at the surface. Therefore a single layer of graphene consisting of carbon atoms without any doping heteroatoms is, if connected by electrodes, described to work as a “metallic” field effect transistor [18].

4 Insect olfaction

Terrestrial animals recognize volatiles from the ambient air as odor if the olfactory system responds to it. The reception of smell implies a multi-step recognition pathway, which is different for various animals. Research of three decades helped to partly decode the molecular and electrical basis of insect olfaction. Figure 11 shows schematically the insect olfactory system and a zoom into the sensillum containing odorants, odorant binding proteins and odorant receptors. First the volatiles are passing the pores of the sensillum cuticle into the lymph and are translocated to the inner membrane bound olfactory receptors by odorant binding proteins. Subsequently an olfactory signal transduction mechanism is processing the information once the receptor is reached by the odorant binding protein-odorant complex and the biochemical information is converted into an electric signal by activating neuronal circuits [32,33,34,35,36].

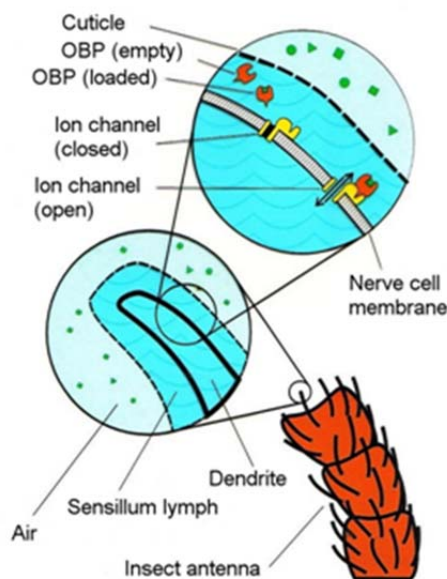


Figure 11. (Source: Paczkowski et al. [37]) Schematic of the proposed concept of insect olfaction. Odorant binding proteins (OBP) are binding and transporting various odorants (green triangles, rectangles, circles) selectively from the surrounding air through the sensillum lymph to the ion channel (olfactory receptors) which are associated in the nerve cell membrane. The resulting channel opening is changing the membrane potential.

4.1 Odorant binding proteins

Odorant binding proteins (OBPs) are triggering the insect's sensing cascade by capturing volatiles from the surrounding air environment and transporting them to the sensitive receptors as described first by Vogt and Riddiford in 1980 [35]. Therewith the odorant binding protein-odorant complex formation serves two roles, dissolving of the hydrophobic proteins for the aqueous lymph medium and concentration of odorants which increases sensing sensitivity. pH dependency of odorant binding favors OBP transport in the alkali lymph medium and uptake/release of odorant binding protein at the acidic membrane/receptor [38]. Here, OBPs were found to bind a full pattern of odorants, thereby certain selectivity provides a pre-selection of structurally similar odorants. In this thesis the following OBPs were applied: i) AmelOBP14 (*Apis mellifera* Odorant Binding Protein 14) one odorant binding protein from the honey bee, ii) AmelOBP14 with additional disulfide bond, iii) TcasOBP9A and TcasOBP9B (*Tribolium castaneum* Odorant Binding Protein 9 A & B).

4.2 AmelOBP14

The odorant binding protein from the honey bee (*Apis mellifera*) 14 (AmelOBP14) consists of seven alpha helices, where the seventh one is formed by the C-terminal end, which was described to form a wall between the outside and the inside of the cavity inside the protein (Figure 12, left). Spinelli et al. 2012 have presented how OBP 14 interacts with distinct odorants and which structural features of the protein are contributing to binding with crystallographic data of the protein solely and in complex [39]. High affinity towards odorant molecules like Eugenol was attributed to specific binding features, which prefer ligands with a hydroxyl group and an aromatic backbone (Figure 12, right) [39].

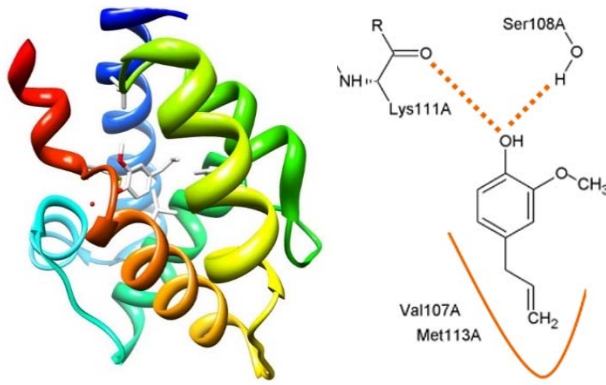


Figure 12. (Source: Spinelli et al. [39]) Left) Schematic structure of AmelOBP14 based on x-ray crystallographic data. Right) AmelOBP14 binding the odorant Eugenol: the hydroxyl group, and the carboxy group as well as an hydrophobic side chain is found to be the basis for binding identified by Spinelli and his colleagues in 2012 by X-ray-spectroscopy.

4.3 TcasOBP9A & TcasOBP9B

TcasOBP9A and TcasOBP9B: both odorant binding proteins from the red flour beetle (*Tribolium castaneum*) were identified to be highly transcribed in the antenna of the beetle, and the latter one was identified on the protein level by Matrix Assisted Laser Desorption and Ionization (MALDI) mass spectrometry (Figure 13) [40].

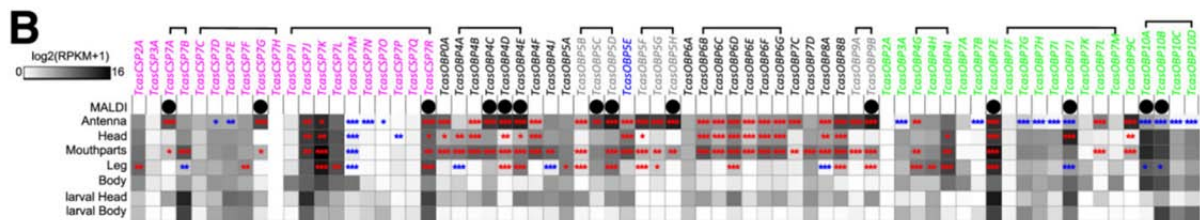


Figure 13. (Dippel et al. [40]) Transcription levels of OBPs and CSPs in different body parts of the *T. castaneum*. The black dot in the first row named MALDI, indicate that the protein was expressed in the antenna. The transcription levels are represented by a log2 grayscale, black labeled indicate high levels. Asterisks label significantly transcribed genes compared to the body part, red asterisks (up-regulation), and blue ones (down-regulation).

4.4 BmorPBP1

Leal and his colleagues have shown already some first complex formations between the *Bombyx mori* pheromone binding protein 1 (BmorPBP1) and non-pheromone ligands revealing the role of BmorPBP1 as pheromone transport vehicle. The study of the capability of BmorPBP1 to bind structurally different ligands, shows a broad adaptability of the BmorPBP1 to various ligands, and on the other hand a remarkable selectivity by showing no binding to structurally very similar but biologically non-relevant ligands. The affinity of Bombykol to BmorPBP1 is reported to be in the μM range [41,42, 43,44].

Our preliminary data show remarkable stability of BmorPBP1 in buffer up to 20 vol% of ethanol (personal communication Andreas Schwaighofer). In this buffer the ligand Bombykol is soluble, showing a Critical Micelle Concentration (CMC) of 50-100 μM (unpublished data Caroline Kotlowski). The rGO-FET based affinity measurements confirmed the previously published low μM range (unpublished data Caroline Kotlowski).

Furthermore, the capability of BmorPBP1 to bind Bombykol in a pH dependent manner (Figure 14), which is interesting in context of selective odorant binding protein transport and pre-receptor concentration [38], could be confirmed by real time-FET measurements in this thesis.

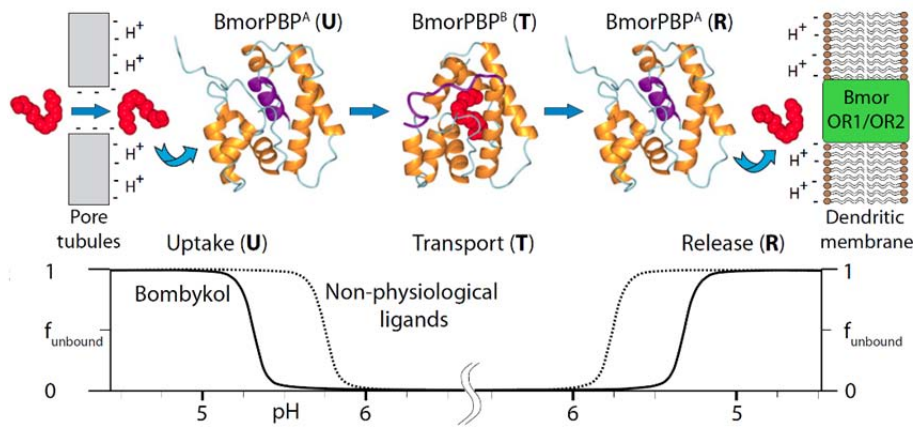


Figure 14. (Damberger et al. [38]) Described mechanism for Bombykol transport in the *Bombyx mori* sensillum based on the pH and ligand dependent structural changes between the BmorPBP1-Bombykol complex (BmorPBP^B) and the protein BmorPBP1 without bound ligand Bombykol (BmorPBP^A). Top) The locally reduced pH near the membrane was shown to be responsible for the preferential uptake and release of Bombykol. The transport phase of ligands complexed with BmorPBP1 is protecting the ligand from degradation by enzymes present in the sensillum lymph. When the BmorPBP1-Bombykol complex reaches the membrane co-located receptor Bombykol is released. Bottom) the fraction of ligand not bound to BmorPBP, f_{unbound} , indicated along the vertical axis, and pH profile, indicated along the horizontal axis, across the *Bombyx mori* sensillum cross-section. Bombykol not bound to BmorPBP1 may be temporary associated with the pore wall before being taken up by BmorPBP1, after release, it would be initially be associated with the surface of the neuron membrane, where it would diffuse to the receptor binding site. Bombykol is preferentially uptaken at locally reduced pH near the membrane pore over the non-physiological ligands (BmorPBP1=BmorPBP in figure 14 and figure caption).

5 Electrical measurements

The reduced graphene based effect transistor functionalised with the OBP (rGO-FET based biosensor) is mounted into a flow cell, which consists of an inlet and an outlet for the odorant solution. The latter is directed over the biosensor consisting of three electrodes: a liquid gate electrode, the source and the drain electrode (Figure 15). This set-up enables continuous and real-time measurements of the immobilised proteins interacting with the odorants in solution. Therewith the measured data (change of the source-drain current with time) consist kinetic information of the association and dissociation of odorants with the OBP. A schematic overview of the biosensor with the electrode connections is given in Figure 15 Top. The photograph of the flow cell with the electrical connections and the immobilized OBP interacting with odorant ligand are shown in Figure 15 left bottom and right bottom, respectively. The biosensor source and drain electrodes are evaporated onto the reduced graphene oxide flakes, which are adsorbed on a solid Silicon/Silicon dioxide substrate (with a defined silicon dioxide layer of 300nm), and functionalized by OBPs that are covalently coupled via a linker molecule.

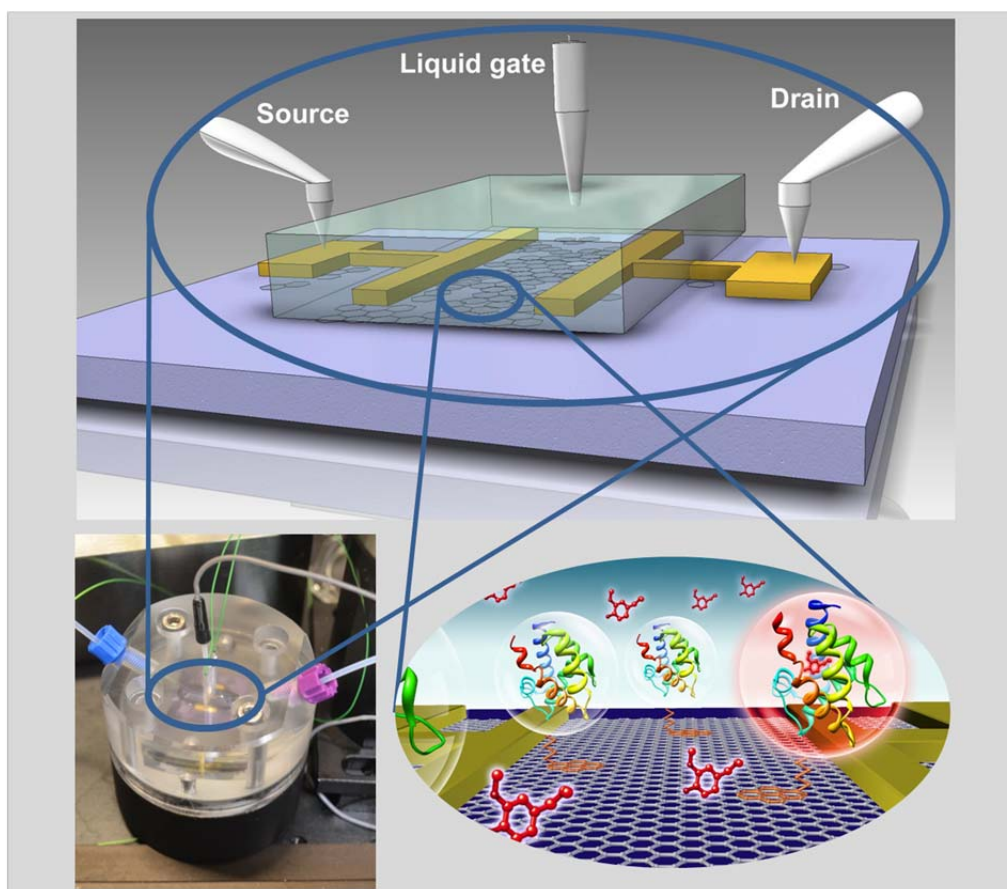


Figure 15. (Kotlowski et al. in preparation) Schematics of the set-up and the device configuration.

6 Langmuir model based affinity evaluation

The model of monolayer adsorption was proposed from Langmuir [45-48]. Langmuir regarded adsorption of an ideal gas to an idealized surface. The gas was considered to bind to distinct sites at the surface and the adsorption was taken as a reaction of the gas molecule with the empty site on the surface. The reaction was considered as an equilibrium reaction. The derivation is starting with the equilibrium reaction and the Langmuir isotherm is calculated with including the mass balance, resulting in the Langmuir adsorption isotherm:

$$\Theta = K_A c / (K_A c + 1) \quad \text{Equation 1}$$

With Θ the surface coverage from 0 to 1; with K_A being defined as $K_A = k_{\text{association}}/k_{\text{dissociation}}$ (in this thesis named: $k_{\text{on}}/k_{\text{off}}$) and c being the concentration of the adsorbate.

The rGO-FET approach for the detection of bi-molecular recognition is based on the immobilization of the protein on the rGO-FET (Figure 15), which is exposed to different ligand concentrations. The ligand interaction with the protein is measured continuously and directly, and the ligand dissociation is measured if the immobilized protein is flushed with pure buffer. Thus the generated data contain rate and equilibrium constants which are unique for the protein-ligand interaction, reproducible and fully reversible. The method given constraints qualify the Langmuir model for the affinity analysis (giving the rate and equilibrium constants k_{on} , k_{off} , K_A).

Only by subjecting the data to the complete multistep self consistency analysis as described in this work, signals could be converted into reliable affinity constants for a broad spectrum of odorants binding to the odorant binding protein.

Figure 16 presents the full quantitative evaluation of one ligand: the odorant Methyl vanillate, which is binding to the odorant binding protein AmelOBP14 immobilized on the rGO-FET (Figure 15, Right bottom). The sensor response was measured by monitoring changes in source-drain current (ΔI_{DS}) with time, while different aqueous solutions of the ligand Methyl vanillate were applied through the flow cell and across the sensing area (Figure 16A). At each concentration step one can observe a change of I_{SD} reaching a new stationary current level with a rate constant typical for the bulk Methyl vanillate concentration in the analyte solution. The rate constants are evaluated by fitting the raw data resulting in a K_A for each measured concentration. As the fit of each concentration step

has a reaction rate constant $k(c)$ for the association (k_{on}) and dissociation (k_{off}), the given relations are $k_{on}=k*c$ & $K_A=k_{on}/k_{off}$; k_{on} is concentration independent and thus for each concentration the same value is expected. This provides a check of how self-consistent the data are. Figure 17 shows such a step for one concentration (30 μ M Methyl vanillate) and the $k=k_{on}/c$ evaluated by fitting (red line) the data (black).

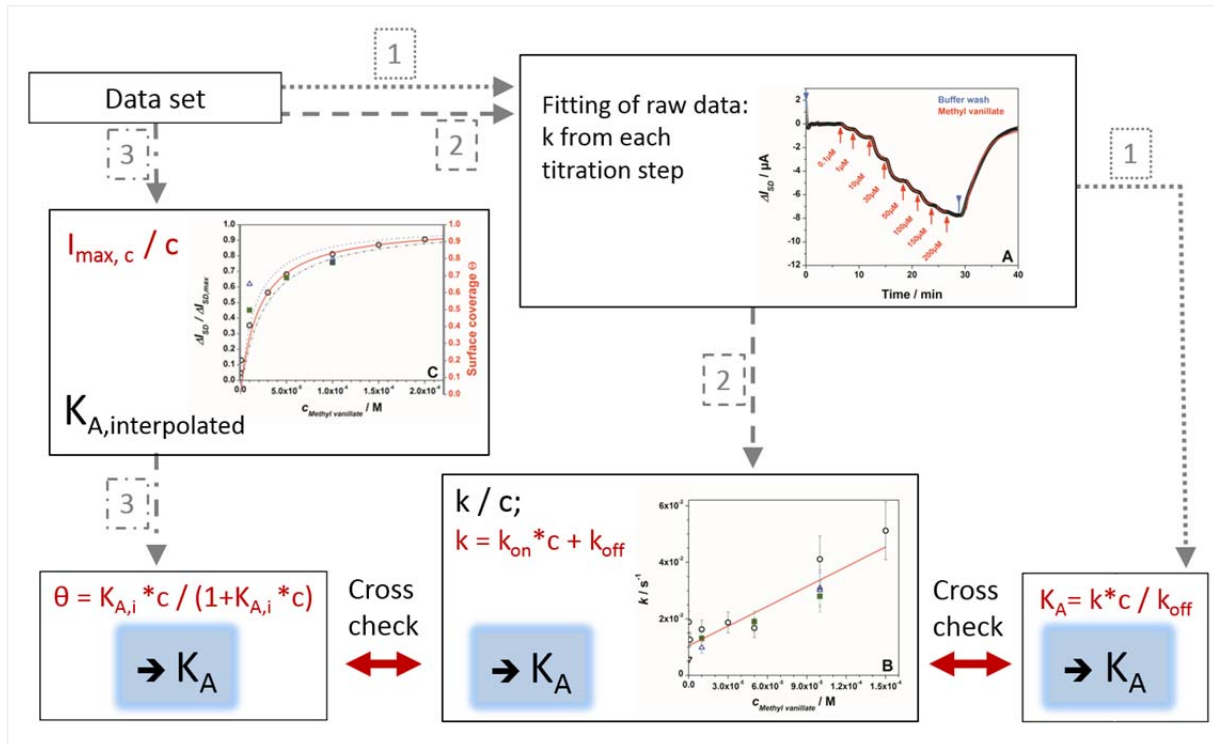


Figure 16. Schematics of the multivariate data-analysis based on the Langmuir model. Kinetic constants were calculated following three ways (indicated in Figure 16 with dotted, dashed and dash-dot lines): (1.) fitting the raw data yields a K_A for each measured concentration: as the fit of each concentration step has a reaction rate constant $k(c)$ for the association and dissociation ($k_{on}=k*c$; k_{off} ; $K_A=k_{on}/k_{off}$). K_A is concentration independent thus for each concentration the same value is expected – this provides a check of how self-consistent the data are. (2.) Correlating all obtained reaction rate constants $k(c)$ with the concentration, yields a linear regression from which a K_A value is extracted (K_A =slope: k_{on} /intercept: k_{off}). Notably this K_A is based on all concentration steps. (3.) The current changes were correlated with the concentration, fitting this data result in the characteristic Langmuir isotherm, which shows the saturating surface over a concentration range, this surface coverage: $\theta=K_A c_0 / (K_A c_0 + 1)$ is extracting again the K_A . All three ways give consistent results if the recorded signals are reflecting binding, as this is the assumption underlying the Langmuir model. This extended kinetic analysis based on the Langmuir model serves as a multi-step self-consistency check.

Plotting the k -values as a function of the bulk concentration like in Figure 16B, one finds a linear increase of the rate constant as it is predicted by the Langmuir model:

$$k = k_{\text{on}} C_{\text{Methyl vanillate}} + k_{\text{off}} \quad \text{Equation 2}$$

The linear regression through the data points in Figure 16B yields in $k_{\text{on}} = 235 \text{ M}^{-1}\text{s}^{-1}$ for the binding of Methyl vanillate to AmelOBP14. The intersection of the fit line with the ordinate, i.e., k for $C_{\text{Methyl vanillate}} = 0$, yields $k_{\text{off}} = 0.01 \text{ s}^{-1}$.

The plot of the observed (changes of the) values of stationary current levels, ΔI_{SD} , relative to its extrapolated maximum value, i.e., $\Theta = \Delta I_{\text{SD}} / \Delta I_{\text{SD,max}}$, as a function of the applied Methyl vanillate concentration, gives a typical Langmuir binding isotherm (Figure 16C). The data points can be well described by the equation:

$$\Theta = K_A C_{\text{Methyl vanillate}} / (K_A C_{\text{Methyl vanillate}} + 1) \quad \text{Equation 3}$$

with $K_A = 5 \times 10^4 \text{ M}^{-1}$ (full curve in Figure 16 C). The dotted and the dashed-dotted curves give the error margins for the determination of the affinity constant: $6 \times 10^4 \text{ M}^{-1} < K_A < 4 \times 10^4 \text{ M}^{-1}$, as derived from the Langmuir isotherm.

As an internal consistency check, the dissociation process can also be observed as an increase of the source-drain current (back to the background current) upon switching the bulk odorant concentration to zero, i.e., rinsing again pure buffer through the flow cell. According to the Langmuir model (cf. equation 2 with $C_{\text{Methyl vanillate}} = 0$), the corresponding data can be fitted by a single exponential function giving the dissociation rate constant and its error margin: $k_{\text{off}} = 0.01 \text{ s}^{-1} \pm 20\%$ (0.008 s^{-1} ; 0.012 s^{-1}), in good agreement with the extrapolated value from Figure 16B.

According to the Langmuir model the relation between the rate constants and the affinity constant is described by

$$K_A = k_{\text{on}} / k_{\text{off}} \quad \text{Equation 4}$$

With the rate constants derived from fitting the raw data, a K_A can be determined for each measured concentration. K_A is concentration independent and thus, for each concentration the same value is expected. This allows a check of how self-consistent the data are.

The kinetic analysis of the measured association data points allow for a further quantification of the binding events: Figure 17 shows a detailed plot of the time dependent current change, ΔI_{SD} , from the steady state value reached at $10 \mu\text{M}$ ligand concentration to the new stationary level reached after changing the bulk odorant concentration to $30 \mu\text{M}$.

The determination of error limits of the rate constants is shown for the k ($30\mu\text{M}$), as it was applied for each measured k . Shown are the experimental data of the current change, ΔI_{SD} , after injection of a $30\mu\text{M}$ solution of Methyl vanillate into the flow cell (black), together with 3 fit curves: red, $k=0.01872\text{ s}^{-1}$, dark blue with $k'=k+20\%$, light blue, $k''=k-20\%$.

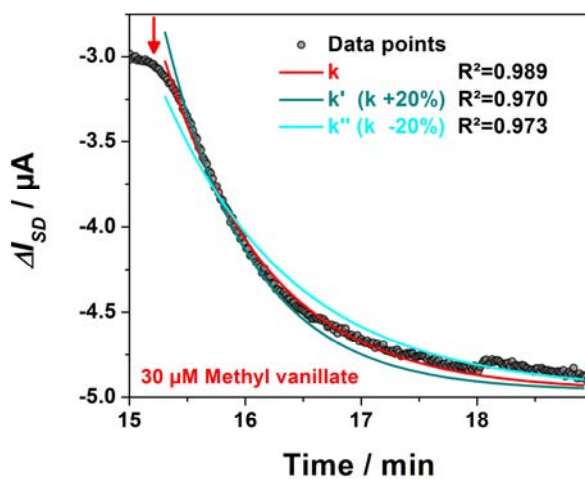


Figure 17. Experimental data of the current change, ΔI_{SD} , after injection of a $30\mu\text{M}$ solution Methyl vanillate and the determination of the rate constants, k , and its error limits, $k\pm 20\%$.

7 Aims of the thesis

This thesis aimed at the development of a biosensor for molecular recognition with a reduced graphene oxide field effect transistor. As graphene is a highly surface sensitive material one major goal was to establish a graphene based field effect transistor as a biosensor. Earlier sensing systems focused on detecting biomolecules, however, selectivity and self-consistency of data still remain an issue, whereas in this thesis I present the detection of molecular recognition between receptors and volatiles. Notably, the task was to develop a system that responds to low affinity molecular recognition. Handling these low affinities required optimizing the graphene quality and a data evaluation, based on a Langmuir adsorption model that proved the specific nature of the measured interactions and yielded kinetic constants.

8 Summary of Results and their Significance

The results of this thesis were published in four papers, two papers are in preparation:

- a) **Electronic Olfactory Sensor Based on *A.mellifera* Odorant Binding Protein 14 on a Reduced Graphene Oxide Field-Effect Transistor,**
(First author), published in Angewandte Chemie International Edition (impact factor 2014: 11.3)
- b) **Electronic Biosensing with Functionalized rGO FETs,**
(First author), published in Biosensors (impact factor 2014: under evaluation)
- c) **Electronic Olfactory Biosensor Based on Honeybee Odorant Binding Protein 14 on a rGO FET,**
(First author), in preparation for Analytical Chemistry (impact factor 2014: 5.6)
- d) **Honey bee odorant-binding protein 14: effects on thermal stability upon odorant binding revealed by FT-IR spectroscopy and CD measurements (Co-authorship paper),**
published in European Biophysics Journal (impact factor 2014: 2.2)
- e) **Insights into structural features determining odorant affinities to honey bee odorant binding protein 14 (Co-authorship paper),**
published in Biochemical and Biophysical Research Communications (impact factor 2014: 2.3)
- f) **Monitoring Crop Disease Markers by Odorant Binding Proteins of *Tribolium castaneum* – Electroantennograms versus Reduced Graphene-Oxide Based Electronic Biosensor,**
(First author), in preparation for Biosensors and Bioelectronics (impact factor 2014: 6.4)

Paper a) presents a biosensor, which mimics the honey bee olfaction based on the recognition of odorants with the odorant binding protein AmelOBP14. It has been shown that OBP14 from the honey bee preferentially recognizes odorants with specific structural binding features. The biosensing method was realized with a reduced graphene oxide based field effect transistor (rGO-FET) design functionalized with the odorant binding proteins. This structure specific recognition was measured by the rGO-FET-biosensor, with a series of sensing experiments using various ligands - structural similar and different ones. The affinity was evaluated basing on the Langmuir model and therewith a correlation between the affinity and structure of the protein was identified. The ligands binding with a high affinity to the protein were sharing structural features, which were previously identified by Spinelli and his colleagues based on X-ray structure analysis of the complex [32]. The Langmuir model based affinity evaluation is shown in a separate chapter as well as in the papers a),b),c) in detail.

While the first paper a) presents the methodical aspects in detail for one protein and one kind of interaction, in paper b) and c) the methods were applied to different bi-molecular applications. In b) the biosensor applicability for the detection of completely different molecular recognition motifs based interactions on antibody-antigen and strong affinity binding interactions of small ligands was shown. However, the sensitivity of the biosensor could be further increased by controlling the orientation of the capture molecules. Therefore in paper c) the impact of protein orientation on sensing was addressed by immobilizing proteins through a His-tag at the N-terminus and therewith exposing the binding pocket. Furthermore in this work the binding behavior of an engineered OBP-mutant with an additional disulfide bond was tested. The OBP-mutant was shown to bind ligands with a higher affinity. With this finding it was shown that the proteins have unexplored potential as tunable recognition elements.

Papers a)-c) lacked information on the stability of ligand-receptor complexes. Therefore in papers d) and e) we studied the effect of thermal denaturation by infrared spectroscopy and circular dichroism in order to determine ligand-receptor complex stabilities. The assumption underlying these experiments is that higher stability of the complex is indicative for higher binding affinity.

The final application of the biosensor was to test and identify ligands for OBPs. Following this challenge unknown ligands were tested as binding partners for the recently identified new proteins TcasOBP9A and TcasOBP9B from the beetle *Tribolium castaneum*. Three ligands were identified. Beside the ligand ability to interact with the proteins, the insect antenna response was investigated with a second biosensor method by electro-antennographic recordings of the antenna being exposed to the ligands.

Taken together the OBP based sensing of *small* ligands revealed the applicability of electronic sensing based on graphene based FETs as an analytical tool for the detection of complex low affinity molecular recognition. OBPs are binding odorants relatively weakly and are discriminating selectively on the basis of structural features. These binding properties are reflected by the biosensor on the same level and are extracted from the sensor signals with the Langmuir model based affinity evaluation.



Electronic Olfactory Sensor Based on *A. mellifera* Odorant-Binding Protein 14 on a Reduced Graphene Oxide Field-Effect Transistor

Melanie Larisika, Caroline Kotlowski, Christoph Steininger, Rosa Mastrogiacomo, Paolo Pelosi, Stefan Schütz, Serban F. Peteu, Christoph Kleber, Ciril Reiner-Rozman, Christoph Nowak, and Wolfgang Knoll*

Abstract: An olfactory biosensor based on a reduced graphene oxide (rGO) field-effect transistor (FET), functionalized by the odorant-binding protein 14 (OBP14) from the honey bee (*Apis mellifera*) has been designed for the *in situ* and real-time monitoring of a broad spectrum of odorants in aqueous solutions known to be attractants for bees. The electrical measurements of the binding of all tested odorants are shown to follow the Langmuir model for ligand–receptor interactions. The results demonstrate that OBP14 is able to bind odorants even after immobilization on rGO and can discriminate between ligands binding within a range of dissociation constants from $K_d = 4 \mu\text{M}$ to $K_d = 3.3 \text{ mM}$. The strongest ligands, such as homovanillic acid, eugenol, and methyl vanillate all contain a hydroxy group which is apparently important for the strong interaction with the protein.

Odorant-binding proteins (OBPs) are small acidic proteins (ca. 13–16 kDa) highly concentrated in the lymph of the

chemosensillae of insects or in the nasal mucus of vertebrates.^[1] They act as carriers for volatile organic compounds, VOCs, (air-borne odorants) shuttling them from the air–water interface to the membrane-integral odorant receptor. Although their full function has not been completely clarified yet, OBPs certainly play a major role in detecting and recognizing olfactory stimuli.^[2]

A large number of OBPs has been expressed in bacterial systems and their ligand-binding properties have been investigated in solution by a fluorescent ligand displacement assay.^[3] Generally, dissociation constants, K_d , are in the upper nanomolar or lower micromolar range for strong odorants.^[1,c,d] An important characteristic of OBPs for technical applications is their stability to extreme temperatures, solvents, and proteolysis, making such proteins ideal elements for biosensors to be used in medical application, for example, in breath analysis for cancer diagnostics, for food quality control, for crop-disease detection, or in general environmental monitoring.^[4a–f]

Various biosensor devices mimicking the olfactory system (artificial noses) have been developed but only few studies have used OBPs as functional elements for the design of a “bio-electronic nose”.^[5] Herein we present the fabrication and functional characterization of a label-free biosensor for odorant detection based on a reduced graphene oxide field-effect transistor functionalized with the odorant-binding protein 14 (OBP14) from the honey bee *Apis mellifera*.

Reduced graphene oxide field-effect transistor (rGO-FET) devices were fabricated according to established methods, schematically given in Figure 1A.^[6] A scanning electron microscopic image of rGO flakes assembled onto the gate substrate before any further surface functionalization is shown in Figure 1B. IR spectra of the linker monolayer, 1-pyrenebutanoic acid succinimidyl ester (PBSE), that is typically used for protein immobilization on graphene substrates,^[7] with partial covalent immobilization of OBP taken at different times during the assembly from solution to the gate are given in Figure 1C, while Figure 1D summarizes the quantitative analysis of the functionalization process by monitoring the time-dependent increase of the amide I and II bands of the protein and the corresponding decrease of the band at 1738 cm^{-1} , assigned to the cleavage of the active ester group of the linker molecules. The entire fabrication process of the olfactory biosensor device, including the successful reduction of GO to rGO, the linker binding, and more details of the protein attachment are described in the Supporting Information. The cloning, expression, and purification of OBPs, the preparation of odorant solutions and the perfor-

[*] Dr. M. Larisika,^[†] C. Kotlowski,^[†] C. Steininger, C. Reiner-Rozman, Dr. C. Nowak, Prof. W. Knoll
BioSensor Technologies
Austrian Institute of Technology
Vienna (Austria)
E-mail: wolfgang.knoll@ait.ac.at

Dr. M. Larisika,^[†] Dr. C. Nowak, Prof. W. Knoll
Centre for Biomimetic Sensor Science
Nanyang Technological University
Singapore 637371 (Singapore)

C. Kotlowski,^[†] Prof. C. Kleber, C. Reiner-Rozman, Dr. C. Nowak, Prof. W. Knoll
Center for Electrochemical Surface Technology
Wiener Neustadt (Austria)

R. Mastrogiacomo, Prof. P. Pelosi
Department of Biology of Agriculture, Food and Environment
University of Pisa (Italy)

Prof. S. Schütz
Buesgen-Institute, Dept. of Forest Zoology and Forest Conservation
Goettingen (Germany)

S. F. Peteu
Michigan State University
Chemical Engineering & Materials Science (USA)

[†] These authors contributed equally to this work.

Supporting information for this article is available on the WWW under <http://dx.doi.org/10.1002/anie.201505712>.

© 2015 The Authors. Published by Wiley-VCH Verlag GmbH & Co. KGaA. This is an open access article under the terms of the Creative Commons Attribution License, which permits use, distribution and reproduction in any medium, provided the original work is properly cited.

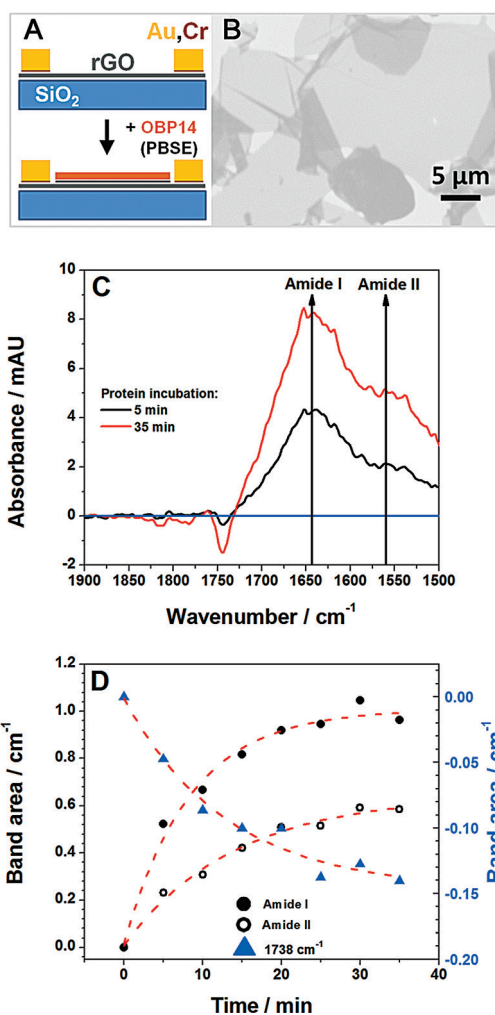


Figure 1. A) Schematic illustration of the individual fabrication steps of the graphene biosensor device. B) Scanning electron microscopic image of the rGO-FET before the functionalization with 1-pyrenebutanoic acid succinimidyl ester (PBSE) linker. C) Infrared spectra of the PBSE linker attached to gate area of the rGO surface, and OBP14 immobilized for 5 and 35 min, respectively, as indicated (spectra measured in ATR configuration and water corrected). D) Time-dependent increase of the amide I and II bands, upon binding of OBP14 to the linker molecules at the gate surface, and the corresponding decrease of the band at 1738 cm^{-1} upon cleavage of the active ester of the linker molecules during the protein immobilization (cf. also Figure S6). The dashed red curves are guides to the eye.

mance of the electrical measurements are also described in the Supporting Information.

The mode of operation of the device as a field-effect transistor is demonstrated in Figure S5. Recording the I_{SD} versus V_G scans under different bulk solution conditions, in particular, in aqueous solutions with different ligand concentrations results in a slightly modified slope of the cathodic branch. We attribute this change to a slight modification of the dipolar layer upon binding of the ligands to the free binding sites in the OBP which act as receptors. The OBP protein monolayer is immobilized on the graphene gate and ligand binding causes a the slight reorientation of its the alpha-helical parts. At the selected gate voltage of $V_G =$

-0.6 V the concentration dependency of the slopes in the I_{SD} versus V_G curves could be used to measure the binding of odorants to OBP14 in real-time, resulting in the quantitative determination of the kinetic rate constants for the association process, k_{on} , and for the dissociation process, k_{off} , as well as for the affinity constant K_A and the dissociation constant K_d . As an example, Figure 2 A shows a global analysis measurement,

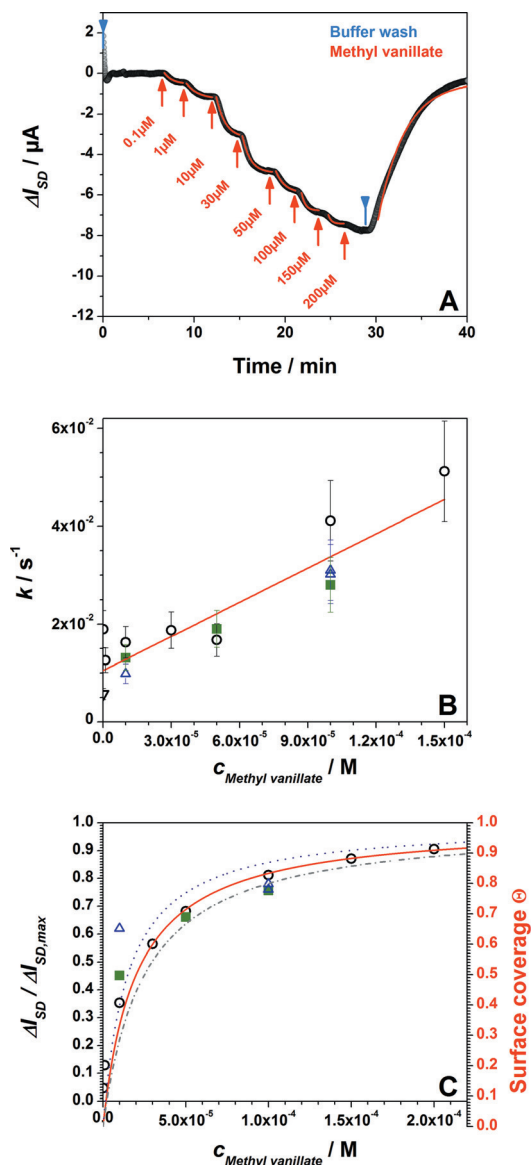


Figure 2. A) Real-time biosensor measurement of the binding of methyl vanillate to OBP14: the current increases with the bulk concentration of methyl vanillate increasing (from 100 nM to $200\text{ }\mu\text{M}$) and then saturates. Blue arrows indicate runs with pure buffer, red arrows indicate experiments with methyl vanillate solutions. Red curves are the fitting of the raw data by kinetic simulations of the association and dissociation processes based on the Langmuir model. (For the estimation of the error limits, see the Supporting Information). B) Analysis of the reaction rate constants, k , obtained from the fitted data in (A) as a function of methyl vanillate concentration; different symbols from three different devices; error bars are $\pm 20\%$. C) Langmuir adsorption isotherm, obtained for three different samples; the red fit curve gives $K_d = 20\text{ }\mu\text{M}$ (plotted are also error limits for K_d of 20%).

that is, the time dependence of the change of the source-drain current, ΔI_{SD} , of the FET as a function of time upon binding of methyl vanillate, a strong binder, from solution to the OBP14-functionalized gate surface at increasing and decreasing odorant bulk concentrations. The error of the kinetic rate constants, k , obtained was estimated to be around 20% (cf. also Figure S8 in the Supporting Information).

Upon plotting the resulting reaction rate constants k , as they were derived from the fits to the kinetic traces as a function of the bulk ligand concentration, $c_0 = c_{\text{Methyl vanillate}}$ (Figure 2B), gives a straight line, the slope of which, according to $k = k_{\text{on}} c_0 + k_{\text{off}}$, with k_{on} being the association and k_{off} the dissociation rate constant, respectively, yields $k_{\text{on}} = 235 \text{ M}^{-1} \text{ s}^{-1}$, and the intersection with the y-axis gives $k_{\text{off}} = 0.01 \text{ s}^{-1}$. According to the Langmuir model the ratio $k_{\text{on}}/k_{\text{off}}$ gives the affinity constant $K_A = 2.3 \times 10^4 \text{ M}^{-1}$, which can be compared to the value derived from the equilibrium titration experiment given in Figure 2C: according to $\theta = K_A c_0 / (1 + K_A c_0)$ the fit to the data (full red curve plus the error limits of $\pm 20\%$) gives the affinity constant $K_A = 5 \times 10^4 \text{ M}^{-1}$ which compares quite well with the value obtained from the kinetic experiments thus confirming the Langmuir model for this binding process.

To exclude false signals arising from, in particular, non-specific binding, several control experiments were performed. Firstly, a sensor was prepared which was covered only with linker molecules, without the coupling of the odorant-binding protein. Even high concentrations of the strong binder homovanillic acid (cf. Figure S7A) or other ligands (Figure S7B) did not result in a significant signal. Coating the gate with OBP14 but exposing it to a totally uncorrelated small molecule, biotin, gave no signal (Figure S7C). And finally, immobilizing a protein (OBP9A from the red flour beetle, *Tribolium castaneum*) that is structurally similar but is not a receptor for these ligand odorants also gave a very weak signal (Figure S7D).

Further evidence for the specificity of the ligand receptor binding originates from a direct comparison of the binding of eugenol and methyl eugenol to the same chip, functionalized with OBP14. Figure 3A shows a real-time current trace recorded during the addition of methyl eugenol at $50 \mu\text{M}$, then rinsing with pure buffer, and then a $5 \mu\text{M}$ solution of eugenol

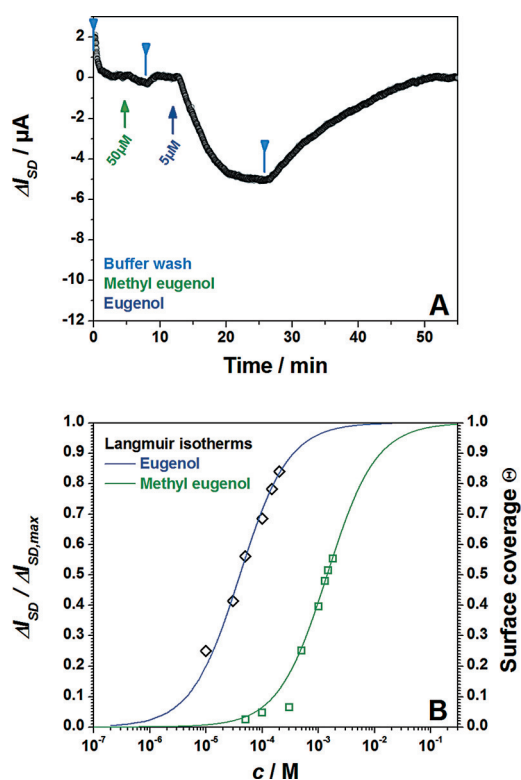


Figure 3. A) Real-time sensor response to the injection of a $50 \mu\text{M}$ solution of methyl eugenol, subsequent buffer wash, and the injection of $5 \mu\text{M}$ eugenol solution. B) Langmuir isotherms of eugenol and methyl eugenol.

being rinsed through the flow cell. Despite the minor chemical variation between the two ligands a large difference in the affinity of their binding reaction to OBP14 confirms the specificity of the sensor. Figure 3B summarizes the Langmuir isotherms for both ligands, demonstrating the significantly different dissociation constants: $K_d = 40 \mu\text{M}$ for eugenol and $K_d = 1400 \mu\text{M}$ for methyl eugenol.

Table 1 summarizes the quantitative data measured for a series of ligands and gives the kinetic rate constants, k_{on} and k_{off} , obtained as well as the dissociation constant K_d . It could

Table 1: Dissociation constants, K_d , association rate constants, k_{on} , and dissociation rate constants, k_{off} , for a variety of odorants binding to OBP14 as obtained by the global analysis.

Odorant	Homovanillic acid	Methyl vanillate	Eugenol	Citral	Methyl eugenol	Geraniol
structural formula						
K_d [$\times 10^{-6} \text{ M}$]	4	20	40	800	1400	3300
k_{on} [$\text{M}^{-1} \text{ s}^{-1}$]	1130	235	170	9	6	3
k_{off} [s^{-1}]	0.008	0.01	0.006	0.003	0.006	0.008

be confirmed also for this label-free sensing format that the odorant binding affinity to OBP14 gradually decreases from homovanillic acid to citral and to geraniol.^[8] Molecules which are structurally related to eugenol also showed strong affinities to OBP14.

Interestingly, also other odorant-binding proteins bind their odorants with affinities in the same order of magnitude.^[9] It is remarkable to note that for all the ligands investigated the dissociation rate constants k_{off} differ by less than a factor of 2.5. The strongly differing affinity constants, varying by nearly three orders of magnitude, can be almost exclusively attributed to the differences in the association rate constants k_{on} , (cf. Table 1).

The Spinelli group used X-ray diffraction analysis to determine the structure of the eugenol–OBP14 complex. They found that the hydroxy group of eugenol interacts with the cavity wall of the OBP14 binding pocket by forming two hydrogen bonds.^[10]

It has been speculated that the hydroxy group, together with the substituted aromatic backbone, plays a key role for the strong binding which is in agreement with the high affinities also of homovanillic acid and methyl vanillate (cf. Table 1).^[10] This hypothesis is further supported by the lower affinity measured for methyl eugenol, in which the hydroxy group is replaced by a methoxy group.

Acknowledgements

This research is supported by the European Science Foundation (ESF), Grant Number: 10-EuroBioSAS-FP-005, by the FFG within the comet program, and from the governments of Lower and Upper Austria. We thank Prof. Lendl (Technical University of Vienna) and his group (Christoph Gasser, Georg Ramer, Karin Wieland) for technical support regarding Raman and FTIR measurements.

Keywords: biosensors · immobilization · odorant-binding protein · olfaction · reduced graphene oxide

How to cite: *Angew. Chem. Int. Ed.* **2015**, *54*, 13245–13248
Angew. Chem. **2015**, *127*, 13443–13446

- [1] a) R. G. Vogt in *Comprehensive Insect Science*, Vol. 8 (Eds.: L. Gilbert, K. Iatrou, S. Gill), Elsevier, London, **2005**, p. 753; b) R. G. Vogt, L. M. Riddiford, *Nature* **1981**, *293*, 161; c) W. S. Leal, *Annu. Rev. Entomol.* **2013**, *58*, 373; d) P. Pelosi, J. J. Zhou, L. P. Ban, M. Calvello, *Cell. Mol. Life Sci.* **2006**, *63*, 1658; e) J. Fan, F. Francis, Y. Liu, J. L. Chen, D. F. Cheng, *GMR Genet. Mol. Res.* **2011**, *10*, 3056.
- [2] a) P. Xu, R. Atkinson, D. N. Jones, D. P. Smith, *Neuron* **2005**, *45*, 193; b) T. Matsuo, S. Sugaya, J. Yasukawa, T. Aigaki, Y. Fuyama,

PLoS Biol. **2007**, *5*, e118; c) S. Swarup, T. I. Williams, R. R. Anholt, *Genes Brain Behav.* **2011**, *10*, 648; d) Y. F. Sun, F. De Biasio, H. L. Qiao, I. Iovinella, S. X. Yang, Y. Ling, L. Riviello, D. Battaglia, P. Falabella, X. L. Yang, P. Pelosi, *PLOS ONE* **2012**, *7*, e32759.

- [3] V. Campanacci, J. Krieger, S. Bette, J. N. Sturgis, A. Lartigue, C. Cambillau, H. Breer, M. Tegoni, *J. Biol. Chem.* **2001**, *276*, 20078.
- [4] a) A. Schwaighofer, C. Kotlowski, C. Araman, N. Chu, R. Mastrogiacomo, C. Becker, P. Pelosi, W. Knoll, M. Larisika, C. Nowak, *Eur. Biophys. J.* **2014**, *43*(2–3), 105–112; b) S. Paolini, F. Tanfani, C. Fini, E. Bertoli, P. Pelosi, *Biochim. Biophys. Acta Protein Struct. Mol. Enzymol.* **1999**, *1431*, 179–188; c) K. Matsumura, M. Opiekun, H. Oka, A. Vachani, S. M. Albelda, K. Yamazaki, G. K. Beauchamp, *PLOS ONE* **2010**, *5*(1), e8819; d) M. Ghasemi-Varnamkhasti, S. S. Mohtasebi, M. Siadat, *J. Food Eng.* **2010**, *100*, 377–287; e) S. Schütz, B. Weißbecker, U. T. Koch, H. E. Hummel, *Biosens. Bioelectron.* **1999**, *14*, 221–228; f) W. Bourgeois, A.-C. Romain, J. Nicolas, R. M. Stuetz, *J. Environ. Monit.* **2003**, *5*, 852–860.
- [5] a) S. J. Park, O. S. Kwon, S. H. Lee, H. S. Song, T. H. Park, J. Jang, *Nano Lett.* **2012**, *12*, 5082; b) H. J. Jin, S. H. Lee, T. H. Kim, J. Park, H. S. Song, T. Park, S. Hong, *Biosens. Bioelectron.* **2012**, *35*, 335; c) T. H. Kim, S. H. Lee, J. Lee, H. S. Song, E. H. Oh, T. H. Park, S. Hong, *Adv. Mater.* **2009**, *21*, 91; d) H. Yoon, S. H. Lee, O. S. Kwon, H. S. Song, E. H. Oh, T. H. Park, J. Jang, *Angew. Chem. Int. Ed.* **2009**, *48*, 2755; *Angew. Chem.* **2009**, *121*, 2793; e) F. Di Pietrantonio, D. Cannatà, M. Benetti, E. Verona, A. Varriale, M. Staiano, S. D'Auria, *Biosens. Bioelectron.* **2013**, *41*, 328; f) S. Sankaran, S. Panigrahi, S. Mallik, *Biosens. Bioelectron.* **2011**, *26*, 3103; g) S. D'Auria, V. Scognamiglio, M. Rossi, M. Staiano, S. Campopiano, N. Cennamo, L. Zeni in *Conference on Biomedical Vibrational Spectroscopy and Biohazard Detection Technologies*, Vol. 5321, SPIE—The International Society for Optical Engineering, San Jose California (USA), **2004**, p. 258.
- [6] a) J. F. Huang, M. Larisika, W. H. D. Fam, Q. Y. He, M. A. Nimmo, C. Nowak, I. Y. A. Tok, *Nanoscale* **2013**, *5*, 2945; b) C. Y. Su, Y. Xu, W. Zhang, J. Zhao, X. Tang, C. H. Tsai, L. J. Li, *Chem. Mater.* **2009**, *21*, 5674–5680.
- [7] V. K. Kodali, J. Scrimgeour, S. Kim, J. H. Hankinson, K. M. Carroll, W. A. de Heer, C. Berger, J. E. Curtis, *Langmuir* **2011**, *27*, 863–865.
- [8] I. Iovinella, F. R. Dani, A. Niccolini, S. Sagona, E. Michelucci, A. Gazzano, S. Turillazzi, A. Felicioli, P. Pelosi, *J. Proteome Res.* **2011**, *10*, 3439.
- [9] a) J. Golebiowski, J. Topin, L. Charlier, L. Briand, *Flavour Fragrance J.* **2012**, *27*, 445; b) L. Briand, C. Eloit, C. Nespoulous, V. Bézirard, J.-C. Huet, C. Henry, F. Blon, D. Trotier, J.-C. Pernollet, *Biochemistry* **2002**, *41*, 7241; c) L. Briand, C. Nespoulous, V. Perez, J.-J. Rémy, J.-C. Huet, J.-C. Pernollet, *Eur. J. Biochem.* **2000**, *267*, 3079.
- [10] S. Spinelli, A. Lagarde, I. Iovinella, P. Legrand, M. Tegoni, P. Pelosi, C. Cambillau, *Insect Biochem. Mol. Biol.* **2012**, *42*, 41.

Received: June 21, 2015

Published online: September 14, 2015

Supporting Information

Electronic Olfactory Sensor Based on *A. mellifera* Odorant-Binding Protein 14 on a Reduced Graphene Oxide Field-Effect Transistor

*Melanie Larisika, Caroline Kotlowski, Christoph Steininger, Rosa Mastrogiacomo, Paolo Pelosi, Stefan Schütz, Serban F. Peteu, Christoph Kleber, Ciril Reiner-Rozman, Christoph Nowak, and Wolfgang Knoll**

ange_201505712_sm_miscellaneous_information.pdf

Table of contents:

1 Materials and Methods

1.1 Cloning and purification of OBPs

1.2 Preparation of odorant solutions

1.3 Setup

1.4 Characterization of the electrical performance of the devices

2 Fabrication process and characterization of OBP-based biosensor device

2.1 FET fabrication

2.2 Reduced Graphene Oxide Gate

2.3 Operation of the FET device

2.4 Hydrolysis of the active ester (PBSE linker)

3 Control measurements

4 Measurements of odorants

1 Materials and Methods

All reagents were purchased from Sigma-Aldrich unless otherwise indicated and used without further purifications.

1.1 Cloning and purification of OBPs

Odorant binding proteins (OBP14) were expressed in bacterial systems using established protocols.^[1] Purification of the proteins was accomplished using a combination of conventional chromatographic techniques followed by a final gel filtration step on Superose-12 (GE-Healthcare) as previously described in standard protocols.^[2] The purity of the proteins was checked by SDS-PAGE and a size of ~14.0 kDa was determined for OBP14 (cf. Figure S1).^[1b]

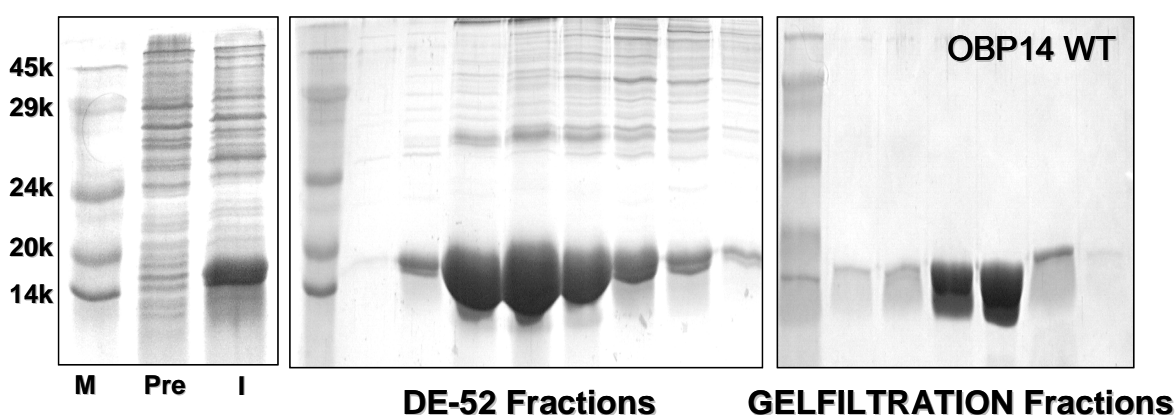


Figure S1. Bacterial expression and purification of OBP14 wt of *A. mellifera*. Purification was accomplished by anion-exchange chromatography on DE-52, followed by a second step on QFF, or gel filtration on Sephacryl-12, as indicated. Molecular weight markers (M) are, from the top, 66, 45, 29, 20 and 14 kDa. Pre: bacterial pellet before induction; I: bacterial pellet after induction with IPTG.

1.2 Preparation of odorant solutions

Odorants were prepared as 5 mM stock solutions in phosphate buffer (1 mM PBS, pH = 8.0) with an addition of 0.01 % ethanol (purity ≥ 99.9 %) and further diluted (from 10^{-3} M to 10^{-7} M) by successive dilutions in PBS buffer. All solutions were freshly prepared on the day of the experiment.

A broad spectrum of ligands was tested known as typical pollen odorants like the benzenoids Eugenol (4-Allyl-2-methoxyphenol) and Methyl eugenol (1,2-Dimethoxy-4-prop-2-enylbenzene).^[3]

Moreover, a few floral volatiles, known to be attractive for bees, were tested. These include Citral ((2E)-3,7-dimethylocta-2,6-dienal) and Geraniol ((2E)-3,7-Dimethylocta-2,6-dien-1-ol), which were also identified as Nasonov pheromone compounds. In addition, two honey flavours, namely Homovanillic acid (2-(4-Hydroxy-3-methoxy-phenyl)acetic acid) and Methyl vanillate (Methyl 4-hydroxy-3-methoxybenzoate) were also tested.

1.3 Setup

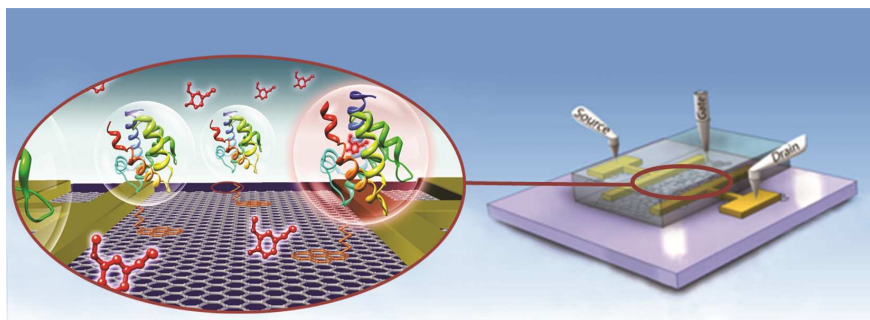


Figure S2. Schematic illustration of the graphene based FET biosensor device with gold source and drain electrodes and an Ag/AgCl gate electrode. The area between the gold electrodes is covered by OBP14 proteins immobilized with a bifunctional linker. Eugenol can be captured into the binding pocket of the protein.

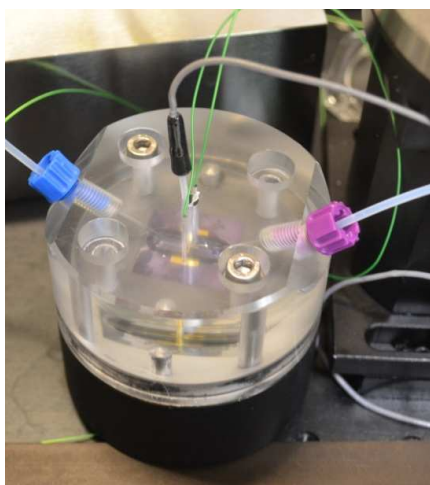


Figure S3. Electrical connections and flow inlet and outlet are realized by a customized polymer block.

1.4 Characterization of the electrical performance of the devices

Electrodes were applied consisting of gold (60-100 nm) with an adhesive layer of chrome (2-3 nm) using a standard evaporation process with a shadow mask. A chip-holder was designed for this process, ensuring the central positioning of the electrodes as well as reducing electrode geometry glazing because of unwanted shadow offset during the evaporation process. Success of the used reduction technique via hydrazine was probed before (Larisika et al., 2012), so resistance of the fabricated devices was measured for check-up of graphene-oxide reduction quality using a Fluke Multimeter "87 V True RMS Multimeter". To assure conductivity of the used electrolyte not being higher than the conductivity of used graphene layers, all devices displaying higher conductivity than ~800 ohm were dismissed, equivalent to the resistance of 170 mM PBS buffer at room temperature. A silver-silver chloride reference electrode (Flex ref, World Precision Instruments) was used to operate the FET device in liquid gate configuration with a constant gate bias (V_g) of -0.6 V and a constant source-drain bias (I_{SD}) of 0.05 V. The general procedure of the whole titration experiment started with continuously flushing the detection area with pure buffer (1 mM PBS, pH = 8.0), until a stable baseline of drain current was established.

2 Fabrication process of OBP-based biosensor device

2.1 FET fabrication

Silicon substrates with a 300 nm oxide layer were chosen as basal layer for the FETs. The SiO₂ substrates were cleaned with a standard RCA cleaning procedure. The substrates were then submerged in a 2% aminopropyltriethoxysilane (APTES) solution in ethanol for 1 h, APTES forming a self-assembled monolayer used to increase the adsorption of graphene oxide sheets. After rinsing with ethanol, the substrates were heated to 120°C for two hours and afterwards cooled to room temperature. Graphene oxide sheets were prepared using a variation of the Hummers method derived for the application on FETs.^[4] The obtained graphene oxide flakes were applied onto the Si-Wafer via drop casting of the top portion of the graphene-oxide solution. The devices were then treated in hermetically sealed glass petri dishes with hydrazine at 70°C overnight to accomplish the graphene-oxide reduction, forming the graphene structure consisting of sp²-hybridized bonds. Flake distribution was first checked with an optical microscope and selected devices then characterized using SEM.

2.2 Reduced Graphene Oxide Gate

The entire fabrication process of the olfactory biosensor device, including successful reduction of GO to rGO, linker binding and protein attachment was carefully examined using Raman and Fourier transform infrared (FTIR) spectroscopy. Raman measurements were done using a Horiba LabRAM HR Raman confocal microscope (a laser with a wavelength of 532 nm (52 mW, 10% filter) and a laser spot size of 0.41 μm² was used).

FTIR Microscope measurements were performed with 256 scans using a Bruker Hyperion 3000 Microscope. For Raman and FTIR Microscope measurements, silicon wafers were used as substrates. Samples were prepared as described previously.^[4] In order to follow the protein immobilization, FTIR measurements were done using a Bruker Vertex 70 V FTIR Spectrometer and a multiple reflection silicon ATR crystal (angle of incidence $\Theta = 45^\circ$, 12.5 active reflections). Spectra were recorded every 5 minutes with a spectral resolution of 4 cm⁻¹ in double-sided acquisition mode; the mirror velocity was set to 80 kHz.

The Raman spectrum of GO shows two prominent bands at 1342 cm⁻¹ (D-Band) and 1581 cm⁻¹ (G-Band) and three smaller bands at 2680 cm⁻¹ (2D Band), 2930 cm⁻¹ (D+G Band) and 3230 cm⁻¹ (2D' Band), respectively (cf. Figure S4).

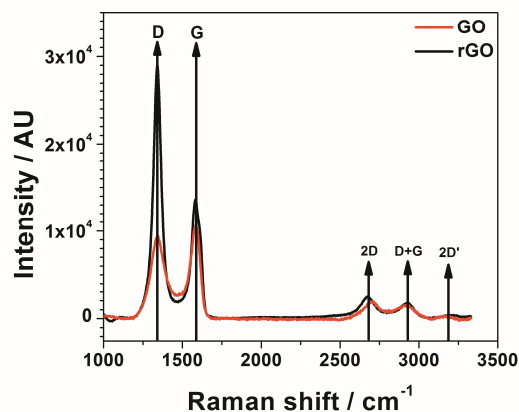


Figure S4. Raman spectra of graphene oxide (GO) and reduced graphene oxide (rGO).

Table ST1. Band positions of Raman spectra.

Band	Graphene oxide		Reduced grapheme oxide	
	Experimental [cm ⁻¹]	Literature [cm ⁻¹]	Experimental [cm ⁻¹]	Literature [cm ⁻¹]
D	1342	1341 ^[4]	1338	1341 ^[4]
G	1581	1595 ^[4]	1573	1595 ^[4]
2D	2680	2700 ^[5]	2671	2726 ^[6]
D+G	2930	2950 ^[5]	2927	2960 ^[5]
2D'	3230		3215	3220 ^[5]

After reduction, the G and 2D bands are shifted to lower wave numbers. The D/G ratio of GO increased from 0.9 to 2.1 after the reduction process. This can be explained by an increase of sp² domains in the carbon.^[7] Table ST1 compares band positions of Raman spectra of GO and rGO with literature data.

2.3 Operation of the FET device

The mode of operation of the device as a field-effect transistor is given in Figure S5. In the I_{SD}-vs-V_G scan one can clearly distinguish between the two ambipolar branches typical for graphene FETs: the cathodic scan which is dominated by the hole mobility and the anodic scan determined by the electron mobility. The Dirac voltage is seen at ca. V_G = 0.4 Volts. Recording these I_{SD}-vs-V_G scans at different bulk solution conditions, in particular, in aqueous solutions of different ligand concentrations results in a slightly modified slope of the cathodic branch which we attribute to a slight modification of the dipolar layer with the OBP protein monolayer immobilized onto the graphene gate surface upon partial binding of the ligand to the free binding sites in the OBP acting as receptors.

Figure S5 shows this effect for different Eugenol concentrations ranging from 100 nM to 250 μM. Therewith we selected a negative gate voltage of V_G = -0.6 V for all ligand binding measurements.

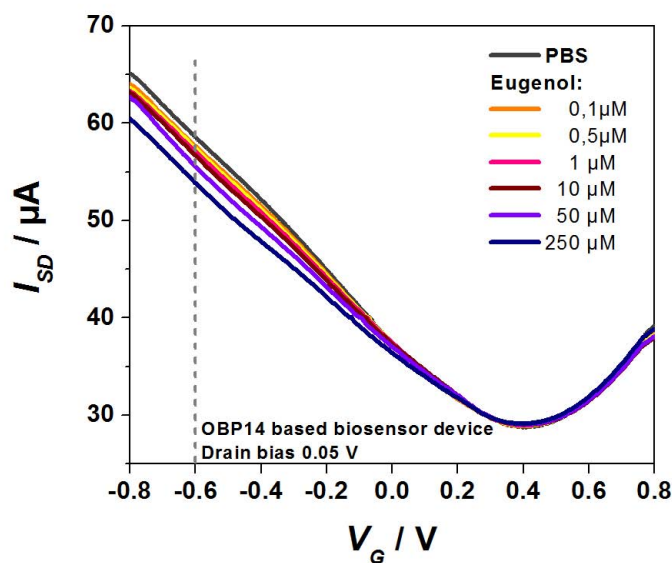


Figure S5. Current-voltage characteristics of the OBP14 based biosensor device without Eugenol (PBS buffer) and with 100 nM - 250 μM Eugenol.

2.4 Hydrolysis of the active ester (PBSE linker)

Figure S6 shows FTIR measurements of the immobilized PBSE linker, incubated in PBS buffer (A). The bands of the active ester (1738, 1781, and 1815 cm^{-1} , respectively) decrease as a function of time because of spontaneous hydrolysis. Figure S6 B shows the exponential decrease of all three bands. For the attachment of the protein to the sensing area, the graphene surface was chemically modified by a bi-functional linker, 1-pyrenebutanoic acid succinimidyl ester (PBSE). On one end the linker firmly

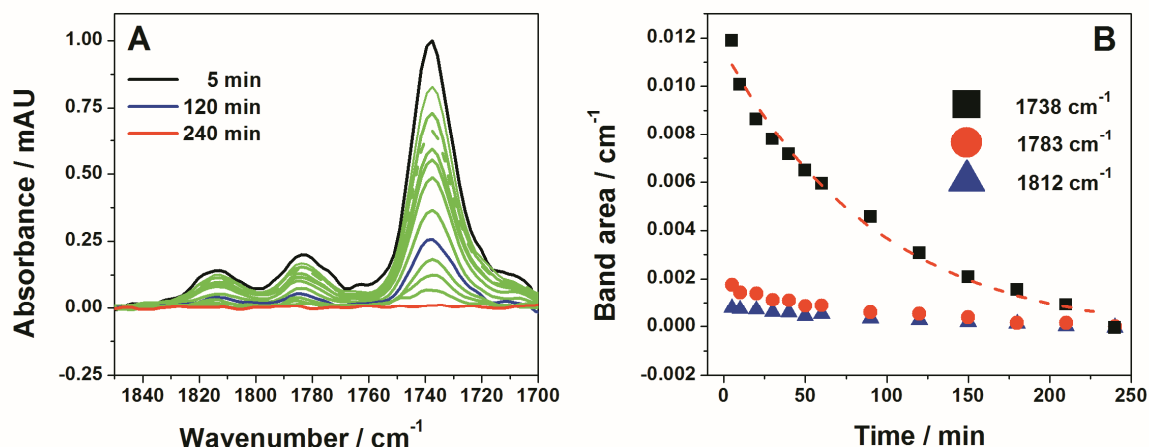


Figure S6. (A) Hydrolysis of the active ester in PBS leads to a decrease of the bands at 1738, 1781 and 1815 cm^{-1} , respectively. (B) The area of the 1738, 1783, and 1812 cm^{-1} band, respectively, decrease as a function of time. The dashed red curve guides the eye.

attaches to the graphene surface through π - π interactions with a pyrene group and on the other hand covalently reacts with the amino group of the protein to form an amide bond. Therefore, 20 μL of a 5 μM PBSE solution in Tetrahydrofuran was placed onto the rGO-FET channel. Fast evaporation of Tetrahydrofuran allowed immediate deposition of 30 μL of a 10 μM OBP14 solution in PBS buffer (1 mM; pH = 8.0) onto the detection area and incubated for 2h at 4 $^{\circ}\text{C}$. Loosely or unbound linker/OBP14 was ensured by rinsing the detection area with same PBS buffer. The entire fabrication process of the olfactory biosensor device, including successful reduction of GO to rGO, linker binding and protein attachment was carefully examined using spectroscopic methods, as described in chapter Fabrication process of OBP-based biosensor device.

3 Control measurements

Figure S7 shows different types of control measurements that were performed in order to demonstrate that the response signals obtained by the olfactory biosensor are specific and thus clearly assignable as protein-ligand interactions rather than non-specific interaction of the tested odorants with the rGO surface. Firstly, rGO-FET devices were fabricated and functionalized as described above but without any odorant binding protein (OBP) immobilized. Figure S7 A demonstrates that after addition of different concentrations of a phenolic structured odorant like Homovanillic acid, no sensor signal could be observed. Similar observations were made for other ligands (Figure S7 B).

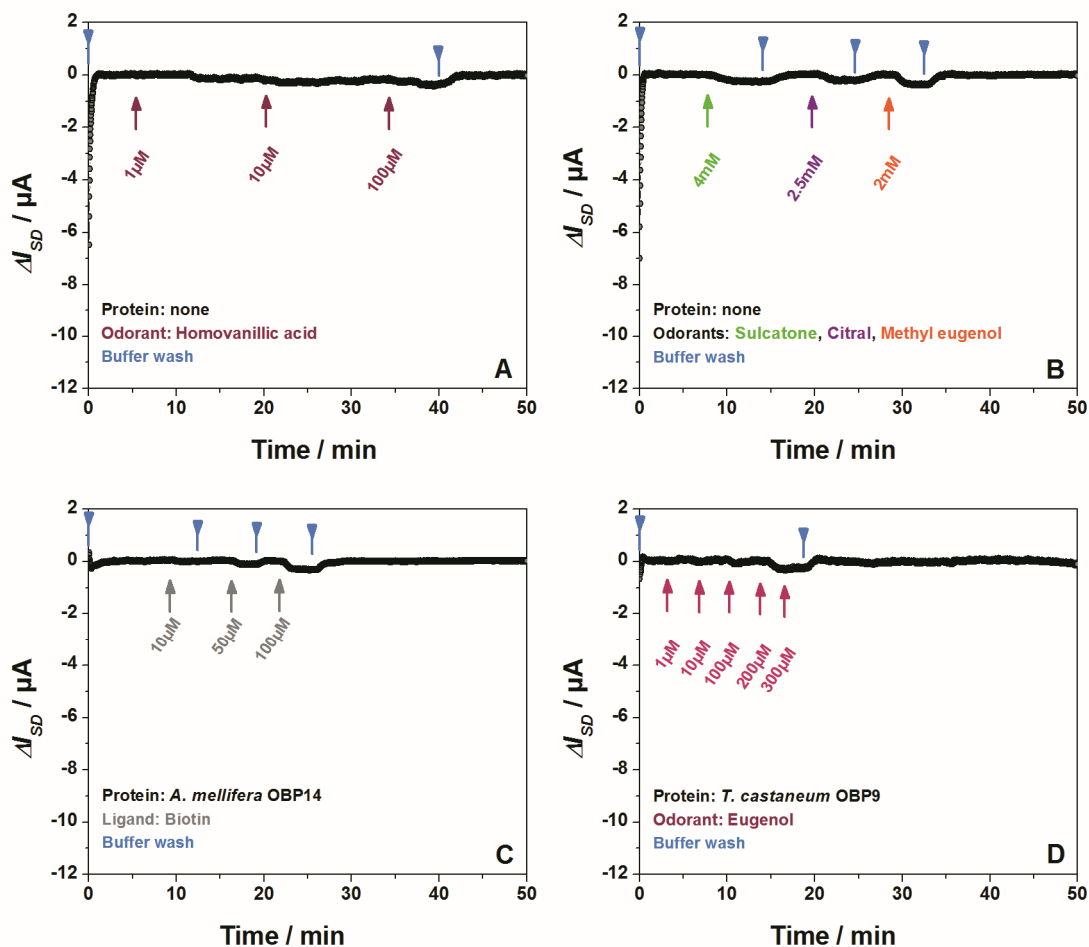


Figure S7. (A) Real-time response of PBSE-functionalized rGO-FETs to different concentrations of Homovanillic acid. (B) ΔI_{SD} vs. time measurement of PBSE-functionalized rGO-FETs to high concentrations (mM range) of different odorants. (C) Real-time response of OBP14-functionalized biosensor to different concentrations of a nontarget ligand, i.e., biotin. (D) Real-time response of an OBP9-functionalized biosensor to different Eugenol concentrations.

Figure S7 C demonstrates that introducing a small but unnatural ligand like biotin to the OBP14 functionalized sensor surface, does not show a distinct response signal. And finally, after immobilizing an odorant binding protein from a different species, namely OBP9 from *Tribolium castaneum* to the rGO surface, different concentrations of Eugenol do not cause a detectable change in the source-drain-current, whereas this odorant proved to be an extremely strong ligand to OBP14 from the honeybee (cf. Fig. 7 D).

In conclusion, all negative control experiments have clearly demonstrated that although it seems likely that π -orbitals of phenolic compounds like Eugenol or Homovanillic acid are easily stacked on the rGO surface similar to pyrene derivatives (e.g., PBSE), the sensor response signals clearly reflect the

affinity between OBPs and their ligands and is not caused by unspecific interactions of odorants with the rGO surface.

4 Measurements of all odorants

In the following Figures S9 – S13, individual real-time biosensor measurements of the binding of different ligands (one example each) to OBP14 are summarized: In each case, (A) shows the current increase upon increasing the bulk concentration of the ligands in solution (red arrows). Blue arrows indicate runs with pure buffer.

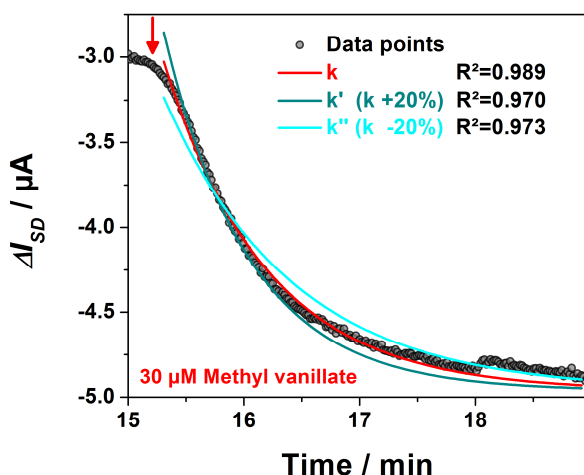


Figure S8. On the determination of the rate constant, k , and its error limits.

An example of how we determine the error limits of the rate constants is given in Figure S8. Shown are the experimental data of the current change, ΔI_{SD} , after injection of a 30 μM solution of Methyl vanillate into the flow cell, together with 3 fit curves: red, $k=0.01872 \text{ s}^{-1}$, dark blue with $k'=k+20\%$, light blue, $k''=k-20\%$. This error limit is added to all rate constants in the following figures.

(B) Plotting the reaction rate constants as derived from the fits to the kinetic traces (full red curves shown in (A)) as a function of the respective bulk ligand concentration, $c_0=c_{\text{ligand}}$, (for all ligands given in (B)) one obtains a straight line, the slope of which yields k_{on} , and the intersection with the y-axis gives k_{off} , respectively. According to the Langmuir model the ratio $k_{\text{on}}/k_{\text{off}}$ gives the affinity constant K_A . The obtained values for all ligands are indicated. (C) According to $\theta=K_A c_0/(1+K_A c_0)$ one obtains from the fit to the equilibrium surface coverage, θ , ($=\Delta I_{SD}/\Delta I_{SD,\text{max}}$) (full red curve) the affinity constant K_A , which typically compares quite well with the value obtained from the kinetic experiments thus confirming the Langmuir model for this binding process. Obtained affinity constants are given for each.

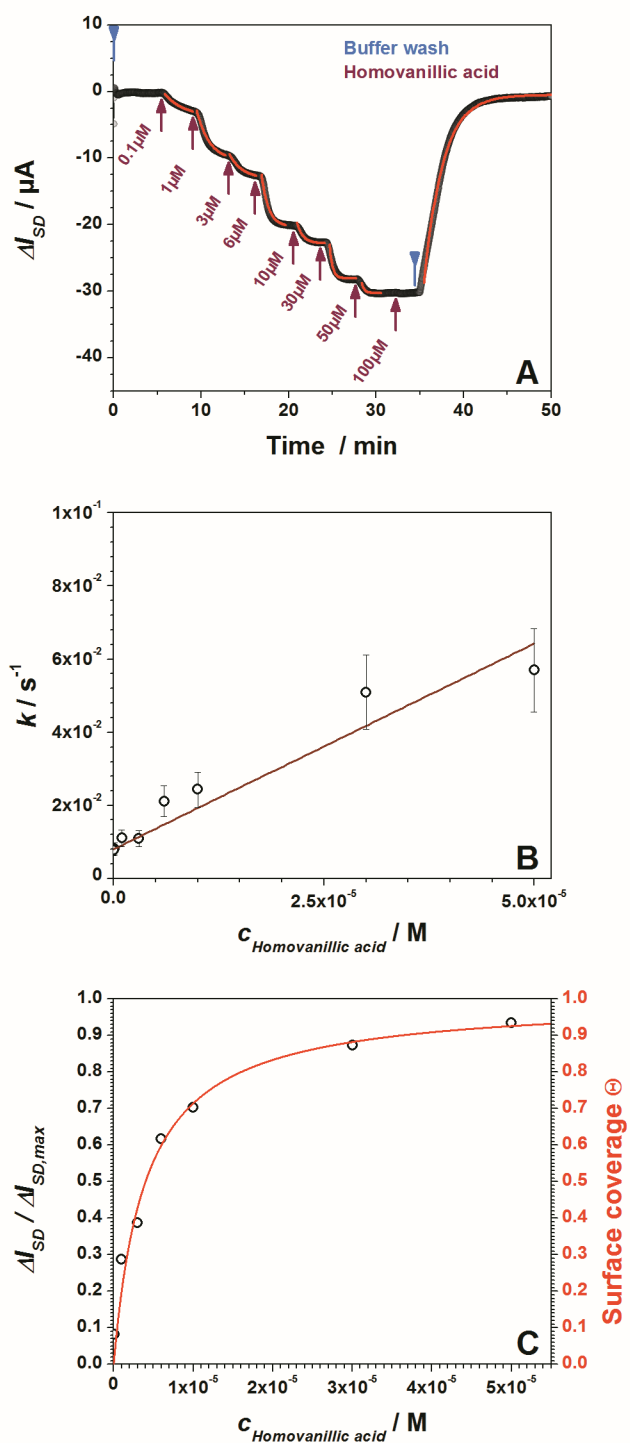


Figure S9. Homovanillic acid

Obtained affinity constants:

Figure S9 A $k_{off} = 0.008\ s^{-1}$; $k_{on} = 1126\ M^{-1}\ s^{-1}$; $K_d = 7.1 \times 10^{-6}\ M$

Figure S9 B $K_d = 4 \times 10^{-6}\ M$

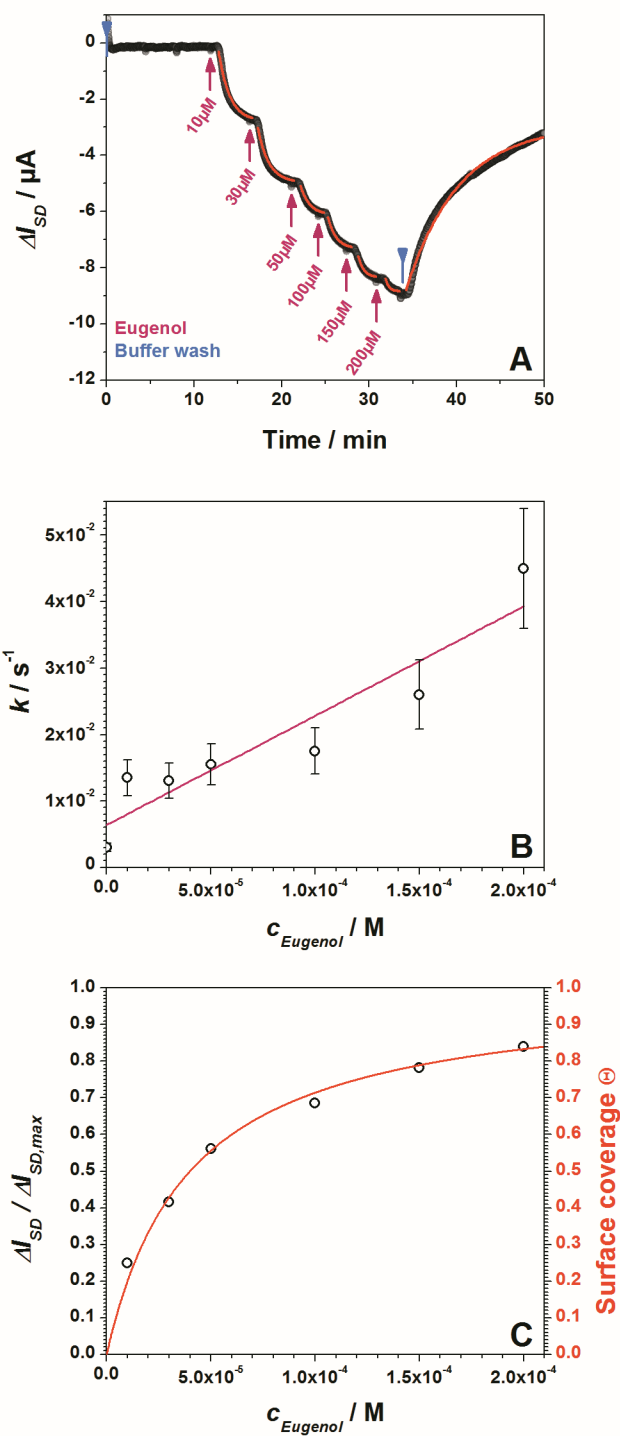


Figure S10. Eugenol

Obtained affinity constants:

Figure S10 A $k_{off} = 0.006 s^{-1}$; $k_{on} = 170 M^{-1} s^{-1}$; $K_d = 3.5 \times 10^{-5} M$
 Figure S10 B $K_d = 4 \times 10^{-5} M$

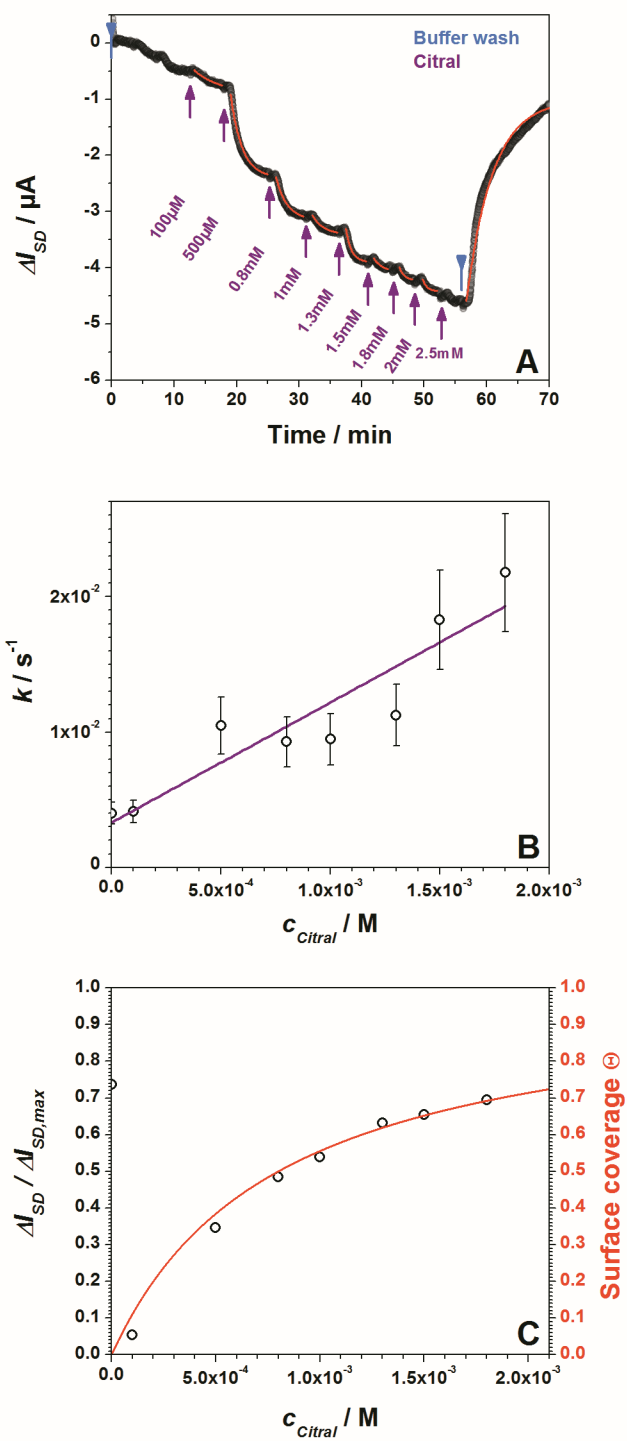


Figure S11. Citral

Obtained affinity constants:

Figure S11 A $k_{off} = 0.0033 s^{-1}$; $k_{on} = 8.9 M^{-1} s^{-1}$; $K_d = 3.1 \times 10^{-4} M$
 Figure S11 B $K_d = 8 \times 10^{-4} M$

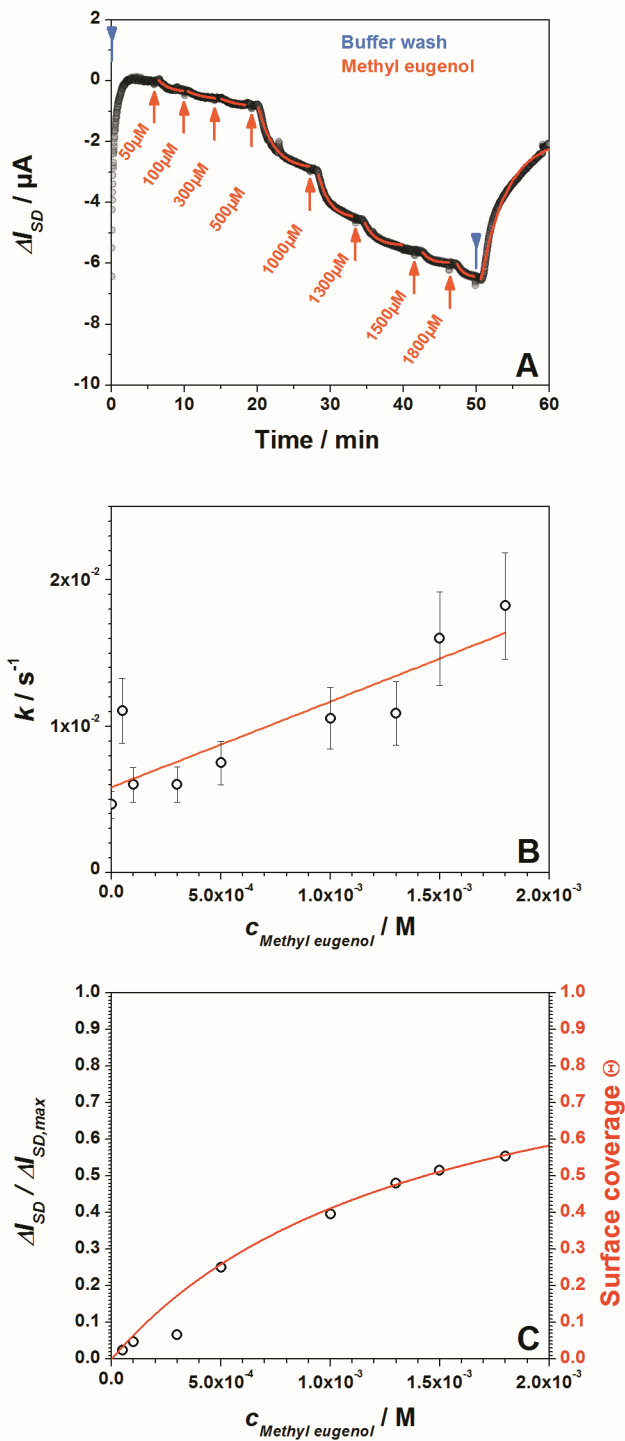


Figure S12. Methyl eugenol

Obtained affinity constants:

Figure S12 A $k_{off} = 0.0058\ s^{-1}$; $k_{on} = 5.9\ M^{-1}\ s^{-1}$; $K_d = 1.1 \times 10^{-3}\ M$

Figure S12 B $K_d = 1.4 \times 10^{-3}\ M$

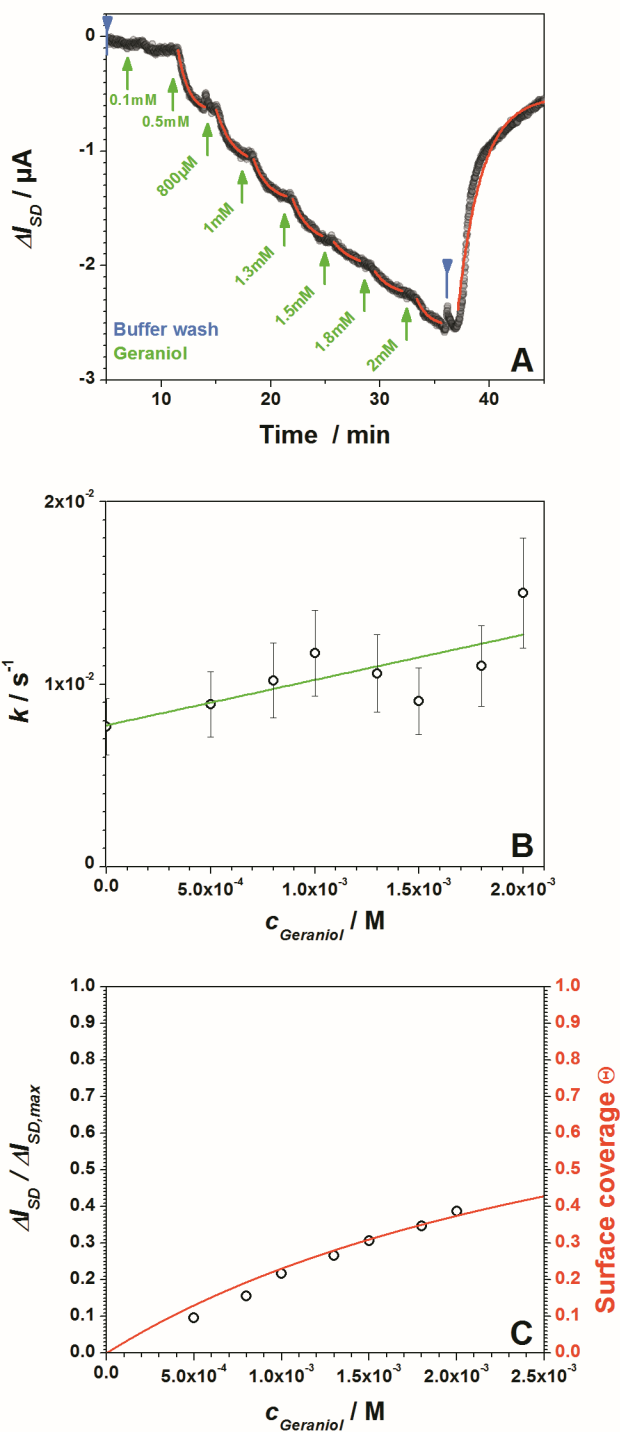


Figure S13. Geraniol

Obtained affinity constants:

Figure S13 A $k_{off} = 0.0078 s^{-1}$; $k_{on} = 2.5 M^{-1} s^{-1}$; $K_d = 3.25 \times 10^{-3} M$

Figure S13 B $K_d = 3.3 \times 10^{-3} M$

References

- [S1] a) F. R. Dani, I. Iovinella, A. Felicioli, A. Niccolini, M. A. Calvello, M. G. Carucci, H. Qiao, G. Pieraccini, S. Turillazzi, G. Moneti, P. Pelosi, *J. Proteome Res.* 2010, *9*, 1822; b) A. Felicioli, P. Pelosi, *J. Proteome Res.* 2011, *10*, 3439.
- [S2] a) L. Ban, A. Scaloni, A. Brandazza, S. Angeli, L. Zhang, Y. Yan, P. Pelosi, *Insect Mol. Biol.* 2003, *12*, 125; b) M. Calvello, N. Guerra, A. Brandazza, C. D'Ambrosio, A. Scaloni, F. R. Dani, S. Turillazzi, P. Pelosi, *Cell. Mol. Life Sci.* 2003, *60*, 1933.
- [S3] a) H. E. M. Dobson, G. Bergstrom, I. Groth, *Israel J. Bot.* 1990, *39*, 143; b) S. Dötterl, N. J. Vereecken, *Can. J. Zool.* 2010, *88*, 668; c) D. Laloi, M. Gallois, B. Roger, M. H. Pham-Delegue, *Apidologie* 2001, *32*, 231; d) M. Trhlin, J. Rajchard, *Vet. Med.* 2011, *56*, 265; e) V. A. Isidorov, U. Czyzewska, E. Jankowska, S. Bakier, *Food Chem.* 2011, *124*, 387; f) C. Guyot, V. Scheirman, S. Collin, *Food Chem.* 1999, *64*, 3.
- [S4] M. Larisika, J. Huang, A. Tok, W. Knoll, C. Nowak, *C. Mater. Chem. Phys.* 2012, *136*, 304.
- [S5] C. Y. Su, Y. P. Xu, W. J. Zhang, J. W. Zhao, X. H. Tang, C. H. Tsai, L. J. Li, *Chem. Mater.* 2009, *21*, 5674.
- [S6] F. T. Thema, M. J. Moloto, E. D. Dikio, N. N. Nyangiwe, L. Kotsedi, M. Maaza, M. Khenfouch, *J. Chem.* 2013, 2013.
- [S7] T. N. Lambert, C. A. Chavez, B. Hernandez-Sanchez, P. Lu, N. S. Bell, A. Ambrosini, T. Friedman, T. J. Boyle, D. R. Wheeler, D. L. Huber, *J. Phys. Chem. C* 2009, *113*, 19812.

Article

Electronic Biosensing with Functionalized rGO FETs

Ciril Reiner-Rozman ^{1,2,†}, Caroline Kotlowski ^{1,2,†} and Wolfgang Knoll ^{1,2,*}

¹ Center for Electrochemical Surface Technology (CEST), Wiener Neustadt 2700, Austria; rozman.ciril.fl@ait.ac.at (C.R.-R.); caroline.kotlowski@boku.ac.at (C.K.)

² AIT Austrian Institute of Technology, Wien 1220, Austria

* Correspondence: wolfgang.knoll@ait.ac.at; Tel.: +43-50-550-4002

† These authors contributed equally to this work.

Academic Editors: Mark A. Reed and Mathias Wipf

Received: 28 February 2016; Accepted: 31 March 2016; Published: 22 April 2016

Abstract: In the following we give a short summary of examples for biosensor concepts in areas in which reduced graphene oxide-based electronic devices can be developed into new classes of biosensors, which are highly sensitive, label-free, disposable and cheap, with electronic signals that are easy to analyze and interpret, suitable for multiplexed operation and for remote control, compatible with NFC technology, *etc.*, and in many cases a clear and promising alternative to optical sensors. The presented areas concern sensing challenges in medical diagnostics with an example for detecting general antibody-antigen interactions, for the monitoring of toxins and pathogens in food and feed stuff, exemplified by the detection of aflatoxins, and the area of smell sensors, which are certainly the most exciting development as there are very few existing examples in which the typically small and hydrophobic odorant molecules can be detected by other means. The example given here concerns the recording of a honey flavor (and a cancer marker for neuroblastoma), homovanillic acid, by the odorant binding protein OBP 14 from the honey bee, immobilized on the reduced graphene oxide gate of an FET sensor.

Keywords: reduced graphene oxide (rGO graphene); FET; liquid-gate; biosensing; receptor immobilization; antigen-antibody interaction; food toxins; aflatoxins; odorant-binding proteins; olfaction; smell sensor

1. Introduction

The detection and quantitative monitoring of biomolecules in air, in water, in complex liquids like bodily fluids or similar is still a challenge, both from a fundamental point of view as well as in the context of practical applications. Whether it is the need for sensors in general air management scenarios—e.g., to detect air pollutants (including explosives), to sense crop disease markers, in food quality management for the identification of toxins, or in medical applications like breath analysis—Or for the detection of certain markers in blood, plasma, saliva, urine, wound liquids, *etc.*, that report a patient's health and/or disease status, in all cases we are dealing with three major problems; (i) the sensitivity of the technical device for the quantification of a particular molecule of interest; (ii) the selectivity needed to differentiate between similar molecules; and (iii) the suppression of non-specific interactions with and binding to the sensor surface by other components in the sample volume, typically in excess to the actually targeted molecule.

Numerous concepts and formats for sensors based on optical transduction principles have been reported in the literature, some of which even made it to the market place and are commercialized [1]. Not so widespread are sensors based on electrical, electrochemical or electronic transduction principles [2]. The latter category, in particular, is the youngest member of the huge family of current-based bio-sensors; typical examples are CMOS-transistor-based devices that have been used to

monitor action potentials of excited neurons [3] or cardiomyocytes [4] grown on the gate surface of the device, Si-nanowire based transistor read-out of protein and DNA binding [5], or the promising use of organic (“plastic”) electronics for the development of cheap and, hence, disposable sensors [6,7]. The most recent development in this area, the use of the novel carbon materials, *i.e.*, carbon nanotubes or graphene, opens a totally new but very promising range of options for biosensors based on electronic devices made from these highly interesting materials [8].

In this short summary, we will report some of our own efforts in designing, fabricating, bio-functionalizing and characterizing biosensors based on reduced graphene oxide as the gate material. We will give a very brief overview of the basic preparation protocols, and describe the electronic performance of the devices as transistors [9]. The practical examples given are (i) the detection of a standard biomolecule, bovine serum albumin (BSA), binding from solution to its antibody, immobilized on the sensor surface; (ii) the detection and quantification of food toxins (mycotoxins) binding to their antibodies; and (iii) the monitoring of an odorant molecule (dissolved in an aqueous solution) to the surface-bound odorant binding protein from an insect, the honey bee *Apis mellifera* [10].

2. Preparation and General Electronic Performance of rGO-FET Biosensors

Reduced graphene oxide field-effect transistor (rGO-FET) devices were fabricated with a typical channel width of 40 μm . Figure 1A briefly summarizes the individual preparation steps for the devices [10]. Silicon wafers with a 300 nm oxide layer were chosen as base substrates. They were cleaned following a standard RCA cleaning procedure and then submerged in a 1%–2% 3-amino-propyl-triethoxy-silane-(APTES) solution in ethanol for 1 h, with APTES forming a monolayer on the substrate that increases the adhesion of graphene (reduced graphene oxide).

Graphene oxide sheets were prepared using a variation of Hummers method [11,12]. The obtained graphene oxide flakes were deposited onto Si-wafers via spin coating. A scanning electron microscopic image of the GO flakes on the substrate before reduction of rGO and before the evaporation of the Au electrodes for the transistor are shown in Figure 1B. After rinsing with ethanol, the substrates were heated to 120 $^{\circ}\text{C}$ for two hours and then cooled to room temperature. They were then treated overnight in hermetically sealed glass petri dishes with hydrazine at 70 $^{\circ}\text{C}$ in order to reduce the graphene oxide, forming the graphene structure consisting of sp^2 -hybrid bonds.

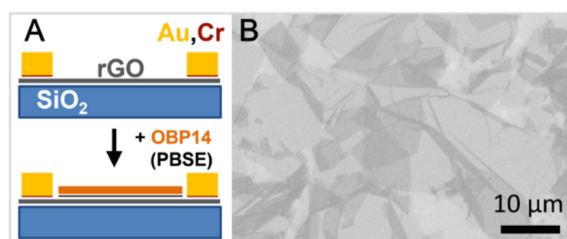


Figure 1. (A) Schematic illustration of the individual fabrication steps of the graphene biosensor device: After the reduction of the GO flakes to rGO, source and drain Au electrodes were evaporated (with a thin layer of Cr as an adhesion promotor), then coated (via self-assembly) by a linker, PBSE, and finally functionalized by the attachment of antibodies or by odorant binding proteins, here OBP 14 from the honey bee; (B) Scanning electron microscopic image of the GO flakes on the chip substrate (before reduction to rGO and before being coated with the electrodes).

For the attachment of the antibodies (here, antibodies against bovine serum albumin, BSA, and aflatoxin B1, respectively) to the sensing area, the graphene surface was chemically modified by a bi-functional linker, 1-pyrenebutanoic acid succinimidyl ester (PBSE). One end the linker firmly attaches to the graphene surface through π - π interactions with the pyrene group while the other hand covalently reacts with one of the amino group of the protein to form an amide bond. All reagents were purchased from Sigma-Aldrich unless otherwise indicated and used without further purifications.

For the detection of different odorants, the biosensors were functionalized with an odorant binding protein 14 (OBP 14) from the honey Bee, *Apis mellifera*. The protein was expressed in bacterial systems using established protocols [13,14]. Purification of the proteins was accomplished using a combination of conventional chromatographic techniques followed by a final gel filtration step on Superose-12 (GE-Healthcare) as previously described in standard protocols [14].

The chip was then mounted into a flow cell for *in situ* real-time kinetic measurements (in order to quantify the association, k_{on} , and dissociation rate constants, k_{off} , respectively) as well as for titration experiments for the determination of affinity, K_A , and dissociation constants, K_d , respectively. An artist's sketch of the FET setup and the immobilized OBP interacting with the odorant ligand, together with a photograph of the whole flow cell, are given in Figure 2.

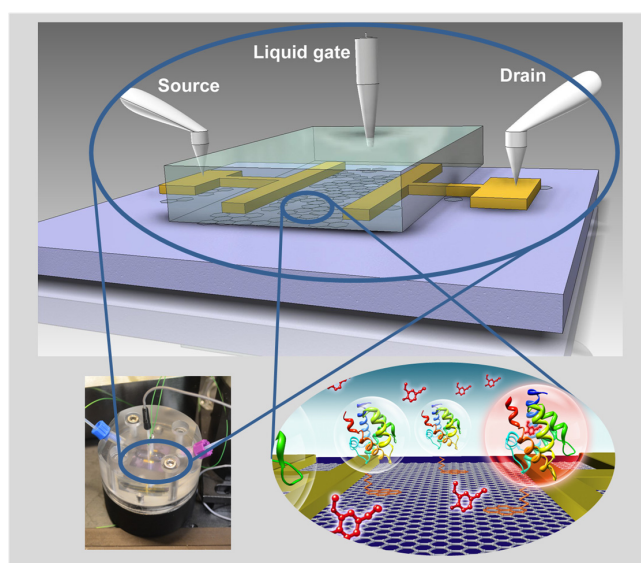


Figure 2. Schematics of the set-up and the device configuration consisting of a liquid gate electrode, source and drain electrodes, evaporated onto the reduced graphene oxide flakes on a solid Si/SiO₂ substrate, functionalized by OBPs that are covalently coupled via a linker molecule. In the lower left corner is a photograph of the mounted flow cell.

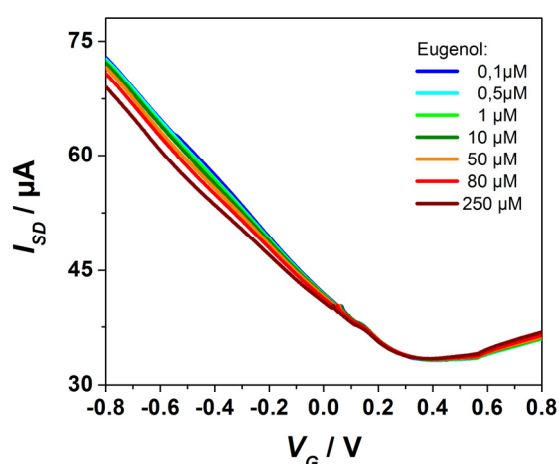


Figure 3. Source-drain current I_{SD} -vs-gate voltage V_G characteristics of the OBP14 functionalized rGO FET-biosensor device at different Eugenol concentrations (as indicated) flowing through the cell.

The electrical properties of the FET devices were tested as described before [15]. Electrical measurements were performed using a Keithley 4200 semiconductor characterization system.

An Ag/AgCl reference electrode (Flexref, World Precision Instruments) was used to operate the FET device in a liquid gate configuration with a constant source-drain bias of $V_{SD} = 50$ mV. The cathodic branches of the I_{SD} -vs- V_G scans (*cf.* Figure 3) are dominated by the hole mobility [9]. The Dirac voltage is seen at ca. $V_G = 0.4$ V. Recording these I_{SD} -vs- V_G scans at different bulk solution conditions, in particular in aqueous solutions of different ligand concentrations, results in a distinct shift of the cathodic branch which we attribute to a slight modification of the dipolar layer with the OBP protein monolayer immobilized on the graphene gate surface upon partial binding of the ligands to the free binding sites in the OBP acting as receptors.

3. Antigen–Antibody Interaction and the Limit of Detection

The first example that we describe for the use of these rGO-FETs as biosensors concerns the “classical” system, *i.e.*, the binding of the protein bovine serum albumin, BSA, as antigen to its FET-immobilized antibody. The global analysis protocol, *i.e.*, the stepwise increase of the bulk analyte concentration while simultaneously recoding the time-dependent change of the source-drain current, ΔI_{SD} , is given in Figure 4. One can see that the current decreased each time the bulk concentration was increased from an initial concentration $c_0 = 100$ nM, until it gradually reached a saturation level for a bulk concentration near $c_0 = 25$ μ M. The current decrease following each concentration change contains kinetic information (*cf.* the red curves that fit the current traces) occurs by a single exponential giving a time constant, k , that is concentration dependent (increases with bulk concentration). This is in agreement with the Langmuir model for this 1:1 complex between the analyte (the antigen) from solution and the surface-immobilized receptor (the antibody). Upon rinsing with pure buffer, the current returns to its original baseline level with a single exponential (*cf.* the blue fit curve) indicating the full reversibility of the binding event (a prerequisite for any analysis according the Langmuir model). The fit to this dissociation process results in a quantitative measure of the dissociation rate constant, k_{off} . From the slope of the plot of all the rate constants determined as a function of the bulk concentration, one obtains the association rate constant, k_{on} , which together with k_{off} gives the affinity constant, K_A . This has been documented recently and reported to result in an affinity constant for the binding of BSA to this antibody of $K_A = 1.6 \times 10^5$ M^{-1} [9], corresponding to a dissociation constant of $K_d = 6.2$ μ M.

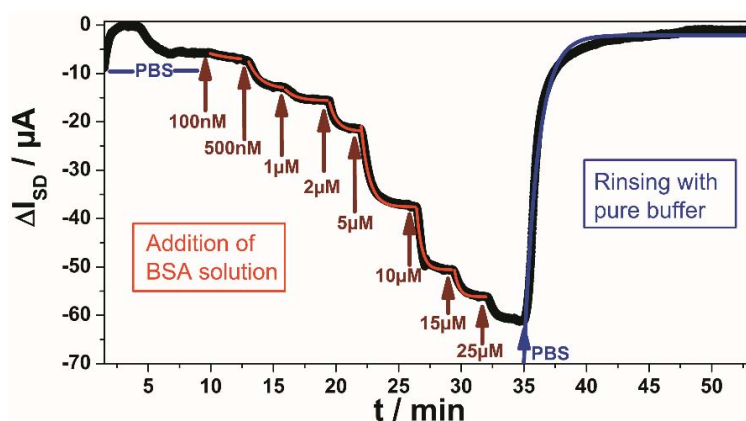


Figure 4. Global analysis of BSA binding from solution to surface-immobilized anti-BSA antibody; solutions with concentrations from 100 nM to (near) saturation at 25 μ M (as indicated in red) were rinsed through the flow cell. The first few minutes show a drift due to the graphene charging behavior, which stabilizes after 7 min.

Figure 5 summarizes the results taken from Figure 4, focusing here on the titration of the equilibrium surface coverage (*i.e.*, the new source-drain current that one reads after the new equilibrium has been established) as a function of the bulk analyte concentration in solution, *i.e.*, the Langmuir isotherm. By plotting the surface coverage, Θ , *i.e.*, the source-drain current at a given concentration,

$I_{SD}(c_0)$, divided by $I_{SD}(c_\infty)$, the source drain current at infinite bulk analyte concentration, one obtains the affinity constant, K_A :

$$\Theta = I_{SD}(c_0)/I_{SD}(c_\infty) = K_A c_0 / (1 + K_A c_0) \quad (1)$$

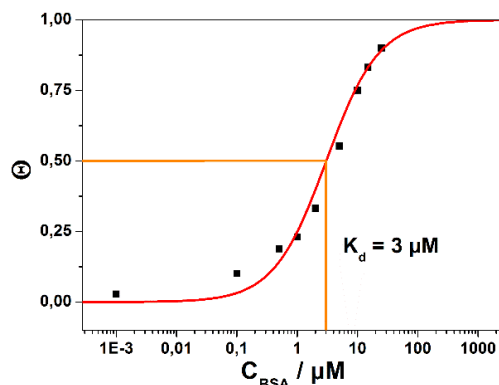


Figure 5. Langmuir adsorption isotherm obtained by plotting the (negative) change in the source-drain current, ΔI_{SD} , as obtained from Figure 4 from the new stationary current after changing the concentration in the bulk solution to a new value. The red curve is a fit to the data according to the Langmuir model, resulting in a dissociation constant (half saturation concentration) $K_d = 3 \mu\text{M}$.

In Figure 5, we have plotted the surface coverage as a function of the (logarithm of the) bulk analyte concentration, and obtain the expected S-shaped curve. The corresponding fit to the data (full red curve in Figure 5) results in an affinity constant $K_A = 3.3 \times 10^5 \text{ M}^{-1}$, corresponding to a dissociation constant, *i.e.*, a half-saturation constant, $K_d = 3 \mu\text{M}$. Compared to the value obtained from the kinetic measurements ($K_d = 6.2 \mu\text{M}$) this can be considered as an excellent confirmation of the applicability of the Langmuir model to the quantitative description of the binding assay of BSA to its surface-immobilized antibody. Furthermore, it confirms that the electronic read-out of this model binding reaction can be considered as a quantitative method for general biosensing purposes.

The next question that naturally comes up is that of the limit of detection of this electronic monitoring of antigen-antibody interactions. To this end, we show in Figure 6 the kinetic recording of the current change upon switching the solution that was running through the flow cell from pure PBS buffer to a 1 nM BSA solution and then again back to pure buffer. As one can see, ΔI_{SD} can still be monitored with a superb signal-to-noise ratio. Based on this measurement, the LOD could be estimated to be in the 100 pM analyte concentration range.

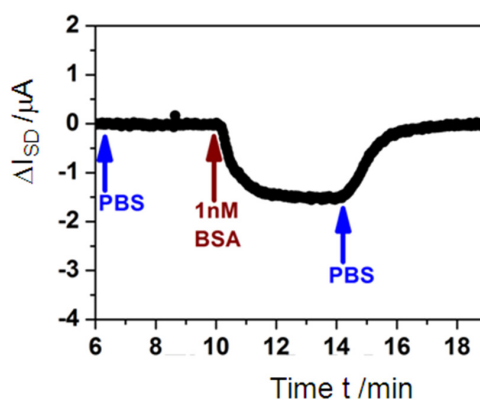


Figure 6. Single kinetic run, *i.e.*, recording of the change in the source-drain current, ΔI_{SD} , after switching in the flow cell from pure PBS buffer (blue arrow) to a 1 nM BSA solution (brown arrow) in order to monitor the association rate constant, and back to pure buffer again (blue arrow), in order to monitor the dissociation rate constant.

Within the Langmuir model this means that, according to Equation (1) with $c_0 \ll 1 / K_A$, the coverage at this low concentration is given by

$$\Theta = K_A c_0 \quad (2)$$

and with $K_A = 3.3 \times 10^5 \text{ M}^{-1}$, and $c_0 = 100 \text{ pM}$, this then corresponds to a coverage of bound analyte of $\Theta = 3.3 \times 10^{-5}$. In other words, the minute change of the interfacial surface potential that is induced if only 1 out of 30,000 antibodies on the sensor surface binds an analyte molecule is enough to generate a current signal that can be quantified.

4. Food Toxin Detection, Comparison with Optical Sensing

The next example that we discuss concerns the detection of food pathogens, aflatoxins, in particular. They constitute a class of mycotoxins produced mainly by *Aspergillus flavus* and *Aspergillus parasiticus* which grow in a number of agricultural products. Aflatoxin M1 (AFM1) is the hydroxylated metabolite of aflatoxin B1 (AFB1) and can be found in urine, blood, milk, and internal organs of animals that have ingested AFB1-contaminated feed [16]. Due to its hepatotoxic and carcinogenic effects [17] and the relative stability during pasteurization or other thermal treatments, control measurements were established. For instance, the European Commission stipulates a maximum level of $50 \text{ pg} \cdot \text{ml}^{-1}$ for AFM1 in milk [18].

As a reference and benchmark, we start with the presentation of an optical assay based on surface-plasmon fluorescence spectroscopy, developed in our own group, combined with an inhibition immunoassay in which a derivative of AFM1 was immobilized on the sensor surface and monoclonal anti-AFM1 antibodies from the rat were used as recognition elements [19]. In this protocol the analyte sample is first incubated with a solution of anti-AFM1 antibodies of a known concentration. Some of the antibodies bind to the free AFM1 molecules; upon rinsing this cocktail through the sensor flow cell, the remaining unoccupied antibodies can then bind to the surface-immobilized AFM1 antigens, and are detected by decoration with a secondary, fluorescently labeled goat anti-rat antibody (Cy5-GaR, approximately 10.2 dyes per antibody).

The result of a series of measurements with sample solutions of different AFM1 concentrations is presented in Figure 7. The lower the bulk aflatoxin concentration the higher is the sensor signal from the unoccupied antibodies, now being immobilized on the sensor surface. The half-saturation value as a measure of the sensitivity of the optical assay is at $c_0 = 100 \text{ pM}$, with a LOD of about $0.6 \text{ pg} \cdot \text{ml}^{-1}$ at a processing time of 1 h.

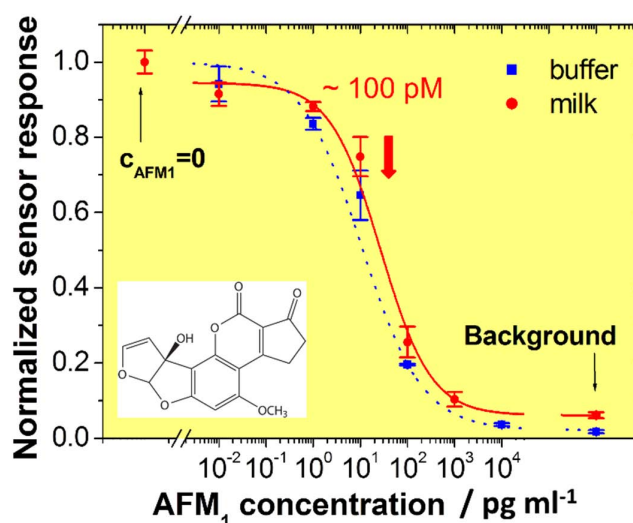


Figure 7. Normalized calibration curves for the detection of AFM1 in buffer (squares) and milk samples (circles).

In contrast to the optical reference assay, the electronic read-out has a number of advantages: (i) the sensor monitors the analyte binding in real time; hence is only diffusion limited and therefore faster; (ii) it gives direct kinetic information, *i.e.*, one also obtains association and dissociation rate constants; (iii) the assay does not use any secondary antibody, and hence requires fewer processing steps; (iv) the electronic sensing device based on “plastic electronics” is a disposable and does not need any sophisticated optical detection instrumentation, and hence is cheaper.

We first addressed the question of non-specific binding of the analyte aflatoxin to the bare rGO gate. Figure 8A demonstrates that—Not totally unexpected given the molecular structures of the analyte molecule and graphene, respectively, suggesting a significant non-specific binding by π - π -interactions—A change in the source-drain current, I_{SD} , upon the injection of a 64 nM solution of AFB1 into the flow cell, can indeed be monitored.

However, this non-specific binding can be totally suppressed for a test surface that is first functionalized by an antibody specific for a totally different analyte (BSA in this case). As can be seen in Figure 8B, even significant concentrations of AFB1 rinsed through the flow cell do not lead to any detectable change in the source-drain current, ΔI_{SD} .

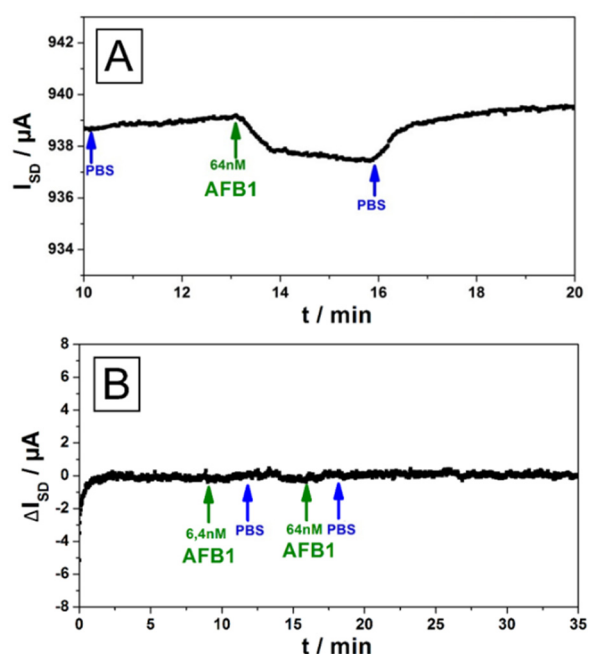


Figure 8. (A) Analysis of the binding of aflatoxin B1 (structure formula given in the inset of Figure 9) on a bare rGO gate surfaces using a blank FET. The signal strength for nanomolar concentrations was found to be only around 10% compared to the measurements were the target antibody was used (*cf.* Figure 9); (B) Unspecific responses for aflatoxin B1 were measured on graphene FET's with immobilized PBSE-linker and BSA antibodies. For all tested devices no response signal was observed, indicating that no binding of AFB1 to the linker or to a non-target antibody is occurring.

The specific binding of AFB1 to its antibody on the sensor gate surface and the sensitivity issue can be best judged by referring to the data displayed in Figure 9. Here, the antibody against AFB1, was directly immobilized on the rGO gate of the transistor. Rinsing analyte solutions of different concentrations (as indicated by the green arrows in Figure 9, alternating with pure PBS buffer, blue arrows) through the attached flow cell led to a direct sensor signal, *i.e.*, a change in the source-drain current, ΔI_{SD} , of the FET. As one can see the sensor responds with a change of its source-drain current, with a good signal-to-noise ratio, already at analyte concentrations in the several 10 pM range. This is quite comparable to the much more demanding optical approach described in Figure 7.

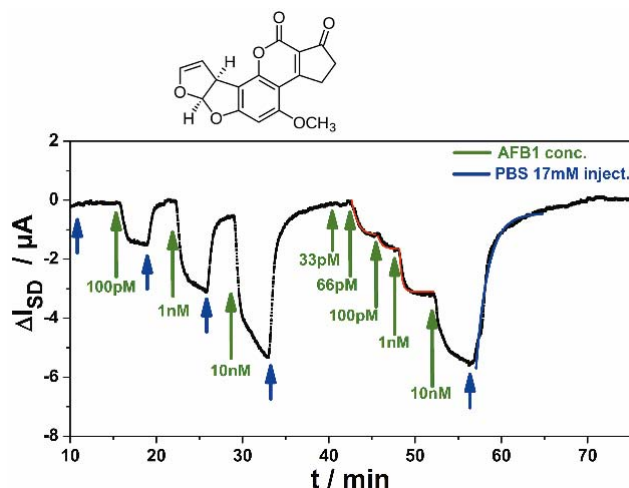


Figure 9. Real-time food pathogen sensor output, *i.e.*, ΔI_{SD} , as a function of time, while AFB1 solutions of different concentrations (green arrows), alternating with pure buffer (blue arrows) were rinsed through the sample cell.

A more comprehensive and quantitative evaluation of the kinetic and titration data of this electronic food toxin sensor is currently being performed by our group.

5. Smell Sensing

The final example that we give for the performance of the rGO FET-based biosensors concerns the development of a smell detector. Despite the enormous importance of chemical communication in nature we have essentially no technical device or sensor that could detect smells with the sensitivity and selectivity required for most applications in food quality control, for the detection of crop diseases, for medical applications like breath analysis, *etc.* Despite the fact that monitoring chemicals in chemotaxis, *i.e.*, in the search for food of many organisms or the exchange of chemicals between species as a way to communicate with each other is the oldest of our sensory repertoire, we have no sensor that offers the sensitivity and the bandwidth needed to sense and to differentiate many different odors.

The concept for a smell sensor that we are currently developing in our group is based on the functionalization of a thin film transistor with a graphene gate by the immobilization of odorant binding proteins (OBPs) from insects as a functional element, as a bio-mimetic building block. This approach is aiming at reducing the complexity of nature to just the use of these proteins as a particularly robust element for the build-up of a first device in a bio-inspired sensor concept. OBPs from insects like those from mammals (and humans) are at the beginning of a complex amplification scheme in odorant perception that translates a first event, the binding of an odorant molecule to such an odorant binding protein, and eventually ends with the trigger of action potentials that run down the smell nerve directly into the brain.

Figure 10 gives a complete set of experimental data taken with a reduced graphene oxide (rGO) FET, functionalized with OBP14 from the honey bee (*A. mellifera*). The example concerns the monitoring of Homovanillic acid (structure formula given in Figure 10D), an odorant for bees which is also considered to be a tumor marker for neuroblastoma and malignant pheochromocytoma.

We start with the recordings of the change of the source-drain current from a transistor with an rGO gate that was coated with the linker molecule PBSE (*cf.* Section 2) but without an OBP coupled to it. As one can see from Figure 10A, this test for non-specific binding of the analyte leads to only a negligible signal which may result from residual π -stacking interactions between the odorant molecule and free sites on the reduced graphene oxide gate surface.

However, after the covalent immobilization of the receptor OBP14, the global analysis with both kinetic and titration information in one run results in a clear sensor signal with an excellent signal-to-noise ratio (Figure 10B). The different concentrations of the analyte solutions that were rinsed through the flow cell in this experiment are indicated by red arrows, and the flow of pure buffer, indicating the full reversibility of the ligand binding to the sensor-immobilized receptor is marked by a blue arrow.

The analysis of the kinetic data is given in Figure 10C. As predicted by the Langmuir model, the association process becomes faster with increasing bulk concentration, $c_{\text{Homovanillic acid}}$. By plotting the corresponding rate constant, k , as a function of the analyte concentration, c_0 , one obtains a straight line. Also, according to $k = k_{\text{on}}c_0 - k_{\text{off}}$, the slope of this line gives $k_{\text{on}} = 1.1 \times 10^3 \text{ M}^{-1}\text{s}^{-1}$, and the intersection with the ordinate results in $k_{\text{off}} = 8 \times 10^{-3} \text{ s}^{-1}$. This then leads to the kinetically determined affinity constant $K_A = k_{\text{on}}/k_{\text{off}} = 1.4 \times 10^5 \text{ M}^{-1}$, corresponding to a dissociation constant $K_d = 7.1 \text{ }\mu\text{M}$.

This value can be compared with the data obtained from the titration experiment displayed in Figure 10D. The fit here yields $K_A = 2.5 \times 10^5 \text{ M}^{-1}$ in excellent agreement with the kinetic determination. This confirms the applicability of the Langmuir model to this affinity binding reaction. It should be pointed out that by testing other ligands (odorants), dissociation constants ranging from a few μM to several mM were found, indicating the selectivity of this sensor concept based on an OBP receptor/FET bio-hybrid device [20].

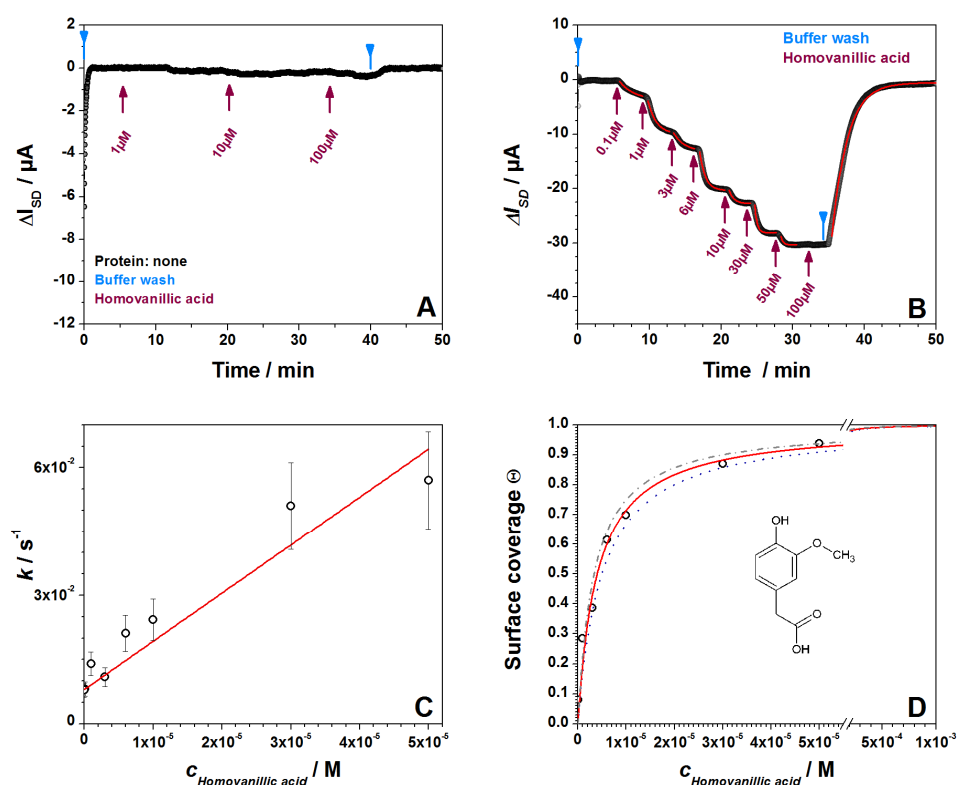


Figure 10. Full analysis of the recognition and binding of the odorant homovanillic acid to the odorant binding protein OBP14. (A) Taken with a sensor that was functionalized by the linker PBSE, however, had no protein coupled to it; (B) shows the global analysis for homovanillic acid binding to OBP 14 on the FET gate surface; (C) rate constants taken from the fits of (B), plotted as a function of the bulk concentration c_0 ; (D) Langmuir isotherm of the titration data taken from (B).

6. Outlook

Electronic biosensing shows great promise for complementing electrochemical detection schemes on the one hand and optical concepts for the quantitative monitoring of bioanalytes on the other. In particular, the use of graphene as the conductive gate material in the preparation of thin film transistors as the sensing device offers a tremendous advantage compared to the use of organic semiconducting materials or compared to Si-based transistors, which both require far more demanding preparation protocols.

The few examples that we presented here demonstrate the versatility of the graphene-based transistor concept for biosensing in different fields of application. It should be noted that the use of monomolecular graphene oxide flakes obtained by exfoliating graphite and their reduction to reduced graphene oxide (rGO) eventually may be replaced by higher quality graphene gate materials prepared by chemical vapor deposition (which needs to be seen, though!). The basic concept, however, of functionalizing this gate material by different types of biorecognition elements, receptors, antibodies, *etc.*, able to bind the analyte molecule of interest, has proven already to yield the sensitivity and selectivity needed for practical applications of these devices.

Some of the fundamental issues associated with rGO FET-based biosensing still need further work and clarification; e.g., the role of local pH changes, direct but also indirect modifications of the surface potential at the gate-electrolyte interface by variations of the local ionic milieu, the concentration, profile and chemical nature of ions and counter-ions associated with the biorecognition reaction, the role of dipole potentials, *etc.*, are far from being completely understood. Other than in optical biosensing, this also gives the concept of anti-fouling coatings a different meaning: it is absolutely not clear how to best minimize non-specific binding. What determines eventually the limit of detection in rGO-based electronic biosensing? What is the relationship between the gate architecture and the minimal surface coverage that is needed in order to sense an electronic signal? Would eventually a single occupied site on the biofunctionalized gate surface be enough to modify the source-drain current?

A final comment refers to the last application, *i.e.*, the sensing of smells. The example given was based on monitoring of changes induced in an odorant binding protein immobilized on the gate surface of the transistor by the binding of a ligand, an odorant, from the aqueous phase of the respective analyte solution in contact with the sensor. This format mimics to some extent the situation in the nose of vertebrates where the sensory neurons and the associated odorant binding proteins are covered and, hence, protected and hydrated by the mucosa. It also reflects properly the situation in the sensilla of the insect antennae, where the OBPs are in the lymph, *i.e.*, also in an aqueous environment. In that sense, the presented results are quite relevant also for the development of a smell sensor. In fact, a direct comparison between the sensitivity of a whole insect antenna from an insect, the red flour beetle *Tribolium castaneum*, responding to a certain partial pressure of an odorant in a carrier gas, with that of a rGO transistor functionalized by one of the key OBPs from this species, responding to an aqueous solution of the same odorant, gave very comparable results [21]. Of course, our final goal is to operate these devices also in air, which seems to be absolutely possible by using hydrogels as a protective coating of the device, mimicking the mucosa that keeps all the biocomponents of the sensor in a hydrated and therefore functional environment.

Acknowledgments: We would like to thank Barbara Cvak, Alois Schiessl, and Romer Labs Division Holding GmbH for their continued support. We are grateful to a number of colleagues that contributed with their advice: Jakub Dostalek, Christoph Kleber, Melanie Larisika, Rosa Mastrogiacomio, Christoph Nowak, Paolo Pelosi, and Serban F. Peteu. Partial support for this work was provided by the European Science Foundation (ESF), Grant Number: 10-EuroBioSAS-FP-005, by the European Union's Horizon 2020 program under the Sklodowska-Curie Grant Agreement No. 645686, the Austrian Science Fund (FWF) (I681-N24), the Austrian Federal Ministry for Transport, Innovation and Technology (GZ BMVIT-612.166/0001-III/I1/2010) and the Austrian Research Promotion Agency (FFG) within the COMET framework, by the Province of Lower Austria.

Author Contributions: Ciril Reiner-Rozman, Caroline Kotlowski, Wolfgang Knoll conceived and designed the experiments; Ciril Reiner-Rozman, Caroline Kotlowski performed the experiments; Ciril Reiner-Rozman,

Caroline Kotlowski, Wolfgang Knoll analyzed the data; Ciril Reiner-Rozman, Caroline Kotlowski, Wolfgang Knoll wrote the paper.

Conflicts of Interest: The authors declare no conflict of interest.

References

1. Jones, R.; Meixner, H. *Sensors, A. Comprehensive Survey, Volume 8, Micro- and Nanosensor Technology: Trends in Sensor Markets*; Jones, R., Meixner, H., Eds.; Wiley: New York, NY, USA, 2008.
2. Zhang, X.J.; Ju, H.X.; Wang, J. *Electrochemical Sensors, Biosensors and Their Biomedical Applications*; Elsevier: Amsterdam, The Netherlands, 2008.
3. Offenhäusser, A.; Maelicke, C.; Matsuzawa, M.; Knoll, W. Field-Effect Transistor Array for Monitoring Electrical Activity from Mammalian Neurons in Culture. *Biosens. Bioelectron.* **1997**, *12*, 819–826. [[CrossRef](#)]
4. Yeung, C.K.; Ingebrandt, S.; Krause, M.; Sprössler, C.; Denyer, M.; Britland, S.T.; Offenhäusser, A.; Knoll, W. The use of Field Effect Transistors (FETs) in pharmacological research. *J. Anat.* **2002**, *200*, 210.
5. Ingebrandt, S. Bioelectronics: Sensing Beyond the Limit. *Nat. Nanotechnol.* **2015**, *10*, 734–735. [[CrossRef](#)] [[PubMed](#)]
6. Khan, H.U.; Jang, J.; Kim, J.J.; Knoll, W. *In Situ* Antibody Detection and Charge Discrimination Using Aqueous Stable Pentacene Transistor Biosensors. *J. Am. Chem. Soc.* **2011**, *133*, 2170–2176. [[CrossRef](#)] [[PubMed](#)]
7. Khan, H.U.; Roberts, M.E.; Johnson, O.; Förch, R.; Knoll, W.; Bao, Z. *In Situ*, Label-Free DNA Detection Using Organic Transistor Sensors. *Adv. Mater.* **2010**, *22*, 4452–4456. [[CrossRef](#)] [[PubMed](#)]
8. Kuila, T.; Bose, S.; Khanra, P.; Mishra, A.K.; Kim, N.H.; Lee, J.H. Recent Advances in Graphene-Based Biosensors. *Biosens. Bioelectron.* **2011**, *26*, 4637–4648. [[CrossRef](#)] [[PubMed](#)]
9. Reiner-Rozman, C.; Larisika, M.; Nowak, C.; Knoll, W. Graphene-based liquid-gated field effect transistor for biosensing: Theory and experiments. *Biosens. Bioelectron.* **2015**, *70*, 21–27. [[CrossRef](#)] [[PubMed](#)]
10. Larisika, M.; Kotlowski, C.; Steininger, C.; Mastrogiacomio, R.; Pelosi, P.; Schütz, S.; Peteu, S.F.; Kleber, C.; Reiner-Rozman, C.; Nowak, C.; *et al.* Electronic Olfactory Sensor Based on *A. mellifera* Odorant Binding Protein 14 on a Reduced Graphene Oxide Field-Effect Transistor. *Angew. Chem. Int. Ed. Engl.* **2015**, *54*, 13245–13248. [[CrossRef](#)] [[PubMed](#)]
11. Larisika, M.; Huang, J.F.; Tok, A.; Knoll, W.; Nowak, C. An Improved Synthesis Route to Graphene for Molecular Sensor Applications. *Mater. Chem. Phys.* **2012**, *136*, 304–308. [[CrossRef](#)]
12. Stankovich, S.; Dikin, D.A.; Piner, R.D.; Kohlhaas, K.A.; Kleinhammes, A.; Jia, Y.; Wu, Y.; Nguyen, S.B.T.; Ruoff, R.S. Synthesis of Graphene-Based Nanosheets via Chemical Reduction of Exfoliated Graphite Oxide. *Carbon* **2007**, *45*, 1558–1565. [[CrossRef](#)]
13. Dani, F.R.; Iovinella, I.; Felicioli, A.; Nicolini, A.; Calvello, M.A.; Carucci, M.G.; Qiao, H.; Pieraccini, G.; Turillazzi, S.; Moneti, G.; *et al.* Mapping the Expression of Soluble Olfactory Proteins in the Honeybee. *J. Proteome Res.* **2010**, *9*, 1822–1833. [[CrossRef](#)] [[PubMed](#)]
14. Iovinella, I.; Dani, F.R.; Nicolini, A.; Sagona, S.; Michelucci, E.; Gazzano, A.; Turillazzi, S.; Felicioli, A.; Pelosi, P. Differential Expression of Odorant-Binding Proteins in the Mandibular Glands of the Honey Bee According to Caste and Age. *J. Proteome Res.* **2011**, *10*, 3439–3449. [[CrossRef](#)] [[PubMed](#)]
15. Ban, L.P.; Zhang, L.; Yan, Y.H.; Pelosi, P. Binding Properties of a Locust's Chemosensory Protein. *Biochem. Biophys. Res. Commun.* **2002**, *293*, 50–54. [[CrossRef](#)]
16. Shreeve, B.J.; Patterson, D.S.P.; Roberts, B.A. Mycotoxins and Their Metabolites in Humans and Animals. *Food Cosmet. Toxicol.* **1979**, *17*, 151–152. [[CrossRef](#)]
17. Paniel, N.; Radoi, A.; Marty, J.L. Development of an electrochemical biosensor for the detection of aflatoxin M1 in milk. *Sensors* **2010**, *10*, 9439–9448. [[CrossRef](#)] [[PubMed](#)]
18. Commission Regulation (EC) No. 466/2001. Available online: http://ec.europa.eu/food/fs/sfp/fcr/fcr02_en.pdf (accessed on 12 April 2016).
19. Wang, Y.; Dostalek, J.; Knoll, W. Long Range Surface Plasmon-enhanced Fluorescence Spectroscopy for the Detection of Aflatoxin M-1 in milk. *Biosens. Bioelectron.* **2009**, *24*, 2264–2267. [[CrossRef](#)] [[PubMed](#)]

20. Kotlowski, C.; Larisika, M.; Guerin, P.; Kleber, C.; Kröber, T.; Mastrogiacomo, R.; Nowak, C.; Pelosi, P.; Schütz, S.; Schwaighofer, A.; *et al.* Electronic Olfactory Biosensor Based on Honeybee Odorant Binding Protein 14 on a rGO FET. In preparation.
21. Kotlowski, C.; Ramach, U.; Balakrishnan, K.; Brey, J.; Gabriel, M.; Kleber, C.; Mastrogiacomo, R.; Pelosi, P.; Schütz, S.; Knoll, W. Monitoring Crop Disease Markers by Odorant Binding Proteins of *Tribolium castaneum*—Electroantennograms *versus* Reduced Graphene-Oxide Based Electronic Biosensor. In preparation.



© 2016 by the authors; licensee MDPI, Basel, Switzerland. This article is an open access article distributed under the terms and conditions of the Creative Commons Attribution (CC-BY) license (<http://creativecommons.org/licenses/by/4.0/>).

Analytical Chemistry, to be submitted (2016)

Electronic Olfactory Biosensor Based on Honeybee Odorant Binding Protein 14 on a rGO FET

Caroline Kotlowski^{a,b,†}, Melanie Larisika^{a,b,†}, Patrick Guerin^c, Christoph Kleber^a,
Thomas Kröber^c, Rosa Mastrogiacomo^d, Christoph Nowak^{a,b}, Paolo Pelosi^d,
Stephan Schütz^e, Andreas Schwaighofer^b, Wolfgang Knoll^{a,b,*}

^{a)} Center for Electrochemical Surface Technology, 2700 Wiener Neustadt, Austria

^{b)} AIT Austrian Institute of Technology, 1190 Vienna, Austria

^{c)} University of Neuchâtel, Institute of Zoology, 2009 Neuchâtel, Switzerland

^{d)} Dept. of Biology of Agriculture, Food & Environment, University of Pisa,
56124 Pisa, Italy

^{e)} Buesgen-Institute, Dept. of Forest Zoology and Forest Conservation,
University of Göttingen, Göttingen, Germany

[†] These authors contributed equally to this work. * Corresponding author: E-mail address: wolfgang.knoll@ait.ac.at

Abstract

Most insect species like the honeybee (*Apis mellifera Ligustica*) primarily rely on olfactory cues to find suitable host plants or to regulate various aspects of their social life. In this study, we used an odorant binding protein (OBP14) of the honeybee as sensing element in an olfactory biosensor device. Reduced graphene oxide (rGO) transistors were fabricated and functionalized with OBPs and then mounted into a liquid flow cell. These biosensors were then used to study the affinity of OBP14 towards various odorants known as plant volatiles or originating from honeybee food sources. Protein-ligand interactions were monitored in real-time by recording the electrical responses obtained from the rGO-based devices operated as liquid-gated field-effect transistors. Kinetic parameters for all ligands were determined together with dissociation constants ranging from $K_d = 4 \mu\text{M}$ to 1.4 mM, similar to those found for ligand binding to free OBP14 in solution. In addition to being able to distinguish between good, moderate and low affinity ligands, the sensor device exhibited a high selectivity, capable of recognizing and discriminating between even structurally very similar odorants. We found that the best ligands were phenolic compounds, such as Eugenol, Coniferyl aldehyde and Homovanillic acid, whose interaction with the protein likely involves the free hydroxyl residues. Hence, this observation provides a strong indication that OBP14 is tuned towards a distinct chemical class of odorants.

Studies with the wild type OBP14 were complemented by studies with mutants. One of them, HisTag-OBP14, contained a segment of 6 histidines at the N-terminus allowing the oriented immobilization of the protein on the rGO gate surface. It was found, both by fluorescence displacement assay in solution, as well as by the rGO FET measurements, that this modification of the odorant protein did not change significantly its affinities to a variety of odorant ligands. Another mutant, S-S-OBP14, with a S-S bond introduced for enhanced temperature stability, exhibited a dissociation constant for Eugenol $K_d = 4\mu\text{M}$, about an order of magnitude higher than that of the wild type OBP14. This opens the door for the design and genetic manipulations of the affinities and selectivities of odorant binding proteins as active components in smell sensors for technical applications.

Keywords: honeybee (*Apis mellifera*), odorant detection, olfactory biosensor, odorant-binding protein, reduced graphene oxide, electronic biosensor, field effect transistor

1. Introduction

Insect detect and discriminate olfactory cues with specialized sensilla mainly located on antennae and through the action of membrane-bound olfactory receptors (Clyne et al. 1999; Vosshall et al. 1999) and soluble odorant binding proteins (OBPs). The latter are small acidic polypeptides (~13-16 kDa) highly concentrated in the lymph of the chemosensilla (Leal 2013; Pelosi et al. 2006; Vogt 2005; Vogt and Riddiford 1981). Based on their ligand-binding properties, OBPs have been suggested to act as carriers for hydrophobic odorants and pheromones through the aqueous sensillar lymph to the odorant receptor sitting in the membrane of olfactory neurons. Recently, however, evidence has been reported that OBPs play a role in the discrimination of different volatile organic compounds (Matsuo 2007; Sun et al. 2012; Swarup et al. 2011; Xu et al. 2005); Qiao et al., 2009; Pelletier et al., 2010; Biessman et al., 2010) Moreover, functional studies with receptors expressed in heterologous systems have reported that the presence of the appropriate OBPs increases the sensitivity and selectivity of the receptors to pheromones (Grosse-Wilde et al., 2006; Forstner et al., 2009; Sun et al., 2013; Chang et al., 2015)

Thanks to genome sequencing, a very large number of OBP sequences are available and three-dimensional structures have been solved for 20 of them (Horst et al. 2001b; Kruse et al. 2003; Lagarde et al. 2011; Lescop et al. 2009; Sandler et al.

2000; Spinelli et al. 2012; Wogulis et al. 2006). They all share a common folding of six α -helical domains, further stabilized by three interlocked disulfide bridges (Leal et al. 1999; Scaloni et al. 1999).

Such compact structure endows OBPs with extreme stability to temperature, solvents and proteolysis (Ban et al. 2002; Pelosi et al. 2006) making them ideal components for biosensors to be used in challenging situation, such as medical diagnostics, environmental monitoring or food quality control.

A large number of OBPs has been expressed in bacterial systems and their ligand-binding properties have been investigated in solution. The most commonly used method involves measuring the fluorescence of a probe able to bind to the protein (generally 1-aminoanthracene: 1-AMA, and N-phenyl-1-naphthylamine: 1-NPN) and its decrease due to competitive displacement of the probe by a (non-fluorescent) ligand (Ban et al. 2003; Ban et al. 2002; Campanacci et al. 2001). Generally, dissociation constants are in the upper nM and lower μ M range for good ligands (Leal 2013; Pelosi et al. 2006). In a few cases, as with OBP14 of the honeybee, binding of ligands inside the hydrophobic cavity of the protein has been visualized by X-ray crystallography (Spinelli et al. 2012).

The fluorescent binding assay requires the availability of a fluorescent probes with good affinity for the protein (Fan et al. 2011; Pelosi et al. 2006) and relies on the ability of the ligands of interest to displace the probe from the complex.

An alternative label-free approach to investigate binding affinities of odorant molecules to OBPs is highly desirable and could found applications in the area of biosensor research. In recent years, various biosensor devices mimicking the olfactory system have been developed (Hou et al. 2007; Jin et al. 2012; Kim et al. 2009; Lee et al. 2012; Lee et al. 2009; Liu et al. 2013; Park et al. 2012a; Park et al. 2012b; Yoon et al. 2009) but only limited studies using OBPs as target element for the design of a 'bio-electronic nose' have been reported in the literature (D'Auria et al. 2004; Di Pietrantonio et al. 2013; Hou et al. 2005; Sankaran et al. 2011).

In this work we present the fabrication and successful operation of a label-free biosensor for odor detection based on reduced graphene oxide (rGO) functionalized with an odorant binding protein (honeybee OBP14) as the active bio-mimetic sensing element (Iovinella et al. 2011; Spinelli et al. 2012). We illustrate its performance with the determination of kinetic rate constants and affinity constants for a set of odorants binding from aqueous solutions to the sensor device.

2 Material and methods

2.1. Cloning and purification of OBPs

Odorant binding proteins (wt-OBP14, His-tag-OBP14, a his-tagged mutant, and S-S-OBP14, a mutant with a disulfide bond, were expressed in bacterial systems using established protocols (Dani et al. 2010b; Iovinella et al. 2011). In particular, the gene encoding the mature sequence of wt-OBP14 and bearing NdeI and EcoRI restriction sites at the 5'- and 3'- ends, respectively, was ligated into pET-5b vector (Novagen, Darmstadt, Germany) previously linearized with the same enzymes. A double mutant bearing two extra cysteine residues (Gln44Cys, His97Cys), which allowed for the establishment of a third disulfide bridge, was prepared using the same approach (Spinelli et al., 2012). Both proteins did not contain other modifications in their sequences, except for the presence of an additional methionine. A version of OBP14 bearing a segment of 6 histidine residues at the N-terminus (His-tag-OBP14) was prepared by cloning the wild-type gene into the vector pET15b (Novagen, Darmstadt, Germany), as previously described (Schwaighofer et al., 2014). After transformation of BL-21 *E. coli* cells with the modified plasmids, the expressed recombinant proteins were purified by conventional ion-exchange chromatographic techniques followed by a final gel filtration step on Superose-12 (GE-Healthcare) (Ban et al. 2003; Calvello et al. 2003). Purification was monitored by SDS-PAGE (cf. Figure 1).

2.2. Preparation of odorant solutions

All reagents were purchased from Sigma-Aldrich unless otherwise indicated and used without further purifications.

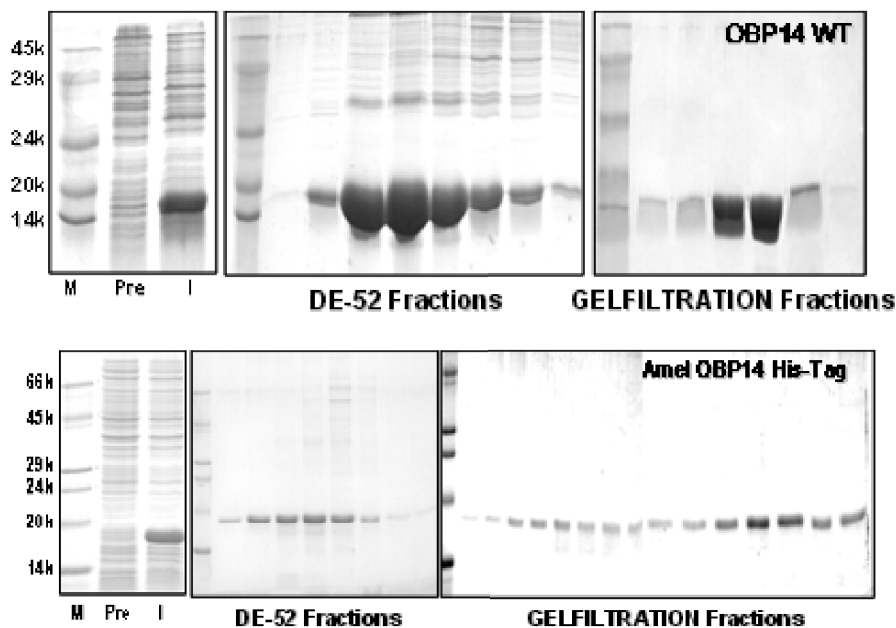


Figure 1: Bacterial expression and purification of wt-OBP14 (upper panel) and His-tag-OBP14 (lower panel) of *Apis mellifera*. Purification was accomplished by anion-exchange chromatography on DE-52, followed by a second step on QFF, or gel filtration on Sephacryl-12, as indicated. Molecular weight markers (M) are, from the top, 66, 45, 29, 20 and 14 kDa. Pre: bacterial pellet before induction; I: bacterial pellet after induction with isopropyl- β -D-thiogalactopyranoside. Odorants were prepared as 5 mM stock solutions in phosphate buffer (1 mM PBS, pH 8.0) with an addition of 0.01% ethanol (purity \geq 99.9%) and further dilution (from 10^{-3} M to 10^{-6} M) by successive dilutions in PBS buffer (ionic strength 17 mM, adjusted to pH 8.0 with NaOH or KOH). All solutions were freshly prepared on the day of the experiment.

A broad spectrum of tested ligands included typical pollen odorants like the benzenoids Eugenol (4-Allyl-2-methoxyphenol) and Methyl eugenol (1,2-Dimethoxy-4-prop-2-enylbenzene) (Dobson et al. 1990; Dötterl and Vereecken 2010) or Sulcatone (6-Methylhept-5-en-2-one), an irregular terpene which was also identified in propolis (Bee glue, Dobson et al. 1996; Nunes and Guerreiro 2012).

Other ligands comprise the propolis component, Coniferyl aldehyde, ((E)-3-(4-hydroxy-3-methoxyphenyl) prop-2-enal) (Banskota et al. 2001) and floral volatiles, known to be attractants for bees, such as Vanillin (4-Hydroxy-3-methoxybenzaldehyd) (Thiery et al. 1990), Vanillyl acetone (4-(4-hydroxy-3-methoxyphenyl)butan-2-one) (Tan and Nishida 2007), Citral ((2E)-3,7-dimethylocta-2,6-dienal) (Dötterl and Vereecken 2010) and Geraniol ((2E)-3,7-Dimethylocta-2,6-

dien-1-ol) (Laloi et al. 2001); the latter two compounds were also identified in the product of Nasonov gland (Trhlin and Rajchard 2011). Linalool (3,7-dimethylocta-1,6-dien-3-ol) is an attractant for honey bees (J. A. Henning et al. 1992); Coniferyl alcohol (4-(3-hydroxy-1-propenyl)-2-methoxyphenol) belongs to the queen retinue type of *Apis mellifera* pheromones; 2-isobutyl-3-methoxypyrazine a floral scent and the structurally similar odorant (2-Methoxy-3-(2-methylpropyl)pyrazine) was tested as a control odorant. In addition, two honey flavours, namely Homovanillic acid (2-(4-Hydroxy-3-methoxy-phenyl)acetic acid) (Isidorov et al. 2011) and Methyl vanillate (Methyl 4-hydroxy-3-methoxybenzoate) (Guyot et al. 1999) as well as Isoamyl acetate (3-methylbutyl acetate), an alarm pheromone (Iovinella et al. 2011) were also tested.

2.3. Ligand-binding in solution

Emission, spectra were recorded on a Jasco FP-750 instrument at 25 C in a right angle configuration, with a 1 cm light path quartz cuvette and 5 nm slits for both excitation and emission. Dissociation constants of the fluorescent probe N-phenyl-1-aminonaphthalene (1-NPN) to each protein were evaluated by titrating a 2 μ M solution of the protein in 50 mM Tris–HCl buffer pH 7.4, with aliquots of 0.1 mM ligand in methanol to final concentrations of 0.1–2 μ M. The probe was excited at 337 nm and emission spectra were recorded between 380 and 450 nm. Dissociation constants were evaluated using GraphPad Prism software (Iovinella et al., 2011). The affinities of other ligands were measured in competitive binding assays, where a solution of the protein and 1-NPN, both at the concentration of 2 μ M, was titrated with 1 mM methanol solutions of each competitor to final concentrations of 2–16 μ M. Dissociation constants of the competitors were calculated from the corresponding IC₅₀ values (concentrations of ligands halving the initial fluorescence value of 1-NPN), using the equation: $K_D = [IC_{50}]/1 + [1-NPN]/K_{1-NPN}$, [1-NPN] being the free concentration of free 1-NPN and K_{1-NPN} the dissociation constant of the complex protein/1-NPN.

2.4. Fabrication of OBP based biosensor devices

Reduced graphene oxide field-effect transistor (rGO-FET) devices were fabricated as schematically sketched in Figure 2 with a channel width of 30-50 μ m. Silicon substrates with a 300 nm oxide layer were chosen as basal layer for the FETs. The

SiO₂ substrates were cleaned with a standard RCA cleaning procedure. The substrates were then submerged in a 2% aminopropyltriethoxysilane (APTES) solution in ethanol for 1 h, APTES forming a self-assembled monolayer used to increase the adsorption of graphene oxide sheets. After rinsing with ethanol, the substrates were heated to 120°C for two hours and afterwards cooled to room temperature. Graphene oxide sheets were prepared using a variation of the Hummers method derived for the application on FETs (Su et al. 2009). The obtained graphene oxide flakes were applied onto the Si-Wafer via drop casting of the top portion of the graphene-oxide solution. The devices were then treated in hermetically sealed glass petri dishes with hydrazine at 70°C overnight to accomplish the graphene-oxide reduction.

For the detection of different odorants, the rGO-based biosensors were functionalized with OBP14. For the attachment of the

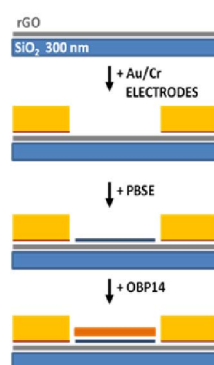


Figure 2: Fabrication and functionalization of rGO-FETs: a silicon wafer with 300 nm SiO₂ and reduced graphene oxide (rGO) flakes was coated with Au/Cr electrodes (5 nm Cr, 70 nm Au); next the linker, 1-pyrenebutanoic acid succinimidyl ester (PBSE), was coupled to the substrate, followed by protein (here: OBP14) immobilization (randomly) by active ester chemistry.

protein to the sensing area, the graphene surface was chemically modified by a bi-functional linker, 1-pyrenebutanoic acid succinimidyl ester (PBSE). With its pyrene end the linker firmly attaches to the graphene surface through π - π interactions, while the other end covalently reacts randomly with amino group of the protein to form an amide bond. 20 μ L of a 5 μ M PBSE solution in THF was placed onto the rGO-FET channel, followed by incubation (for 2h at 4°C) of 10 μ L of a 10 μ M OBP14 solution in PBS buffer (10 mM; pH 8.0) The entire fabrication process of the olfactory biosensor device, including successful reduction of GO to rGO, the linker binding and the

protein attachment was carefully examined using spectroscopic methods (Larisika et al. 2015).

For the attachment of the his-tagged OBP14 to the graphene surface a different linker molecule was needed: for protein immobilization one end was having an Ni-NTA protein binding chelate and the same pyrene based graphene immobilization strategy like in the case of PBSE on the other end.

The chip was then mounted into a flow cell for *in-situ* real-time kinetic measurements (association, k_{on} , and dissociation, k_{off} , rates) as well as for titration experiments for the determination of affinity constants, K_A , and dissociation constants, K_d . An artist's sketch of the FET setup and the immobilized OBP interacting with the odorant ligand, together with a photograph of the whole flow cell are reported in Figure 3.

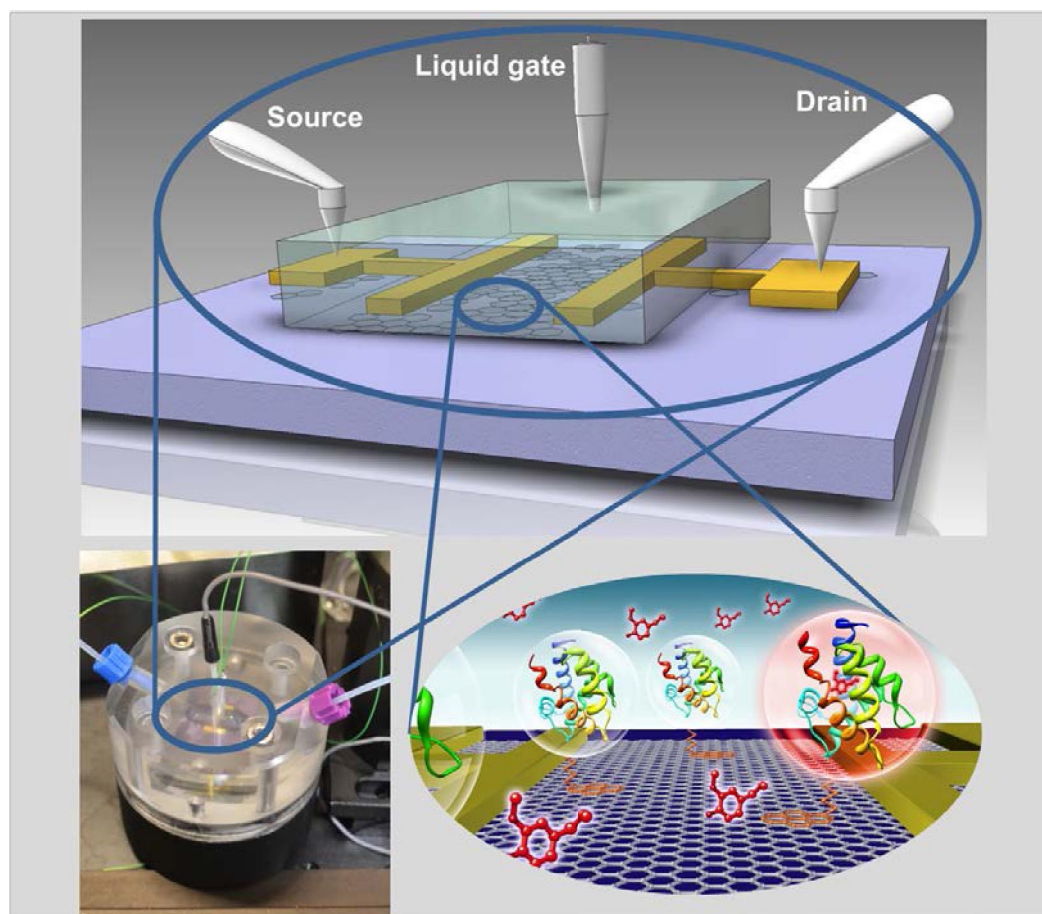


Figure 3: Schematics of the set-up and the device configuration consisting of a liquid gate electrode, source- and drain electrodes, evaporated onto the reduced graphene oxide flakes on a solid Si/SiO₂ substrate, functionalized by OBPs that are covalently coupled via a linker molecule. In the lower left corner is a photograph of the mounted flow cell.

2.5. Electrical measurements

The electrical properties of the FET devices were tested as described before (Huang et al. 2013; Larisika et al. 2015). Electrical measurements were performed using a Keithley 4200 semiconductor characterization system. An Ag/AgCl reference electrode (Flex ref, World Precision Instruments) was used to operate the FET device in a liquid gate configuration with a constant source-drain bias of $V_{SD} = 50$ mV. In the I_{SD} -vs- V_G scans (cf. Figure 4) one can clearly distinguish between the two ambipolar branches typical for graphene FETs: the cathodic scan which is dominated by the hole mobility and the anodic scan determined by the electron mobility (Reiner-Rozman et al., 2015). The Dirac voltage is seen at ca. $V_G = 0.4$ V. Recording these I_{SD} -vs- V_G scans at different bulk solution conditions, in particular, in aqueous solutions of different ligand concentrations, results in a distinct shift of the cathodic branch which we attribute to a slight modification of the dipolar layer with the OBP protein monolayer immobilized on the graphene gate surface upon partial binding of the ligands to the free binding sites in the OBP acting as receptors.

Fig. 4 shows this effect for a transistor with an OBP 14 modified rGO gate, and recorded at different Eugenol concentrations, ranging from 100 nM to 250 μ M. From these measurements we selected a negative gate voltage of $V_G = -0.6$ V for all ligand binding measurements.

A flow rate of 300 μ L/min was chosen in order to minimize mass transfer limitations of the analytes to the sensor surface (Adamczyk et al. 2000; Karlsson and Falt 1997; Khan et al. 2011). The general procedure of the whole titration experiment started with continuously flushing the detection area with pure buffer (1mM PBS, pH = 8.0), until a stable baseline of the source-drain current was established. Subsequently, the biosensor was titrated with different odorant concentrations (100 nM – 4 mM) and the

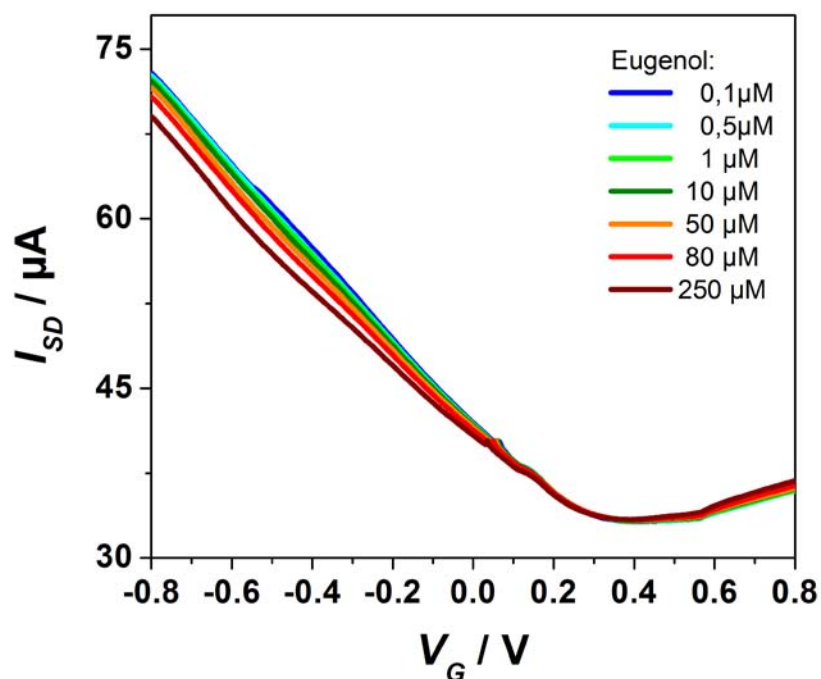


Figure 4: Current I_{SD} -vs-gate voltage V_G characteristics of the OBP14 functionalized FET-biosensor device at different Eugenol concentrations (as indicated) flowing through the cell.

change in source-drain current (ΔI_{SD}) was monitored in real time. Typically, a solution with a certain odorant concentration was injected and the odorant was allowed to interact with the surface immobilized OBP14 to reach equilibrium, as indicated by a constant source-drain current. This process was repeated with odorant solutions of different concentrations, up to an upper concentration for which the surface was eventually fully saturated with the target analyte and no significant change in the source-drain current occurred anymore. Surface titration experiments were terminated by a final washing step using pure buffer in order to dissociate all bound OBP14-odorant complexes, resulting in an almost complete restoration of the initial baseline current. However, in almost all devices, a moderate drift of the source-drain current was observed with time. For this reason, the drain current response curves were normalized by subtraction to the (interpolated) baseline current. Kinetic parameters as well as equilibrium surface coverages of the above described global analysis experiments were analysed using the Langmuir model.

3 Results

3.1. Kinetic and Titration experiments

Upon exposure of the OBP-functionalized rGO-FETs to different odorant solutions applied through the flow cell, we observed changes in the source-drain current (ΔI_{DS}) (conductance) of the rGO-FETs. An example is shown in Figure 5 where the original I_{DS} -vs-time recording is reported when a sensor was exposed to a series of Eugenol concentrations (100 μM , 10 μM , 50 μM). Rinsing steps with buffer between measurements are indicated by blue arrows.

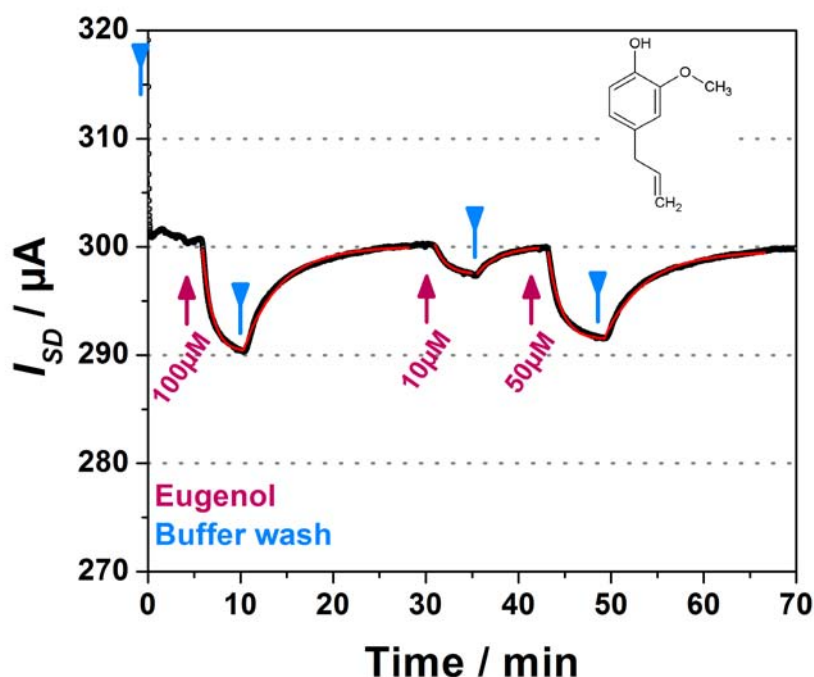


Figure 5: Typical experiment of the global analysis (kinetic as well as titration): measured is the change in source-drain-current (I_{DS}) as a function of time after addition of various concentrations of odorant molecules (Eugenol in this case, cf. inset) to the buffer solution (PBS, 10 mM phosphate, pH 8) flowing across the gate of a rGO field-effect-transistor in a flow cell (red arrows) and rinsing again pure buffer through the cell (blue arrow) upon which the current signal returns to the baseline level, indication the reversible binding process (a prerequisite to describe this binding process by a Langmuir model). The red curves though the experimental data are fits based on the Langmuir analysis, cf. the text below.

Since the ligand electrically neutral (cf. the inset in Fig. 5) the recorded signals suggest that binding of the ligand affects the electrical charge (dipole) distribution of the protein immobilized on the gate, coupling capacitively to the conductive channel of the transistor.

What is important for the use of this electronic device as a quantitative bio-sensor is the fact that the current change depends in a unique (and reproducible) way on the analyte occupancy in the binding pocket and therefore on its concentration in the bulk solution. Furthermore, this interaction is fully reversible, i.e., the analyte can be fully washed out by buffer rinsing. This is a prerequisite for applying the Langmuir model for the quantitative analysis of the kinetic and thermodynamic parameters of the system.

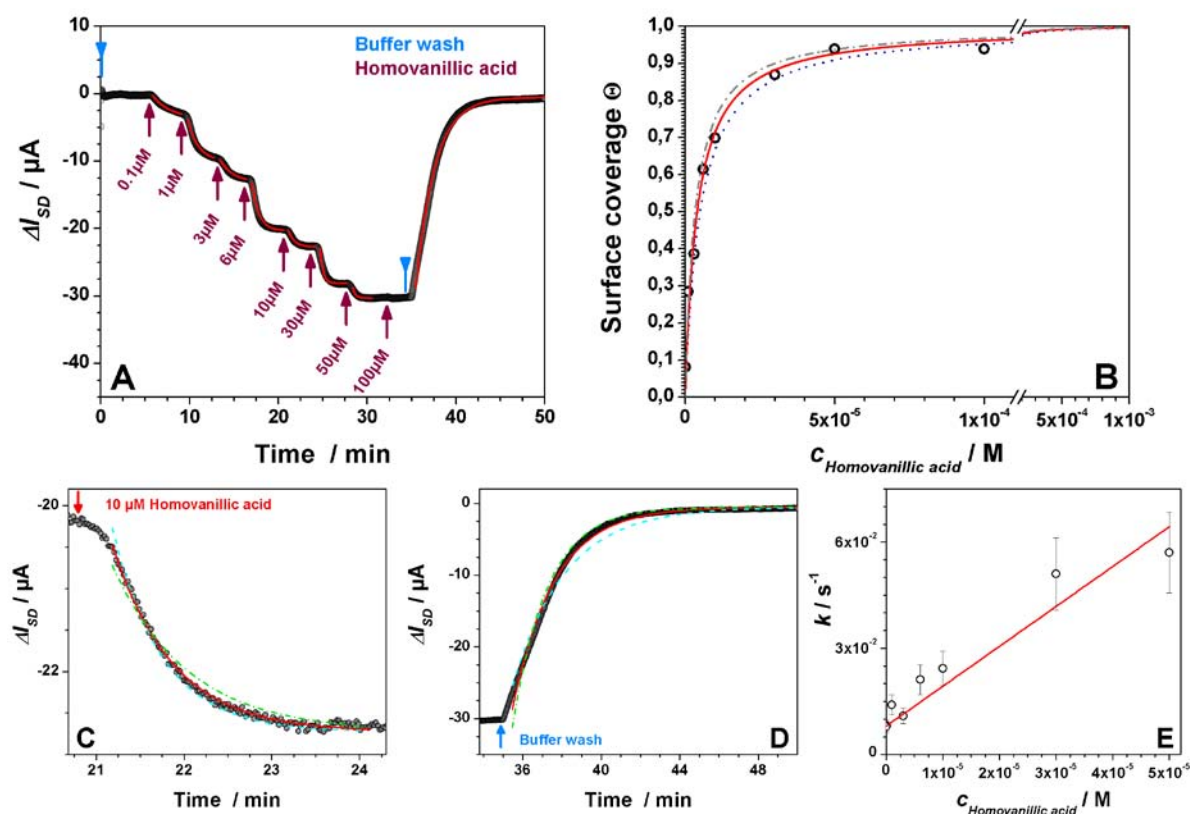


Figure 6: Full analysis of the recognition and binding of the odorant Homovanillic acid to the odorant binding protein OBP14. (A) shows the global analysis for Homovanillic acid binding to OPB 14 on the FET gate surface; (B) Langmuir isotherm of the titration data taken from (A); (C) The determination of the rate constant k and its error margins, exemplified with the experimental data of the current change, ΔI_{SD} , after injection of a 10 μM solution, together with 3 fit curves: red $k=0.024\ s^{-1}$, dark blue with $k'=k+20\%$, light blue, $k''=k-20\%$. (D) The determination of the rate constant k_{off} and its error margins, showing the experimental data of the buffer wash, ΔI_{SD} , together with 3 fit curves: red $k=0.0078\ s^{-1}$, dark blue with $k'=k+20\%$, light blue, $k''=k-20\%$. (E) Rate constants taken from the fits of (A-C), plotted as a function of the bulk concentration c_0 ;

The full set of data for the quantitative evaluation of the binding of Homovanillic acid to OBP14 immobilized on the rGO-FET (global analysis) is reported in Figure 6. The sensor response was measured by monitoring changes in source-drain current (ΔI_{DS})

with time, while different aqueous solutions of the odorant were applied through the flow cell and across the sensing area (Fig. 6 A). At each concentration step we can observe a change of I_{SD} reaching a new stationary current level with a time constant typical for the bulk Homovanillic acid concentration in the analyte solution.

If we plot the observed (changes of the) values of stationary current levels, ΔI_{SD} , relative to its extrapolated maximum value, i.e., $\Theta = \Delta I_{SD} / \Delta I_{SD,max}$, as a function of the applied Homovanillic acid concentration, we obtain a typical Langmuir binding isotherm (Fig. 6, B). The data points can be well described by the equation:

$$\Theta = K_A C_{\text{Homovanillic acid}} / (K_A C_{\text{Homovanillic acid}} + 1) \quad (1)$$

with $K_A = 2.5 \cdot 10^5 \text{ M}^{-1}$ (full curve in Fig 6 B). The dotted and the dashed-dotted curves give the error margins for the determination of the affinity constant: $2.0 \cdot 10^5 \text{ M}^{-1} < K_A < 3.0 \cdot 10^5 \text{ M}^{-1}$, as derived from the Langmuir isotherm.

A closer inspection of the association and the dissociation measurements of the kinetic runs allow for a further quantification of the binding events: Fig. 6 C gives a detailed plot of the time dependent current change, ΔI_{SD} , from the steady state value reached at 6 μM ligand concentration to the new stationary level reached after changing the bulk odorant concentration to 10 μM . Again, the full fit curve and the dotted and dash-dotted curves give the error margin for the determination of the rate constant: $k = 0.0243 \text{ s}^{-1} \pm 20\%$ (0.0194 s^{-1} ; 0.02916 s^{-1})

If one plots all the measured k -values as a function of the bulk concentration as it is done in Fig. 6 E, one finds a linear increase of the rate constant as it is predicted by the Langmuir model:

$$k = k_{\text{on}} C_{\text{Homovanillic acid}} + k_{\text{off}} \quad (2)$$

From the straight line through the data points in Fig 6 E one obtains $k_{\text{on}} = 1130 \text{ M}^{-1}\text{s}^{-1}$ for the binding of Homovanillic acid to OBP 14 from the honey bee. The intersection of the fit line with the ordinate, i.e., k for $C_{\text{Homovanillic acid}} = 0$, yields $k_{\text{off}} = 0.008 \text{ s}^{-1}$.

As an internal consistency check, the dissociation process can also be observed as an increase of the source-drain current (back to the background current) upon switching the bulk odorant concentration to zero, i.e., rinsing again pure buffer through the flow cell. According to the Langmuir model (cf. Eqn 2 with $C_{\text{Homovanillic acid}} =$

0), the corresponding data can be fitted by a single exponential curve giving the dissociation rate constant and its error margin: $k_{\text{off}} = 0.008 \text{ s}^{-1} \pm 20\%$ (0.0064 s^{-1} ; 0.0096 s^{-1}), in good agreement with the extrapolated value from Fig. 6 E.

According to the Langmuir model the relation between the rate constants and the affinity constant is given according to

$$K_A = k_{\text{on}} / k_{\text{off}} . \quad (3)$$

With the rate constants derived from fitting the raw data gives a K_A for each measured concentration, being consonant – as for each concentration the same value is expected – this gives a check of how self-consistent the data are.

3.2. Negative control measurements

Before going into a detailed description of the quantitative evaluation of the binding behavior of a whole set of odorants/ligands measured for OBP 14 we demonstrate that the response signals obtained by the olfactory biosensor are specific and thus result from the protein-ligand binding rather than reflect non-specific interactions of the tested odorants, e.g., with the rGO surface.

Firstly, rGO-FET devices were fabricated and functionalized by the linker (PBSE) monolayer as described above; however, no odorant binding protein was immobilized. Figure 7 A demonstrates that after addition of different concentrations of the phenolic odorant Homovanillic acid, (nearly) no sensor signal could be observed. Similar observations were made for other ligands (not shown). A likely explanation for these findings is the fact that the carboxyl groups after hydrolyzing the

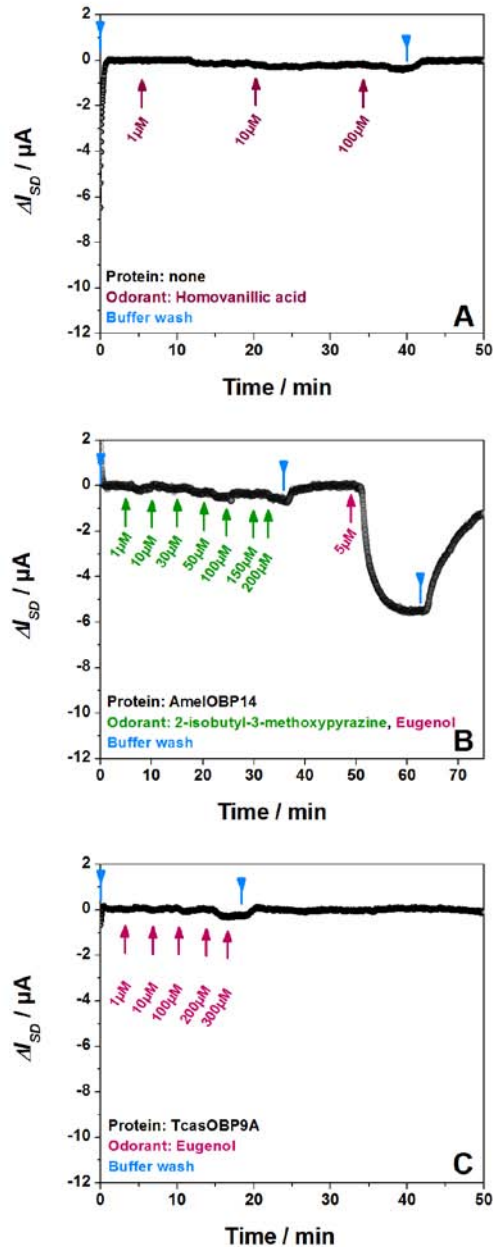


Figure 7: (A) Real-time response, ΔI_{DS} -vs-time measurement, of PBSE-functionalized rGO-FET to different concentrations of Homovanillic acid. (B) ΔI_{DS} vs. time measurement of OBP14-functionalized rGO-FETs barely responding to increasing concentrations (up to 200 μM) of 2-isobutyl-3-methoxy pyrazine (bell pepper smell), a non-ligand to honey bees. However, if a solution of low concentration of Eugenol is rinsed through the cell the device responds in the expected way. (C) Real-time response of OBP9A-functionalized biosensor (an odorant binding protein from the red flour beetle *Tribolium castaneum*) to different concentrations of Eugenol a very weakly binding ligand (note the response to a solution of 300 μM Eugenol, as compared to the response to a 5 μM solution rinsed across OBP14).

active ester (PBSE, cf. Fig. 1D, in Larisika et al., 2015) by the aqueous buffer solution (working pH = 8.0) exerts a repellent effect against the odorants tested by blocking all non-specific interaction sites on the graphene gate surface.

Figure 7B demonstrates further that introducing a small but unnatural ligand to OBP14, i.e., 2-isobutyl-3-methoxypyrazine (bell pepper smell), the sensor did not show a significant response signal. Just to prove that the sensor was sensitive and not dead by whatever reasons, we introduced a Eugenol solution of only 5 μM and monitored the signal shown in Fig. 7B.

And finally, by immobilizing on the rGO surface OBP9A from *Tribolium castaneum*, an odorant binding protein from a different species, increasing concentrations of Eugenol did not cause a detectable change in the drain-source current (ΔI_{SD}), whereas this odorant proved to be an extremely strong ligand to OBP14 from the honeybee as demonstrated in Figs. 5 and 7B.

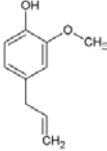
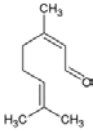
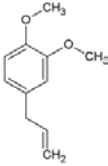
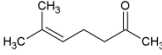
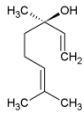
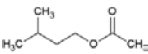
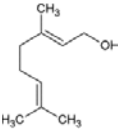
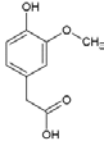
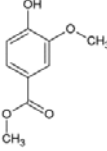
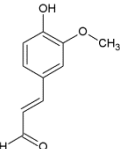
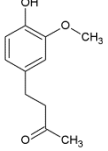
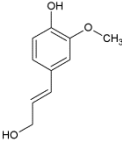
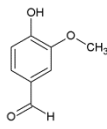
In conclusion, all negative control experiments have clearly demonstrated that the signals measured by OBP functionalized rGO FET devices reflect the bioaffinity reaction between the receptor and its ligands. Although it seems likely that the π -orbitals of phenolic compounds like Eugenol or Homovanillic acid could easily stick to the rGO surface similar to the pyrene derivatives (e.g., PBSE) used as linker systems, and that this attachment could result in a decrease in currents of the biosensor device, the sensor response signals is not compromised by any unspecific interactions of odorants with the rGO surface.

3.3. Spectrum of Ligands binding to OBP14

With this approach we then measured a whole set of different ligands for OBP14 and analysed the (change in the) source-drain current data, ΔI_{SD} , on the basis of the Langmuir model: from the kinetic runs we determined the association and the dissociation rate constants, k_{on} and k_{off} , respectively, as well as from titration experiments the affinity constant, K_{A} , and the dissociation (half-saturation) constant, K_{d} .

The whole set of data collected is summarized in Table 1, together with the structure formula of the various odorants (or other small volatile molecules) used as ligands.

Table1: Binding affinities of odorants with different chemical structure (upper part) and comparison of structural related compounds (lower part).

Odorant	Eugenol	Citral	Methyl eugenol	Sulcatone	Linalool	Isoamyl acetate	Geraniol
Chemical structure							
$K_d / \mu\text{M}$	40	800	1400	1400	1600	1000	3300
$k_{\text{on}} / \text{M}^{-1} \text{s}^{-1}$	170	9	6	5	5	8	3
$k_{\text{off}} / \text{s}^{-1}$	0.006	0.003	0.006	0.007	0.008	0.008	0.008
Odorant	Homovanillic acid	Methyl vanillate	Coniferyl aldehyde	Vanillyl acetone	Coniferyl alcohol	Vanillin	
Chemical structure							
$K_d / \mu\text{M}$	4	20	30	40	40	60	
$k_{\text{on}} / \text{M}^{-1} \text{s}^{-1}$	1100	240	260	250	180	120	
$k_{\text{off}} / \text{s}^{-1}$	0.008	0.01	0.008	0.01	0.008	0.007	

A few findings are particularly noteworthy:

- (i) The affinity constants for this set of ligands vary by almost 3 orders of magnitude. This is further visualized in Figure 8, where the Langmuir isotherms for strong (Homovanillic acid and Eugenol), medium (Citral) and weak binders (Sulcatone) are displayed.

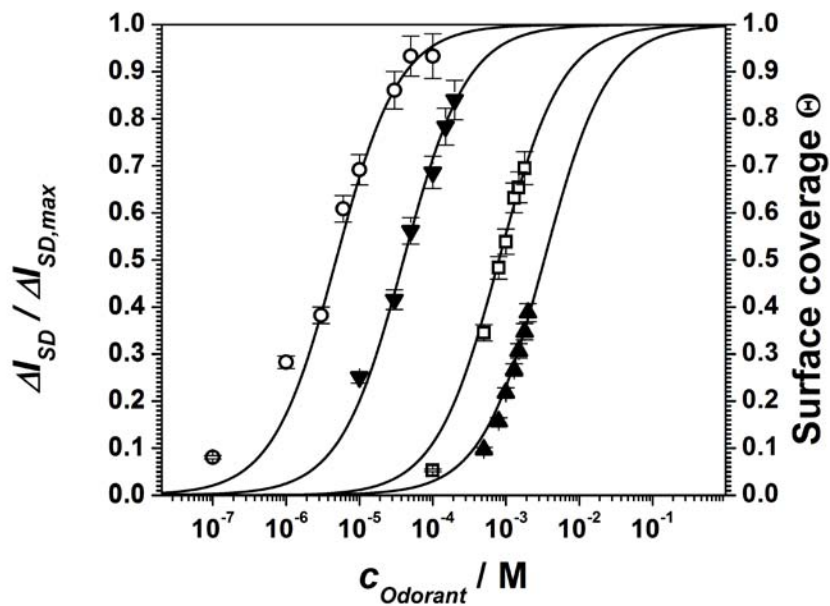


Figure 8: Langmuir adsorption isotherms for: o, Homovanillic acid; ▼, Eugenol; □, Citral; ▲, Sulcatone

- (ii) The affinity constants for ligands with a seemingly very similar structure, e.g., Eugenol and Methyleugenol, can vary by a factor of 35. This is another strong evidence that the measured values, indeed, are given by the specific binding behavior of the ligands to their receptor and do not reflect any non-specific interactions of the analyte with the sensor (surface).
- (iii) All ligands that exhibit a rather strong interaction with OBP14 (Homovanillic acid, Vanilline, Methyl vanillate, Eugenol, Coniferyl aldehyde, Vanillyl acetone) share a phenolic group as a common structural feature (cf. discussion below).
- (iv) For all ligands, irrespective of being strong or weak binders, the dissociation rate constant, k_{off} , varies by only a factor of three.
- (v) The difference in the binding strength originates almost exclusively from the difference in the association rate constants, k_{on} , that vary by nearly 3 orders of magnitude. Again this confirms the specificity of the information derived by the FET sensor as giving a quantitative picture of the binding between receptor and ligand rather than the non-specific adsorption of the analyte to the sensor surface.

3.4. Ligands binding to different mutants of OBP 14

The final set of experiments was performed with two mutants of OBP14. The first contained an additional segment of six histidines at its N-terminus. This modification was introduced with the aim of immobilising the protein on the sensor surface in an oriented fashion, using a bifunctional pyrene-NTA-linker.

First we measured the affinity of the fluorescent probe N-phenyl-1-aminonaphthalene (1-NPN) to the His-tag OBP14 in solution (Figure 9). This mutant showed a lower affinity to the fluorescent ligand ($K_d = 1.9 \mu\text{M}$) than the wild type protein ($K_d = 0.32 \mu\text{M}$, Spinelli et al., 2012).

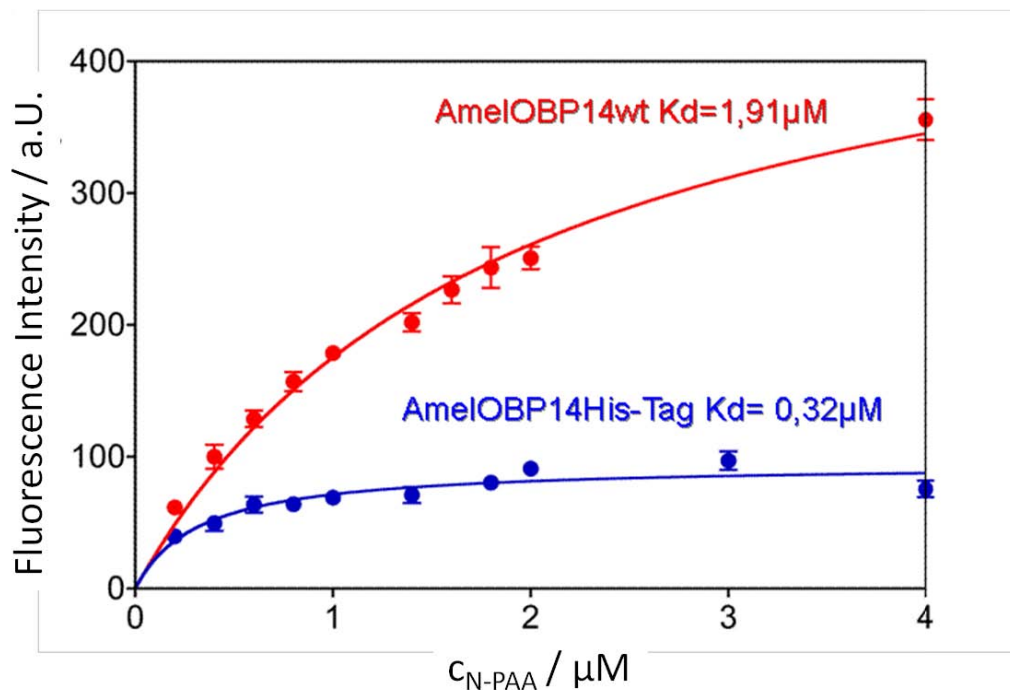


Figure 9: Langmuir adsorption isotherms of the binding of the fluorescent ligand, N-phenyl-1-aminonaphthalene (1-NPN), to HisTag-OBP14 from honey bee ($K_d = 1.9 \mu\text{M}$, SEM: 0.20).

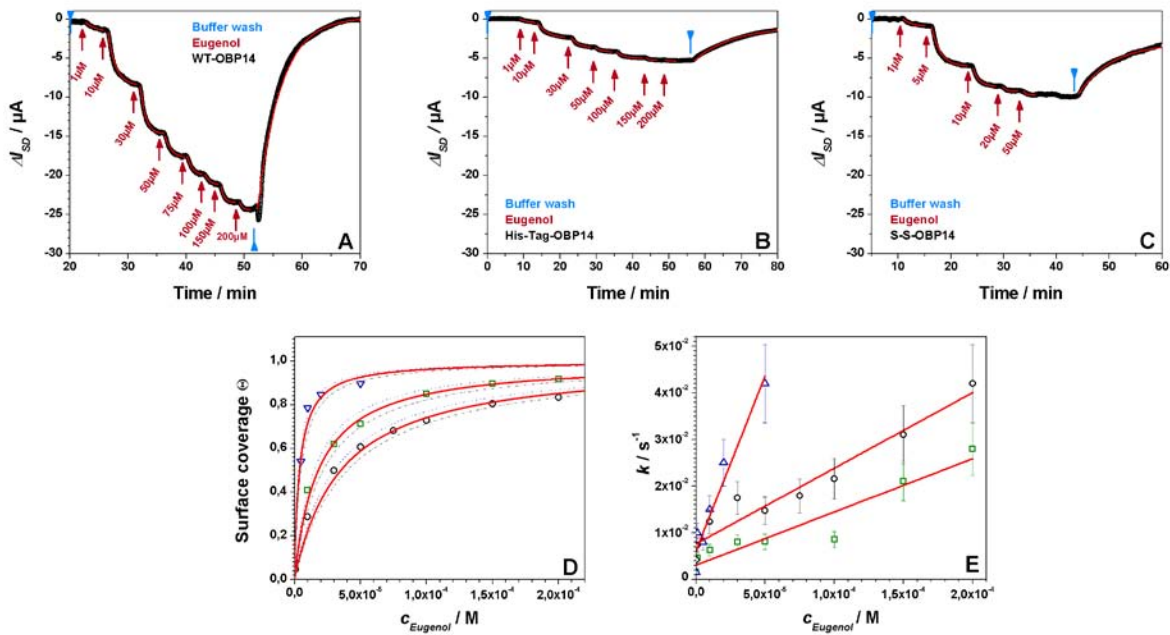


Figure 10: Full analysis of the recognition and binding of the odorant Eugenol to the odorant binding proteins: OBP14, to the His-Tag-OBP14, and to the S-S-OBP14. (A-C) shows the global analysis for Eugenol binding to these proteins on the FET gate surface. (D) Langmuir isotherm of the titration data taken from (A-C). (E) Rate constants taken from the fits of (B), plotted as a function of the bulk concentration c_0 .

Figure 10 reports the results of binding experiments of Eugenol to the three samples of OBP14 immobilised on the sensor. The oriented immobilization of the His-Tag-OBP14 produced a sensor with lower sensitivity when compared to the WT-OBP14 which was randomly oriented immobilised (compare Fig. 10 A and B). This effect could be due to an increased distance of the protein from the surface of the sensor when using the relatively longer NTA spacer.

The His-Tag-OBP14 mutant shows only little changes in the rate constants and the affinity constant compared to the WT-OBP14 (cf. Table 2), less than those measured in solution (Fig. 9.). This fact was observed with Eugenol, Isoamyl acetate and Geraniol, representing strong, medium and weak binding ligands, respectively (cf. Table 2).

Concerning the double mutant S-S-OBP14 (Gln44Cys, His97Cys), the introduction of a third disulphide bridge strongly affects the binding properties of the protein. This can be seen in the shift of the Langmuir isotherm in Fig. 10D, as well as in the slope of the rate constants in Fig. 10E (cf. also the values for k_{on} , k_{off} , and K_d , respectively, given in Table 2). The increase in the binding strength by a factor of 5 is quite significant, and offers the possibility of modifying the binding properties of OBPs by site-directed mutagenesis.

Table 2: Binding affinities of three samples of OBP14 immobilised on the sensor to the odorants known to bind significantly with a different degree of affinity to WT-OBP14.

	WT-OBP14	His-tag-OBP14	S-S-OBP14
<i>Eugenol</i>			
$k_{on} / M^{-1} s^{-1}$	160	114	750
k_{off} / s^{-1}	0.0076	0.003	0.006
$K_d / \mu M$	22	18	4
<i>Isoamyl acetate</i>			
$k_{on} / M^{-1} s^{-1}$	7.8	6.1	
k_{off} / s^{-1}	0.0077	0.009	
K_d / mM	1.5	1.2	
<i>Geraniol</i>			
$k_{on} / M^{-1} s^{-1}$	2.5	1.8	
k_{off} / s^{-1}	0.0078	0.00641	
K_d / mM	3.3	3.7	

4. Discussion

4.1. Affinity constants for ligands with a basic phenolic structure

From the full set of data obtained by our biosensor, we can conclude that OBP14 preferentially binds odorants containing phenolic structures, with the presence of a free hydroxyl group on the molecule playing an important role in the fitting of these ligands to the OBP14 binding pocket. This observation is in agreement with a crystallization study of OBP14 complexed with Eugenol (Spinelli et al. 2012). Elucidating by X-ray diffraction analysis the structure of OBP14 in a complex with the strong ligand Eugenol it was shown that an ensemble of hydrogen bonds including a strong hydrogen bond between the hydroxyl group of the ligand and the C=O moiety of Lys 111 in the protein binding site are responsible for the favorable binding of this ligand (Spinelli et al. 2012). However, a recognizable pattern in terms of a preferential class of odorants to OBP14 could not be detected so far, although structurally similar ligands to Eugenol, including Homovanillic acid and Coniferyl aldehyde have been tested (Iovinella et al. 2011). It was assumed that both the ligand shape and the functional group play complementary roles in favored binding into the OBP14 cavity (Spinelli et al. 2012). Our measurements, indeed, confirm that cyclic bulky compounds like Eugenol and Homovanillic acid displaying a hydrogen bond acceptor

are favored by OBP14, whereas elongated compounds, such as Isoamyl acetate or Sulcatone behave poorly.

It is generally acknowledged that honeybees, like other social insects, recognize and react to a wide range of different odorants and pheromone molecules mediating communication in honey bee hives or for locating floral rewards (pollen, nectar, etc.) (Dani et al. 2010a; Iovinella et al. 2011; Liu et al. 2013). Here, OBPs work as a first filter for odor recognition (Fan et al. 2011). With our results obtained with an electronic biosensor we could confirm the possible functional role of OBP14 in odor recognition by detecting various odorants with dissociation constants K_d in the micromolar range, as known for OBPs (Briand et al. 2002; Briand et al. 2000; Di Pietrantonio et al. 2013; Golebiowski et al. 2012; Hou et al. 2005; Iovinella et al. 2011; Liu et al. 2013; Sankaran et al. 2011; Spinelli et al. 2012). Comparing the different binding properties of OBP14 towards the chosen ligands (cf. Table1) our results further confirm the general tendency previously demonstrated by fluorescence measurements (Iovinella et al. 2011; Spinelli et al. 2012) that Eugenol exhibits a high affinity to OBP14, whereas Citral and Geraniol are moderate or weak binders. However, for two compounds, i.e., Homovanillic acid and Coniferyl aldehyde affinity constants to OBP14 could only be determined by our label-free method, since both ligands did not show good affinity to OBP14 according to fluorescent displacement assays (Iovinella et al. 2011).

4.2. Tuning affinities for ligand binding by genetic manipulations of OBPs

The biosensor data have shown a stronger binding of eugenol compared to the wild type OBP14. The additional disulfide bond brings more binding strength and compared to our previously shown higher stability upon thermal denaturation it is noteworthy that these investigated proteins are having unexplored potential as tunable recognition elements for future biosensor applications.

5. Conclusions

We have developed and presented an olfactory biosensor based on a rGO-FET which constitutes a first step towards the development of a bioelectronic smell sensor by using OBP14 from the honeybee. Besides a successful detection of various floral and pollen specific odorants with a detection limit in the micromolar range, this biosensor could classify the tested ligands as good, moderate and low affinity

odorants. Since our study provided evidence for a distinct ligand specificity for OBP14, molecular modeling should help to find correlations between protein-ligand characteristics and the change of the source-drain-current of the biosensor in a future project. Due to a manageable number of existing OBPs in this species, further ligand-binding studies are pursued in order to obtain a better impression of the chemical language used by bees.

6. Acknowledgements

Partial support for this work was provided by the European Science Foundation (ESF), the Austrian Science Fund (FWF) (I681-N24) and the Austrian Federal Ministry for Transport, Innovation and Technology (GZ BMVIT-612.166/0001-III/I1/2010).

7. Literature

Adamczyk, M., Moore, J.A., Yu, Z.G., 2000. Application of surface plasmon resonance toward studies of low-molecular-weight antigen-antibody binding interactions. *Methods - a Companion to Methods in Enzymology* 20(3), 319-328.

Ban, L., Scaloni, A., Brandazza, A., Angeli, S., Zhang, L., Yan, Y., Pelosi, P., 2003. Chemosensory proteins of *Locusta migratoria*. *Insect Molecular Biology* 12(2), 125-134.

Ban, L.P., Zhang, L., Yan, Y.H., Pelosi, P., 2002. Binding properties of a locust's chemosensory protein. *Biochemical and Biophysical Research Communications* 293(1), 50-54.

Banskota, A.H., Tezuka, Y., Kadota, S., 2001. Recent progress in pharmacological research of propolis. *Phytotherapy Research* 15(7), 561-571.

Briand, L., Eloit, C., Nespoulous, C., Bézirard, V., Huet, J.-C., Henry, C., Blon, F., Trotier, D., Pernollet, J.-C., 2002. Evidence of an Odorant-Binding Protein in the Human Olfactory Mucus: Location, Structural Characterization, and Odorant-Binding Properties†. *Biochemistry* 41(23), 7241-7252.

Biessmann H, Andronopoulou E, Biessmann MR, Douris V, Dimitratos SD, Eliopoulos E et al. (2010) The *Anopheles gambiae* odorant binding protein 1 (AgamOBP1) mediates indole recognition in the antennae of female mosquitoes. *PLoS One*. 5:e9471.

Briand, L., Nespoulous, C., Perez, V., Rémy, J.-J., Huet, J.-C., Pernellet, J.-C., 2000. Ligand-binding properties and structural characterization of a novel rat odorant-binding protein variant. *European Journal of Biochemistry* 267(10), 3079-3089.

Calvello, M., Guerra, N., Brandazza, A., D'Ambrosio, C., Scaloni, A., Dani, F.R., Turillazzi, S., Pelosi, P., 2003. Soluble proteins of chemical communication in the social wasp *Polistes dominulus*. *Cellular and Molecular Life Sciences* 60(9), 1933-1943.

Campanacci, V., Krieger, J., Bette, S., Sturgis, J.N., Lartigue, A., Cambillau, C., Breer, H., Tegoni, M., 2001. Revisiting the specificity of *Mamestra brassicae* and *Antheraea polyphemus* pheromone-binding proteins with a fluorescence binding assay. *J Biol Chem* 276(23), 20078-20084.

Chang H, Liu Y, Yang T, Pelosi P, Dong S, Wang G. (2015) Pheromone binding proteins enhance the sensitivity of olfactory receptors to sex pheromones in *Chilo suppressalis*. *Sci Rep.* 5:13093.

Clyne, P.J., Certel, S.J., de Bruyne, M., Zaslavsky, L., Johnson, W.A., Carlson, J.R., 1999. The odor specificities of a subset of olfactory receptor neurons are governed by *Acj6*, a POU-domain transcription factor. *Neuron* 22(2), 339-347.

D'Auria, S., Scognamiglio, V., Rossi, M., Staiano, M., Campopiano, S., Cennamo, N., Zeni, L., 2004. Odor binding protein as probe for a refractive index-based biosensor: new perspectives in biohazard assessment, 258-264.

Damberger, F., Nikonova, L., Horst, R., Peng, G.H., Leal, W.S., Wuthrich, K., 2000. NMR characterization of a pH-dependent equilibrium between two folded solution conformations of the pheromone-binding protein from *Bombyx mori*. *Protein Sci* 9(5), 1038-1041.

Dani, F.R., Iovinella, I., Felicioli, A., Niccolini, A., Calvello, M.A., Carucci, M.G., Qiao, H., Pieraccini, G., Turillazzi, S., Moneti, G., Pelosi, P., 2010a. Mapping the Expression of Soluble Olfactory Proteins in the Honeybee. *Journal of Proteome Research* 9(4), 1822-1833.

Dani, F.R., Iovinella, I., Felicioli, A., Niccolini, A., Calvello, M.A., Carucci, M.G., Qiao, H., Pieraccini, G., Turillazzi, S., Moneti, G., Pelosi, P., 2010b. Mapping the expression of soluble olfactory proteins in the honeybee. *J Proteome Res* 9(4), 1822-1833.

Di Pietrantonio, F., Cannatà, D., Benetti, M., Verona, E., Varriale, A., Staiano, M., D'Auria, S., 2013. Detection of odorant molecules via surface acoustic wave biosensor array based on odorant-binding proteins. *Biosensors and Bioelectronics* 41(0), 328-334.

Dobson, H.E.M., Bergstrom, G., Groth, I., 1990. Differences in Fragrance Chemistry between Flower Parts of *Rosa-Rugosa* Thunb (Rosaceae). *Israel J Bot* 39(1-2), 143-156.

Dobson, H.E.M., Groth, I., Bergstrom, G., 1996. Pollen advertisement: Chemical contrasts between whole-flower and pollen odors. *Am J Bot* 83(7), 877-885.

Dötterl, S., Vereecken, N.J., 2010. The chemical ecology and evolution of bee–flower interactions: a review and perspectives. The present review is one in the special series of reviews on animal–plant interactions. *Canadian Journal of Zoology* 88(7), 668-697.

Fan, J., Francis, F., Liu, Y., Chen, J.L., Cheng, D.F., 2011. An overview of odorant-binding protein functions in insect peripheral olfactory reception. *Genet Mol Res* 10(4), 3056-3069.

Forstner M, Breer H, Krieger J. (2009) A receptor and binding protein interplay in the detection of a distinct pheromone component in the silkworm *Antheraea polyphemus*. *Int J Biol Sci*. 5:745-757.

Sun M, Liu Y, Walker WB, Liu C, Lin K, Gu S, et al. (2013) Identification and characterization of pheromone receptors and interplay between receptors and pheromone binding proteins in the diamondback moth, *Plutella xylostella*. *PLoS One* 8:e62098.

Golebiowski, J., Topin, J., Charlier, L., Briand, L., 2012. Interaction between odorants and proteins involved in the perception of smell: the case of odorant-binding proteins probed by molecular modelling and biophysical data. *Flavour and Fragrance Journal* 27(6), 445-453.

Grosse-Wilde E, Svatos A, Krieger J. (2006) A pheromone-binding protein mediates the bombykol-induced activation of a pheromone receptor in vitro. *Chem Senses*. 31:547–555.

Guyot, C., Scheirman, V., Collin, S., 1999. Floral origin markers of heather honeys: *Calluna vulgaris* and *Erica arborea*. *Food Chemistry* 64(1), 3-11.

Horst, R., Damberger, F., Luginbuhl, P., Guntert, P., Peng, G., Nikonova, L., Leal, W.S., Wüthrich, K., 2001a. NMR structure reveals intramolecular regulation mechanism for pheromone binding and release. *P Natl Acad Sci USA* 98(25), 14374-14379.

Horst, R., Damberger, F., Luginbühl, P., Guntert, P., Peng, G., Nikonova, L., Leal, W.S., Wüthrich, K., 2001b. NMR structure reveals intramolecular regulation mechanism for pheromone binding and release. *Proceedings of the National Academy of Sciences* 98(25), 14374-14379.

Hou, Y., Jaffrezic-Renault, N., Martelet, C., Tlili, C., Zhang, A., Pernellet, J.-C., Briand, L., Gomila, G., Errachid, A., Samitier, J., Salvagnac, L., Torbiéro, B., Temple-Boyer, P., 2005. Study of Langmuir and Langmuir–Blodgett Films of Odorant-Binding Protein/Amphiphile for Odorant Biosensors. *Langmuir* 21(9), 4058-4065.

Hou, Y., Jaffrezic-Renault, N., Martelet, C., Zhang, A., Minic-Vidic, J., Gorojankina, T., Persuy, M.-A., Pajot-Augy, E., Salesse, R., Akimov, V., Reggiani, L., Pennetta, C., Alfinito, E., Ruiz, O., Gomila, G., Samitier, J., Errachid, A., 2007. A novel detection strategy for odorant molecules based on controlled bioengineering of rat olfactory receptor I7. *Biosensors and Bioelectronics* 22(7), 1550-1555.

Huang, J., Larisika, M., Fam, D.W.H., He, Q., Nimmo, M.A., Nowak, C., Tok, A.I.Y., 2013. The Extended Growth of Graphene Oxide Flakes Using Ethanol CVD. *Nanoscale*.

Iovinella, I., Dani, F.R., Niccolini, A., Sagona, S., Michelucci, E., Gazzano, A., Turillazzi, S., Felicioli, A., Pelosi, P., 2011. Differential Expression of Odorant-Binding Proteins in the Mandibular Glands of the Honey Bee According to Caste and Age. *Journal of Proteome Research* 10(8), 3439-3449.

Isidorov, V.A., Czyzewska, U., Jankowska, E., Bakier, S., 2011. Determination of royal jelly acids in honey. *Food Chemistry* 124(1), 387-391.

Jin, H.J., Lee, S.H., Kim, T.H., Park, J., Song, H.S., Park, T.H., Hong, S., 2012. Nanovesicle-based bioelectronic nose platform mimicking human olfactory signal transduction. *Biosensors and Bioelectronics* 35(1), 335-341.

Karlsson, R., Falt, A., 1997. Experimental design for kinetic analysis of protein-protein interactions with surface plasmon resonance biosensors. *Journal of Immunological Methods* 200(1-2), 121-133.

Khan, H.U., Jang, J., Kim, J.J., Knoll, W., 2011. In Situ Antibody Detection and Charge Discrimination Using Aqueous Stable Pentacene Transistor Biosensors. *J Am Chem Soc* 133(7), 2170-2176.

Kim, T.H., Lee, S.H., Lee, J., Song, H.S., Oh, E.H., Park, T.H., Hong, S., 2009. Single-Carbon-Atomic-Resolution Detection of Odorant Molecules using a Human Olfactory Receptor-based Bioelectronic Nose. *Advanced Materials* 21(1), 91-94.

Knoll, W., Kasry, A., Liu, J., Neumann, T., Niu, L., Park, H., Paulsen, H., Robelek, R., Yao, D., Yu, F., 2008. Surface Plasmon Fluorescence Techniques for Bioaffinity Studies. In: Schasfoort, R.B.M., Tudos, A.J. (Eds.), *Handbook of Surface Plasmon Resonance*, pp. 275-312. The Royal Society of Chemistry, Cambridge.

Kruse, S.W., Zhao, R., Smith, D.P., Jones, D.N.M., 2003. Structure of a specific alcohol-binding site defined by the odorant binding protein LUSH from *Drosophila melanogaster*. *Nat Struct Mol Biol* 10(9), 694-700.

Lagarde, A., Spinelli, S., Tegoni, M., He, X., Field, L., Zhou, J.-J., Cambillau, C., 2011. The Crystal Structure of Odorant Binding Protein 7 from *Anopheles gambiae* Exhibits an Outstanding Adaptability of Its Binding Site. *Journal of Molecular Biology* 414(3), 401-412.

Laloi, D., Gallois, M., Roger, B., Pham-Delegue, M.H., 2001. Changes with age in olfactory conditioning performance of worker honey bees (*Apis mellifera*). *Apidologie* 32(3), 231-242.

Langmuir, I., 1918. THE ADSORPTION OF GASES ON PLANE SURFACES OF GLASS, MICA AND PLATINUM. *Journal of the American Chemical Society* 40(9), 1361-1403.

Larisika, M., Huang, J., Tok, A., Knoll, W., Nowak, C., 2012. An improved synthesis route to graphene for molecular sensor applications. *Materials Chemistry and Physics* 136(2–3), 304-308.

Larisika, M.; Kotlowski, C.; Steininger, C.; Mastrogiacomo, R.; Pelosi, P.; Schütz, S.; Peteu, S. F.; Kleber, C.; Reiner-Rozman, C.; Nowak, C.; Knoll, W., Electronic Olfactory Sensor Based on A.mellifera Odorant Binding Protein 14 on a Reduced Graphene Oxide Field-Effect Transistor, **Angew. Chem.**, Int. Ed. Engl. **54**, 13245-13248 (2015)

Leal, W.S., 2013. Odorant Reception in Insects: Roles of Receptors, Binding Proteins, and Degrading Enzymes. *Annual Review of Entomology* 58(1), 373-391.

Leal, W.S., Nikonova, L., Peng, G.H., 1999. Disulfide structure of the pheromone binding protein from the silkworm moth, *Bombyx mori*. *Febs Lett* 464(1-2), 85-90.

Lee, S.H., Jin, H.J., Song, H.S., Hong, S., Park, T.H., 2012. Bioelectronic nose with high sensitivity and selectivity using chemically functionalized carbon nanotube combined with human olfactory receptor. *Journal of Biotechnology* 157(4), 467-472.

Lee, S.H., Jun, S.B., Ko, H.J., Kim, S.J., Park, T.H., 2009. Cell-based olfactory biosensor using microfabricated planar electrode. *Biosensors and Bioelectronics* 24(8), 2659-2664.

Lescop, E., Briand, L.c., Pernollet, J.-C., Guittet, E., 2009. Structural Basis of the Broad Specificity of a General Odorant-Binding Protein from Honeybee. *Biochemistry* 48(11), 2431-2441.

Liu, Q., Wang, H., Li, H., Zhang, J., Zhuang, S., Zhang, F., Jimmy Hsia, K., Wang, P., 2013. Impedance sensing and molecular modeling of an olfactory biosensor based on chemosensory proteins of honeybee. *Biosensors and Bioelectronics* 40(1), 174-179.

Matsuo, T., 2007. [Odorant-binding proteins and evolution of host-plant preference in insects]. *Tanpakushitsu Kakusan Koso* 52(15), 1980-1986.

Pelletier J, Guidolin A, Syed Z, Cornel AJ, Leal WS. (2010) Knockdown of a mosquito odorant-binding protein involved in the sensitive detection of oviposition attractants. *J Chem Ecol.* 36:245-248.

Rosa Mastrogiacomo Fluorescence Binding studies

Nunes, C.A., Guerreiro, M.C., 2012. Characterization of Brazilian green propolis throughout the seasons by headspace GC/MS and ESI-MS. *J Sci Food Agric* 92(2), 433-438.

O'Shannessy, D.J., Brigham-Burke, M., Soneson, K.K., Hensley, P., Brooks, I., 1993. Determination of rate and equilibrium binding constants for macromolecular interactions using surface plasmon resonance: use of nonlinear least squares analysis methods. *Anal Biochem* 212(2), 457-468.

O'Shannessy, D.J., Winzor, D.J., 1996. Interpretation of deviations from pseudo-first-order kinetic behavior in the characterization of ligand binding by biosensor technology. *Analytical Biochemistry* 236(2), 275-283.

Park, J., Lim, J.H., Jin, H.J., Namgung, S., Lee, S.H., Park, T.H., Hong, S., 2012a. A bioelectronic sensor based on canine olfactory nanovesicle-carbon nanotube hybrid structures for the fast assessment of food quality. *Analyst* 137(14), 3249-3254.

Park, S.J., Kwon, O.S., Lee, S.H., Song, H.S., Park, T.H., Jang, J., 2012b. Ultrasensitive Flexible Graphene Based Field-Effect Transistor (FET)-Type Bioelectronic Nose. *Nano Letters* 12(10), 5082-5090.

Pelosi, P., Zhou, J.J., Ban, L.P., Calvello, M., 2006. Soluble proteins in insect chemical communication. *Cell Mol Life Sci* 63(14), 1658-1676.

Qiao H, Tuccori E, He X, Gazzano A, Field L, Zhou JJ et al. (2009) Discrimination of alarm pheromone (*E*)- β -farnesene by aphid odorant-binding proteins. *Insect Biochem Mol Biol.* 39:414-419.

Reiner-Rozman, C; Larisika, M; Nowak; Knoll, W., Graphene-based liquid-gated field effect transistor for biosensing: Theory and experiments, *Biosens. Bioelectron.* **70**, 21-27 (2015)

Sandler, B.H., Nikonova, L., Leal, W.S., Clardy, J., 2000. Sexual attraction in the silkworm moth: structure of the pheromone-binding-protein–bombykol complex. *Chemistry & Biology* 7(2), 143-151.

Sankaran, S., Panigrahi, S., Mallik, S., 2011. Odorant binding protein based biomimetic sensors for detection of alcohols associated with Salmonella contamination in packaged beef. *Biosensors and Bioelectronics* 26(7), 3103-3109.

Scaloni, A., Monti, M., Angeli, S., Pelosi, P., 1999. Structural analysis and disulfide-bridge pairing of two odorant-binding proteins from *Bombyx mori*. *Biochem Biophys Res Commun* 266(2), 386-391.

Schuck, P., 1997. Reliable determination of binding affinity and kinetics using surface plasmon resonance biosensors. *Curr Opin Biotech* 8(4), 498-502.

Spinelli, S., Lagarde, A., Iovinella, I., Legrand, P., Tegoni, M., Pelosi, P., Cambillau, C., 2012. Crystal structure of *Apis mellifera* OBP14, a C-minus odorant-binding protein, and its complexes with odorant molecules. *Insect Biochemistry and Molecular Biology* 42(1), 41-50.

Su, C. Y., Xu, Y., Zhang, W., Zhao, J., Tang, X., Tsai, C. H., & Li, L. J. (2009). Electrical and spectroscopic characterizations of ultra-large reduced graphene oxide monolayers. *Chemistry of Materials*, 21(23), 5674-5680.

Sun, Y.F., De Biasio, F., Qiao, H.L., Iovinella, I., Yang, S.X., Ling, Y., Riviello, L., Battaglia, D., Falabella, P., Yang, X.L., Pelosi, P., 2012. Two odorant-binding proteins mediate the behavioural response of aphids to the alarm pheromone (*E*)- β -farnesene and structural analogues. *PLoS One* 7(3), e32759.

Swarup, S., Williams, T.I., Anholt, R.R., 2011. Functional dissection of Odorant binding protein genes in *Drosophila melanogaster*. *Genes Brain Behav* 10(6), 648-657.

Tan, K.H., Nishida, R., 2007. Zingerone in the floral synomone of *Bulbophyllum baileyi* (Orchidaceae) attracts *Bactrocera* fruit flies during pollination. *Biochem Syst Ecol* 35(6), 334-341.

Thiery, D., Bluet, J.M., Phamdelegue, M.H., Etievant, P., Masson, C., 1990. Sunflower Aroma Detection by the Honeybee - Study by Coupling Gas-Chromatography and Electroantennography. *J Chem Ecol* 16(3), 701-711.

Trhlin, M., Rajchard, J., 2011. Chemical communication in the honeybee (*Apis mellifera* L.): a review. *Vet Med-Czech* 56(6), 265-273.

Vogt, R.G., 2005. Molecular basis of pheromone detection in insects. In: Gilbert, L., Latro, K., Gill, S. (Eds.), *Comprehensive Insect Physiology, Biochemistry, Pharmacology and Molecular Biology*, pp. 753-804. Elsevier, London.

Vogt, R.G., Riddiford, L.M., 1981. Pheromone binding and inactivation by moth antennae. *Nature* 293(5828), 161-163.

Vosshall, L.B., Amrein, H., Morozov, P.S., Rzhetsky, A., Axel, R., 1999. A spatial map of olfactory receptor expression in the *Drosophila* antenna. *Cell* 96(5), 725-736.

Wogulis, M., Morgan, T., Ishida, Y., Leal, W.S., Wilson, D.K., 2006. The crystal structure of an odorant binding protein from *Anopheles gambiae*: Evidence for a common ligand release mechanism. *Biochemical and Biophysical Research Communications* 339(1), 157-164.

Xu, P., Atkinson, R., Jones, D.N., Smith, D.P., 2005. *Drosophila* OBP LUSH is required for activity of pheromone-sensitive neurons. *Neuron* 45(2), 193-200.

Yoon, H., Lee, S.H., Kwon, O.S., Song, H.S., Oh, E.H., Park, T.H., Jang, J., 2009. Polypyrrole Nanotubes Conjugated with Human Olfactory Receptors: High-Performance Transducers for FET-Type Bioelectronic Noses. *Angewandte Chemie International Edition* 48(15), 2755-2758.

Honey bee odorant-binding protein 14: effects on thermal stability upon odorant binding revealed by FT-IR spectroscopy and CD measurements

Andreas Schwaighofer · Caroline Kotlowski · Can Araman ·
Nam Chu · Rosa Mastrogiacomo · Christian Becker · Paolo Pelosi ·
Wolfgang Knoll · Melanie Larisika · Christoph Nowak

Received: 1 October 2013 / Revised: 18 November 2013 / Accepted: 6 December 2013 / Published online: 21 December 2013
© European Biophysical Societies' Association 2013

Abstract In the present work, we study the effect of odorant binding on the thermal stability of honey bee (*Apis mellifera* L.) odorant-binding protein 14. Thermal denaturation of the protein in the absence and presence of different odorant molecules was monitored by Fourier transform infrared spectroscopy (FT-IR) and circular dichroism (CD). FT-IR spectra show characteristic bands for intermolecular aggregation through the formation of intermolecular β -sheets during the heating process. Transition temperatures in the FT-IR spectra were evaluated using moving-window 2D correlation maps and confirmed by CD measurements. The obtained results reveal an increase of the denaturation temperature of the protein when bound to an odorant molecule. We could also

discriminate between high- and low-affinity odorants by determining transition temperatures, as demonstrated independently by the two applied methodologies. The increased thermal stability in the presence of ligands is attributed to a stabilizing effect of non-covalent interactions between odorant-binding protein 14 and the odorant molecule.

Keywords Odorant-binding protein · *Apis mellifera* · Infrared spectroscopy · Circular dichroism · Ligand binding · Moving window 2D spectroscopy

Introduction

Odorant-binding proteins (OBPs) are the object of growing interest as biosensing elements for the fabrication of odorant sensors based on the olfactory system (Park et al. 2012a; Persaud 2012; Glatz and Bailey-Hill 2011; Lee et al. 2012b). Applications are manifold and include disease diagnostics (Sankaran et al. 2011), food safety (Di Pietrantonio et al. 2013), and environmental monitoring (Misawa et al. 2010; Capone et al. 2011). Currently, so-called “electronic noses” are based on metal oxides and conducting polymers, but biomimetic sensors promise to show higher sensitivity and selectivity combined with lower detection limits and faster response time (Sankaran et al. 2012; Park et al. 2012b; Lee et al. 2012a; Jin et al. 2012). OBPs are small acidic proteins (~13–16 kDa) present in very high concentrations (10–20 mM) at the interface between olfactory receptors and the external environment (Pelosi 1994; Tegoni et al. 2000; Bohbot and Vogt 2005; Pelosi et al. 2006). Their physiological role has not yet been clarified, but they have been associated with transfer of the odorant molecules to the receptor proteins.

Electronic supplementary material The online version of this article (doi:10.1007/s00249-013-0939-4) contains supplementary material, which is available to authorized users.

A. Schwaighofer · W. Knoll · M. Larisika · C. Nowak
Austrian Institute of Technology GmbH, AIT, Donau-City Str. 1,
1220 Vienna, Austria

C. Kotlowski · C. Nowak
Center of Electrochemical Surface Technology, CEST, Viktor-
Kaplan-Straße 2, 2700 Wiener Neustadt, Austria

C. Araman · N. Chu · C. Becker
Institut für Biologische Chemie, Universität Wien, Währinger
Straße 38, 1090 Vienna, Austria

R. Mastrogiacomo · P. Pelosi
Department of Agriculture, Food and Environment, University
of Pisa, Via del Borghetto 80, 56124 Pisa, Italy

C. Nowak (✉)
Biosensor Technologies, AIT Austrian Institute of Technology,
Muthgasse 11, 1190 Vienna, Austria
e-mail: c.nowak@ait.ac.at

Odorants predominantly are lipophilic molecules and need to be carried through the aqueous olfactory mucus of vertebrates respectively the sensillar lymph of insects to the membrane-bound olfactory receptors (Sankaran et al. 2011). The number of OBP subtypes is different for each species suggesting a role in discriminating semiochemicals.

Despite a mutual name, OBPs of vertebrates and those of insects are completely different in structure. Vertebrates OBPs are folded into eight antiparallel β -strands and a short α -helical segment, in the typical β -barrel structure of lipocalins (Bianchet et al. 1996; Tegoni et al. 1996). OBPs of insects, instead, contain six α -helical domains arranged in a very compact and stable structure. The stability of these proteins is further increased by the presence of three interlocked disulphide bonds (Leal et al. 1999; Scaloni et al. 1999). In the honey bee (*Apis mellifera* L.), 21 genes encode proteins of the OBP family (Foret and Maleszka 2006). OBP14, which is the subject of this study, has been identified in different tissues of adult bees, as well as in larvae (Iovinella et al. 2011). Using fluorescence displacement arrays, affinities of several odorants to OBP14 have been determined, and geraniol has been identified as a representative of low-affinity ligands and eugenol as a high-affinity ligand. A crystallographic study of the three-dimensional structure of this protein and its complexes with some ligands supports the ligand-binding experiments (Iovinella et al. 2011; Spinelli et al. 2012).

Stabilizing effects of proteins upon ligand binding have been reported for a large variety of systems (Celej et al. 2003, 2005; Moreau et al. 2010). Weak non-covalent forces such as hydrogen bonds as well as hydrophobic and aromatic interactions have been identified to play an important role in increasing the structural stability of the protein-ligand complexes (Williams et al. 2004; Bissantz et al. 2010; Stepanenko et al. 2008; Kumar et al. 2000). Thermal denaturation measurements employing differential scanning calorimetry or isothermal denaturation are a commonly used way to study the stability of proteins (Moreau et al. 2010). However, these methods lack the ability to provide structural information of the protein during the heating process.

Fourier transform infrared (FT-IR) spectroscopy is an established and powerful method for investigating the structure and dynamics of proteins (Barth 2007). In FT-IR spectroscopy, the amide I ($1,650\text{ cm}^{-1}$) and amide II ($1,550\text{ cm}^{-1}$) bands are most commonly used for secondary structure determination of proteins. Since the OH-bending band of water overlaps with the amide I band in the IR spectrum at $1,640\text{ cm}^{-1}$, measurements of proteins are often performed in D_2O solution. The OD-bending band is located at $\sim 1,200\text{ cm}^{-1}$, thus creating a region of relatively low absorbance between $1,500$ and $1,800\text{ cm}^{-1}$. Upon solvent exchange, the amide II band (predominantly

originating from N–H vibrations) is shifted from $\sim 1,550$ to $\sim 1,450\text{ cm}^{-1}$, then referred to as the amide II' band. Since the amide I band is mainly composed of CO vibrations, its shift is relatively small ($5\text{--}10\text{ cm}^{-1}$) compared to the amide II band (Fabian and Mäntele 2006). In combination with thermal denaturation experiments, FT-IR was extensively used to reveal structural changes of proteins induced by increasing temperatures (Pedone et al. 2003; Zhang et al. 1998; Arrondo et al. 2005), including thermal transitions of the β -barrel structure of vertebrae OBPs (Marabotti et al. 2008a, b; Paolini et al. 1999; Scire et al. 2009). Unlike previously applied evaluation methods, we employ moving-window two-dimensional (MW2D) correlation maps to highlight the transition points in the FT-IR spectra. MW2D correlation maps are an extension to generalized 2D correlation (2D-COS) spectroscopy, but here the spectral information is sub-divided into slices along the perturbation range, and the autocorrelation intensity is plotted versus the perturbation variable. Interpretation of MW2D correlation maps is more intuitive compared to the rather complex evaluation algorithms of 2D-COS spectra, and it has been proven to be an excellent tool for analyzing spectral changes caused by external perturbation (Ashton and Blanch 2010; Thomas and Richardson 2000; Du et al. 2010). Further, circular dichroism (CD) is a convenient method for studying the structure of proteins in solution (Kelly et al. 2005). To the best of our knowledge, this is the first report applying FT-IR studies to insect OBPs. We investigated the changes of thermal stability upon odorant binding of low- and high-affinity ligands to OBP14. To address this question, FT-IR and CD have been adopted to study the structural changes of the protein induced by thermal denaturation, in both the presence and absence of odorants. The denaturation temperatures in the FT-IR spectra were visualized by MW2D correlation maps and corroborated by CD measurements.

Materials and methods

Materials

Deuterium oxide (D_2O , 99.9 % D), geraniol (2,6-dimethyl-trans-2,6-octadien-8-ol, 98 %) and eugenol (4-hydroxy-3-methoxy-1-allyl-benzol, 99 %) were provided by Sigma–Aldrich (Steinheim, Germany). Dithiobis (nitrioloacetic acid butylamidyl propionate) (DTNTA, $\geq 95.0\%$) was obtained from Dojindo Laboratories (Kumamoto, Japan).

Expression and purification of OBP14

The nucleotide sequence encoding OBP14 and flanked by restriction sites NdeI and BamHI was ligated into the

expression vector pET15b (Novagen, Darmstadt, Germany), which provides a His-tag at the N-terminus of the protein. Bacterial expression was performed along with established protocols (Dani et al. 2010; Iovinella et al. 2011), and purification was accomplished using conventional chromatographic techniques (Ban et al. 2003; Calvello et al. 2003). The purity of the protein was checked by SDS-PAGE.

Infrared spectroscopy

Infrared absorption measurements were performed using a Bruker 70v FTIR spectrometer (Karlsruhe, Baden-Württemberg, Germany), equipped with a Harrick Horizon attenuated total reflection (ATR) measuring unit with a temperature-controlled liquid sample cell (400 μ l), containing a ZnSe ATR crystal (angle of incidence $\theta = 45^\circ$, 12.5 active reflections). Recombinant OBP14 from *E. coli* with a His-tag engineered on the N-terminus was expressed as described by Iovinella et al. (2011). ATR crystals were immersed in a solution of 5 mM DTNTA and 5 mM 3,3'-dithiodipropionic acid (DTP) in dry DMSO for 20 h. After rinsing with purified water, the crystals were immersed in 40 mM NiCl₂ in acetate buffer (50 mM, pH 5.5) for 30 min, followed by thorough rinsing with purified water to remove excess NiCl₂. OBP14 dissolved in phosphate buffer (140 mM NaCl, 3 mM KCl, 10 mM Na₂HPO₄, 2 mM KH₂PO₄, pH = 8) was adsorbed at 25 °C onto the NTA-functionalized surface at a final concentration of 20 μ M. After 4-h adsorption time, the cell was rinsed with phosphate buffer. Hydrogen/deuterium (H/D) exchange was initiated by exchanging the buffer in the measurement cell by D₂O-phosphate buffer (pD = 8.0, corresponding to the pH meter reading +0.4) (Glasoe and Long 1960) followed by pumping the deuterated buffer through the sample cell for 20 h at 0.15 ml/min. For measurements in the presence of odorants, the protein was incubated in 100 μ M odorant solution in D₂O-buffer for 1 h. In thermal-denaturation experiments, the temperature was raised by 5 °C steps from 25 to 90 °C. Spectra were obtained after a 5-min equilibration time for stabilizing the cell temperature.

During FT-IR measurements, the sample chamber was continuously purged with dry carbon dioxide-free air, and the total reflected IR beam intensity was measured using a liquid nitrogen-cooled photovoltaic mercury cadmium telluride (MCT) detector. Spectra were recorded with a spectral resolution of 4 cm⁻¹ in double-sided acquisition mode; the mirror velocity was set to 80 kHz. At least 1,000 scans were taken for each spectrum, which was calculated using a Blackman-Harris 3-term apodization function and a zero filling factor of 2. Spectra were analyzed using the software package OPUS 6.5 and OriginLab's Origin software.

Moving-window 2D correlation spectroscopy

MW2D correlation spectra were calculated using the difference spectra after baseline correction with the freely available 2Dshige software (available at <http://sci-tech.ksc.kwansei.ac.jp/~ozaki/2D-shige.htm>) with a window size of $2m + 1 = 11$.

Circular dichroism

Far UV (260–195 nm) CD measurements were carried out using an Applied Photophysics Chirascan plus spectrophotometer (Leatherhead, Surrey, UK) equipped with a temperature control unit (Quantum TC125) in a 1-mm quartz cell at 1-nm resolution. Protein solutions (0.5 mg/ml; 41.8 μ M) were prepared in phosphate buffer, pH = 8. For static measurements, ten spectra with the acquisition time of 0.5 s were taken at room temperature, and the results were averaged. For measurement of OBP14 in the presence of odorants, the protein was incubated in 200 μ M odorant solution for 1 h. In temperature-controlled experiments, spectra were taken in the range of 20–85 °C ($\Delta T = 5$ °C) with an acquisition time of 0.2 s after an equilibration time of 30 s at each temperature step. Thermal stability measurements were repeated four times.

Results and discussion

Infrared spectroscopy

OBP14 engineered with a His-tag at its N-terminus was immobilized on the NTA-linker functionalized on the ZnSe crystal (see Fig. S1 in the Supporting Information). Because of the increased noise level in the amide I region due to the high absorption of the OH-bending band of water in this area, H/D exchange was performed to permit secondary structure determination. During exchange of the aqueous buffer with deuterated buffer solution (not shown), the amide II ($\sim 1,550$ cm⁻¹) band, primarily consisting of N–H bending modes, decreased and shifted to the amide II' band ($\sim 1,450$ cm⁻¹), which partly overlaps with the HOD vibration (1,450 cm⁻¹) (Walrafen 1972). Since the N–H bending vibration only marginally contributes to the amide I band, it only exhibits a smaller shift to lower wavenumbers upon H/D exchange (Wu et al. 2001; Barth 2007; Barth and Zscherp 2002). Figure 1 shows a FT-IR spectrum in the amide I' region of the immobilized OBP14 after H/D exchange. A curve fit with Gaussian line shapes was performed to estimate components of the secondary structure. The measured spectrum (black line) is in good agreement with the sum of fitted lines (dashed red line). The band at 1,648 cm⁻¹ was attributed to the α -helix,

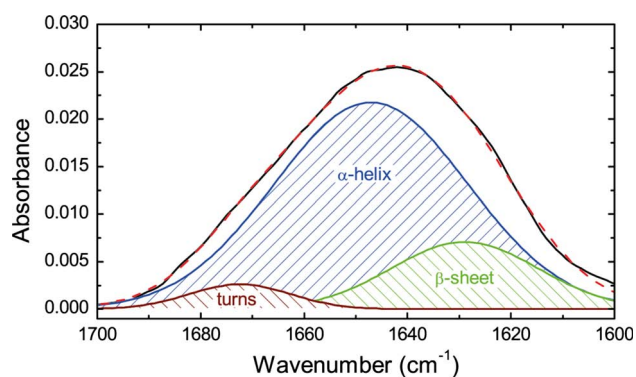


Fig. 1 FT-IR spectrum of immobilized OBP14 after H/D exchange with Gaussian curve fits. The sum of fits (*dashed red line*) is in good agreement with the measured spectrum (*black line*)

whose band position is slightly shifted to lower wavenumbers in D₂O buffer compared to aqueous buffer solution (Barth 2007; Arrondo et al. 1993; Pelton and McLean 2000). Bands at 1,628.9 and 1,672.4 cm⁻¹ were assigned to β -sheets and turns, respectively (Barth and Zscherp 2002). Evaluation of the band areas shows that the protein consists of 76.3 % α -helix, 18.9 % β -sheets and 4.8 % turns. This is in good agreement with X-ray diffraction studies that showed a high abundance of α -helix (Spinelli et al. 2012), in particular when considering that curve-fitting tends to overestimate β -sheets of overly α -helical proteins at the cost of α -helix (Oberger et al. 2004; Byler and Susi 1986). For measurements in complex with geraniol and eugenol, the odorants were incubated with the protein. IR absorbance spectra of OBP14 in the presence of ligands do not show significant differences in the amide I' region compared to the bare protein spectra (see Fig. S2 in the Supporting Information). This indicates that binding of the odorant does not considerably modify the secondary structure in the protein, as reported previously for odorant-binding proteins of other species (Scire et al. 2009; Paolini et al. 1999; Vincent et al. 2000; Zhou et al. 2009).

The effects of odorant binding on the thermal stability of honey bee OBP14 were determined by monitoring the amide I' band, in both the absence and presence of geraniol and eugenol during the heating process. Figure 2a shows changes of the amide I' band while increasing the temperature from 25 to 90 °C. With increasing temperature, the band shifts to higher frequencies. In spectroscopic methods, a band shift usually is the cumulative effect of the decrease of intensity at one vibration frequency combined with the increase of intensity at another vibration frequency. To study the structural changes during thermal denaturation in greater detail, difference spectra of OBP14 at various temperatures are shown in Fig. 2b. At lower temperatures up to 40 °C (blue lines), there are only minor changes in the spectra. Significant changes occur at

temperatures between 40 and 70 °C (black spectra) with an increase in absorbance between 1,670 and 1,680 cm⁻¹ and a decreasing band intensity around 1,625 cm⁻¹. At high temperatures between 75 and 90 °C, only small changes take place, and it seems that the structural changes upon thermal denaturation are completed. Similar behavior has been found for other α -helix-rich proteins, in particular serum albumin (Saguer et al. 2012). The negative band at \sim 1,630 cm⁻¹ is assigned to the loss of native β -sheet structure. Increasing bands in the high-frequency region can be attributed to evolving turns (\sim 1,670 cm⁻¹) and intermolecular β -sheets (\sim 1,680 cm⁻¹) due to heat induced aggregation (Saguer et al. 2012). The shift of the amide I' band to higher wavenumbers at high temperatures may also indicate an increase of disordered structures, which have been linked to thermal denaturation (Panick et al. 1999; Ngarize et al. 2004). In several reports, intermolecular β -sheets associated with thermal aggregation are also attributed to a band at \sim 1,620 cm⁻¹ (Tatulian 2013). As depicted in Fig. 2a, this band is weakly pronounced in the present spectra. This may be due to an overlap of the decreasing portion with the native β -sheet structures, resulting in an overall negative band in the difference spectra. A further explanation for the absent band at \sim 1,620 cm⁻¹ may be the high number of turns and lower extent of β -sheet structures. Turns and intermolecular β -sheets attributed to intermolecular aggregation are known to occur at high-temperature treatment for proteins with various native secondary structures (Bai and Dong 2009; Pedone et al. 2003).

For visualization of the transition temperature in FT-IR spectra, MW2D correlation maps have been employed. In these maps, the FT-IR spectrum is plotted versus the perturbation coordinate, i.e., temperature. This method is particularly useful for the identification of spectral changes along the perturbation axis (Noda 2010). The temperature ranges where the largest spectral changes occur are the regions where thermal denaturation takes place and are indicated by a peak in the correlation maps (Thomas and Richardson 2000). Figure 3 shows the MW2D correlation maps for the thermal denaturation measurements of OBP14 in the absence or presence of odorants, monitored by FT-IR spectroscopy. In Fig. 3a, a sharp peak appears at 55 °C indicating that denaturation has almost completed at this temperature. Due to the nature of autocorrelation, all peaks have a positive amplitude in the MW2D correlation maps. The shape of the contour line, however, makes it possible to recognize two distinct structural elements within this peak. The high-frequency peak is attributed to an increasing amount of disordered structures due to unfolding (Panick et al. 1999), and the spectral region of \sim 1,630 cm⁻¹ is attributed to a loss of native β -sheets, as discussed above. For OBP14 + geraniol, the peak for this

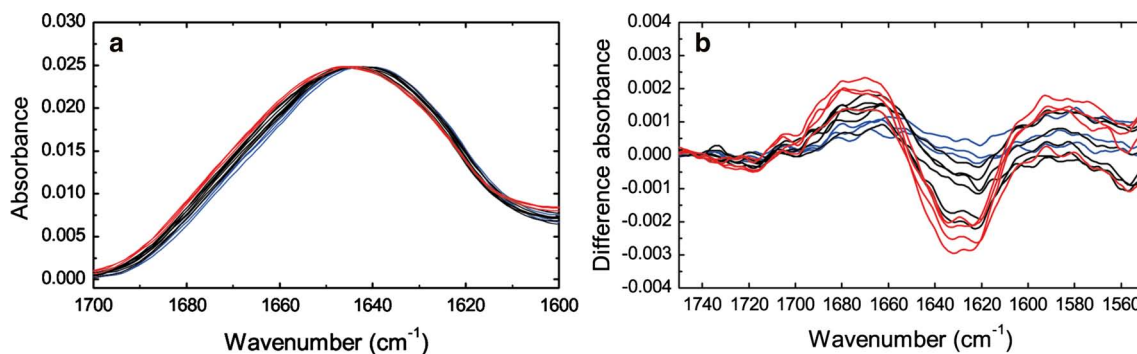


Fig. 2 **a** FT-IR spectra of OBPI4 in the absence of an odorant at temperatures from 25 to 90 °C in the amide I' region. Spectra in *blue* are taken at low temperatures (25–40 °C), *black* spectra denote intermediate temperatures (45–70 °C), and *red* spectra indicate high

temperatures (75–90 °C). The amide I' band shifts to higher frequencies with increasing temperature. **b** Difference spectra with the spectrum at 25 °C as a reference

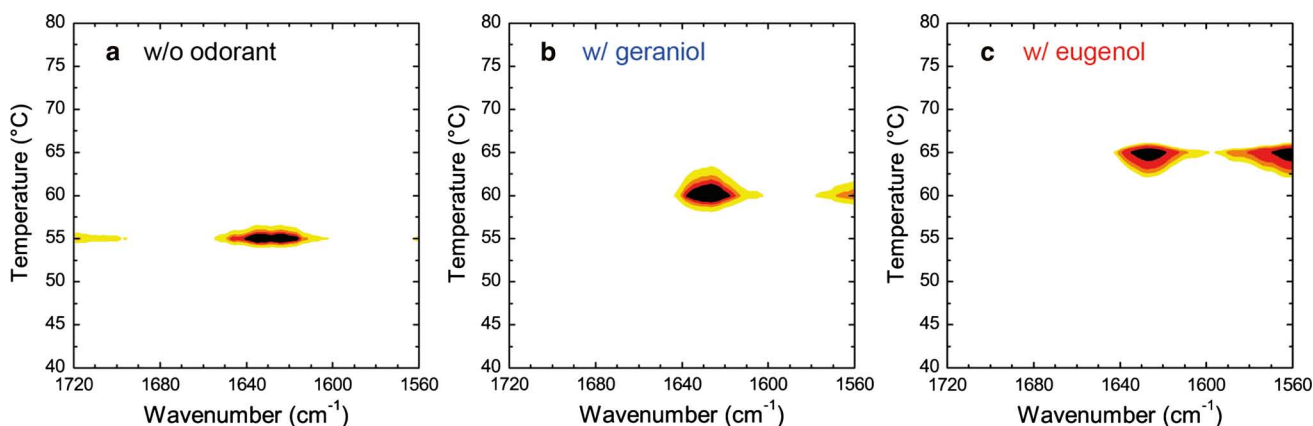


Fig. 3 MW2D correlation maps for OBPI4 alone (**a**), or incubated with geraniol (**b**) and with eugenol (**c**)

structural feature is located at 60 °C (Fig. 3b) and for OBPI4 + eugenol at a temperature of 65 °C (Fig. 3c). These results indicate that the presence of odorants increases the thermal stability of the protein and that strong ligands, such as eugenol, are more effective than weak ligands, such as geraniol.

Similar thermal stabilization effects of ligands have been reported for other proteins such as porcine (Paolini et al. 1999) and bovine (Marabotti et al. 2008a) OBPs, with an increase of denaturation temperature of up to 15 °C. The higher thermal stability is attributed to non-covalent forces such as hydrophobic and aromatic interactions as well as hydrogen bonds between OBPI4 and the odorant molecule. Furthermore, correlation maps of OBPI4 in the presence of odorants (Fig. 3b, c) display an additional peak at $\sim 1,550\text{ cm}^{-1}$, which is not present in the map of OBPI4 alone (Fig. 3a). Bands in this spectral region are assigned to H/D exchange. Their appearance at elevated temperatures indicates that H/D exchange has not been completed at room temperature or that prior buried structural features

were exposed upon odorant binding (Paolini et al. 1999). This is in agreement with previous findings, which showed that the binding site of OBPI4 undergoes geometry changes with small displacements of helices upon ligand binding that are subject of further H/D exchange (Spinelli et al. 2012). Particularly for eugenol, it was reported that strong hydrogen bonds are involved in protein-odorant interaction (Spinelli et al. 2012), explaining the higher intensity of this peak.

Circular dichroism

CD measurements of OBPI4 were employed in the presence and absence of odorants (Fig. S3 in the Supporting Information). The spectra display two negative peaks centered at 208 and 222 nm, which is a clear indication of high α -helical content (Yang et al. 2011; Briand et al. 2002; Kelly and Price 2000). Hence, assignment of the secondary structure of OBPI4 by CD is in agreement with X-ray diffraction and IR spectroscopy, as discussed above. As in

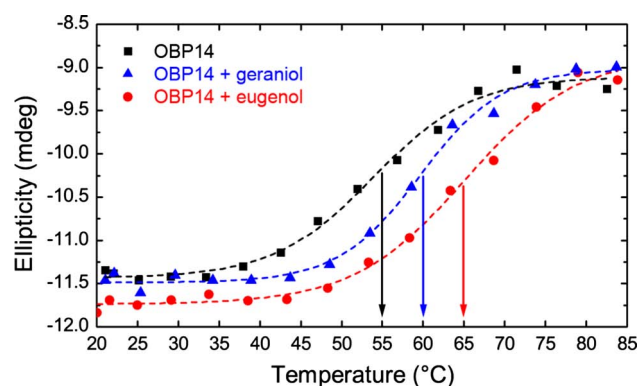


Fig. 4 Ellipticity at a wavelength of 222 nm of OBP14 in the absence and presence of odorants (data points). Dashed lines indicate a Boltzmann fit for sigmoidal line shapes

FT-IR measurements, there is no significant change of secondary structure in CD measurements at room temperature due to ligand binding.

Effects on thermal stability of OBP14 due to odorant binding were investigated by acquiring CD spectra while increasing the temperature between 20 and 85 °C in 5 °C steps (see Fig. S4 in the Supporting Information). Control measurements of the buffer and odorant solutions without protein are shown in Fig. S5 in the Supporting Information and do not reveal any changes with increasing temperatures. Thermal denaturation measurements were repeated four times and show excellent reproducibility. Denaturation transition curves and denaturation temperatures of repeated measurements are summarized in Fig. S6 and Table S1. Thermal denaturation of the protein was followed by evaluation of the CD signal at 222 nm, which is particularly sensitive to changes of the secondary structure (Staiano et al. 2007; Kelly et al. 2005). Figure 4 shows the ellipticity at 222 nm plotted versus temperature for OBP14 with and without odorants present. The data points were fitted with a Boltzmann function for sigmoidal line shapes (dashed line). The points of inflection, i.e., the temperature of maximum change for OBP14 alone, with geraniol and with eugenol are 55, 60 and 65 °C, respectively. These results agree very well with the data obtained by FT-IR spectroscopy, thus providing another tool to demonstrate that the thermal stability of OBP14, and likely other insect OBPs, is higher in the presence of ligands and depends on the strength of binding (Spinelli et al. 2012).

Conclusions

In conclusion, we have shown that the interaction of honey bee OBP14 with its ligands leads to an increase in the thermal stability of the protein. This finding was

corroborated by two independent analytical methods, FT-IR spectroscopy and circular dichroism. The absence of significant changes in the secondary structure upon ligand binding suggests that weaker forces such as hydrogen bonds and hydrophobic interactions are involved, as previously reported for OBP14 (Spinelli et al. 2012). Low- and high-affinity odorants can be discriminated by their effect on the denaturation temperature, which represents the different binding strengths and affinities for the tested odorants. Further, our measurements demonstrate the thermostability of OBP14 under ambient temperature up to 45 °C. This is of great interest with regard to possible usage of this protein in biosensor applications.

Acknowledgments Partial support for this work was provided by the European Science Foundation (ESF), the Austrian Science Fund (FWF) (I681-N24) and the Austrian Federal Ministry for Transport, Innovation and Technology (GZ BMVIT-612.166/0001-III/II/2010).

References

- Arrondo JLR, Muga A, Castresana J, Goñi FM (1993) Quantitative studies of the structure of proteins in solution by Fourier-transform infrared spectroscopy. *Prog Biophys Mol Biol* 59(1):23–56
- Arrondo JLR, Pacios M, Iloro I, Goni FM (2005) Protein stability studied by 2D-infrared spectroscopy. *Biophys J* 88(1):561a–562a
- Ashton L, Blanch EW (2010) pH-induced conformational transitions in alpha-lactalbumin investigated with two-dimensional Raman correlation variance plots and moving windows. *J Mol Struct* 974(1–3):132–138
- Bai S, Dong A (2009) Effects of immobilization onto aluminum hydroxide particles on the thermally induced conformational behavior of three model proteins. *Int J Biol Macromol* 45(1):80–85
- Ban L, Scaloni A, Brandazza A, Angeli S, Zhang L, Yan Y, Pelosi P (2003) Chemosensory proteins of *Locusta migratoria*. *Insect Mol Biol* 12(2):125–134
- Barth A (2007) Infrared spectroscopy of proteins. *Biochim Biophys Acta Bioenerg* 1767(9):1073–1101
- Barth A, Zscherp C (2002) What vibrations tell about proteins. *Q Rev Biophys* 35(04):369–430
- Bianchet MA, Bains G, Pelosi P, Pevsner J, Snyder SH, Monaco HL, Amzel LM (1996) The three-dimensional structure of bovine odorant binding protein and its mechanism of odor recognition. *Nat Struct Biol* 3(11):934–939
- Bissantz C, Kuhn B, Stahl M (2010) A medicinal chemist's guide to molecular interactions. *J Med Chem* 53(14):5061–5084
- Bohbot J, Vogt RG (2005) Antennal expressed genes of the yellow fever mosquito (*Aedes aegypti* L.); characterization of odorant-binding protein 10 and takeout. *Insect Biochem Mol Biol* 35(9):961–979
- Briand L, Swadipan N, Nespoulous C, Bézirard V, Blon F, Huet J-C, Ebert P, Pernollet J-C (2002) Characterization of a chemosensory protein (ASP3c) from honeybee (*Apis mellifera* L.) as a brood pheromone carrier. *Eur J Biochem* 269(18):4586–4596
- Byler DM, Susi H (1986) Examination of the secondary structure of proteins by deconvolved FTIR spectra. *Biopolymers* 25(3):469–487

- Calvello M, Guerra N, Brandazza A, D'Ambrosio C, Scaloni A, Dani FR, Turillazzi S, Pelosi P (2003) Soluble proteins of chemical communication in the social wasp *Polistes dominulus*. *Cell Mol Life Sci* 60(9):1933–1943
- Capone S, Pascali C, Francioso L, Siciliano P, Persaud KC, Pisanelli AM (2011) Odorant binding proteins as sensing layers for novel gas biosensors: an impedance spectroscopy characterization. In: Neri G, Donato N, d'Amico A, Di Natale C (eds) *Sensors and microsystems*, vol 91. Lecture notes in electrical engineering. Springer, Netherlands, pp 317–324
- Celej MS, Montich GG, Fidelio GD (2003) Protein stability induced by ligand binding correlates with changes in protein flexibility. *Protein Sci* 12(7):1496–1506
- Celej MS, Dassie SA, Freire E, Bianconi ML, Fidelio GD (2005) Ligand-induced thermostability in proteins: thermodynamic analysis of ANS-albumin interaction. *Biochim Biophys Acta* 1750(2):122–133
- Dani FR, Iovinella I, Felicioli A, Niccolini A, Calvello MA, Carucci MG, Qiao HL, Pieraccini G, Turillazzi S, Moneti G, Pelosi P (2010) Mapping the expression of soluble olfactory proteins in the honeybee. *J Proteome Res* 9(4):1822–1833
- Di Pietrantonio F, Cannata D, Benetti M, Verona E, Varriale A, Staiano M, D'Auria S (2013) Detection of odorant molecules via surface acoustic wave biosensor array based on odorant-binding proteins. *Biosens Bioelectron* 41:328–334
- Du HY, Zhou T, Zhang JH, Liu XY (2010) Moving-window two-dimensional correlation infrared spectroscopy study on structural variations of partially hydrolyzed poly(vinyl alcohol). *Anal Bioanal Chem* 397(7):3127–3132
- Fabian H, Mäntele W (2006) Infrared spectroscopy of proteins. In: *Handbook of vibrational spectroscopy*. Hoboken, New Jersey
- Foret S, Maleszka R (2006) Function and evolution of a gene family encoding odorant binding-like proteins in a social insect, the honey bee (*Apis mellifera*). *Genome Res* 16(11):1404–1413
- Glase PK, Long FA (1960) Use of glass electrodes to measure acidities in deuterium oxide. *J Phys Chem* 64(1):188–190
- Glatz R, Bailey-Hill K (2011) Mimicking nature's noses: from receptor deorphaning to olfactory biosensing. *Prog Neurobiol* 93(2):270–296
- Iovinella I, Dani FR, Niccolini A, Sagona S, Michelucci E, Gazzano A, Turillazzi S, Felicioli A, Pelosi P (2011) Differential expression of odorant-binding proteins in the mandibular glands of the honey bee according to caste and age. *J Proteome Res* 10(8):3439–3449
- Jin HJ, Lee SH, Kim TH, Park J, Song HS, Park TH, Hong S (2012) Nanovesicle-based bioelectronic nose platform mimicking human olfactory signal transduction. *Biosens Bioelectron* 35(1):335–341
- Kelly SM, Price NC (2000) The use of circular dichroism in the investigation of protein structure and function. *Curr Protein Pept Sci* 1(4):349–384
- Kelly SM, Jess TJ, Price NC (2005) How to study proteins by circular dichroism. *Biochim Biophys Acta Proteins Proteomics* 1751(2):119–139
- Kumar S, Tsai C-J, Nussinov R (2000) Factors enhancing protein thermostability. *Protein Eng* 13(3):179–191
- Leal WS, Nikonova L, Peng GH (1999) Disulfide structure of the pheromone binding protein from the silkworm moth, *Bombyx mori*. *FEBS Lett* 464(1–2):85–90
- Lee SH, Jin HJ, Song HS, Hong S, Park TH (2012a) Bioelectronic nose with high sensitivity and selectivity using chemically functionalized carbon nanotube combined with human olfactory receptor. *J Biotechnol* 157(4):467–472
- Lee SH, Kwon OS, Song HS, Park SJ, Sung JH, Jang J, Park TH (2012b) Mimicking the human smell sensing mechanism with an artificial nose platform. *Biomaterials* 33(6):1722–1729
- Marabotti A, Lefevre T, Staiano M, Crescenzo R, Varriale A, Rossi M, D'Auria S (2008a) Mutant bovine odorant-binding protein: Temperature affects the protein stability and dynamics as revealed by infrared spectroscopy and molecular dynamics simulations. *Proteins Struct Funct Genet* 72(2):769–778
- Marabotti A, Scire A, Staiano M, Crescenzo R, Aurilla V, Tanfani F, D'Auria S (2008b) Wild-type and mutant bovine odorant-binding proteins to probe the role of the quaternary structure organization in the protein thermal stability. *J Proteome Res* 7(12):5221–5229
- Misawa N, Mitsuno H, Kanzaki R, Takeuchi S (2010) Highly sensitive and selective odorant sensor using living cells expressing insect olfactory receptors. *Proc Natl Acad Sci* 107(35):15340–15344
- Moreau MJ, Morin I, Schaeffer PM (2010) Quantitative determination of protein stability and ligand binding using a green fluorescent protein reporter system. *Mol BioSyst* 6(7):1285–1292
- Ngarize S, Herman H, Adams A, Howell N (2004) Comparison of changes in the secondary structure of unheated, heated, and high-pressure-treated β -lactoglobulin and ovalbumin proteins using fourier transform raman spectroscopy and self-deconvolution. *J Agric Food Chem* 52(21):6470–6477
- Noda I (2010) Two-dimensional correlation spectroscopy—biannual survey 2007–2009. *J Mol Struct* 974(1–3):3–24
- Oberg KA, Ruyschaert JM, Goormaghtigh E (2004) The optimization of protein secondary structure determination with infrared and circular dichroism spectra. *Eur J Biochem* 271(14):2937–2948
- Panick G, Malessa R, Winter R (1999) Differences between the pressure- and temperature-induced denaturation and aggregation of β -lactoglobulin A, B, and AB monitored by FT-IR spectroscopy and small-angle X-ray scattering. *Biochemistry* 38(20):6512–6519
- Paolini S, Tanfani F, Fini C, Bertoli E, Paolo P (1999) Porcine odorant-binding protein: structural stability and ligand affinities measured by Fourier-transform infrared spectroscopy and fluorescence spectroscopy. *Biochim Biophys Acta, Protein Struct Mol Enzymol* 1431(1):179–188
- Park J, Lim JH, Jin HJ, Namgung S, Lee SH, Park TH, Hong S (2012a) A bioelectronic sensor based on canine olfactory nanovesicle-carbon nanotube hybrid structures for the fast assessment of food quality. *Analyst* 137(14):3249–3254
- Park SJ, Kwon OS, Lee SH, Song HS, Park TH, Jang J (2012b) Ultrasensitive flexible graphene based field-effect transistor (FET)-type bioelectronic nose. *Nano Lett* 12(10):5082–5090
- Pedone E, Bartolucci S, Rossi M, Pierfederici FM, Scire A, Cacciamani T, Tanfani F (2003) Structural and thermal stability analysis of *Escherichia coli* and *Alicyclobacillus acidocaldarius* thioredoxin revealed a molten globule-like state in thermal denaturation pathway of the proteins: an infrared spectroscopic study. *Biochem J* 373:875–883
- Pelosi P (1994) Odorant-binding proteins. *Crit Rev Biochem Mol* 29(3):199–228
- Pelosi P, Zhou JJ, Ban LP, Calvello M (2006) Soluble proteins in insect chemical communication. *Cell Mol Life Sci* 63(14):1658–1676
- Pelton JT, McLean LR (2000) Spectroscopic methods for analysis of protein secondary structure. *Anal Biochem* 277(2):167–176
- Persaud KC (2012) Biomimetic olfactory sensors. *IEEE Sens J* 12(11):3108–3112
- Saguer E, Alvarez P, Ismail AA (2012) Heat-induced denaturation/aggregation of porcine plasma and its fractions studied by FTIR spectroscopy. *Food Hydrocolloids* 27(1):208–219
- Sankaran S, Panigrahi S, Mallik S (2011) Odorant binding protein based biomimetic sensors for detection of alcohols associated with *Salmonella* contamination in packaged beef. *Biosens Bioelectron* 26(7):3103–3109

- Sankaran S, Khot LR, Panigrahi S (2012) Biology and applications of olfactory sensing system: a review. *Sens Actuator B-Chem* 171:1–17
- Scaloni A, Monti M, Angeli S, Pelosi P (1999) Structural analysis and disulfide-bridge pairing of two odorant-binding proteins from *Bombyx mori*. *Biochem Biophys Res Commun* 266(2):386–391
- Scire A, Marabotti A, Staiano M, Briand L, Varriale A, Bertoli E, Tanfani F, DAuria S (2009) Structure and stability of a rat odorant-binding protein: another brick in the wall. *J Proteome Res* 8(8):4005–4013
- Spinelli S, Lagarde A, Iovinella I, Legrand P, Tegoni M, Pelosi P, Cambillau C (2012) Crystal structure of *Apis mellifera* OBP14, a C-minus odorant-binding protein, and its complexes with odorant molecules. *Insect Biochem Mol Biol* 42(1):41–50
- Staiano M, D'Auria S, Varriale A, Rossi M, Marabotti A, Fini C, Stepanenko OV, Kuznetsova IM, Turoverov KK (2007) Stability and dynamics of the porcine odorant-binding protein. *Biochemistry* 46(39):11120–11127
- Stepanenko OV, Marabotti A, Kuznetsova IM, Turoverov KK, Fini C, Varriale A, Staiano M, Rossi M, D'Auria S (2008) Hydrophobic interactions and ionic networks play an important role in thermal stability and denaturation mechanism of the porcine odorant-binding protein. *Proteins Struct Funct Genet* 71(1):35–44
- Tatulian S (2013) Structural characterization of membrane proteins and peptides by FTIR and ATR-FTIR spectroscopy. In: Kleinschmidt JH (ed) *Lipid-protein interactions. Methods in molecular biology*, vol 974. Humana Press, USA, pp 177–218
- Tegoni M, Ramoni R, Bignetti E, Spinelli S, Cambillau C (1996) Domain swapping creates a third putative combining site in bovine odorant binding protein dimer. *Nat Struct Biol* 3(10):863–867
- Tegoni M, Pelosi P, Vincent F, Spinelli S, Campanacci V, Grolli S, Ramoni R, Cambillau C (2000) Mammalian odorant binding proteins. *Biochim Biophys Acta-Protein Struct Molec Enzymol* 1482(1–2):229–240
- Thomas M, Richardson HH (2000) Two-dimensional FT-IR correlation analysis of the phase transitions in a liquid crystal, 4'-n-octyl-4-cyanobiphenyl (8CB). *Vib Spectrosc* 24(1):137–146
- Vincent F, Spinelli S, Ramoni R, Grolli S, Pelosi P, Cambillau C, Tegoni M (2000) Complexes of porcine odorant binding protein with odorant molecules belonging to different chemical classes. *J Mol Biol* 300(1):127–139
- Walrafen GE (1972) Raman and infrared spectral investigations of water structure. In: Franks F (ed) *Water a comprehensive treatise*, vol 1. Plenum Press, New York, pp 151–214
- Williams DH, Stephens E, O'Brien DP, Zhou M (2004) Understanding noncovalent interactions: ligand binding energy and catalytic efficiency from ligand-induced reductions in motion within receptors and enzymes. *Angew Chem Int Ed* 43(48):6596–6616
- Wu Y, Murayama K, Ozaki Y (2001) Two-dimensional infrared spectroscopy and principle component analysis studies of the secondary structure and kinetics of hydrogen-deuterium exchange of human serum albumin. *J Phys Chem B* 105(26):6251–6259
- Yang G, Winberg G, Ren H, Zhang SG (2011) Expression, purification and functional analysis of an odorant binding protein AaegOBP22 from *Aedes aegypti*. *Protein Expres Purif* 75(2):165–171
- Zhang HM, Ishikawa Y, Yamamoto Y, Carpentier R (1998) Secondary structure and thermal stability of the extrinsic 23 kDa protein of photosystem II studied by Fourier transform infrared spectroscopy. *FEBS Lett* 426(3):347–351
- Zhou J-J, Robertson G, He X, Dufour S, Hooper AM, Pickett JA, Keep NH, Field LM (2009) Characterisation of *bombyx mori* odorant-binding proteins reveals that a general odorant-binding protein discriminates between sex pheromone components. *J Mol Biol* 389(3):529–545

Supplementary Data

Honey bee odorant-binding protein 14: effects on thermal stability upon odorant binding revealed by FT-IR spectroscopy and CD measurements

Andreas Schwaighofer[†], Caroline Kotlowski[‡], Can Araman[§], Nam Chu[§], Rosa Mastrogiamoco^{||}, Christian Becker[§], Paolo Pelosi,^{||} Wolfgang Knoll[†], Melanie Larisika[†], and Christoph Nowak^{†,‡,}*

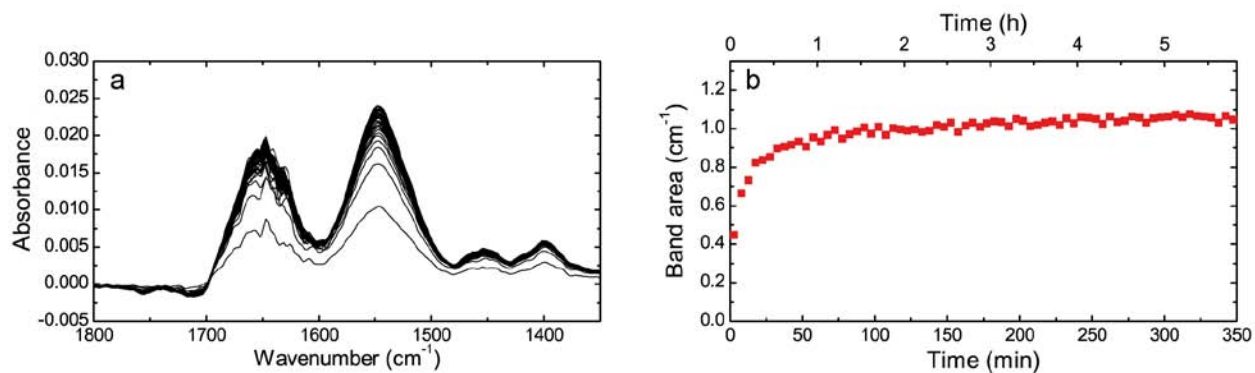
[†]Austrian Institute of Technology GmbH, AIT, Donau-City Str. 1, 1220 Vienna, Austria

[‡]Center of Electrochemical Surface Technology, CEST, Viktor-Kaplan-Straße 2, 2700 Wiener Neustadt, Austria

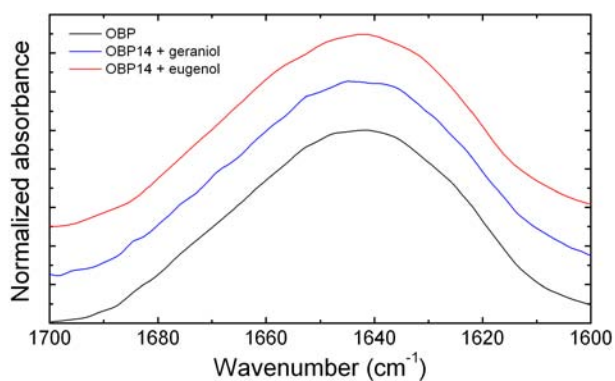
[§]Institut für Biologische Chemie, Universität Wien, Währinger Straße 38, 1090 Wien, Austria

^{||}Department of Biology of Agriculture, Food and Environment, University of Pisa, Via del Borghetto 80, 56124 Pisa, Italy

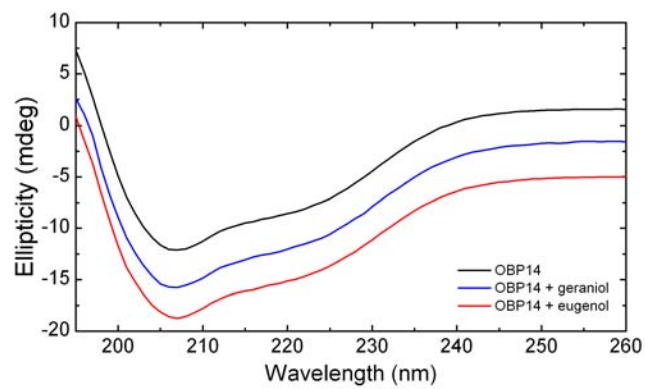
*Author to whom correspondence should be addressed: Christoph Nowak, c.nowak@ait.ac.at



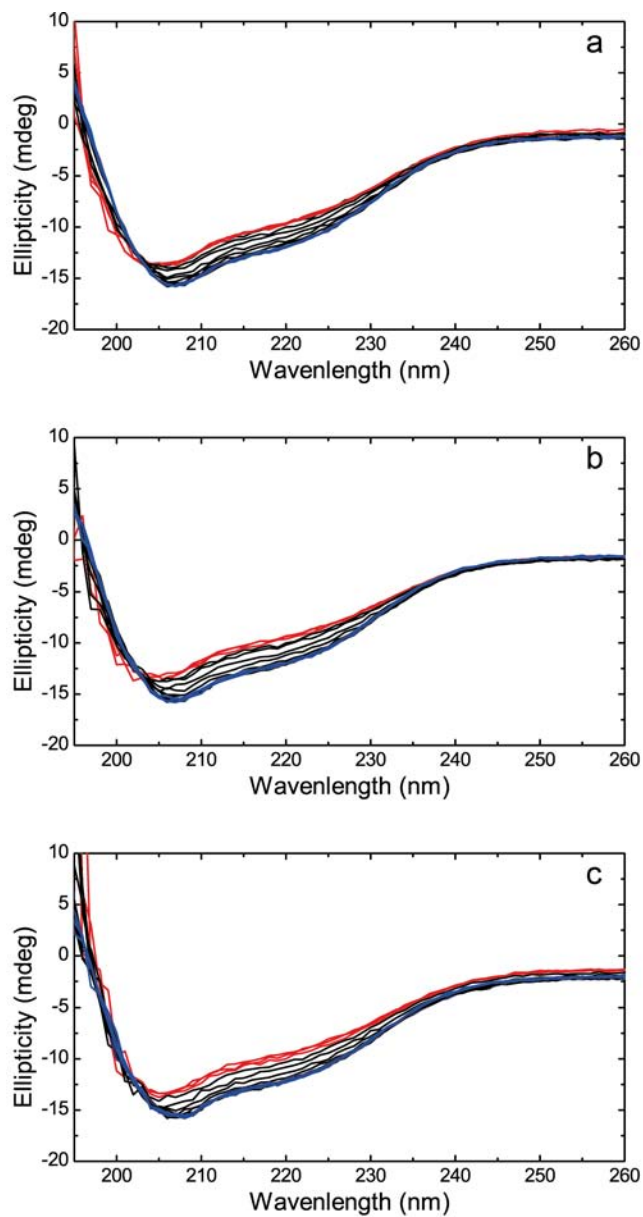
Supplementary Fig. 1 a FT-IR difference spectra of OBP14 in the amide I and II region recorded as a function of time. Spectra are taken every 5 mins. The reference spectrum of the DTNTA-modified ZnSe ATR crystal was taken before adsorption of the protein. The high noise in the amide I region is attributed to the high absorption of the OH-bending band of water. **b** Area of the amide II band plotted versus adsorption time



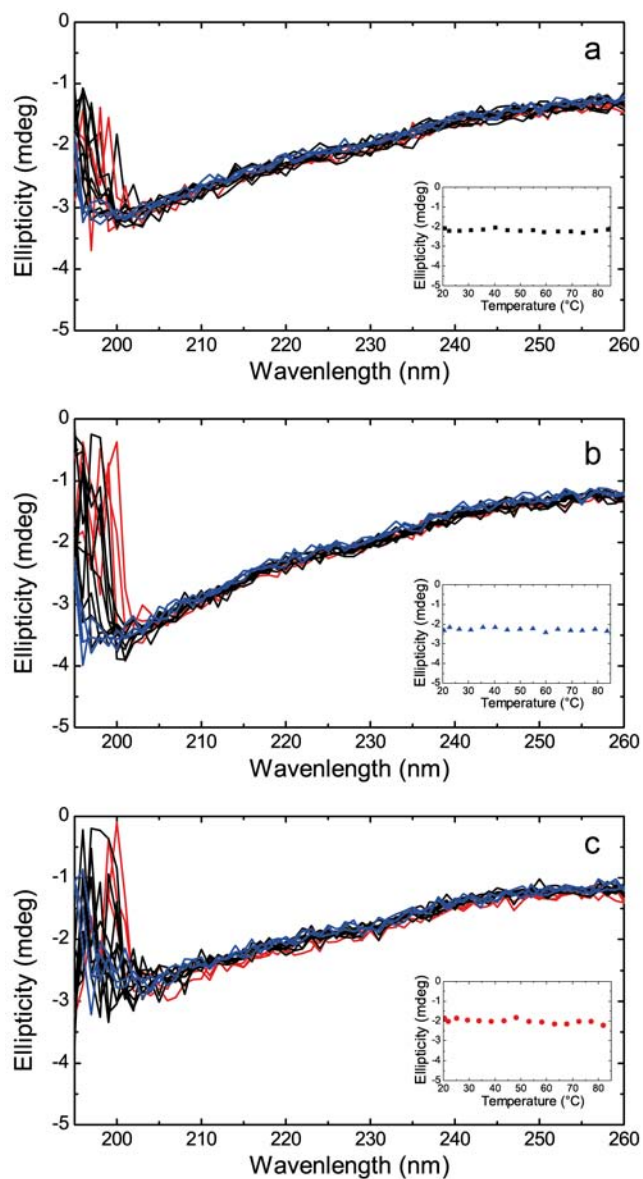
Supplementary Fig. 2 FT-IR spectra in the amide I' region of OBP14 (black), OBP14 incubated with geraniol (blue) and OBP14 incubated with eugenol (red) taken at 25 °C



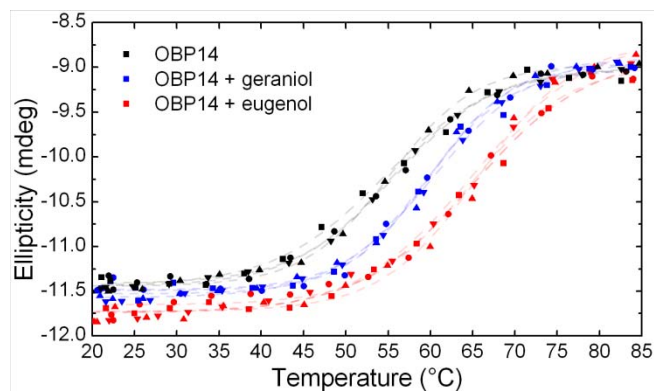
Supplementary Fig. 3 CD spectra obtained at 25 °C of OBP14 (black), OBP14 incubated with geraniol (blue) and OBP14 incubated with eugenol (red)



Supplementary Fig. 4: Circular dichroism measurements of **a** OBP14, **b** OBP14 + geraniol, **c** OBP14 + eugenol at temperatures between 20-85 °C. Spectra in blue are taken at low temperatures and red lines indicate spectra recorded at high temperatures



Supplementary Fig. 5 Circular dichroism measurements of **a** phosphate buffer, **b** 200 μM geraniol in phosphate buffer, **c** 200 μM eugenol in phosphate buffer at temperatures between 20-85 °C. Spectra in blue are taken at low temperatures and red lines indicate spectra recorded at high temperatures. Insets show changes of the ellipticity at 222 nm with increasing temperature



Supplementary Fig. 6 Ellipticity at a wavelength of 222 nm of repeated CD measurements of OBP14 in the absence and presence of odorants (data points). Dashed lines indicate a Boltzmann fit for sigmoidal lineshapes

Supplementary Table 1: Transition temperatures of repeated thermal denaturation measurements. Listed values are the inflection points of the Boltzmann fit for sigmoidal lineshapes applied to the ellipticity at 222 nm plotted versus temperature (see Supplementary Figure 6).

	OBP14	OBP14 + geraniol	OBP14 + eugenol
#1	54.5	59.6	65.1
#2	55.9	59.8	64.7
#3	55.2	60.1	65.7
#4	55.4	60.4	65.0
Average	55.3	60.0	65.1
Standard deviation	0.6	0.3	0.4



Insights into structural features determining odorant affinities to honey bee odorant binding protein 14



Andreas Schwaighofer^a, Maria Pechlaner^b, Chris Oostenbrink^b, Caroline Kotlowski^c, Can Araman^d, Rosa Mastrogiacomio^e, Paolo Pelosi^e, Wolfgang Knoll^a, Christoph Nowak^{a,c,*}, Melanie Larisika^{a,*}

^a Austrian Institute of Technology GmbH, AIT, Donau-City Str. 1, 1220 Vienna, Austria

^b Institute of Molecular Modeling and Simulation, University of Natural Resources and Life Sciences, Muthgasse 18, 1190 Vienna, Austria

^c Center of Electrochemical Surface Technology, CEST, Viktor-Kaplan-Straße 2, 2700 Wiener Neustadt, Austria

^d Institut für Biologische Chemie, Universität Wien, Währinger Straße 38, 1090 Wien, Austria

^e Department of Agriculture, Food and Environment, University of Pisa, Via del Borghetto 80, 56124 Pisa, Italy

ARTICLE INFO

Article history:

Received 5 March 2014

Available online 21 March 2014

Keywords:

Odorant binding protein

Circular dichroism

Thermal stability

Ligand binding

Molecular dynamics

ABSTRACT

Molecular interactions between odorants and odorant binding proteins (OBPs) are of major importance for understanding the principles of selectivity of OBPs towards the wide range of semiochemicals. It is largely unknown on a structural basis, how an OBP binds and discriminates between odorant molecules. Here we examine this aspect in greater detail by comparing the C-minus OBP14 of the honey bee (*Apis mellifera* L.) to a mutant form of the protein that comprises the third disulfide bond lacking in C-minus OBPs. Affinities of structurally analogous odorants featuring an aromatic phenol group with different side chains were assessed based on changes of the thermal stability of the protein upon odorant binding monitored by circular dichroism spectroscopy. Our results indicate a tendency that odorants show higher affinity to the wild-type OBP suggesting that the introduced rigidity in the mutant protein has a negative effect on odorant binding. Furthermore, we show that OBP14 stability is very sensitive to the position and type of functional groups in the odorant.

© 2014 Elsevier Inc. All rights reserved.

1. Introduction

Odorant binding proteins (OBPs) attracted increasing attention in recent years due to their potential application as biosensing elements for the fabrication of odorant sensors based on the olfactory system [1–4]. Applications are diverse and include disease diagnostics [5], food safety [6], and environmental monitoring [7]. These biomimetic sensor platforms potentially provide higher sensitivity combined with lower detection limits and faster response time compared to odorant sensors based on metal oxides and conducting polymers [8–10].

OBPs are abundant small proteins (~13–16 kDa) found in the olfactory epithelium of vertebrates and the sensillar lymph of insects [11]. The functional role of OBPs in olfaction is not fully resolved yet. However, high concentrations (10 mM) of OBPs in olfactory dendrites and the relatively high number of OBPs in the genome indicate important contributions [12,13]. A meanwhile

widely accepted hypothesis describes OBPs as a carrier for hydrophobic odorant molecules through the sensillar lymph to the membrane which holds the odorant receptor cells [12,14].

The focus of this work is OBP14 of the honey bee (*Apis mellifera* L.). Investigation of the olfactory system in honey bees is of particular interest due to the high complexity of the chemical language used by these social insects to communicate among the members of the bee hive [15]. The genome of the honey bee comprises 21 OBPs [16], 13 of which are classified as classic OBPs (OBP1–13) and seven as C-minus OBPs with four Cys residues (OBP15–21). OBP14, also a member of the C-minus class, is unique, featuring five cysteines. It has been identified in different tissues of adult bees, as well as in larvae [17]. OBP14 exhibits 119 amino acid residues with a molecular weight of 13.5 kDa [18]. Typical for insect OBPs, its three dimensional structure predominantly consists of α -helical domains arranged in a very compact and stable structure, as depicted in Fig. 1A. Featuring five cysteines, OBP14 exhibits two disulfide bonds between residues 17(α 1)–49(α 3) and 88(α 5)–106(α 6) as well as an unpaired cysteine at position 47(α 3) [18]. For investigation of the functional implications arising from structural differences between classic and C-minus OBPs, a double mutant Q44C-H97C of OBP14 was employed in this study, which

* Corresponding authors. Address: Austrian Institute of Technology (AIT), Muthgasse 11, 1190 Vienna, Austria. Fax: +43 505504450.

E-mail addresses: c.nowak@ait.ac.at (C. Nowak), Melanie.Larisika@ait.ac.at (M. Larisika).

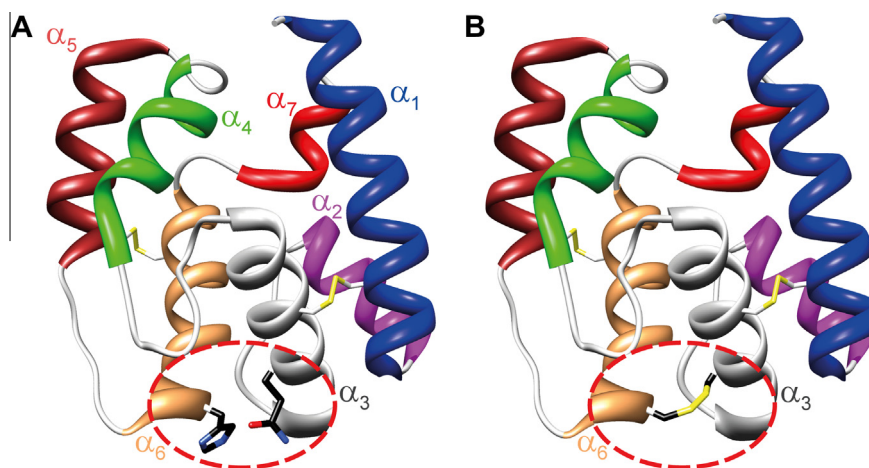


Fig. 1. Three dimensional model of (A) wild-type OBP14 and (B) mutant OBP14 featuring an additional disulfide bond between α_3 and α_6 . OBP14 natively possesses two disulfide bonds between α_1 – α_3 and α_5 – α_6 , respectively, thus being classified as a C-minus OBP.

comprises the third disulfide bond present in classical OBPs (see Fig. 1B) [18].

Ligand-binding characteristics and affinities of a wide range of odorants to OBPs of various species have been the subject of intensive research [19–21]. Typically, fluorescence binding studies are employed to indirectly determine the affinity of an odorant relative to a fluorescence reporter molecule [17,18,22,23]. Most recently, our lab presented a method of estimating odorant affinities to OBPs by monitoring the changes of thermal stability of the protein upon odorant binding by circular dichroism (CD) spectroscopy. This approach has been successfully applied to OBP14 and has been validated by infrared (IR) spectroscopy [24]. By evaluation of the different transition temperatures of geraniol and eugenol, it was possible to distinguish between the affinities of the two ligands. CD is a convenient method for studying the structure of proteins in solution and is particularly applicable to monitor dynamic changes in the secondary structure triggered by an external perturbation such as a temperature increase [25].

Increased protein stability upon ligand binding has been observed for a wide variety of biological systems [26–28]. Weak non-covalent forces such as hydrogen bonds as well as electrostatic, hydrophobic and aromatic interactions have been recognized to play a significant role in increasing the structural stability of the protein–ligand complexes [29–31].

In this work, we systematically analyze and evaluate structural parameters that influence an odorant's affinity to OBP14. So far, this has only been accomplished for odorant receptors [32,33]. However, with the growing interest in OBPs and their crucial role in olfaction, structural properties of their binding cavity are the consequential target of future investigations. To address this question, we employed CD spectroscopy to compare the effect of ligand binding on the thermal stability of wild-type and mutant OBP14 and correlate the increase of stability with odorant affinity. The tested odorants include eugenol and its structural analogues, which belong to the family of phenyl propanoids, a group of compounds known for their role as semiochemicals for many insects [34]. Comparison of the wild-type and a mutant form of OBP14 reveals the impact of protein flexibility on the OBP's ability to adapt its binding cavity to fit different odorants with varying functional groups.

2. Materials and methods

2.1. Materials

Eugenol (4-prop-2-enyl-2-methoxyphenol, 99%), methyl eugenol (4-allyl-1,2-dimethoxybenzene, 98%), 4-vinylguaiaacol

(2-methoxy-4-vinylphenol, 98%), homovanillic acid (2-(4-hydroxy-3-methoxy-phenyl)acetic acid, 98%), coniferyl aldehyde (3-(4-hydroxy-3-methoxyphenyl)prop-2-enal, 98%), coniferyl alcohol (4-(3-hydroxy-1-propenyl)-2-methoxyphenol, 98%), isoeugenol (2-methoxy-4-(prop-1-en-1-yl)phenol, 98%), dihydroeugenol (2-methoxy-4-propylphenol, 99%), 3,4-dimethoxystyrene (techn.) were provided by Sigma–Aldrich (Steinheim, Germany).

2.2. Expression and purification of OBP14

Expression of recombinant proteins was done as described in Spinelli et al. [18]. Bacterial expression was performed along with established protocols [17,35] and purification was accomplished using conventional chromatographic techniques [36,37]. The purity of the protein was checked by SDS–PAGE.

2.3. Circular dichroism

Far UV (260–195 nm) CD measurements were carried out using an Applied Photophysics Chirascan plus spectrophotometer (Leatherhead, Surrey, United Kingdom) equipped with a temperature control unit (Quantum TC125) in a 1 mm quartz cell at 1 nm resolution. Protein solutions (0.5 mg/mL; 41.8 μ M) were prepared in phosphate buffer (140 mM NaCl, 3 mM KCl, 10 mM Na₂HPO₄, 2 mM KH₂PO₄, pH 8). For static measurements, ten spectra with the acquisition time of 0.5 s were taken at room temperature and the results were averaged. For measurement of OBP14 in the presence of odorants, the protein was incubated in solution with 200 μ M odorant for 1 h. For temperature-controlled experiments, two acquisition techniques were employed. In spectra-kinetic mode, spectra were taken in the range of 20–90 °C ($\Delta T = 5$ °C) with an acquisition time of 0.2 s after an equilibration time of 45 s at each temperature step. In the kinetic mode, the ellipticity was recorded at a fixed wavelength of 222 nm with an acquisition time of 0.5 s.

2.4. MD simulations

MD simulations were performed using the GROMOS11 package for biomolecular simulations [38] and the GROMOS force field 54A8 [39] starting from the native and mutant OBP14 crystal structures (PDB ID: 3S0A and 3S0G) [18]. Three 50-ns simulations each were performed at 300, 340, 360, 370, and 400 K. Detailed simulation settings are provided in the [Supporting Information](#).

3. Results and discussion

3.1. Thermal stability of wild-type and mutant OBP14

Circular dichroism measurements of wild-type and mutant OBP14 at room temperature are shown in Fig. S1. The negative peak at 208 nm and the negative shoulder at 222 nm are a clear indication for the high α -helical content of the proteins [40,41]. This secondary structure assignment is in agreement with X-ray diffraction and IR-spectroscopy [24].

Effects of the additional disulfide bond introduced to the protein on thermal stability of OBP14 were investigated by acquiring CD spectra while increasing the temperature between 20 and 90 °C in 5 °C steps. Thermal denaturation of the proteins was followed by evaluation of the CD signal at 222 nm, which has been reported to be particularly sensitive to changes of the secondary structure [25,42]. Fig. S2 shows the ellipticity at 222 nm plotted versus temperature. The data points were fitted with a Boltzmann function for sigmoidal line shapes. The points of inflection, i.e., the temperature of maximum change for wild-type and mutant OBP14 are 56.6 and 64.9 °C, respectively. The transition temperature of wild-type OBP14 agrees well with the one reported for OBP14 (55.3 °C) in a previous study [24]. As expected, the transition temperature is higher for mutant OBP14 due to the introduced third disulfide bond that confers additional constraints in flexibility to the structure, thus preventing thermal denaturation [43]. MD simulations confirm a higher stability of the mutant as observed by the secondary structure content and atom-positional root-mean-square deviations from the X-ray structures (Fig. S3). Stabilization of proteins by disulfide bonds has been attributed to a decrease of conformational entropy [44]. Disulfide bonds form a covalent link between secondary structure elements and consequently increase protein thermostability by preventing the formation of incorrectly folded structures [45]. Consequently, an increase of thermal stability has been observed for many biological systems [46–48], most notably it was found that removal of a native disulfide bond in porcine OBP results in a decrease of the transition temperature of more than 30 °C [49].

3.2. Effect of functional group variation on odorant affinity

Odorant binding does not affect the structure of OBPs to a degree that can be monitored with instrumental techniques that detect alterations in the overall secondary structure, such as IR or CD spectroscopy [24,50,51]. Thus, changes in thermal stability of the protein upon odorant binding were assessed to estimate odorant affinities.

Effects on thermal stability of wild-type and mutant OBP14 due to odorant binding were studied by acquiring CD spectra while increasing the temperature between 20 and 90 °C in 5 °C steps (exemplary spectra shown in Figs. S4 and S5). Control measurements of the buffer and odorant solutions without protein do not show any changes with increasing temperatures (Fig. S6). Thermal denaturation of the protein was evaluated by plotting the CD signal at 222 nm versus temperature. Fig. 2 shows the transition curves of the (A) wild-type and (B) mutant OBP14 in absence and presence of the investigated odorants. By applying a Boltzmann fit for sigmoidal line shapes, the points of inflection were determined (temperatures indicated by arrows). The results are collected in Table S1. In Fig. 3, the change in transition temperature of the protein–ligand complex is shown relative to the transition temperature of the proteins in absence of odorants.

Consistent with earlier studies, the extent of temperature increase due to ligand binding is correlated with the affinity of the examined odorants [24,51].

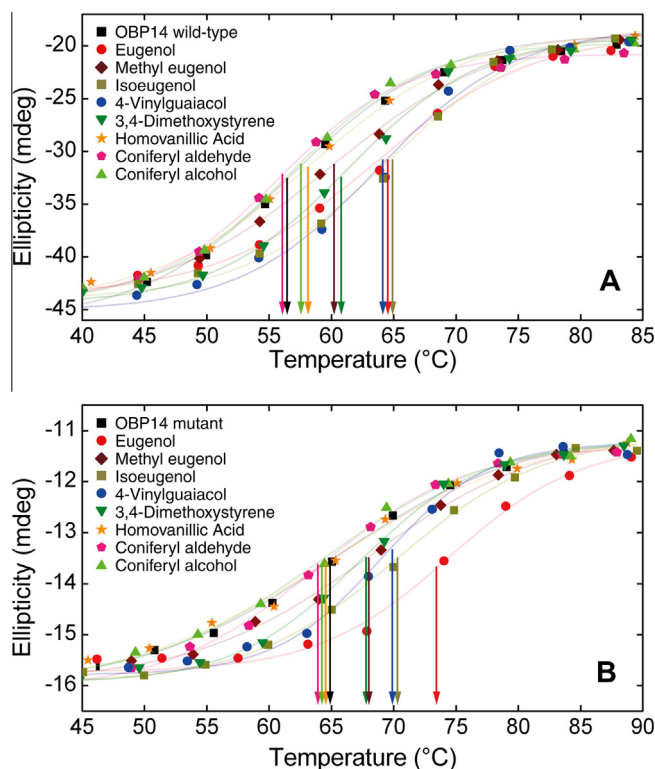


Fig. 2. Ellipticity at a wavelength of 222 nm of (A) wild-type and (B) mutant OBP14 in the absence and presence of odorants (data points). Lines indicate a Boltzmann fit for sigmoidal line shapes.

In this study, odorants with a phenolic ring structure were systematically investigated, with a methoxy group as the R_3 substituent and variations at the R_1 and R_4 substituents on the benzene ring. Changes of the transition temperature due to ligand binding as represented in Fig. 3 allow identifying trends of odorant affinity associated with the different side groups that will be discussed in the following part. For the wild-type protein, eugenol (1), isoeugenol (3) and 4-vinylguaiaicol (4) exhibit the highest observed affinities as measured by the increasing thermal stability due to odorant binding. The high affinity of this odorant to wild-type OBP14 has been confirmed with a graphene-based FET sensor [4] in our lab as well as with fluorescence binding studies [17,18]. Out of the odorants listed above, eugenol shows a comparable affinity to mutant OBP14. Common structural features of these odorants are the hydroxyl group as R_4 and a hydrophobic chain as R_1 . Strong hydrogen bonds between the hydroxyl group and adjacent amino acid residues in a particularly favorable tetrahedral geometry have been identified to play an important role in this strong binding [18].

Compared to odorants 1 and 4, in methyl eugenol (2) and 3,4-dimethoxystyrene (5) the hydroxyl group is exchanged with a methoxy group, while exhibiting the same functional group as R_1 . Thus, the influence of the hydroxyl group on the affinity is directly experimentally observable. In the presence of the methoxy group, affinities to the wild-type protein decrease drastically with an additional decline for mutant OBP14. These results confirm the importance of the hydroxyl group to the protein–ligand interaction, as explained above.

For further investigations, the functionalities of the R_1 group were varied. Compounds 4 and 5 have a vinyl side chain, whereas odorants 1 and 2 exhibit an allyl side group. Particularly intriguing is the case of isoeugenol (3), which is a structural isomer of eugenol with the double bond in R_1 shifted from the second to the first carbon of the side chain. This means, the two molecules have the same

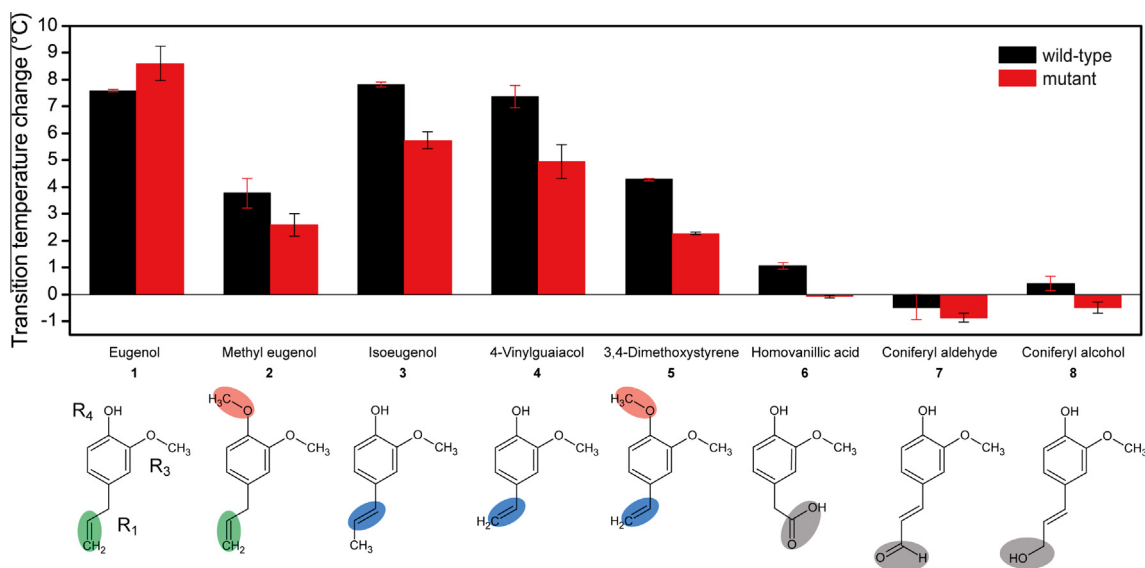


Fig. 3. Change in transition temperatures of the protein-odorant complexes of wild-type (black) and mutant (red) OBP14 relative to the transition temperature of the proteins in absence of odorants. Error bars indicate the standard deviation. Substituent R_3 contains a methoxy group for all odorants. At R_4 , there is either a hydroxyl group or a methoxy group, whereas the R_1 position varies between hydrophobic and hydrophilic side groups. (For interpretation of the references to colour in this figure legend, the reader is referred to the web version of this article.)

size, but the location of the double bond is different. As shown in Fig. 3, for wild-type OBP the transition temperatures of odorants 3 and 4 featuring a vinylic side chain is comparable with eugenol, which is otherwise structurally analogous. For the mutant protein however, the transition temperatures of these odorants are significantly decreased. A possible explanation for the lower odorant affinity of mutant OBP14 is the constricted flexibility introduced by the additional disulfide bond. Whereas the more flexible wild-type protein can adjust the shape of its binding cavity to form hydrophobic interactions with the vinylic double bond, this adaptation is not possible for the mutant due to conformational restrictions. It has been reported that the binding cavity of OBP14 changes its size up to 20% upon odorant binding [18], and that a certain degree of conformational flexibility is required for OBPs to properly interact with odorants [52]. The equivalently low change in transition temperatures of odorants 2 and 5 for both wild-type and mutant OBP14 may be explained by the dominating influence of the methoxy group as discussed above.

In homovanillic acid (6), coniferyl aldehyde (7) and coniferyl alcohol (8), the position 1 of the benzene ring possesses polar and charged groups in contrast to odorants 1–5 that feature hydrophobic side chains at this position. Evidently, a hydrophilic group is unfavourable at this site for both wild-type and mutant OBP14, because the affinities are significantly lower for these odorants (Fig. 3). This finding is experimental proof for the hypothesis stated in an earlier study that these polar groups have a negative effect on the interaction with the hydrophobic binding pocket of OBP14, despite the evidently similar structures of the involved odorants [17].

In summary, we have systematically investigated the affinities of phenolic odorants with varying side chains to wild-type and mutant OBP14 of the honey bee. CD measurements at elevated temperatures of the proteins in absence of odorants revealed a higher thermal stability of the mutant exhibiting an additional disulfide bond not present in the wild-type C-minus OBP14. This finding was corroborated by molecular dynamics simulations. Relative affinities of odorants have been estimated due to the extent of increased thermal stability of the protein-odorant complex. Our results indicate that eugenol exhibits the highest affinity to both, wild-type and mutant OBP14. Replacing the hydroxyl group

with a methoxy group at position 4 of the benzene ring causes a decreased affinity to both forms of OBP14, whereas exchange of the allylic group with a vinylic side chain at the R_1 substituent leads to an exclusive decline of affinities to mutant OBP14. Differences in odorant affinity between the wild-type and mutant are attributed to lower flexibility of the mutant due to the additional disulfide bond. Odorants featuring a polar or charged group at the R_1 position show very low affinities to both types of OBP14.

In our lab, studies of odorant affinities to wild-type OBP14 utilizing a graphene-based FET sensor confirmed the high affinity of eugenol [4]. However, in that investigation also odorants with a polar side chain show medium to high affinity. In the future, we intend to employ molecular dynamics simulations to explain this variance and to further explore the molecular basis of odorant affinities to OBPs.

Acknowledgments

Partial support for this work was provided by the European Science Foundation (ESF), the Austrian Science Fund (FWF) (I681-N24) and the Austrian Federal Ministry for Transport, Innovation and Technology (GZ BMVIT-612.166/0001-III/11/2010).

Appendix A. Supplementary data

Supplementary data associated with this article can be found, in the online version, at <http://dx.doi.org/10.1016/j.bbrc.2014.03.054>.

References

- [1] K.C. Persaud, Biomimetic olfactory sensors, *IEEE Sens. J.* 12 (2012) 3108–3112.
- [2] H.C. Lau, Y.K. Lee, J.Y. Kwon, Y.S. Sohn, J.O. Lim, LUSH-based SPR sensor for the detection of alcohols and pheromone, in: S.W. Kang, S.H. Park, L.P. Lee, K.B. Song, Y.H. Choi (Eds.), *Nano-Bio Sensing, Imaging, and Spectroscopy*, Spie-Int Soc Optical Engineering, Bellingham, 2013.
- [3] Y. Lu, H. Li, S. Zhuang, D. Zhang, Q. Zhang, J. Zhou, S. Dong, Q. Liu, P. Wang, Olfactory biosensor using odorant-binding proteins from honeybee: ligands of floral odors and pheromones detection by electrochemical impedance, *Sens. Actuators, B* 193 (2014) 420–427.
- [4] M. Larisika, C. Kotlowski, C. Steininger, R. Mastrogiacomo, P. Pelosi, C. Kleber, W. Knoll, C. Nowak, Olfactory biosensor based on odorant binding protein 14

- from honeybee: kinetic analysis of protein–ligand interaction, *Biosens. Bioelectron.* (2014) (submitted for publication).
- [5] S. Sankaran, S. Panigrahi, S. Mallik, Odorant binding protein based biomimetic sensors for detection of alcohols associated with Salmonella contamination in packaged beef, *Biosens. Bioelectron.* 26 (2011) 3103–3109.
 - [6] F. Di Pietrantonio, D. Cannata, M. Benetti, E. Verona, A. Varriale, M. Staiano, S. D'Auria, Detection of odorant molecules via surface acoustic wave biosensor array based on odorant-binding proteins, *Biosens. Bioelectron.* 41 (2013) 328–334.
 - [7] S. Capone, C. Pascali, L. Francioso, P. Siciliano, K.C. Persaud, A.M. Pisanelli, Odorant binding proteins as sensing layers for novel gas biosensors: an impedance spectroscopy characterization, in: G. Neri, N. Donato, A. d'Amico, C. Di Natale (Eds.), *Sensors and Microsystems*, Springer, Netherlands, 2011, pp. 317–324.
 - [8] S. Sankaran, L.R. Khot, S. Panigrahi, Biology and applications of olfactory sensing system: a review, *Sens. Actuators, B* 171 (2012) 1–17.
 - [9] S.H. Lee, H.J. Jin, H.S. Song, S. Hong, T.H. Park, Bioelectronic nose with high sensitivity and selectivity using chemically functionalized carbon nanotube combined with human olfactory receptor, *J. Biotechnol.* 157 (2012) 467–472.
 - [10] H.J. Jin, S.H. Lee, T.H. Kim, J. Park, H.S. Song, T.H. Park, S. Hong, Nanovesicle-based bioelectronic nose platform mimicking human olfactory signal transduction, *Biosens. Bioelectron.* 35 (2012) 335–341.
 - [11] P. Pelosi, Odorant-binding proteins, *Crit. Rev. Biochem. Mol.* 29 (1994) 199–228.
 - [12] J.J. Zhou, Odorant-binding proteins in insects, in: G. Litwack (Ed.), *Vitamins and Hormones: Pheromones*, Elsevier Academic Press Inc., San Diego, 2010, pp. 241–272.
 - [13] R.G. Vogt, R. Rybczynski, M.R. Lerner, Molecular-cloning and sequencing of general odorant binding-proteins Gobp1 and Gobp2 from the tobacco hawk moth *manduca sexta* – comparisons with other insect Obps and their signal peptides, *J. Neurosci.* 11 (1991) 2972–2984.
 - [14] W.S. Leal, Odorant reception in insects: roles of receptors, binding proteins, and degrading enzymes, *Annu. Rev. Entomol.* 58 (2013) 373–391.
 - [15] H.G.S. Consortium, Insights into social insects from the genome of the honeybee *Apis mellifera*, *Nature* 443 (2006) 931–949.
 - [16] S. Foret, R. Maleszka, Function and evolution of a gene family encoding odorant binding-like proteins in a social insect, the honey bee (*Apis mellifera*), *Genome Res.* 16 (2006) 1404–1413.
 - [17] I. Iovinella, F.R. Dani, A. Niccolini, S. Sagona, E. Michelucci, A. Gazzano, S. Turillazzi, A. Felicioli, P. Pelosi, Differential expression of odorant-binding proteins in the mandibular glands of the honey bee according to caste and age, *J. Proteome Res.* 10 (2011) 3439–3449.
 - [18] S. Spinelli, A. Lagarde, I. Iovinella, P. Legrand, M. Tegoni, P. Pelosi, C. Cambillau, Crystal structure of *Apis mellifera* OBP14, a C-minus odorant-binding protein, and its complexes with odorant molecules, *Insect Biochem. Mol. Biol.* 42 (2012) 41–50.
 - [19] L.P. Ban, L. Zhang, Y.H. Yan, P. Pelosi, Binding properties of a locust's chemosensory protein, *Biochem. Biophys. Res. Commun.* 293 (2002) 50–54.
 - [20] M. Wogulis, T. Morgan, Y. Ishida, W.S. Leal, D.K. Wilson, The crystal structure of an odorant binding protein from *Anopheles gambiae*: evidence for a common ligand release mechanism, *Biochem. Biophys. Res. Commun.* 339 (2006) 157–164.
 - [21] F.F. Damberger, E. Michel, Y. Ishida, W.S. Leal, K. Wüthrich, Pheromone discrimination by a pH-tuned polymorphism of the *Bombyx mori* pheromone-binding protein, *Proc. Natl. Acad. Sci. U S A* 110 (46) (2013) 18680–18685.
 - [22] F. Yu, S. Zhang, L. Zhang, P. Pelosi, Intriguing similarities between two novel odorant-binding proteins of locusts, *Biochem. Biophys. Res. Commun.* 385 (2009) 369–374.
 - [23] L. Ban, E. Napolitano, A. Serra, X. Zhou, I. Iovinella, P. Pelosi, Identification of pheromone-like compounds in male reproductive organs of the oriental locust *Locusta migratoria*, *Biochem. Biophys. Res. Commun.* 437 (2013) 620–624.
 - [24] A. Schwaighofer, C. Kotlowski, C. Araman, N. Chu, R. Mastrogiacomo, C. Becker, P. Pelosi, W. Knoll, M. Larisika, C. Nowak, Honey bee odorant-binding protein 14: effects on thermal stability upon odorant binding revealed by FT-IR spectroscopy and CD measurements, *Eur. Biophys. J.* 43 (2–3) (2014) 105–112.
 - [25] S.M. Kelly, T.J. Jess, N.C. Price, How to study proteins by circular dichroism, *Biochim. Biophys. Acta, Proteins Proteomics* 1751 (2005) 119–139.
 - [26] M.S. Celej, S.A. Dassie, E. Freire, M.L. Bianconi, G.D. Fidelio, Ligand-induced thermostability in proteins: thermodynamic analysis of ANS–albumin interaction, *Biochim. Biophys. Acta* 1750 (2005) 122–133.
 - [27] M.J. Moreau, I. Morin, P.M. Schaeffer, Quantitative determination of protein stability and ligand binding using a green fluorescent protein reporter system, *Mol. Biosyst.* 6 (2010) 1285–1292.
 - [28] M.S. Celej, G.G. Montich, G.D. Fidelio, Protein stability induced by ligand binding correlates with changes in protein flexibility, *Protein Sci.* 12 (2003) 1496–1506.
 - [29] D.H. Williams, E. Stephens, D.P. O'Brien, M. Zhou, Understanding noncovalent interactions: ligand binding energy and catalytic efficiency from ligand-induced reductions in motion within receptors and enzymes, *Angew. Chem. Int. Ed.* 43 (2004) 6596–6616.
 - [30] O.V. Stepanenko, A. Marabotti, I.M. Kuznetsova, K.K. Turoverov, C. Fini, A. Varriale, M. Staiano, M. Rossi, S. D'Auria, Hydrophobic interactions and ionic networks play an important role in thermal stability and denaturation mechanism of the porcine odorant-binding protein, *Proteins Struct. Funct. Genet.* 71 (2008) 35–44.
 - [31] S. Kumar, C.-J. Tsai, R. Nussinov, Factors enhancing protein thermostability, *Protein Eng.* 13 (2000) 179–191.
 - [32] S. Katada, T. Hirokawa, Y. Oka, M. Suwa, K. Touhara, Structural basis for a broad but selective ligand spectrum of a mouse olfactory receptor: mapping the odorant-binding site, *J. Neurosci.* 25 (2005) 1806–1815.
 - [33] O. Baud, S. Etter, M. Spreafico, L. Bordoli, T. Schwede, H. Vogel, H. Pick, The mouse eugenol odorant receptor: structural and functional plasticity of a broadly tuned odorant binding pocket, *Biochemistry* 50 (2011) 843–853.
 - [34] K.H. Tan, R. Nishida, Methyl eugenol: its occurrence, distribution, and role in nature, especially in relation to insect behavior and pollination, *J. Insect Sci.* 12 (2012) 1–60.
 - [35] F.R. Dani, I. Iovinella, A. Felicioli, A. Niccolini, M.A. Calvello, M.G. Carucci, H.L. Qiao, G. Pieraccini, S. Turillazzi, G. Moneti, P. Pelosi, Mapping the expression of soluble olfactory proteins in the honeybee, *J. Proteome Res.* 9 (2010) 1822–1833.
 - [36] L. Ban, A. Scaloni, A. Brandazza, S. Angeli, L. Zhang, Y. Yan, P. Pelosi, Chemosensory proteins of *Locusta migratoria*, *Insect Mol. Biol.* 12 (2003) 125–134.
 - [37] M. Calvello, N. Guerra, A. Brandazza, C. D'Ambrosio, A. Scaloni, F.R. Dani, S. Turillazzi, P. Pelosi, Soluble proteins of chemical communication in the social wasp *Polistes dominulus*, *Cell. Mol. Life Sci.* 60 (2003) 1933–1943.
 - [38] N. Schmid, C.D. Christ, M. Christen, A.P. Eichenberger, W.F. van Gunsteren, Architecture, implementation and parallelisation of the GROMOS software for biomolecular simulation, *Comput. Phys. Commun.* 183 (2012) 890–903.
 - [39] M.M. Reif, P.H. Hunenberger, C. Oostenbrink, New interaction parameters for charged amino acid side chains in the GROMOS force field, *J. Chem. Theory Comput.* 8 (2012) 3705–3723.
 - [40] L. Briand, N. Swasdipan, C. Nespoulous, V. Bézirard, F. Blon, J.-C. Huet, P. Ebert, J.-C. Pernollet, Characterization of a chemosensory protein (ASP3c) from honeybee (*Apis mellifera* L.) as a brood pheromone carrier, *Eur. J. Biochem.* 269 (2002) 4586–4596.
 - [41] S.M. Kelly, N.C. Price, The use of circular dichroism in the investigation of protein structure and function, *Curr. Protein Pept. Sci.* 1 (2000) 349–384.
 - [42] M. Staiano, S. D'Auria, A. Varriale, M. Rossi, A. Marabotti, C. Fini, O.V. Stepanenko, I.M. Kuznetsova, K.K. Turoverov, Stability and dynamics of the porcine odorant-binding protein, *Biochemistry* 46 (2007) 11120–11127.
 - [43] P. Pelosi, R. Mastrogiacomo, I. Iovinella, E. Tuccori, K.C. Persaud, Structure and biotechnological applications of odorant-binding proteins, *Appl. Microbiol. Biotechnol.* 98 (2014) 61–70.
 - [44] C.N. Pace, G.R. Grimsley, J.A. Thomson, B.J. Barnett, Conformational stability and activity of ribonuclease-T1 with Zero, One, and 2 intact disulfide bonds, *J. Biol. Chem.* 263 (1988) 11820–11825.
 - [45] Y. Li, P.M. Coutinho, C. Ford, Effect on thermostability and catalytic activity of introducing disulfide bonds into *Aspergillus awamori* glucoamylase, *Protein Eng.* 11 (1998) 661–667.
 - [46] M. Ramazzotti, C. Parrini, M. Stefani, G. Manao, D. Degl'Innocenti, The intrachain disulfide bridge is responsible of the unusual stability properties of novel acylphosphatase from *Escherichia coli*, *FEBS Lett.* 580 (2006) 6763–6768.
 - [47] D. Fass, Disulfide bonding in protein biophysics, *Annu. Rev. Biophys.* 41 (2012) 63–79.
 - [48] M. Luckey, R. Ling, A. Dose, B. Malloy, Role of a disulfide bond in the thermal stability of the LamB protein trimer in *Escherichia coli* outer membrane, *J. Biol. Chem.* 266 (1991) 1866–1871.
 - [49] M. Parisi, A. Mazzini, R. Tibor Sorbi, R. Ramoni, S. Grolli, R. Favilla, Role of the disulfide bridge in folding, stability and function of porcine odorant binding protein: spectroscopic equilibrium studies on C63A/C155A double mutant, *Biochim. Biophys. Acta, Proteins Proteomics* 1750 (2005) 30–39.
 - [50] A. Scire, A. Marabotti, M. Staiano, L. Briand, A. Varriale, E. Bertoli, F. Tanfani, S. D'Auria, Structure and stability of a rat odorant-binding protein: another brick in the wall, *J. Proteome Res.* 8 (2009) 4005–4013.
 - [51] S. Paolini, F. Tanfani, C. Fini, E. Bertoli, P. Paolo, Porcine odorant-binding protein: structural stability and ligand affinities measured by Fourier-transform infrared spectroscopy and fluorescence spectroscopy, *Biochim. Biophys. Acta, Protein Struct. Mol. Enzymol.* 1431 (1999) 179–188.
 - [52] B.P. Ziemba, E.J. Murphy, H.T. Edlin, D.N.M. Jones, A novel mechanism of ligand binding and release in the odorant binding protein 20 from the malaria mosquito *Anopheles gambiae*, *Protein Sci.* 22 (2013) 11–21.

Supplementary Data

Insights into structural features determining odorant affinities to honey bee odorant-binding protein 14

Andreas Schwaighofer^a, Maria Pechlaner^b, Chris Oostenbrink^b, Caroline Kotlowski^c, Can Araman^d, Rosa Mastrogiacomo^e, Paolo Pelosi^e, Wolfgang Knoll^a, Christoph Nowak^{a,c,*} and Melanie Larisika^{a,*}

^aAustrian Institute of Technology GmbH, AIT, Donau-City Str. 1, 1220 Vienna, Austria

^bInstitute of Molecular Modeling and Simulation, University of Natural Resources and Life Sciences, Muthgasse 18, 1190 Vienna, Austria

^cCenter of Electrochemical Surface Technology, CEST, Viktor-Kaplan-Straße 2, 2700 Wiener Neustadt, Austria

^dInstitut für Biologische Chemie, Universität Wien, Währinger Straße 38, 1090 Wien, Austria

^eDepartment of Agriculture, Food and Environment, University of Pisa, Via del Borghetto 80, 56124 Pisa, Italy

Corresponding Author

* Dr. Melanie Larisika and Dr. Christoph Nowak

Address

Austrian Institute of Technology (AIT)
Muthgasse 11, 1190
Vienna, Austria
E-mail: c.nowak@ait.ac.at ; Melanie.Larisika@ait.ac.at
T: +43 505504430, F: +43 505504450

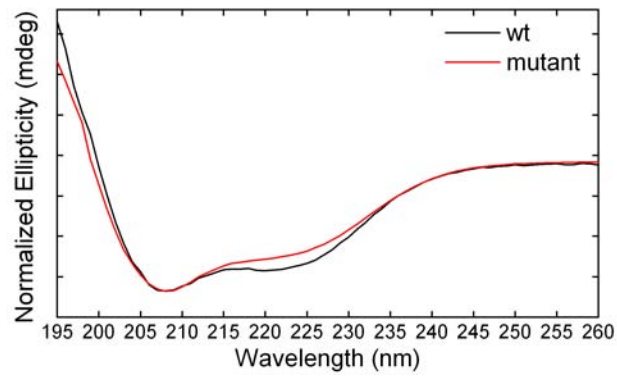


Fig. S1. CD spectra obtained at 25 °C of wild-type OBP14 (black) and mutant OBP14 (red).

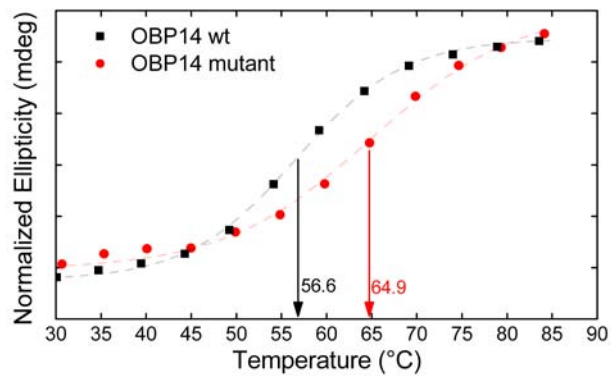


Fig. S2. Ellipticity at a wavelength of 222 nm of CD measurements of wild-type OBP14 (black) and mutant OBP14 (red). Dashed lines indicate a Boltzmann fit for sigmoidal lineshapes.

Settings of MD simulations

MD simulations were performed with GROMOS11 [1] using the GROMOS forcefield 54A8 [2]. The crystal structures of *Apis mellifera* OBP14 (PDB ID: 3S0A) and its mutant (PDB ID: 3S0G) [3], respectively, were energy minimized using the steepest-descent algorithm and placed in a rectangular periodic box with 4671 (wild-type) and 4581 (mutant) simple point charge waters (SPC) [4], respectively. 3 Na⁺ ions were added to achieve an overall neutral box.

Maxwellian random initial velocities were generated at 50 K, then the system was gradually heated up to 300 K during 100 ps, while decreasing positional restraints on solute atoms (initial force constant of $2.5 \times 10^4 \text{ kJ mol}^{-1} \text{ nm}^{-2}$). Subsequently, roto-translational restraints on the solute were introduced to keep its longest axis aligned with the longest edge of the box and the system was equilibrated for another 320 ps. This was followed by 50 ns of free simulation at 300, 340, 360, 370 and 400 K using a leap-frog algorithm with a 2 fs-timestep. Temperature and pressure (1 atm) were maintained using the weak coupling scheme (with coupling times $\tau_T = 0.1 \text{ ps}$ and $\tau_P = 0.5 \text{ ps}$ and an estimated isothermal compressibility of $4.575 \times 10^{-4} \text{ (kJ mol}^{-1} \text{ nm}^{-3})^{-1}$ [5]. Bond lengths were constrained to their ideal values through the SHAKE algorithm [6]. Long-range electrostatic interactions beyond a cutoff of 1.4 nm were truncated and approximated via a generalized reaction field approach (with dielectric permittivity of 61).

Each simulation was repeated three times, each starting with a different set of initial velocities.

Trajectory configurations were written out every 2 ps and analysed using the GROMOS++ package [7]. Secondary structure elements were classified according to the DSSP rules [8]. Atomic positional root-mean-square deviations (RMSDs) of backbone heavy atoms (C α , N, C) were determined with respect to the energy minimized initial structures after superposition of centres of mass and a rotational least-squares superposition [9]. Results are depicted as block averages (extrapolated to infinite block lengths) over 5 or 10 ns of simulation time, averaged over the three simulations.

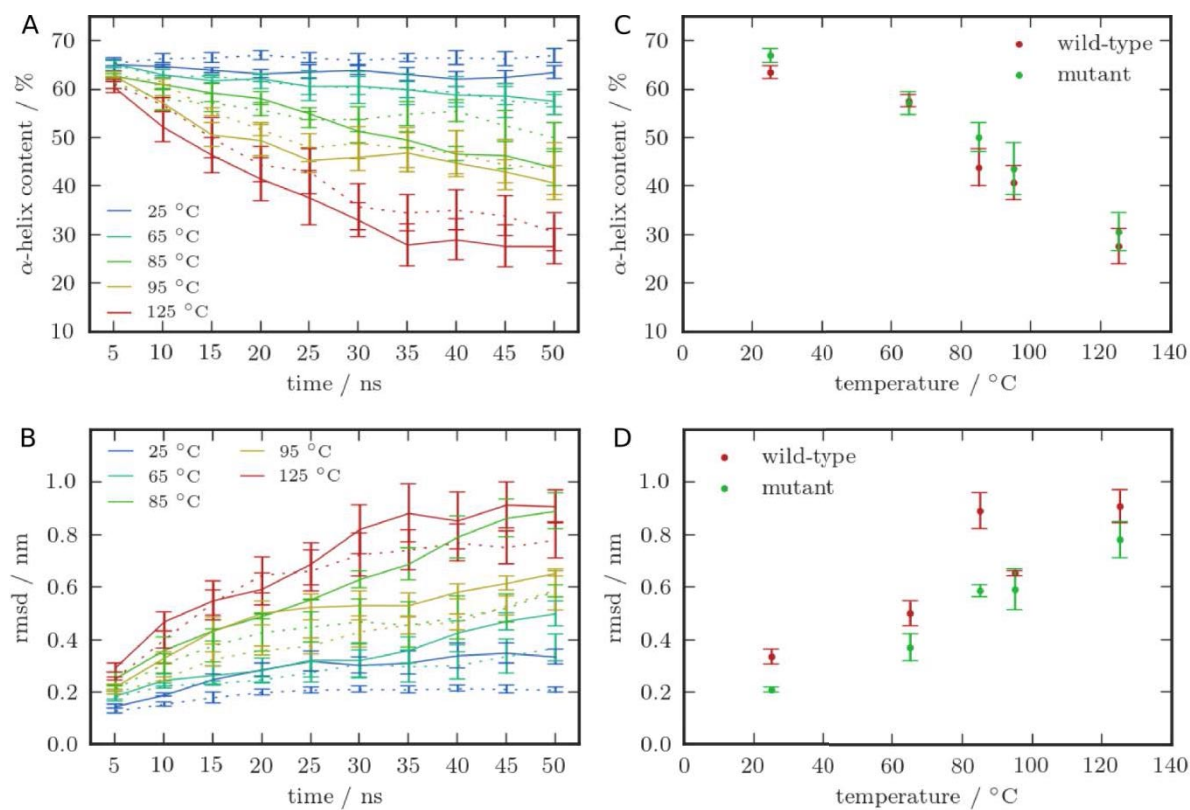


Fig. S3. (A) α -helical content and (B) root-mean-square deviations of backbone heavy atoms (B) of the OBP14 wild-type (straight lines) and its mutant (dashed lines) in the course of MD simulations at different temperatures. Averages over three independent simulations are plotted, averaged over 5 ns periods. (C) α -helical content and (D) root-mean-square deviations during the last 5 ns of the simulations plotted against temperature.

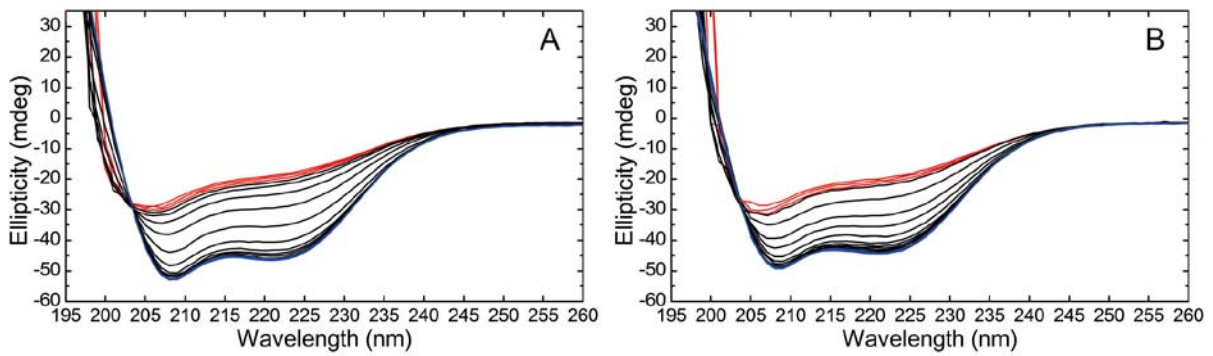


Fig. S4. Circular dichroism measurements of (A) wild-type OBP14 and (B) wild-type OBP14 + eugenol at temperatures between 20-90 °C. Spectra in blue are taken at low temperatures and red lines indicate spectra recorded at high temperatures.

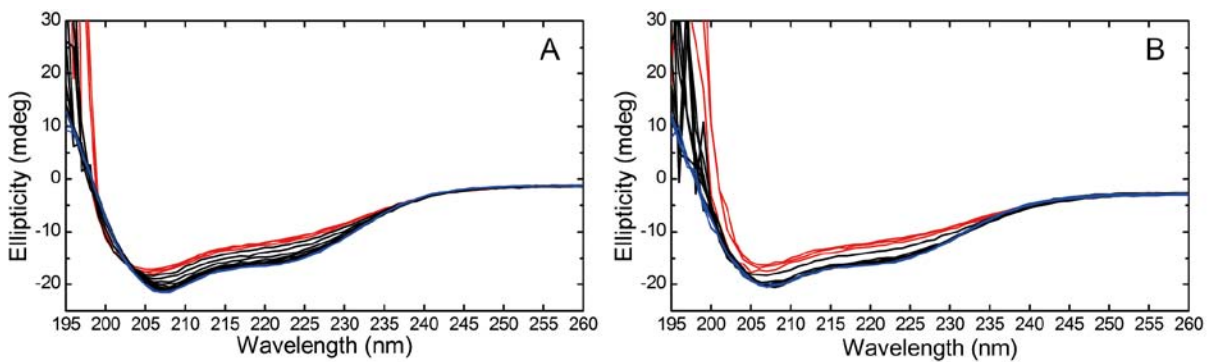


Fig. S5. Circular dichroism measurements of (A) mutant OBP14 and (B) mutant OBP14 + eugenol at temperatures between 20-90 °C. Spectra in blue are taken at low temperatures and red lines indicate spectra recorded at high temperatures.

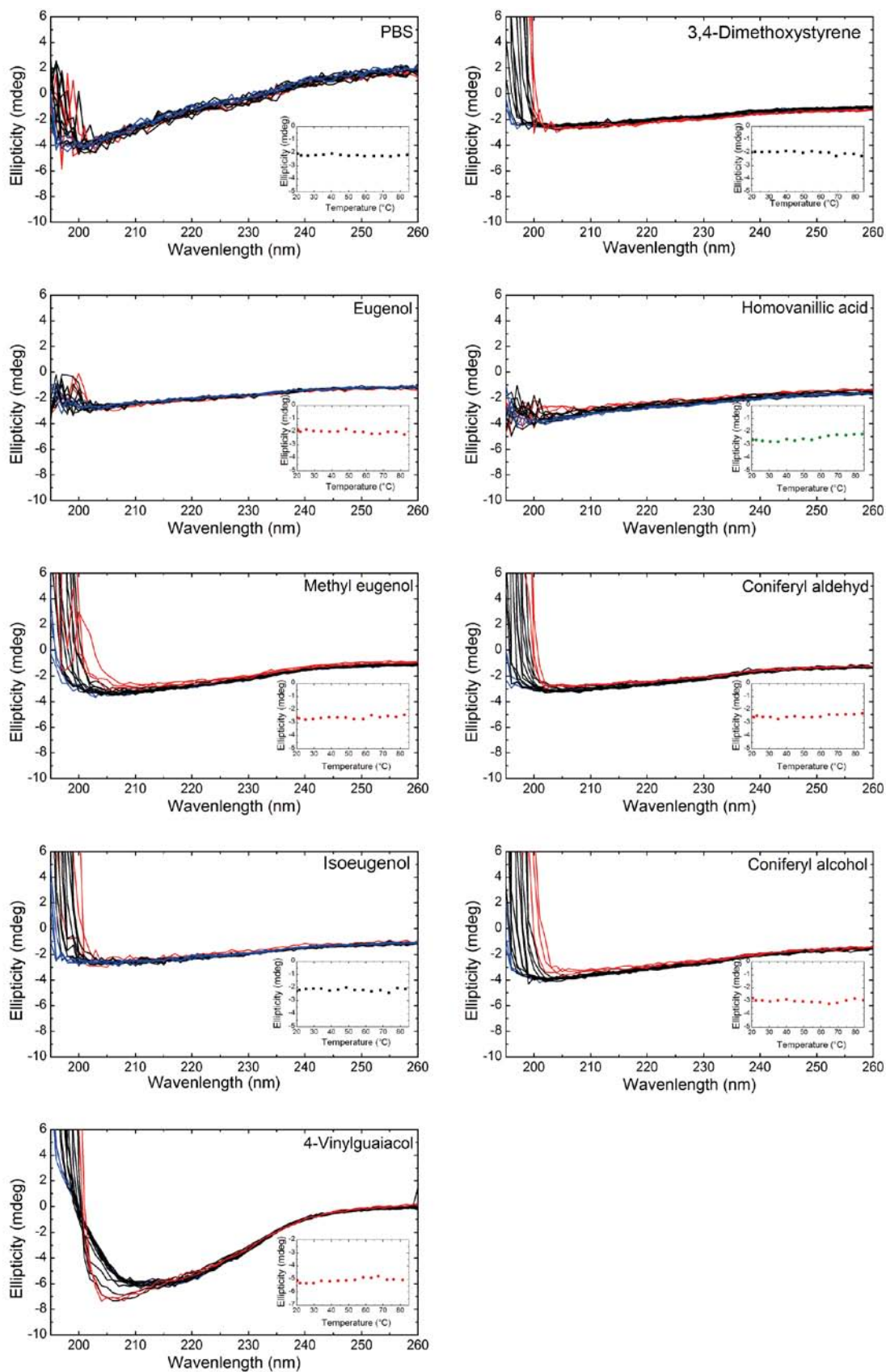


Fig. S6. Circular dichroism measurements of the pure PBS as well as solutions of 200 μM odorant in PBS at temperatures between 20-90°C. Spectra in blue are taken at low temperatures and red lines indicate spectra recorded at high temperatures. Insets show changes of the ellipticity at 222 nm with increasing temperature.

Table S1: Transition temperatures of wild-type and mutant OBP14 acquired by a Boltzmann fit for sigmoidal lineshapes applied to the results of repeated CD measurements.

	Wild-type			Mutant		
	Analysis #1 (°C)	Analysis #2 (°C)	Average(°C)	Analysis #1(°C)	Analysis #2(°C)	Average(°C)
OBP	56.59	57.18	56.89	64.94	64.97	64.95
Eugenol	64.40	64.55	64.48	74.45	72.64	73.55
Methyl eugenol	59.89	61.46	60.67	68.11	66.96	67.54
Isoeugenol	64.58	64.84	64.71	70.25	71.13	70.69
4-Vinylguaiacol	63.68	64.85	64.27	69.03	70.80	69.91
3,4-Dimethoxystyrene	61.24	61.12	61.18	67.16	67.27	67.22
Homovanillic acid	58.12	57.80	57.96	64.82	64.93	64.87
Coniferyl aldehyde	55.77	57.07	56.42	63.87	64.32	64.09
Coniferyl alcohol	56.76	57.49	57.12	64.17	64.75	64.46

References

- [1] N. Schmid, C.D. Christ, M. Christen, A.P. Eichenberger, W.F. van Gunsteren, Architecture, implementation and parallelisation of the GROMOS software for biomolecular simulation, *Comput. Phys. Commun.* 183 (2012) 890–903.
- [2] M.M. Reif, P.H. Hünenberger, C. Oostenbrink, New Interaction Parameters for Charged Amino Acid Side Chains in the GROMOS Force Field, *J. Chem. Theory Comput.* 8 (2012) 3705–3723.
- [3] S. Spinelli, A. Lagarde, I. Iovinella, P. Legrand, M. Tegoni, P. Pelosi, et al., Crystal structure of *Apis mellifera* OBP14, a C-minus odorant-binding protein, and its complexes with odorant molecules, *Insect Biochem. Mol. Biol.* 42 (2012) 41–50.
- [4] H.J.C. Berendsen, J.P.M. Postma, W.F. van Gunsteren, J. Hermans, Interaction models for water in relation to protein hydration, in: B. Pullman (Ed.), *Intermolecular Forces*, Reidel, Dordrecht, The Netherlands, 1981: pp. 331–342.
- [5] H.J.C. Berendsen, J.P.M. Postma, W.F. Vangunsteren, A. DiNola, J.R. Haak, Molecular-dynamics with coupling to an external bath, *J. Chem. Phys.* 81 (1984) 3684–3690.
- [6] J.P. Ryckaert, G. Ciccotti, H.J.C. Berendsen, Numerical-integration of cartesian equations of motion of a system with constraints - molecular-dynamics of N-Alkanes, *J. Comput. Phys.* 23 (1977) 327–341.
- [7] A.P. Eichenberger, J.R. Allison, J. Dolenc, D.P. Geerke, B.A.C. Horta, K. Meier, et al., GROMOS++ Software for the Analysis of Biomolecular Simulation Trajectories, *J. Chem. Theory Comput.* 7 (2011) 3379–3390.
- [8] W. Kabsch, C. Sander, Dictionary of protein secondary structure: Pattern recognition of hydrogen-bonded and geometrical features, *Biopolymers.* 22 (1983) 2577–2637.
- [9] S.K. Kearsley, On the orthogonal transformation used for structural comparisons, *Acta Crystallogr. Sect. A.* 45 (1989) 208–210.

Biosensors and Bioelectronics, to be submitted (2016)

Monitoring crop disease markers by odorant binding proteins of *Tribolium castaneum* - Electroantennograms versus reduced graphene-oxide based electronic biosensor

Caroline Kotlowski ^{a,e)}, Ulrich Ramach ^{a,e)}, Karthi Balakrishnan ^{b)}, Josef Breu ^{c)}, Martin Gabriel ^{b)}, Christoph Kleber ^{a)}, Rosa Mastrogiacomo ^{d)}, Paolo Pelosi ^{d)}, Stefan Schütz ^{b)}, and Wolfgang Knoll ^{a,e)}

^{a)} Center for Electrochemical Surface Technology (CEST), Wiener Neustadt (Austria)

^{b)} Buesgen-Institute, Department of Forest Zoology and Forest Conservation, Göttingen (Germany)

^{c)} Inorganic Chemistry I, University of Bayreuth, Bayreuth (Germany)

^{d)} Department of Biology of Agriculture, Food and Environment, University of Pisa, Pisa (Italy)

^{e)} AIT Austrian Institute of Technology, Vienna (Austria)

Abstract

Early stage detection of crop diseases is highly desirable for economical, ecological and food safety reasons. The method of choice is a sensor based detection of low concentrations of volatile disease markers. Inspired by insect olfaction, the latest generation of biosensors relies on the binding of these markers to odorant binding proteins, functionally coupled to a technical transducer.

Along these lines, we recently established a reduced graphene-oxide field effect transistor, functionalized by an odorant binding protein, for real-time detection of unlabelled volatiles. Here we report on the use of this high-throughput analytical tool, capable of detecting small, low affinity ligands in a reversible, concentration dependent manner, for screening the insect proteome for its interactions with ligands of canola and corn disease markers. The odorant binding proteins (OBPs) *TcasOBP9A* and *TcasOBP9B* from the red flour beetle *Tribolium castaneum* were identified as capture molecules for the analytes 6-Methyl-5-hepten-2-one (sulcatone), (S)-(+)-3-Octanol, and 2-Octanone. This is the key for a bioelectro-interfacial nano-sensor, towards future agricultural applications.

Deciphering the odorant's capability i) to interact with proteins and ii) to activate the insect's olfactory response of the antenna was investigated with two biosensors, in-vitro and in-vivo. The in-vitro method is an OBP-functionalized rGO-FET based sensor which monitors the odorant interaction with the odorant binding protein. A second, orthogonal method was capable to identify the odorant's capability to activate the insect's olfactory response of the antenna in-vivo.

1. Introduction

The beetle *Tribolium castaneum* is a dangerous pest for stored products, infesting granaries, flour storage and processing units all over the world causing damages of billions of dollars every year [1]. The beetle is conspicuous of attacking grains that are slightly damaged and show early symptoms of disease. Grains showing severe disease symptoms repel the beetles in order to avoid intoxication by plant defence compounds and mycotoxins [2]. Thus, olfaction of the beetle might provide binding proteins for marker compounds related to early stages of plant diseases in important crops like wheat and maize. This can help to detect stored products prone to insect attack and to detect early symptoms of disease in the field. Reducing crop diseases in the field and reducing storage losses in storehouses are important strategies to fight poverty and hunger in the world and are key steps toward a sustainable and safe food production [3].

The whole genome of *Tribolium castaneum* is annotated [4] and provides an excellent starting position for screening the insect's proteome for identifying proteins that bind marker compounds of interest [5].

To this end, we introduce a technical sensing platform for real-time and high-throughput, quantitative analysis of protein-ligand interactions based on rGO-FET sensing [6] and compare it with in-vivo antenna response [7]. We demonstrate the systematic screening of potential interaction partners of odorant binding proteins from the beetle *Tribolium castaneum* (TcasOBP9A and TcasOBP9B, the molecular structure and the amino acid sequence are given in Figure 1) in order to generate a specific reaction map ("kinetic ligand fingerprint").

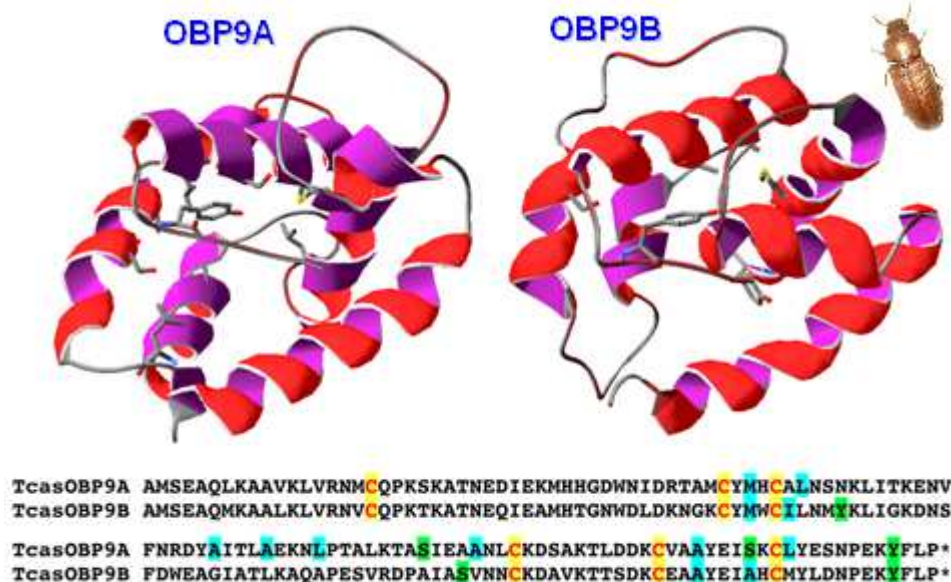


Figure 1: Differences of (parts of) the amino acid sequence and the resulting tertiary structure of the two odorant binding proteins, TcasOBP9A and TcasOBP9B, respectively, from the red flour beetle, *Tribolium castaneum*.

As a proof of principle, two marker compounds with different chemical structure and different biochemical pathways were selected from a list of more than 100 compounds known to be detected by *Tribolium castaneum* [8]. 6-Methyl-5-hepten-2-one (Sulcatone), a branched unsaturated ketone being a degradation product of terpenes and thus indicating breakdown of plant defences, and (S)-(+)-3-Octanol, a linear saturated secondary alcohol being a degradation product of lipids and indicating the activity of fungi [9] and thus potential presence of mycotoxins [10]. For comparison, the binding 2-Octanone to the OBPs on the rGO -FET sensors were also recorded.

2. Experimental

2.1. Preparation of the FET sensors and their electrical characterization

2.1.1. Preparation of large graphene oxide (GO) sheets

Graphene oxide (GO) was prepared by a modified Hummers/Offeman method [11]. In a typical experiment flake graphite (1 g, 125–250 μm) [12] and sodium nitrate (1 g) were mixed with concentrated sulfuric acid (30 ml, 98%). The suspension was mixed in an overhead shaker for 1 h at 25 °C (RT). Subsequently, potassium permanganate (3 g) was interspersed over a period of 3 h and the reaction was kept shaking for 12 h at RT. Thereafter, the mixture was slowly poured into ice-cooled deionized water (30 ml) and hydrogen peroxide (30%) was then added until the suspension turned golden. After centrifugation it was dialyzed until the conductivity of the washing water was below 2 $\mu\text{S}/\text{cm}$. The low ionic strength is essential to achieve delamination of GO by osmotic swelling.

In a second approach, we replaced the last steps by skimming the GO from the water-air interface, diluting it directly in 0.5 l distilled H_2O , and stirring this solution at a low velocity (250 rpm) for 2-3 days in order to obtain better exfoliation results.

2.1.2. Preparation of rGO-FETs

The employed protocol followed a procedure summarized before [13]. Briefly, silicon substrates with a 300 nm oxide layer were chosen as basal layer for the FETs. The SiO_2 substrates were cleaned with a standard RCA cleaning procedure. The substrates were then submerged in a 2% aminopropyltriethoxysilane (APTES) solution in ethanol for 1 h; APTES forming a self-assembled monolayer used to increase the adsorption of graphene oxide sheets. After rinsing with ethanol, the substrates were heated to 120°C for two hours and afterwards cooled to room temperature. The graphene oxide flakes were applied onto the APTES-modified Si-wafer via drop casting of the supernatant of the graphene-oxide solution. The devices were then treated in hermetically sealed glass petri dishes with hydrazine at 70°C overnight to accomplish the graphene-oxide reduction. Flake distribution was first checked with an optical microscope and selected devices then characterized using SEM.

2.1.3. Characterization of the electrical performance of the devices

Electrodes were applied consisting of gold (60-100 nm) with an adhesive layer of chromium (2-3 nm) using a standard evaporation process with a shadow mask. A chip-holder was designed for this process, ensuring the central positioning of the electrodes as well as reducing electrode geometry glazing because of unwanted shadow offset during the evaporation process. Success of the used reduction technique via hydrazine was probed as described before [14]. In order to assure a sufficient conductivity of used graphene layers, all devices displaying higher conductivity than ~800 Ohms were dismissed. A silver-silver chloride reference electrode (Flex ref, World Precision Instruments) was used to operate the FET device in a liquid gate configuration with a constant gate bias, $V_G = -0.6$ V (cf. Fig. 3), and a constant source-drain bias, $V_{SD} = 0.05$ V.

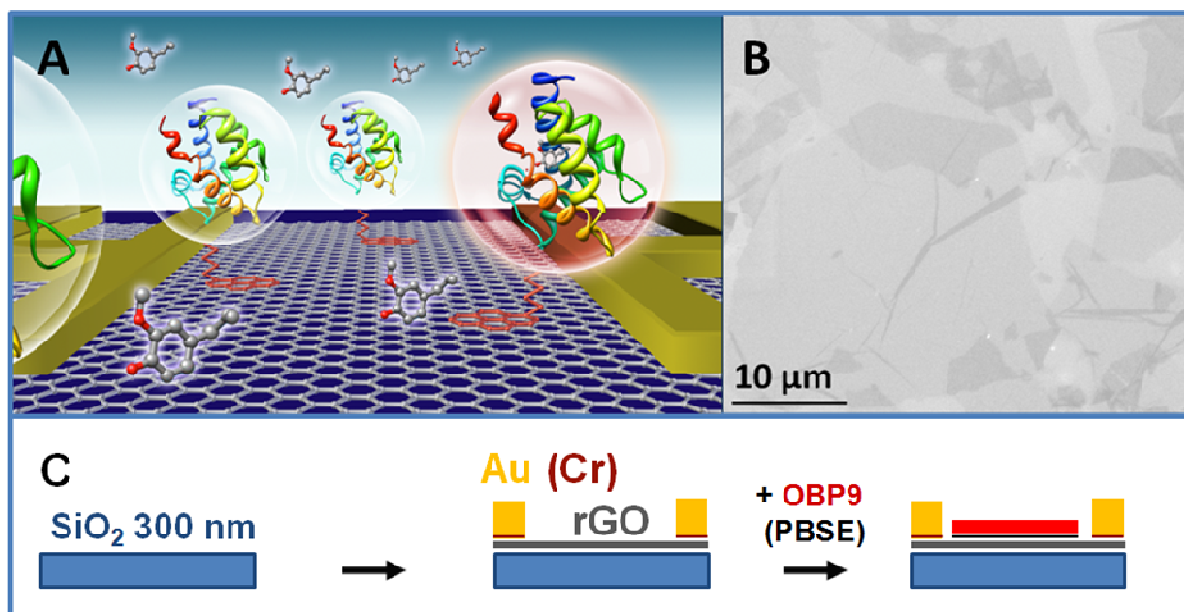


Figure 2: (A) Artist's view of the graphene-based transistor with immobilized odorant binding proteins used for odorant binding studies; (B) light microscopic image of the GO flakes on the chip substrate (before reduction to rGO and before being coated by the electrodes); (C) schematic illustration of the individual fabrication steps of the graphene biosensor device: onto a SiO₂ coated Si substrate, GO flakes from a dispersion were assembled and reduced to rGO; next, source and drain Au electrodes were evaporated (with a thin layer of Cr as an adhesion promotor) and coated (by self-assembly) by a linker, PBSE, and finally functionalized by the attachment of odorant binding proteins.

2.1.4 Odorant sensing with OBP-functionalized rGO-FETs

For the detection of different odorants, the rGO-based biosensors were functionalized with odorant binding proteins TcasOBP9A or TcasOBP9B, respectively, from *Tribolium castaneum*. For the attachment of the recombinantly synthesized protein to the sensing area, the graphene surface was chemically modified by a bi-functional linker, 1-pyrenebutanoic acid succinimidyl ester (PBSE). On one end the linker firmly attaches to the graphene surface through π - π

interactions with a pyrene group and on the other end covalently reacts with the amino groups of the protein to form an amide bond. Therefore, 20 μL of a 5 μM PBSE solution in THF was placed onto the rGO-FET channel, followed by 10 μL of a 10 μM OBP solution in PBS buffer (10 mM; pH 8.0) which was deposited onto the detection area and incubated for 2h at 4°C.

The general procedure of the sensing experiment started with continuously flushing the detection area with pure buffer (1 mM PBS, pH = 8.0), until a stable baseline of the source-drain current, I_{SD} , was established [15].

As we will show, the odorant binding protein based biosensor is able to discriminate between different odorants and responds in a quantitative way to different concentrations of a given ligand binding to its receptor, the OBP, immobilized on the sensor surface. The fundamental concept for sensing of different odorant concentrations by a field-effect-transistor is based on the observation by the biosensor's response of the source-drain-current, I_{SD} , being a function of the applied gate voltage, V_{G} , depends on the presence of ligands bound to the receptor proteins immobilized on the gate. This is demonstrated in Figure 3: the characteristic V-shaped current change upon tuning the gate voltage, V_{G} , from -0.75 V to +0.75 V shows an appreciable dependence on the concentration of the ligand in solution. This concentration controls the surface coverage with the ligand binding to the OBP. The set-up is therefore very well suited for ligand sensing.

Given this dependence of I_{SD} on the ligand concentration a gate voltage of $V_{\text{G}} = -0.6$ V was chosen in the following experiments.

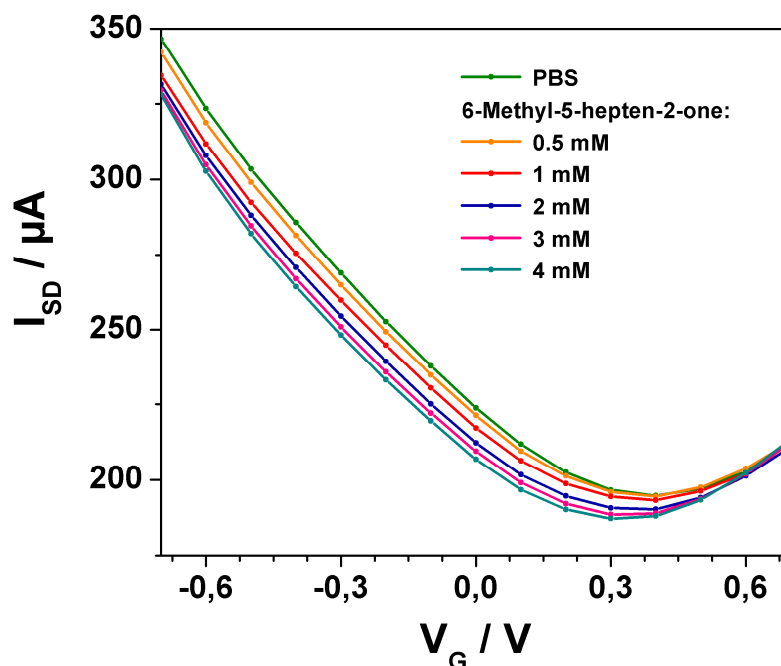


Figure 3: Gate voltage dependent biosensor response: source-drain-current I_{SD} -vs-gate voltage V_{G} , of a rGO FET sensor, functionalized with TcasOBP9B, at different concentrations of 6-Methyl-5-heptene-2-one (Sulcatone).

2.1.5 Preparation of odorant solutions for FET measurements

Odorant solutions of Sulcatone (6-Methyl-5-hepten-2-one), (S)-(+)-3-Octanol and 2-Octanone (chemical structures of the employed ligands are given in Figure 4) were prepared as 1 mM stock solutions in phosphate buffer (1 mM PBS, pH = 8.0) and further diluted (from $0.3 \cdot 10^{-3}$ M to $6 \cdot 10^{-3}$ M) by successive dilutions in PBS buffer. All solutions were freshly prepared on the day of the experiment.

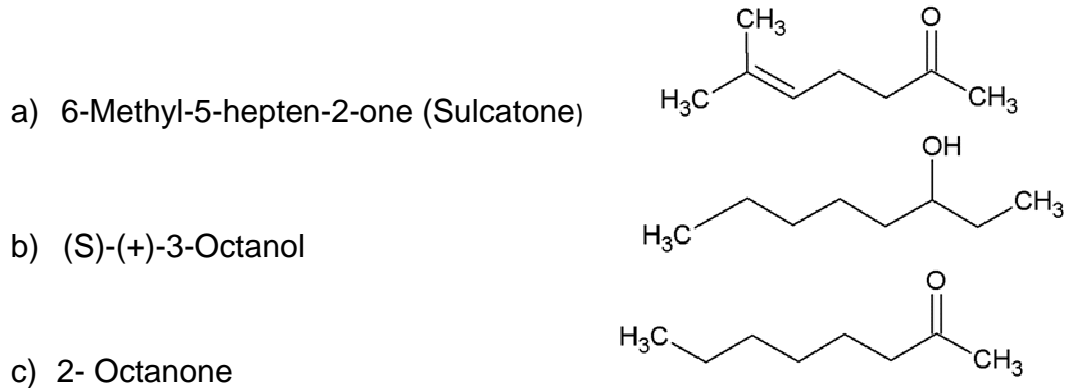


Figure 4: Chemical structure of the ligands investigated by the *in-vivo* sensor, EAG (a,b) and by the *in-vitro* rGO-FET sensor (a-c).

2.2. Electroantennographic measurements

2.2.1. Insect

Stock cultures of San Bernardino (SB) strain of *T. castaneum* were reared at 30 °C, 40 % relative humidity, and 12h photophase. Adults were provided with 95 % organic whole wheat flour seeded with 5% w/w brewer's yeast. The beetles were separated into male and female as pupa, based on their genital organ and were kept separately.

2.2.2. Stimulus compounds

Sulcatone (6-Methyl-5-hepten-2-one), (S)-(+)-3-Octanol and 2-Octanone were diluted in silicone oil M 200 (Carl Roth GmbH + Co. KG, Germany) and concentrations of 10^{-1} , $0.3 \cdot 10^{-1}$, 10^{-2} , $0.3 \cdot 10^{-2}$, 10^{-3} , and $0.3 \cdot 10^{-3}$ (v/v) were prepared. A glass Pasteur pipette (Pasteur capillary pipette, 150 mm Wu Mainz, Deutschland), containing a folded piece of filter paper (approx. 7×40 mm, Whatman No.1) was impregnated with 20 μ l of diluted stimulus compound. The stimulus delivery system (CS-55, Syntech, Hilversum, Netherlands) was used to deliver an one second-puff of odour to the antenna of EAG recording allowing non-intermittent stimulus application at a continuous flow (3 l/min) of charcoal-filtered and humidified air through the tube, placed at 1 cm distance from the antennae. The stimulus carrying Pasteur pipette was inserted into the rear end of the tube (18 cm from the hole to the outlet of the

tube), and the stimulus flow was triggered by the automated controller. The pheromone 4,8-Dimethyldecanal (DMD) at 10^{-3} (w/w) concentration was applied as positive control and silicone oil was applied as a blank control to monitor possible changes in EAG sensitivity. Intervals between series and stimuli were 1 and 2 minutes respectively. Throughout the EAG recording, ascending doses of different stimuli were applied in order to minimize the effect of olfactory adaptation. Responses from ten antennae of different adult beetles were recorded with every compound.

2.2.3 Electroantennography (EAG)

The beetle was put into a plastic micropipette tip. We used slight air pressure to wedge the beetle into the tip, with the head turned forward protruding the antenna out of the plastic tip along with part of the thorax that would later carry the reference electrode. Due to toughness of the cuticle, a small hole was made at the thorax region of the beetle with an electrolytically sharpened tungsten wire. This hole was used to insert a reference glass electrode containing Ringer solution, in contact with an Ag/AgCl wire. After making a puncture at the last antennal segment with a sharpened tungsten wire by using a micromanipulator (Joystick Manipulator, MN-151, Narishige-Japan). A recording glass electrode (GB150F-8P, 0.86×1.50×80 mm with filament, Science products GmbH, Hofheim-Deutschland) filled with Ringer solution and in contact with a Ag/AgCl wire was immediately inserted. Glass capillary electrodes were drawn from borosilicate glass by electrode puller (Puller, Model No. PP-830, Narishige group, Japan). The recorded EAG signal was amplified with a pre-amplifier (Universal AC/DC probe, Syntech, Netherlands), which was connected to an EAG amplifier (x10). A data acquisition controller (IDAC-4, Syntech) processed and digitized the amplified signals. With the customized EAG program (Version 2.7, EAG 2000, Syntech), the resulting EAG amplitude was computed as the difference between the baseline level and the maximum amplitude reached during odour stimulation.

3. Results

3.1. In vitro measurements with the rGO FET sensors

A first series of odorant sensing experiments was performed with a sensor architecture schematically depicted in Figure 5 A: the rGO gate surface was modified with the linker system PBSE used to immobilize the odorant binding protein TcasOBP9A. After the baseline was established, the change in the source-drain current, ΔI_{SD} , was *on-line* in real time monitored while the odorant, 6-Methyl-5-hepten-2-one (6-MHO), concentration in the analyte solution was stepwise increased from $c_0 = 500 \mu\text{M}$ to 6 mM. This global analysis is shown in Fig. 5 B. The following rinsing step with pure buffer re-set the system to the pristine baseline level, demonstrating the full reversibility of the affinity reaction between the surface immobilized receptor and its ligand binding from solution. This is an important prerequisite for the applicability of the Langmuir model for the quantitative analysis of the binding data, allowing for the evaluation of kinetic rate constants, k_{on} and k_{off} , respectively, as well as for the titration of the equilibrium surface coverages, allowing for the determination of affinity constants, K_A . An important aspect that we address next before going into a detailed analysis of the binding data is the question of non-specific adsorption of ligand molecules to the sensor surface. To this end we

assembled FET devices with only the linker layer, i.e., without the final preparation step of immobilizing an odorant binding protein (Fig. 5 C). Upon rinsing various high concentration solutions of the studied ligand systems through the attached flow cell a small, almost negligible response of the device could be observed (Fig 5 D). The recorded current changes were all below the 5-10% level of the response of the sensor in the presence of odorant proteins binding the ligands specifically.

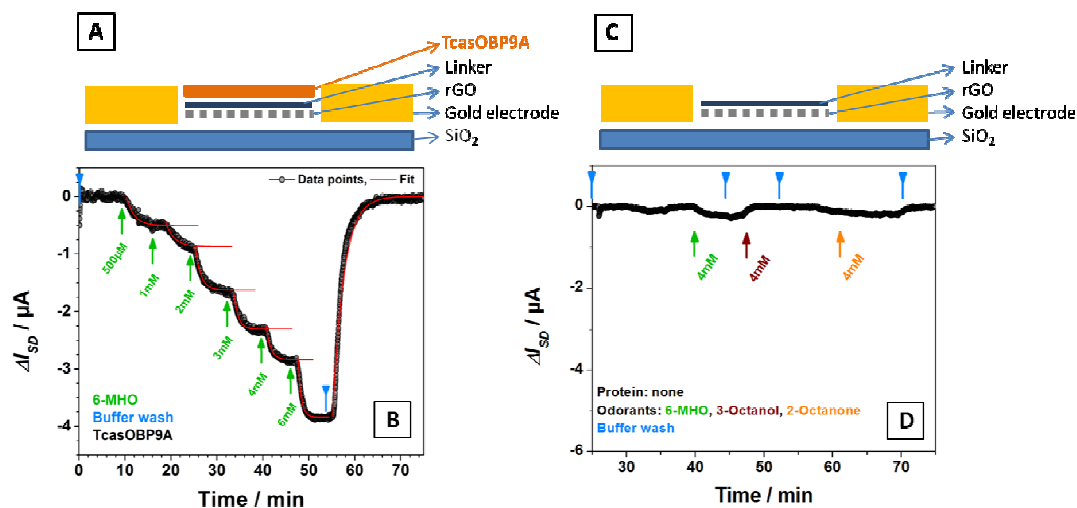


Figure 5: (A) Schematic illustration of the biosensor device with the rGO gate, a linker layer, PBSE, for the chemical coupling of the receptor, and the odorant binding protein, TcasOBP9A. (B) Real-time monitoring of the current change, ΔI_{SD} -vs-time, of a TcasOBP9A-functionalized biosensor to different concentrations of 6-Methyl-5-hepten-2-one (global analysis). (C) rGO-FET device design without protein functionalisation. (D) Control measurement without protein, ΔI_{SD} -vs-time response to 4 mM solutions of 6-MHO, 3-Octanol and 2-Octanone, respectively, as indicated by the different colors.

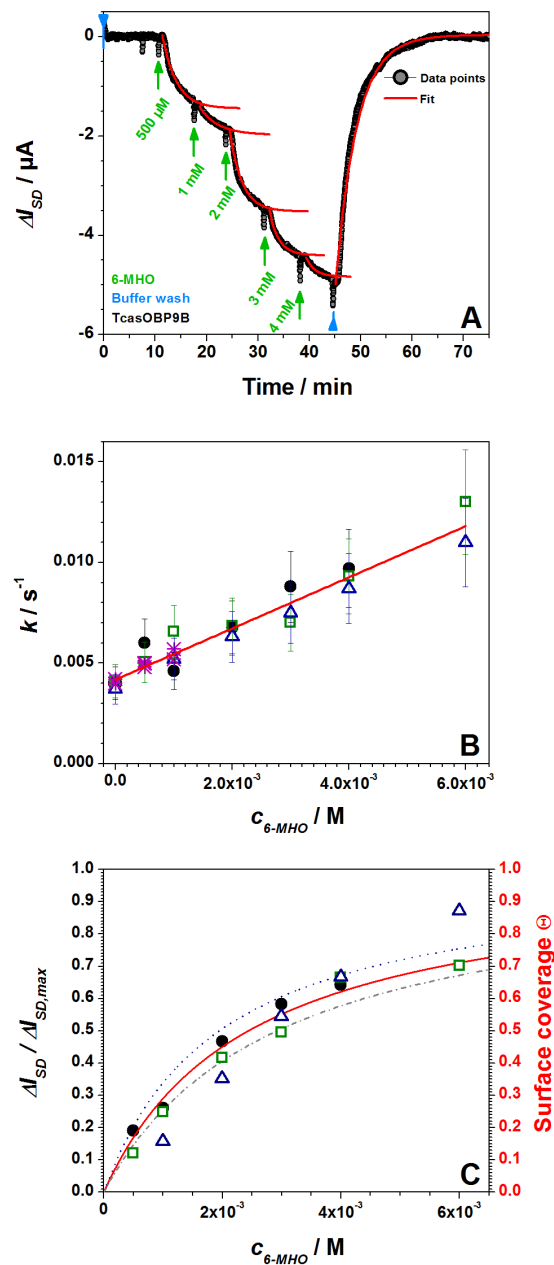


Figure 6: Affinity data and kinetic analysis of 6-Methyl-5-hepten-2-one (6-MHO) binding to the protein TcasOBP9B. (A) Real-time response of a TcasOBP9B-functionalized biosensor to the binding of 6-MHO: the current decreases with the increase of the bulk concentration of 6-MHO (from $c_0 = 500 \mu\text{M}$ to 6 mM) and gradually saturates. Blue arrows indicate runs with pure buffer, while green arrows indicate experiments with 6-MHO solutions. Red curves indicate the fitting of the raw data by kinetic simulations of the association and dissociation processes based on the Langmuir model. (B) Analysis of the reaction rate constants, k , obtained from the fitted data of (A) as a function of the 6-MHO concentration; different symbols were taken from 3 individual repeats. Linear regression gives the kinetic constants $k_{\text{off}} = 0.004 \text{ s}^{-1}$, $k_{\text{on}} = 1.3 \text{ M}^{-1} \text{ s}^{-1}$, and the dissociation constant $K_d = 3.0 \times 10^{-3} \text{ M}$. (C) Langmuir adsorption isotherm, obtained for 3 individual repeats; the red fit curve gives $K_d = 2.5 \times 10^{-3} \text{ M}$.

Figure 6 summarizes a complete set of data of the global analysis with sensors functionalized with TcasOBP9B, exposed to analyte solutions of different concentrations of 6-Methyl-5-hepten-2-one (6-MHO, Sulcatone). Fig. 6A gives the kinetic response of the FETs upon increasing the analyte concentration (from the pure buffer baseline level) in a stepwise fashion from $c_0 = 500 \mu\text{M}$ to 4 mM (green arrows with concentrations as indicated), followed by a pure buffer rinse (blue arrow). The black dots are the experimental data; the red curves are fits assuming a single exponential time dependence.

If one plots all the measured (fit) k -values as a function of the bulk concentration as it is done in Fig. 6B, one finds a linear increase of the rate constant as it is predicted by the Langmuir model :

$$k = k_{\text{on}} c_0 + k_{\text{off}} \quad (2)$$

From the straight line through the data points in Fig. 6B, one obtains $k_{\text{on}} = 1.3 \text{ M}^{-1}\text{s}^{-1}$ for the binding of 6-MHO to TcasOBP9B from the beetle *Tribolium castaneum*. The intersection of the fit line with the ordinate, i.e., k for $c_0 = 0$, yields $k_{\text{off}} = 0.004 \text{ s}^{-1}$.

According to the Langmuir model the relation between the rate constants and the affinity constant is given according to

$$K_A = k_{\text{on}} / k_{\text{off}} \quad (3)$$

which results then in $K_A = 3.2 \times 10^2 \text{ M}^{-1}$ or $K_d = 3.0 \text{ mM}$.

Alternatively, one can analyze the surface coverages obtained at equilibrium with any new bulk concentration. Such a titration data set can be also derived from the global analysis presented in Fig. 6A by plotting the level of the source-drain current after changing the concentration of the bulk odorant solution. The result is

Table 1. Individual affinity constants K_A and reaction rate constants, k_{on} and k_{off} , respectively, of odorants binding to different OBPs, as indicated.

Protein (Species)	Ligand	Dissociation constant/ 10^{-6}M	$k_{\text{on}}/\text{M}^{-1}\text{s}^{-1}$	$k_{\text{off}}/\text{s}^{-1}$
<i>TcasOBP9A</i> (<i>Tribolium castaneum</i>)	6-Methyl-5-hepten-2-one	3000	3	0.008
	(S)-(+)-3-Octanol	2000	3	0.006
	2-Octanone	3000	2	0.006
<i>TcasOBP9B</i> (<i>Tribolium castaneum</i>)	6-Methyl-5-hepten-2-one	4000	1	0.004
	(S)-(+)-3-Octanol	3000	2	0.006
	2-Octanone	2000	2	0.004
<i>AmelOBP14</i> (<i>Apis mellifera</i>)	Homovanillic acid	4	1130	0.008
	Methyl vanillate	20	235	0.010
	Eugenol	40	170	0.006
	Citral	800	9	0.003
	Methyl eugenol	1400	6	0.006
	Geraniol	3300	3	0.003

shown in Fig. 6C for 3 different sets of measurements. The fit to the data gives a dissociation constant of $K_d = 2.5$ mM, in excellent agreement with the value from the pure kinetic analysis. This supports the approach of using the Langmuir model for a quantitative evaluation of the binding data recorded by rGO FETs.

Table 1 summarizes the obtained results for the two employed odorant binding proteins, TcasOBP9A and TcasOBP9B, respectively, and for another protein, AmelOPB14 from the honey bee to a series of different odorants (ligands) as indicated.

Particularly in view of the following affinity measurements by whole antenna recordings we focus on two more aspects of these odorant binding studies with an artificial device, i.e., the repeatability of the kinetic association and dissociation measurements, as well as the accuracy and LOD for the recording of any change of the source-drain current upon exposing the sensor to a very low bulk concentration of the analyte solution way below the half saturation concentration $c_{1/2}$ ($= K_d$).

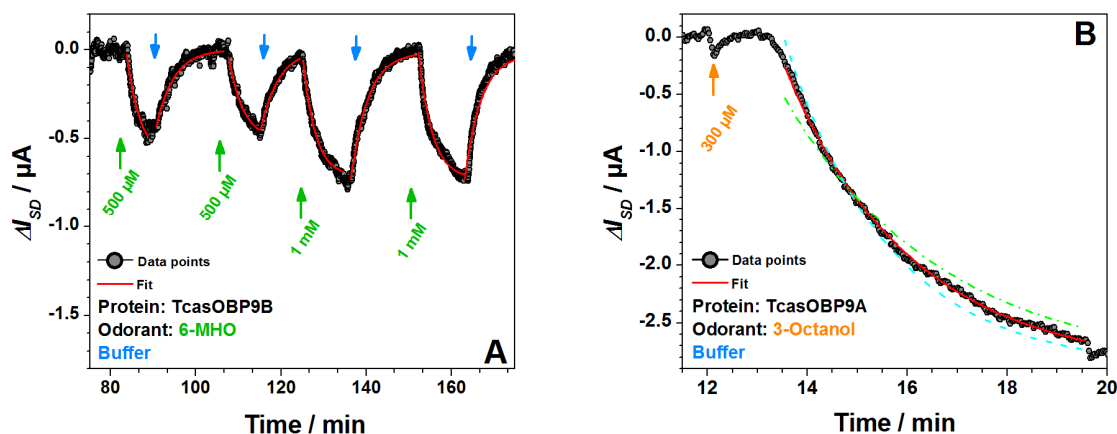


Figure 7: A, Repeatability test for the kinetic association and dissociation response of an TcasOBP9B functionalized FET sensor upon exposure to low and moderate concentrations of 6-MHO solutions and to pure buffer, respectively; B, kinetic response of the sensor, functionalized with TcasOBP9A, to a change of the analyte solution from pure buffer to a 300 μ M solution of Octanol. The full red curve is a (single-exponential) fit to the experimental data points with a rate constant $k = 0.0243$ s^{-1} , with the dashed light blue curve being a lower ($k=0.0194$ s^{-1}) and the dash-dotted light blue curve being an upper bound of the rate constant ($k=0.02916$ s^{-1}).

Table 2:

6-MHO / mM	k / s^{-1}	$k_{on} / s^{-1} M^{-1}$	k_{off} / s^{-1}	K_d / M
0.5	0.0050	2	0.0040	2×10^{-3}
0.5	0.0048	1.6	0.0040	3×10^{-3}
1	0.0057	1.5	0.0042	3×10^{-3}
1	0.0052	1	0.0042	4×10^{-3}

The results of the repeatability test with a FET device that was functionalized by TcasOBP9B upon repeated exposure to a low ($c_0 = 500$ μ M) and a moderate ($c_0 = 1$ mM) concentration of the analyte 6-MHO, alternating with pure buffer solutions, is given in Fig. 7A. The full red curves represent single exponential fits to the data and result in kinetic rate constants that are summarized in Table 2. As one can see, the

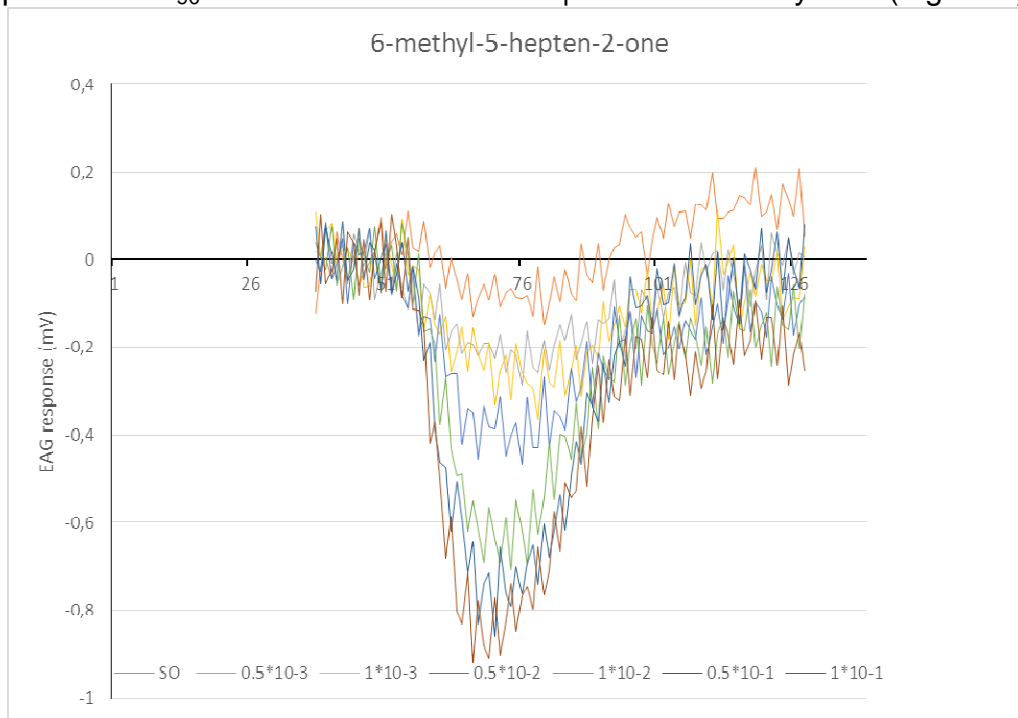
repeatability is quite satisfactory. The typical time constants for both, the association and the dissociation process, are in the few minutes regime.

The second important aspect concerns the accuracy of the rate constant determination and the limit of detection (LOD). Fig. 7B gives an example for a measurement with a sensor that was functionalized with TcasOBP9A, and was exposed – after equilibration with pure buffer – to a 300 μ M solution of Octanol. Note the excellent signal-to-noise of the recorded current change! The full red curve is a single exponential fit to the experimental data and confirms further the excellent quality of the fit by a single-exponential curve with an acceptable accuracy as far as the rate constant determination is concerned. The dashed and dash-dotted light blue curves correspond to rate constants that are 20% higher or lower than the best value.

3.2. EAG

In order to demonstrate the insect's olfactory response to 6-Methyl-5-hepten-2-one and (S)-(+)-3-Octanol, we measured the antenna's odorant reception *in vivo* using electroantennography of the antenna of *Tribolium castaneum*.

The response of the antenna follows a similar kinetics for both compounds with a response time t_{90} of 200 ms and a dose-dependent recovery time (Figure 8).



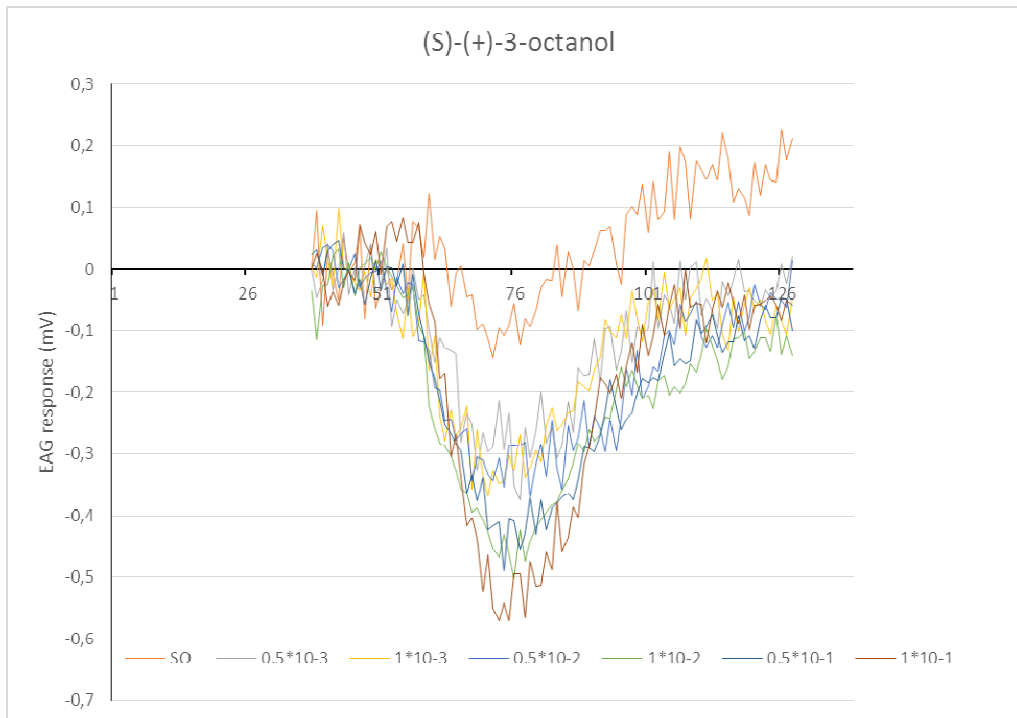


Figure 8: Overlay of real-time responses by a *T. castaneum* antenna to the stimulation by 6-MHO. The electroantennographic potential increases with the increase of the concentration of 6-MHO in air (from 0.23 μ bar to 23 μ bar partial pressure) and gradually saturates. Response times are below 1 s and recovery times are in the range of fractions of a minute.

Both odorants show concentration dependent electroantennographic response by the antenna (Figure 9). Blank measurements with silicon oil (SO) show a small and reproduceable response by mechanoreceptors whereas positive control measurements with the pheromone 4,8-dimethyldecanal (DMD) show the expected high response. The detected response represents the potential of multiple responding neurons within the antenna to the odorant. Our results show the relevance of the investigated odorants for the insect as a potential marker for damaged grains and diseased plants.

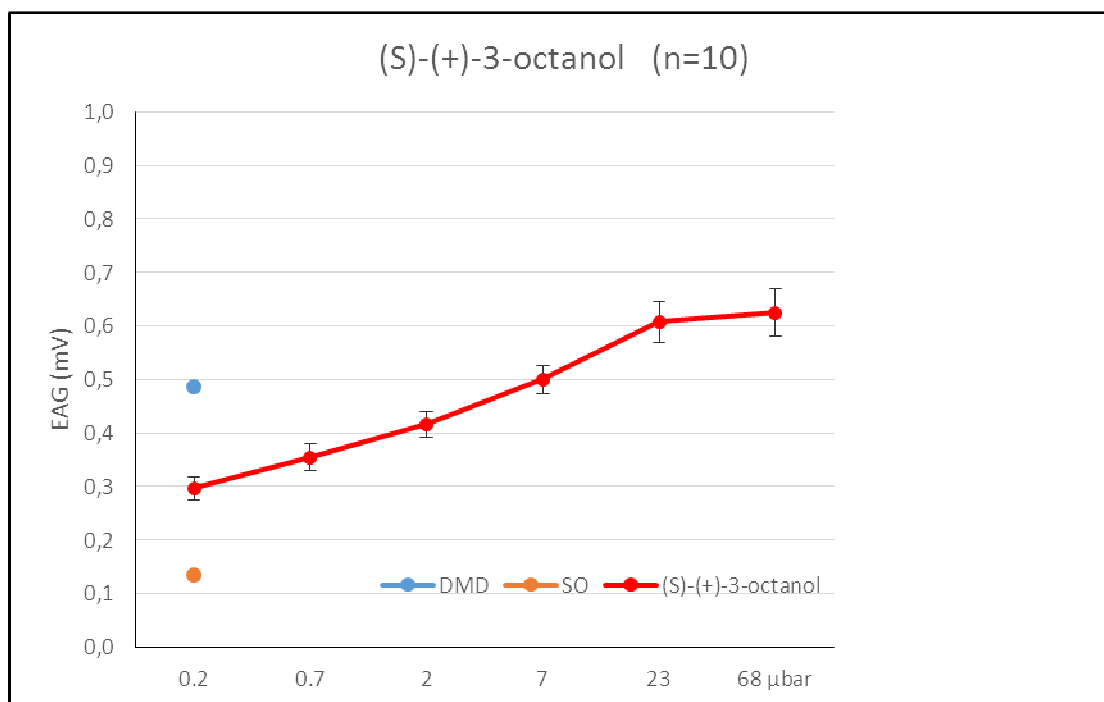
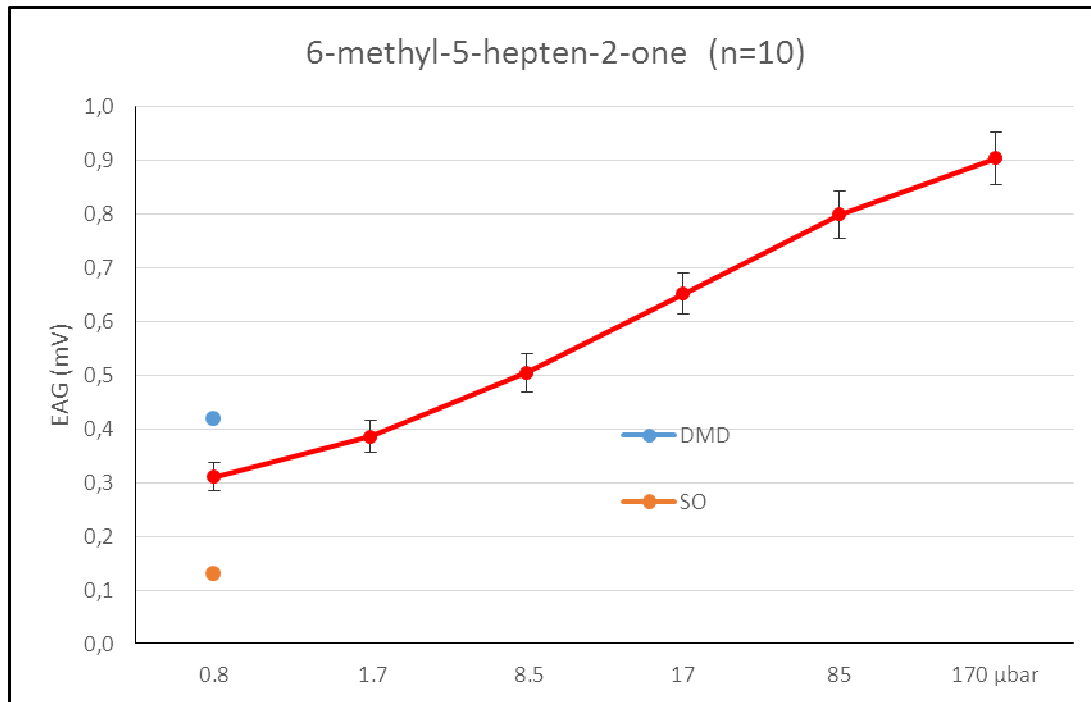


Figure 9: *In-vivo* antennal dose-response relation. EAG measurements of the responses to a dilution series of 6-Methyl-5-heptene-2-one (A) and (S)-(+)-3-Octanol (B) in air (Concentration of stimuli provided as equilibrium vapour-pressure above the employed silicone-oil dilutions): the EAG response increases with the odorant concentration. Error bars show standard deviations from 10 repeats. Controls are shown with silicon oil (SO) and the response to the *Tribolium castaneum* pheromone 4,8-dimethyldecanal (DMD).

3.3. Comparison between in-vitro and in-vivo studies

The comparison of an artificial nanosensor-system based on a rGO field-effect transistor with a natural insect antenna has to be interpreted with care. The natural system is stimulated by an odor stimulus in air, consists of a porous hydrophobic chitin cuticle, an aqueous layer of sensillum lymph containing soluble carrier proteins (OBPs), and a set of membrane bound odorant receptors (ORs) for further selective binding and amplification of the signal by opening of ion channels in the membrane of the sensory neuron.

In contrast, the electronic nanosensor-system is stimulated by an odor dissolved in water, consists of OBPs immobilized to a graphene gate of a FET for further amplification of the signal by opening the gate channel for electric conduction.

However, a more detailed comparison might only be useful if the OBP utilized for the experiment is one with a major contribution to the sum signal of the whole insect antenna.

The choice of the TcasOBP9A and TcasOBP9B were based on their high and antenna-specific expression level (Dippel et al. 2015) and the fact that experiments with *T. castaneum* beetles which were subjected to a RNA-i-treatment knocking down both of these OBPs showed massively decreased detectivity to the stimulus compounds. This makes a major role in olfactory detection of the stimulus compounds highly likely.

For a first step of a more detailed comparison, the stimulus quantity has to be aligned. Henry's law provides a relation between the concentration of a compound in an aqueous solution, c_a , and its vapor pressure, p :

$$c_a = H^{cp} \cdot p \quad (4)$$

As an example, we compare the situation for (S)-(+)-3-Octanol for which Henry's law constant, H^{cp} , is known $H^{cp} = 0.31 \text{ Mol m}^{-3} \text{ Pa}^{-1}$. It is further known for 2-Octanone, but not for 6-MHO. With $1 \text{ Mol m}^{-3} \text{ Pa}^{-1} = 101 \text{ M atm}^{-1}$ at $6.8 \text{ } \mu\text{bar}$ ($= 6.8 \text{ } \mu\text{atm}$) partial pressure this corresponds then to a solution concentration of $c_a = 200 \text{ } \mu\text{M}$. Our lowest concentration of Octanol in the flow cell was $300 \text{ } \mu\text{M}$ (which makes sense given the $K_d = 3 \text{ mM}$, but it could have been much lower (certainly measurements are possible with $30 \text{ } \mu\text{M}$, corresponding to a partial pressure of $1 \text{ } \mu\text{bar}$). Hence, the dilutions measured by the two techniques are in a similar range of magnitude and the two techniques have comparable sensitivity.

This hints at the fact that binding of the ligand by the OBP is not significantly hindered by immobilization, but that the removal of the ligand is significantly quicker in the natural system, probably due to removal of the ligand from the OBP binding pocket after binding to the OR at the membrane, avoiding permanent stimulation and providing a short recovery time of the natural system.

Unfortunately, there are no data about rate constants for all the components of the natural *T. castaneum* system available.

4. Conclusions

We have developed an approach to define the ability of the volatile to stimulate the olfactory response of the antenna, and to interact with OBPs using two methods in vivo and in vitro. Therefore the activation of the beetle olfactory response in the antenna can be partly attributed to the antenna proteins TcasOBP9A and TcasOBP9B. In fact the similar sensitivity range of the antenna proteins as well as the antenna indicate that the OBPs are the sensitivity-limiting step in this case. Taken together the developed biosensor turns from an analytical tool for the recognition of odorous volatiles as a proteomics approach into an agricultural-pest marker sensor.

5. Acknowledgement

We are grateful to a number of colleagues that contributed with their advice: Melanie Larisika, Christoph Nowak, and Serban F. Peteu. Partial support for this work was provided by the European Science Foundation (ESF), Grant Number: 10-EuroBioSAS-FP-005, by the European Union's Horizon 2020 program under the Sklodowska-Curie Grant Agreement No 645686, the Austrian Science Fund (FWF) (I681-N24), the Austrian Federal Ministry for Transport, Innovation and Technology (GZ BMVIT-612.166/0001-III/I1/2010) and the Austrian Research Promotion Agency (FFG) within the COMET framework, by the Province of Lower Austria.

6. References

- [1] Throne, J. E., Hallman, G. J., Johnson, J. A., & Follett, P. A. (2003). Post-harvest entomology research in the United States Department of Agriculture–Agricultural Research Service. *Pest management science*, 59(6-7), 619-628.
- [2] Altincicek, B., Knorr, E., & Vilcinskas, A. (2008). Beetle immunity: Identification of immune-inducible genes from the model insect *Tribolium castaneum*. *Developmental & Comparative Immunology*, 32(5), 585-595.
- [3] www.un.org/millenniumgoals
- [4] Richards, S., Gibbs, R. A., Weinstock, G. M., Brown, S. J., Denell, R., Beeman, R. W., ... & Klingler, M. (2008). The genome of the model beetle and pest *Tribolium castaneum*. *Nature*, 452(7190), 949-955.
- [5] Li J, Lehmann S, Weißbecker B, Ojeda-Naharros I, Schütz S, Joop G, Wimmer EA (2013) Odoriferous defensive stink gland transcriptome to identify novel genes for quinone synthesis in the red flour beetle, *Tribolium castaneum*. *PLOS GENET*, 9(7): e1003596.
- [6] Melanie Larisika, Caroline Kotlowski, Christoph Steininger, Rosa Mastrogiacomo, Paolo Pelosi, Stefan Schütz, Serban F. Peteu, Christoph Kleber, Ciril Reiner-Rozman, Christoph Nowak, and Wolfgang Knoll, Electronic Olfactory Sensor Based on *A.mellifera* Odorant Binding Protein 14 on a Reduced Graphene Oxide Field-Effect Transistor, *Angew. Chem., Int. Ed. Engl.* 54 (2015) 13245-8

- [7] Weissbecker, B., Holighaus, G., & Schütz, S. (2004). Gas chromatography with mass spectrometric and electroantennographic detection: analysis of wood odorants by direct coupling of insect olfaction and mass spectrometry. *Journal of Chromatography A*, 1056(1), 209-216.
- [8] Karthi & Schütz (manuscript in preparation)
- [9] Holighaus, G., Weißbecker, B., von Fragstein, M., & Schütz, S. (2014). Ubiquitous eight-carbon volatiles of fungi are infochemicals for a specialist fungivore. *Chemoecology*, 24(2), 57-66.
- [10] Guo, Z., Döll, K., Dastjerdi, R., Karlovsky, P., Dehne, H. W., & Altincicek, B. (2014). Effect of fungal colonization of wheat grains with *Fusarium* spp. on food choice, weight gain and mortality of meal beetle larvae (*Tenebrio molitor*). *PloS one*, 9(6), e100112.
- [11] W. S. Hummers, R. E. Offeman, *J. Am. Chem. Soc.* 1958, 80, 1339.
- [12] Su, Ching-Yuan, et al. "Electrical and spectroscopic characterizations of ultra-large reduced graphene oxide monolayers." *Chemistry of Materials* 21.23 (2009): 5674-5680.
- [13] Melanie Larisika, Caroline Kotlowski, Christoph Steininger, Rosa Mastrogiacomo, Paolo Pelosi, Stefan Schütz, Serban F. Peteu, Christoph Kleber, Ciril Reiner-Rozman, Christoph Nowak, and Wolfgang Knoll, Electronic Olfactory Sensor Based on *A.mellifera* Odorant Binding Protein 14 on a Reduced Graphene Oxide Field-Effect Transistor, *Angew. Chem., Int. Ed. Engl.* 54 (2015) 13245-13248
- [14] Larisika, M.; Huang, JF.; Tok, A.; Knoll, W.; Nowak, C., An Improved Synthesis Route to Graphene for Molecular Sensor Applications, *Mater. Chem. Phys.* 136 (2012) 304-308
- [15] Reiner-Rozman, C; Larisika, M; Nowak; Knoll, W., Graphene-based liquid-gated field effect transistor for biosensing: Theory and experiments, *Biosens. Bioelectron.* 70 (2015) 21-27

10 Further preliminary data

10.1 Aptamer based 17 β -estradiol sensing with rGO-FET

Aiming at maximizing the sensitivity of small molecule sensing a 75-mer aptamer was used as high affinity capture molecule. The linear aptamer molecule was described by Alsager et al. 2014 to assume a more compact conformation if binding its ligand 17 β -estradiol [49,50]. Thereby, it changes its dipole moment significantly which was the peg for a sensing application as the huge dipole moment shift improves the FET sensitivity compared to the structural changes typical for proteins. The basic contribution of the dipole moment change to the detectability of FETs was presented by Frazier et al. with the use of a dipole moment inducing “selector” (Figure 18) [51].

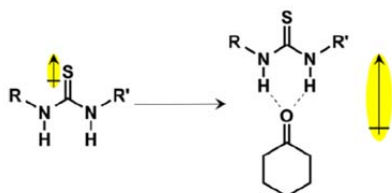


Figure 18. (Frazier et al.[51]) Scheme of the hydrogen bonded complex of the selector with the analyte cyclohexanone, which is enhancing the collective dipole.

10.2 Kinetic analysis of the aptamer –17 β -estradiol

In this chapter, preliminary data of aptamer–17 β -estradiol complex formation measured by rGO-FETs are presented.

Figure 19 (Left) shows repeating detection of 17- β -estradiol with the aptamer (I_{DS} versus time). Unlike in our published work, here, each analyte injection was followed by a washing step, showing the reversibility of the complex formation. For comparison Figure 20 shows the titration measurement method with successively increasing ligand concentrations (no intermediate washing steps). The measurement is very stable which yields a significantly lower signal to noise ratio, than those observed with using odorant binding proteins as sensing molecules. The kinetic constant K_D obtained by the Langmuir model based kinetic analysis of both the reversible and the titration measurement method is 60 nM (Figure 19 Right, Figure 20). This confirmed the affinity to be in agreement with the affinity evaluated by Alsager et al. 2014, who obtained a K_D of 50 nM [49,50].

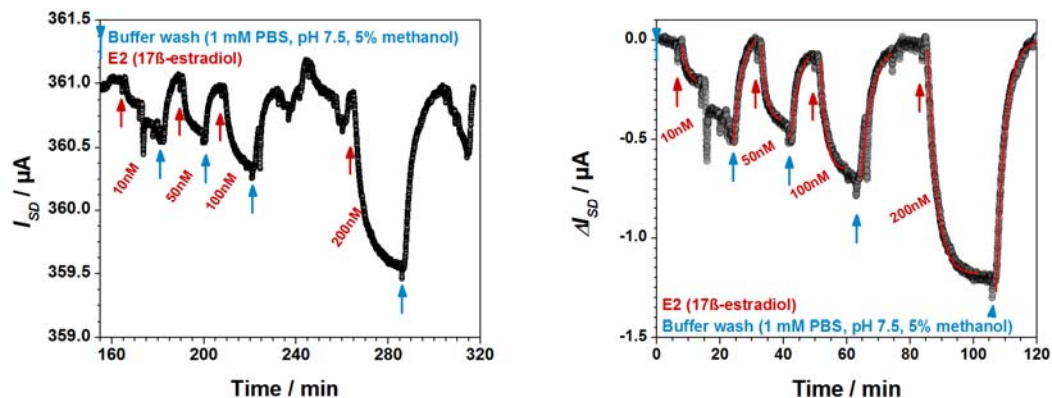


Figure 19. Biosensor measurement of 17 β -estradiol with an aptamer functionalized rGO-FET. Reversibility of the recognition and binding of 17 β -estradiol to the aptamer with increasing analyte concentration is shown. The change in source-drain-current (I_{SD}) measured as a function of time after addition of various concentrations of 17 β -estradiol to the buffer solution (PBS, 1 mM phosphate, pH 7.5) flowing across the gate of a rGO field-effect-transistor in a flow cell (red arrows) and rinsing again pure buffer through the cell (blue arrow) upon which the current signal returns to the baseline level, indicates the reversible binding process. In the right plot the full kinetic analysis is indicated with red fits based on the Langmuir model.

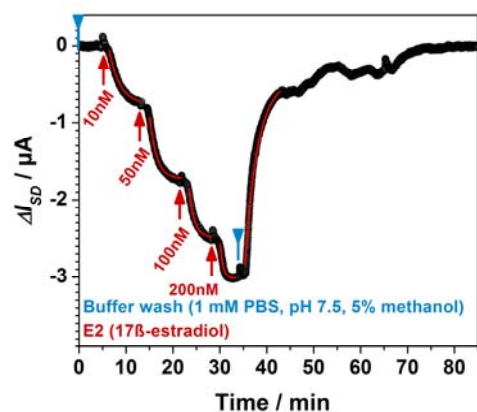


Figure 20. Biosensor measurement of 17 β -estradiol with aptamer functionalized rGO-FET. The titration measurement shows the recognition and binding of the odorant 17 β -estradiol by the aptamer with increasing analyte concentration and the full kinetic analysis.

11 References

- 1 Geim, A., & Novoselov, K. (2010). The Nobel Prize in Physics 2010.
- 2 Guo, S., & Dong, S. (2011). Graphene nanosheet: synthesis, molecular engineering, thin film, hybrids, and energy and analytical applications. *Chemical Society Reviews*, 40(5), 2644-2672.
- 3 Geim, A. K., & Novoselov, K. S. (2007). The rise of graphene. *Nature materials*, 6(3), 183-191.
- 4 Avouris, P. (2010). Graphene: electronic and photonic properties and devices. *Nano letters*, 10(11), 4285-4294.
- 5 Edwards, R. S., & Coleman, K. S. (2013). Graphene synthesis: relationship to applications. *Nanoscale*, 5(1), 38-51.
- 6 Chen, D., Tang, L., & Li, J. (2010). Graphene-based materials in electrochemistry. *Chemical Society Reviews*, 39(8), 3157-3180.
- 7 Zhan, B., Li, C., Yang, J., Jenkins, G., Huang, W., & Dong, X. (2014). Graphene Field-Effect Transistor and Its Application for Electronic Sensing. *Small*, 10(20), 4042-4065.
- 8 Liu, Y., Dong, X., & Chen, P. (2012). Biological and chemical sensors based on graphene materials. *Chemical Society Reviews*, 41(6), 2283-2307.
- 9 Sharma, B. K., & Ahn, J. H. (2013). Graphene based field effect transistors: Efforts made towards flexible electronics. *Solid-State Electronics*, 89, 177-188.
- 10 Mohanty, N., & Berry, V. (2008). Graphene-based single-bacterium resolution biodevice and DNA transistor: interfacing graphene derivatives with nanoscale and microscale biocomponents. *Nano letters*, 8(12), 4469-4476.
- 11 Dong, X., Shi, Y., Huang, W., Chen, P., & Li, L. J. (2010). Electrical detection of DNA hybridization with single-base specificity using transistors based on CVD-grown graphene sheets. *Advanced Materials*, 22(14), 1649-1653.
- 12 Cai, B., Wang, S., Huang, L., Ning, Y., Zhang, Z., & Zhang, G. J. (2014). Ultrasensitive label-free detection of PNA–DNA hybridization by reduced graphene oxide field-effect transistor biosensor. *ACS nano*, 8(3), 2632-2638.
- 13 Ohno, Y., Maehashi, K., & Matsumoto, K. (2010). Label-free biosensors based on aptamer-modified graphene field-effect transistors. *Journal of the American Chemical Society*, 132(51), 18012-18013.
- 14 Huang, Y., Dong, X., Liu, Y., Li, L. J., & Chen, P. (2011). Graphene-based biosensors for detection of bacteria and their metabolic activities. *Journal of Materials Chemistry*, 21(33), 12358-12362.
- 15 He, Q., Sudibya, H. G., Yin, Z., Wu, S., Li, H., Boey, F., ... & Zhang, H. (2010). Centimeter-long and large-scale micropatterns of reduced graphene oxide films: fabrication and sensing applications. *ACS Nano*, 4(6), 3201-3208.
- 16 Ang, P. K., Li, A., Jaiswal, M., Wang, Y., Hou, H. W., Thong, J. T., ... & Loh, K. P. (2011). Flow sensing of single cell by graphene transistor in a microfluidic channel. *Nano letters*, 11(12), 5240-5246.

- 17 Kim, D. J., Sohn, I. Y., Jung, J. H., Yoon, O. J., Lee, N. E., & Park, J. S. (2013). Reduced graphene oxide field-effect transistor for label-free femtomolar protein detection. *Biosensors and Bioelectronics*, *41*, 621-626.
- 18 Novoselov, K. S., Geim, A. K., Morozov, S. V., Jiang, D., Zhang, Y., Dubonos, S. A., ... & Firsov, A. A. (2004). Electric field effect in atomically thin carbon films. *science*, *306*(5696), 666-669.
- 19 Bai, S., & Shen, X. (2012). Graphene–inorganic nanocomposites. *Rsc Advances*, *2*(1), 64-98.
- 20 Park, S., An, J., Jung, I., Piner, R. D., An, S. J., Li, X., ... & Ruoff, R. S. (2009). Colloidal suspensions of highly reduced graphene oxide in a wide variety of organic solvents. *Nano letters*, *9*(4), 1593-1597.
- 21 Li, D., Mueller, M. B., Gilje, S., Kaner, R. B., & Wallace, G. G. (2008). Processable aqueous dispersions of graphene nanosheets. *Nature nanotechnology*, *3*(2), 101-105.
- 22 Hummers Jr, W. S., Offeman, R. E. (1958). Preparation of graphitic oxide. *Journal of the American Chemical Society*, *80*(6), 1339-1339.
- 23 Su, C. Y., Xu, Y., Zhang, W., Zhao, J., Tang, X., Tsai, C. H., & Li, L. J. (2009). Electrical and spectroscopic characterizations of ultra-large reduced graphene oxide monolayers. *Chemistry of Materials*, *21*(23), 5674-5680.
- 24 Guo, H. L., Wang, X. F., Qian, Q. Y., Wang, F. B., & Xia, X. H. (2009). A green approach to the synthesis of graphene nanosheets. *ACS nano*, *3*(9), 2653-2659.
- 25 Bonaccorso, F., Lombardo, A., Hasan, T., Sun, Z., Colombo, L., & Ferrari, A. C. (2012). Production and processing of graphene and 2d crystals. *Materials Today*, *15*(12), 564-589.
- 26 Novoselov, K. S., Jiang, D., Schedin, F., Booth, T. J., Khotkevich, V. V., Morozov, S. V., & Geim, A. K. (2005). Two-dimensional atomic crystals. *Proceedings of the National Academy of Sciences of the United States of America*, *102*(30), 10451-10453.
- 27 Meyer, J. C., Geim, A. K., Katsnelson, M. I., Novoselov, K. S., Booth, T. J., & Roth, S. (2007). The structure of suspended graphene sheets. *Nature*, *446*(7131), 60-63.
- 28 Meyer, J. C., Geim, A. K., Katsnelson, M. I., Novoselov, K. S., Oberfell, D., Roth, S., ... & Zettl, A. (2007). On the roughness of single-and bi-layer graphene membranes. *Solid State Communications*, *143*(1), 101-109.
- 29 Dharma-Wardana, M. W. C. (2007). Electronic structure and the minimum conductance of a graphene layer on SiO₂ from density functional methods. *Journal of Physics: Condensed Matter*, *19*(38), 386228.
- 30 Zhang, Y., Brar, V. W., Wang, F., Girit, C., Yayon, Y., Panlasigui, M., ... & Crommie, M. F. (2008). Giant phonon-induced conductance in scanning tunnelling spectroscopy of gate-tunable graphene. *Nature Physics*, *4*(8), 627-630.
- 31 Rutter, G. M., Jung, S., Klimov, N. N., Newell, D. B., Zhitenev, N. B., & Stroscio, J. A. (2011). Microscopic polarization in bilayer graphene. *Nature Physics*, *7*(8), 649-655.
- 32 Getchell, T. V., & Getchell, M. L. (1977). Early events in vertebrate olfaction. *Chemical Senses*, *2*(3), 313-326.

- 33 Pelosi, P., Pisanelli, A. M., Baldaccini, N. E., & Gagliardo, A. (1981). Binding of [3H]-2-isobutyl-3-methoxypyrazine to cow olfactory mucosa. *Chemical Senses*, *6*(2), 77-85.
- 34 Pelosi, P., Baldaccini, N. E., & Pisanelli, A. M. (1982). Identification of a specific olfactory receptor for 2-isobutyl-3-methoxypyrazine. *Biochemical Journal*, *201*(1), 245-248.
- 35 Vogt, R. G., & Riddiford, L. M. (1981). Pheromone binding and inactivation by moth antennae.
- 36 Buck, L., & Axel, R. (1991). A novel multigene family may encode odorant receptors: a molecular basis for odor recognition. *Cell*, *65*(1), 175-187.
- 37 Paczkowski, S., Weißbecker, B., Schöning, M. J., & Schütz, S. (2011). Biosensors on the basis of insect olfaction. In *Insect Biotechnology* (pp. 225-240). Springer Netherlands.
- 38 Damberger, F. F., Michel, E., Ishida, Y., Leal, W. S., & Wüthrich, K. (2013). Pheromone discrimination by a pH-tuned polymorphism of the *Bombyx mori* pheromone-binding protein. *Proceedings of the National Academy of Sciences*, *110*(46), 18680-18685.
- 39 Spinelli, S., Lagarde, A., Iovinella, I., Legrand, P., Tegoni, M., Pelosi, P., & Cambillau, C. (2012). Crystal structure of *Apis mellifera* OBP14, a C-minus odorant-binding protein, and its complexes with odorant molecules. *Insect biochemistry and molecular biology*, *42*(1), 41-50.
- 40 Dippel, S., Oberhofer, G., Kahnt, J., Gerischer, L., Opitz, L., Schachtner, J., ... & Angeli, S. (2014). Tissue-specific transcriptomics, chromosomal localization, and phylogeny of chemosensory and odorant binding proteins from the red flour beetle *Tribolium castaneum* reveal subgroup specificities for olfaction or more general functions. *BMC genomics*, *15*(1), 1141.
- 41 Mansurova, M., Klusák, V., Nešněrová, P., Muck, A., Doubský, J., & Svatoš, A. (2009). Design and synthesis of bombykol analogues for probing pheromone-binding protein–ligand interactions. *Tetrahedron*, *65*(5), 1069-1076.
- 42 Zhou, J. J., Robertson, G., He, X., Dufour, S., Hooper, A. M., Pickett, J. A., ... & Field, L. M. (2009). Characterisation of *Bombyx mori* odorant-binding proteins reveals that a general odorant-binding protein discriminates between sex pheromone components. *Journal of molecular biology*, *389*(3), 529-545.
- 43 Leal, W. S. (2005). Pheromone reception. In *The Chemistry of Pheromones and Other Semiochemicals II* (pp. 1-36). Springer Berlin Heidelberg.
- 44 Campanacci, V., Krieger, J., Bette, S., Sturgis, J. N., Lartigue, A., Cambillau, C., ... & Tegoni, M. (2001). Revisiting the specificity of mamestra brassicae and *Antheraea polyphemus* pheromone-binding proteins with a fluorescence binding assay. *Journal of Biological Chemistry*, *276*(23), 20078-20084.
- 45 Langmuir, I. (1912). The dissociation of hydrogen into atoms. 1. *Journal of the American Chemical Society*, *34*(7), 860-877.
- 46 Langmuir, I. (1913). Chemical reactions at very low pressures. II. The chemical clean-up of nitrogen in a tungsten lamp. *Journal of the American Chemical Society*, *35*(8), 931-945.

- 47 Langmuir, I. (1918). The adsorption of gases on plane surfaces of glass, mica and platinum. *Journal of the American Chemical society*, 40(9), 1361-1403.
- 48 Masel, R. I. (1996). *Principles of adsorption and reaction on solid surfaces* (Vol. 3). John Wiley & Sons.
- 49 Alsager, O. A., Kumar, S., Willmott, G. R., McNatty, K. P., & Hodgkiss, J. M. (2014). Small molecule detection in solution via the size contraction response of aptamer functionalized nanoparticles. *Biosensors and Bioelectronics*, 57, 262-268.
- 50 Zhu, B., Alsager, O. A., Kumar, S., Hodgkiss, J. M., & Travas-Sejdic, J. (2015). Label-free electrochemical aptasensor for femtomolar detection of 17 β -estradiol. *Biosensors and Bioelectronics*, 70, 398-403.
- 51 Frazier, K. M., & Swager, T. M. (2013). Robust cyclohexanone selective chemiresistors based on single-walled carbon nanotubes. *Analytical chemistry*, 85(15), 7154-7158.